Some aspects of suspension flows: Stokes to turbulent flows

by

Kyongmin Yeo

Sc.M., Applied Mathematics, Brown University, USA, 2007
Sc.M., Mechanical Engineering, Yonsei University, Korea, 2005
Sc.B., Civil Engineering, Yonsei University, Korea, 1999

Thesis

Submitted in partial fulfillment of the requirements for
the Degree of Doctor of Philosophy
in the Division of Applied Mathematics at Brown University

May 2011

This dissertation by Kyongmin Yeo is accepted in its present form
by the Division of Applied Mathematics as satisfying the
dissertation requirement for the degree of Doctor of Philosophy

Date..... .....
Martin R. Maxey, Director

Recommended to the Graduate Council

Date..... .....
George E. Karniadakis, Reader

Date..... .....
Jeffrey F. Morris, Reader

Approved by the Graduate Council

Date..... .....
Peter M. Weber
Dean of the Graduate School

The Vita of Kyongmin Yeo

Kyongmin Yeo was born on 22 February, 1977, in Seoul, Korea. He was an undergraduate student at Yonsei University, graduating with a B.Sc. in Civil Engineering on February 1999. Upon finishing his military service on June 2001 as a First Lieutenant, he started his graduate study in the Department of Civil Engineering at Yonsei University. Later, he changed his major to Mechanical Engineering and earned an M.Sc. in Mechanical Engineering from Yonsei University on February 2005. Subsequently, he came to Brown University to study towards a Ph.D. in Applied Mathematics under the direction of Professor Martin R. Maxey. He attained an Sc.M. in Applied Mathematics in 2007.

Honors and Awards

- Sigma Xi Award for excellence in research 2011
- Dissertation Fellowship, Brown University 2011
- Outstanding Master Thesis in Fluid Engineering, KSME 2005

Bibliography

Peer-reviewed Journal Papers

1. **K. Yeo** & M.R. Maxey, "Force-coupling simulations of dense finite-inertia suspensions in a linear shear flow," in preparation
2. **K. Yeo** & M.R. Maxey, "Numerical simulations of concentrated suspensions of monodisperse particles in a Poiseuille flow," *J. Fluid Mech.* in revision.
3. **K. Yeo** & M.R. Maxey, "Anomalous diffusion in wall-bounded suspensions of non-Brownian particles under steady shear," *Europhys. Lett.*, **92**, 24008 (2010)
4. **K. Yeo**, B.-G. Kim & C. Lee, "On the near-wall characteristics of acceleration in turbulence," *J. Fluid Mech.*, **659**, 405 (2010)
5. **K. Yeo** & M.R. Maxey, "Rheology and ordering transitions of non-Brownian suspensions in a confined shear flow: effects of external torques," *Phys. Rev. E*, **81**, 062501 (2010)

6. **K. Yeo** & M.R. Maxey, "Ordering transitions of non-Brownian suspensions in confined steady shear flow," *Phys. Rev. E*, **81**, 051502 (2010).

7. **K. Yeo** & M.R. Maxey, "Dynamics of concentrated suspensions of non-colloidal particles in Couette flow," *J. Fluid Mech.*, **649**, 205 (2010)

8. **K. Yeo** & M.R. Maxey, "Simulation of concentrated suspensions using the force-coupling method," *J. Comput. Phys.*, **229**, 2401 (2010)

9. **K. Yeo**, S. Dong, E. Climent & M.R. Maxey "Modulation of homogeneous turbulence seeded with finite size bubbles or particles," *Int. J. Multiphase flow*, **36**, 221 (2010)

10. **K. Yeo**, B.-G. Kim & C. Lee, "Eulerian and Lagrangian statistics in stably stratified turbulent channel flows," *J. Turbulence*, **10**, 17 (2009)

11. J. Jung, **K. Yeo** & C. Lee, "Behavior of heavy particles in isotropic turbulence," *Phys. Rev.* E, **77**, 016307 (2008)

12. E. Climent, **K. Yeo**, M.R. Maxey & G.E. Karniadakis "Dynamic self-assembly of spinning particles," *J. Fluid Eng.*, **129**, 379 (2007).

13. A.M. Reynolds, **K. Yeo** & C. Lee, "Anisotropy of acceleration in turbulent flows," *Phys. Rev.* E, **70**, 017302 (2004)

14. C. Lee, **K. Yeo** & J.-I. Choi, "Intermittent nature of acceleration in near wall turbulence," *Phys. Rev. Lett.*, **92**, 144502 (2004)

15. J.-I. Choi, **K. Yeo** & C. Lee, "Lagrangian statistics in turbulent channel flow," *Phys. Fluids*, **16**, 779 (2004)

16. S.-U. Choi, H. Kang & **K. Yeo**, "Flow and sediment transport in emerging vegetated zone," *Ecology Civil Eng.*, **6**, 87 (2003)

Conference Presentations

1. **K. Yeo** & M.R. Maxey, "Anomalous diffusion of non-colloidal suspensions in a Couette flow," APS DFD 63rd Annual Meeting, CA, U.S., 2010

2. **K. Yeo** & M.R. Maxey, "Numerical simulations of concentrated, non-colloidal suspensions in Poiseuille flows," SOR 82nd Annual Meeting, NM, U.S., 2010

3. **K. Yeo** & M.R. Maxey, "Order transition in non-colloidal Couette suspension flows:effects of external torques," APS DFD 62nd Annual Meeting, MN, U.S., 2009

4. **K. Yeo** & M.R. Maxey, "Numerical simulation of concentrated suspensions of non-colloidal particles in Couette flow," SOR 81st Annual Meeting, WI, U.S., 2009

5. **K. Yeo** & M.R. Maxey, "Dynamic self-assembly of non-colloidal particles in Couette flow," SOR 81st Annual Meeting, WI, U.S., 2009

6. L.-P. Wang, H. Gao, L.-S. Luo, Y. Peng, **K. Yeo** & M.R. Maxey, "Comparing particle-resolved simulation methods for moving particles in a viscous fluid," APS DFD 61st Annual Meeting, TX, U.S., 2008

7. J. Lim, **K. Yeo** & C. Lee, "On the modification of near-wall structures in stably stratified turbulence," APS DFD 58th Annual Meeting, IL, U.S., 2005

8. J. Jeong, **K. Yeo** & C. Lee, "Dispersion of heavy particles in isotropic turbulence," APS DFD 58th Annual Meeting, IL, U.S., 2005

9. C. Lee, J. Jeong & **K. Yeo**, "Acceleration, enstrophy and dissipation in isotropic turbulence," APS DFD 58th Annual Meeting, IL, U.S., 2005

10. **K. Yeo** & C. Lee, "On the modification of near-wall structures in stably stratified turbulence," APS DFD 57th Annual Meeting, WA, U.S., 2004.

11. **K. Yeo** & C. Lee, "Modification of near-wall turbulent characteristics under stable stratification," The 6th KSME-JSME Thermal and Fluid Engineering Conference, Jeju, Korea, 2004.

12. **K. Yeo** & C. Lee, "On the acceleration in inhomogeneous turbulence," APS DFD 56th Annual Meeting, NJ, U.S., 2003.

13. A.M. Reynolds, **K. Yeo** & C. Lee, "On the anisotropy of Lagrangian accelerations in turbulence," APS DFD 56th Annual Meeting, NJ, U.S., 2003.

14. **K. Yeo** & C. Lee,"Acceleration statistics in turbulent channel flow," 5th Asian Computational Fluid Dynamics, Busan, Korea, 2003.

Acknowledgments

This thesis is dedicated to the memory of my grandfather, in whose final days I could not be with, and to my grandmother, who is losing memory of me.

First of all, I would like to thank my advisor Professor Martin Maxey for his guidance, support, and particularly patience. I cannot express enough how much I owe him. He has been always kind and supportive in person while keeping high standard in research. Thanks to his help, I could enjoy my life and remain active in research. I would like to express my gratitude to Professor George Karniadakis for his encouragement over the years. In particular, I would like to acknowledge that the huge amount of computing time he provided me in my early graduate years was very helpful for me developing my specialty in high performance computing. I wish to thank Professor Jeffrey Morris for his service as a reader and for his time and effort coming all the way from New York. Although we have not met often, his short lecture at Brown University and discussions with him were very inspiring.

I am indebted to the faculty members and staffs for the high quality classes and the warm, welcoming atmosphere here in the Division of Applied Mathematics. Especially, I thank Madeline Brewster for helping me in many ways throughout my graduate study and for her coffee which is one of the major contributors to the completion of this thesis.

I would like to thank all of the members of the CRUNCH group. It has been always my pleasure chitchatting with them. Particularly, I would like to express my deep gratitude to Igor Pivkin, Eric Keaveny, Wenxiao Pan, and Huan Lei for their insightful discussions and friendship. I am sure our paths will cross again someday. I will never forget the Korean gang for turning a potentially (almost surely?) dull graduate student life into a pleasant one; Hyoungsu (Boss), Minseok (All-round sports player), and Heyrim (Sleeping beauty).

Last, but foremost, I cannot thank enough to my wife, Sung Won, for her love and encouragement over the course of this *long* graduate study. It would have been more difficult if it were not for her love. I would like to express my deepest gratitude to all of my family members in Korea for their continuous support and encouragement. It would have not been possible if it were not for their support. I love all of you!

This work was supported in part by funding from DARPA under an award ATO-Friction Drag Technologies Program and by NSF under an award DUE-0734234. Support of HPC

resources from the Arctic Region Supercomputing Center at the University of Alaska, Fairbanks as part of the DoD HPCMP and from the National Institute for Computational Sciences provided by NSF under TG-CTS090097.

Contents

List of Tables

List of Figures

Chapter 1

Introduction

1.1 Introduction

Solid-fluid multiphase flow is ubiquitous in nature as well as in technological applications. The multiphase flow systems of current interest range from microscale mixing and mass transport, such as blood flow, microbial swimming, suspensions of hard spheres or soft materials in microfluidic devices, to large scale environmental flows, *e.g.* sediment transport in river or ocean, bioagents or pollutant dispersion in atmospheric boundary layer and ocean mixed layer, and droplet formation in wet clouds, to name a few. Due to its immense range of applications, study of the multiphase flow has been an important subject of many disciplines. One of the major branches of the study is "suspension flows" led by Chemical and Biomechanical Engineers. The study of suspension flows has been focused largely on rheology and self-diffusion of solid particles suspended in a very viscous liquid, *i.e.* in the limit of Stokes flows [5, 159, 203]. Particle suspensions in the Stokes limit have been a subject of great interest in the soft matter physics community, where usually systems under thermodynamic equilibrium conditions, *i.e.* without flow, are studied in the framework of statistical mechanics [129, 184]. "Turbulent dispersed flow" has attracted attention of the Mechanical/Environmental Engineering and Atmospheric Science communities [12, 20, 209]. In turbulent dispersed flows, particular interest has been paid to the dispersion of passive tracer or point particles of which radius is assumed to be much smaller than the smallest lengthscale of turbulence, Kolmogorov lengthscale. Major objectives of this thesis are (1) to develop a numerical method which can be easily applied to study these wide range of solid-fluid multiphase flows and (2) to contribute to our understanding on fundamental physics of

solid-fluid interactions in a wide range of flow parameters; from the zero-Reynolds-number Stokes suspensions to high-Reynolds-number turbulent suspensions.

Suspensions of micron or submicron particles in a viscous liquid are prevalent in many biological and engineering systems. For example, the diameter of human red blood cell is about $6 - 7\mu m$ and usually the lengthscale of bacteria is $O(1) \sim O(10)\mu m$. Typical size of colloids in many technological applications is $< O(1)\mu m$ and the particles of current interest in microfluidic lab-on-a-chip devices, MEMS/Bio-MEMS, and food processing are usually in the range of $O(1) \sim O(10)\mu m$. The particle Reynolds number is defined as $Re_p = \frac{\rho_f \dot{\gamma} D^2}{\mu_f}$, in which ρ_f and μ_f are, respectively, density and viscosity of the liquid, $\dot{\gamma}$ is the local shear rate, and D is the characteristic lengthscale of the particle, usually the particle radius. In many of the aforementioned systems, Re_p is in the range of $< O(10^{-3})$, in which case the hydrodynamics is governed by viscous forces, *i.e.* Stokes flow. Another important flow parameter is these microscale systems is the Péclet number, which is the ratio of the advection by the flow to the thermal diffusion, $Pe = \frac{6\pi\mu_f \dot{\gamma} a^3}{k_B T}$, and $k_B T$ is the thermal energy. In many flowing suspensions of $O(1)\mu m$ particles, the timescale of flow-induced self-diffusion is much smaller than that of the thermal diffusion. Here, we consider only non-Brownian or non-colloidal suspension flows, suspensions in the limit of large Pe ($Pe > 10^3$), where the hydrodynamic interaction determines the suspension dynamics.

As the Stokes equations are linear partial differential equations, in principle, hydrodynamic interaction between the suspended particles can be found analytically. However, in practice, analytical computation of multibody interaction becomes mathematically too complicated even for a couple of particles. If we confine our interest to suspensions of solid particles in a Newtonian fluid, thanks to the pioneering works by Batchelor [13, 14, 15], the mechanics of suspension flows up to semi-dilute systems, in which the hydrodynamic interaction of a particle-pair is considered, is now well understood. However, still our understanding on the dynamics of concentrated suspensions is far from complete. Following Stickel & Powell [203], we define concentrated suspensions as the suspension flows in which the average distance between the suspended particles is smaller than the particle radius, where both short-range lubrication and interparticle forces and long-range multibody hydrodynamic interactions are important in the dynamics. Typically, we assume the suspension is concentrated if the volume fraction of solid phase is larger than 10% of the total volume, $\phi > 0.1$. In contrast to the theories in the dilute to semi-dilute limit, concentrated

suspensions of hard spheres in a Newtonian liquid exhibit non-Newtonian behaviors, such as the existence of normal stress differences and transient responses of rheology upon step changes of $\dot{\gamma}$. Over the last three decades, the bulk behavior of suspension flows has been studied extensively notably by the research groups led by Acrivos [5, 6] and Brady [23, 24] (see [159, 203] for review).

While there is a large volume of literature devoted to the bulk behavior of concentrated suspensions in a homogeneous flow, *i.e.* far from a solid boundary, still there are only a very limited number of studies about the suspension dynamics under a geometric confinement, in which the presence of an impenetrable boundary introduces inhomogeneity to the system. If the size of a container is much larger than the characteristic lengthscale of the suspension, the suspension field in the core of the container can be assumed as locally homogeneous. However, in many microfluidic systems of current interest, the confinement size is on the order of 10-particle radii and the effects of the confinement suspension dynamics is significant. For example, Zarraga *et al.* [241] have shown, in their experiments in a parallel plate geometry, that the effective viscosity is a function of the channel height if the gap width is less than forty-particle radii. Theoretical analysis of confined suspensions becomes much more complicated than that in homogeneous suspensions, as the suspension field becomes a function of the distance from the wall. Tözeren & Skalak [210], whose contribution has been largely underappreciated compared to the importance to the theoretical analysis of inhomogeneous suspensions, were one of the first who pointed out that the ergodic principle of equating volume averages to ensemble averages is no longer valid in wall-bounded suspensions. Both experiments and numerical simulations of wall-bounded concentrated suspension flows are very challenging. It is only recently that three-dimensional simulations of wall-bounded concentrated suspensions have become available. Using the novel lattice-Boltzmann approach developed by Nguyen & Ladd [162], there are several studies of concentrated suspensions in wall-bounded Couette flows [116, 119, 215]. Yet, most studies have been focused on the bulk properties and the effects of the wall-induced inhomogeneity on the suspension dynamics has remained largely unexplored. In this thesis, we present a new numerical method to simulate wall-bounded concentrated suspension flows and study the effects of the confinement on the suspension dynamics both in shear and pressure-driven flows.

Study of turbulent dispersed flows has been one of the major research topics in the fluid

mechanics community due to its relevance to a wide range of applications, such as prediction of dispersion of airborne pollutant in atmospheric boundary layer, cloud microphysics, sediment transport in river or ocean, and particle transport in human respiratory system. In turbulent dispersed flows of interest, the volume fraction of the particle phase is usually in the semi-dilute regime ($\phi < 0.1$). While the suspension dynamics are determined by the hydrodynamic interaction between the suspended particles in Stokes-flow suspensions, in turbulent suspension flows, any long-range hydrodynamic interaction between the particles is screened by the fluid inertia and the dynamics is governed mostly by the inertial responses of the suspended particles to the small scale turbulent coherent structures. One of the important parameters in turbulent dispersed flows, which represents the inertial response of the particles, is the turbulent Stokes number St defined as the ratio of the particle relaxation timescale $\tau_p = (2\rho_p + \rho_f)a^2/9\mu_f$ to the turbulent eddy turnover time $T_e = u'^2/\epsilon$. Here, ρ_p and ρ_f are, respectively, density of the particle and the fluid, u'^2 is root-mean square of velocity fluctuations, and ϵ is the dissipation rate. Now, it is well known that, depending on St, the suspended particles tend to be accumulated in some regions of a specific flow topology [145, 202, 220], which simultaneously modifies the turbulent flows. Since an analytical solution is not available for turbulent flows, most of our current knowledge on the physics of turbulent dispersed flows comes from experiments and numerical simulations.

Direct numerical simulation, which solves the Navier-Stokes equations without any turbulence model, has been providing valuable information on the physics of turbulent flows. However, in many of the previous direct numerical studies of turbulent dispersed flows, the radius of the suspended particles is assumed to be much smaller than the Kolmogorov scale and the hydrodynamic interaction between the particles is neglected. In this point particle approach, the momentum transfer between the particle and fluid phases is usually computed from a simple drag force based on the slip velocity. Hwang & Eaton [94, 95] showed in their experiments that, while the point-particle method captures some of the basic features of the particle-turbulence interaction qualitatively, the turbulence modulation by the particle phase is significantly underestimated. With the rapid increase in the computation power, particle-resolved direct numerical simulations of the turbulence modulation by suspensions of finite-size solid particles have become plausible more recently [138, 208, 243]. In this thesis, we study turbulence modulation by suspensions of three different types of finite-size particles; heavy particles, neutrally buoyant particles, and bubbles (massless particles) by

employing the force-coupling method.

1.2 Outline

In Chapter 2, the force-coupling method (FCM) is briefly reviewed. A higher-order FCM multipole (force quadrupole) is discussed. We present the semi-discretized equations of the force-coupling method and show that FCM is equivalent to a matrix-free method to solve a grand-mobility problem. Built upon the matrix relation, we develop the lubrication-corrected FCM (LC-FCM). A solution procedure to use LC-FCM for finite-Reynolds-number suspensions is presented. Here, LC-FCM is tested against various configurations and the results are compared with the previous theoretical, experimental, and numerical results. Most of the results in Chapter 2 are from Yeo & Maxey [233]

Chapter 3 describes the fundamental mechanisms of suspensions of non-colloidal, neutrally-buoyant spheres in a wall-bounded Couette flow at zero Reynolds number. We report the basic effects of the inhomogeneity induced by the solid boundary on suspension dynamics by investigating the particle density fluctuation, rheological parameters, and suspension microstructure as functions of the distance from the wall. A fundamental issue of the appropriate lengthscale of concentrated suspensions is discussed through the changes in the diffusive behavior of the suspended particles. We report on the wall-induced ordering transitions of the suspended particles. Chapter 3 is based on Yeo & Maxey [229, 230, 231, 232].

LC-FCM simulations of concentrated suspensions in a Poiseuille flow are performed and the results are shown in Chapter 4. The ensemble averaged particle-phase velocity and local volume fraction profiles are compared with the previous experiments. Rheological parameters are calculated from a phase-averaging procedure and compared with the rheological models in suspension models. The results are reported in Yeo & Maxey [234].

We consider hydrodynamic interaction between a pair of coplanar spheres co-rotating in response to a rotating magnetic field at finite Reynolds numbers in Chapter 5. It is shown that a pair of rotating coplanar spheres at finite-Reynolds-number flows experiences a repulsive hydrodynamic force in the axis connecting their centers due to the secondary flow induced by the nonlinear interaction. The FCM solution of the secondary flow is compared with the regular-perturbation solution of Bickley [17]. Most of the results in Chapter 5 are from the work with Professor Climent [39].

Chapter 6 reports the LC-FCM results of concentrated suspensions of neutrally buoyant particles in a homogeneous linear shear flow under finite fluid inertia. The changes of the velocity statistics, such as the velocity fluctuations, velocity auto-correlation functions, and self-diffusion, and the rheological parameters, *e.g.* particle stresses, are thoroughly investigated as functions of the particle Reynolds number, $Re_{\dot{\gamma}} = \frac{\rho_f \dot{\gamma} a^2}{\mu_f}$. The behavior of the particle stresses are discussed by studying the changes in the pair-distribution function and a weighted pair-distribution function with $Re_{\dot{\gamma}}$.

In Chapter 7, we report the results of the FCM simulations of turbulence modulation by suspensions of finite size particles of different densities; heavy and neutrally buoyant particles, and (massless) bubbles. We present both Eulerian statistics of the mixture and Lagrangian statistics of the particle phase. The Eulerian statistics for the suspensions of heavy particles are compared with the previous numerical simulations by ten Cate *et al.* [208]. Chapter 7 is based on Yeo *et al.* [228].

Finally, Chapter 8 devoted to concluding remarks and brief discussions. Future research directions are also suggested in this chapter.

Chapter 2

Numerical methods

2.1 Introduction

Numerical simulations of monodisperse suspension flows in uniform shear have had a large impact on the characterization and modeling of low Reynolds number suspensions. The principal tools have been Stokes Dynamics (SD)[24], multipole expansions [35, 121, 187], and boundary integral methods [175]. Lattice-Boltzmann methods (LBM) bridge both finite Reynolds number and low Reynolds number systems and have also contributed [162, 163]. The force-coupling method (FCM) [135, 144] and subsequent developments, bridge both Stokes flows and finite, low Reynolds number systems. FCM may be used to simulate large systems of particles in both open and wall-bounded flows in fully three-dimensional configurations.

For the accurate simulation of Stokes flow, a numerical method should be able to capture both the long-range multi-body interactions and the short-range lubrication interactions. Especially, the singular nature of the lubrication forces hinders the development of numerical schemes. For example, the most straightforward and exact numerical method would be the direct numerical simulation with an arbitrary Lagrangian-Eulerian technique [91, 92]. However, considering that the lubrication forces for the normal and tangential motions between a particle pair are, respectively, $\sim 1/\epsilon$ and $\log \epsilon$, in which $a\epsilon$ denotes the separation distance between two particles and a is the particle radius, the grid spacing should be smaller than at least $10^{-3}a \sim 10^{-4}a$ to resolve the lubrication forces. Correspondingly, the time step size also should be very small, of the order of $10^{-3} \sim 10^{-4}$, making long term simulations of the suspension dynamics too costly.

In Stokes flow, the hydrodynamic interactions are determined solely by the instantaneous configuration of particles. Using the special properties of Stokes flow, several numerical methods have been developed focusing on computing hydrodynamic interactions rather than resolving the whole flow field. The multipole expansion is a representative approach to consider hydrodynamic interactions between particles. However, Cichocki & Felderhof [35] reported that the number of multipole moments needed to resolve the hydrodynamic interaction becomes impractically large as the gap between particles becomes so small that the lubrication force plays an important role. Durlofsky *et al.* [63] developed the Stokesian Dynamics method, which is a low order multipole representation, supplemented by short-range lubrication forces, to compute the position and movement of suspended particles. In the Stokesian Dynamics, they assumed the lubrication interaction can be added in a pair-wise manner in the resistance formulation, which has become a standard approach for incorporating the lubrication forces [36, 121, 162]. Sierou & Brady [196] developed the Accelerated Stokesian Dynamics (ASD) method and performed the simulations of up to 1000 particles [198].

The boundary element method (BEM) is another distinguishing numerical method for Stokes flows, see for example [175]. BEM can calculate the hydrodynamic interactions in particulate suspensions with greater accuracy. However, even here some form of lubrication or contact forces must be included between rigid particles. Ingber *et al.* [97] have developed a traction-corrected BEM which can accurately calculate the lubrication interaction. Although BEM can simulate wall-bounded suspensions and suspension of particles with arbitrary shapes [176, 177], due to the high computational cost most simulations are done in 2-dimensions or with relatively small numbers of particles.

Since Nguyen & Ladd [162] implemented the lubrication interaction into the lattice-Boltzmann simulation, LBM has become popular for the suspensions in the low to finite Reynolds number flows [118, 163, 215]. Compared to SD, LBM is computationally inexpensive and a rigid wall boundary can be included without any special treatment, while present techniques for SD use an image method [18, 207] or wall particles [164, 199] to represent a rigid wall.

Maxey & Patel [144] developed the force-coupling method (FCM) for Stokes flow by replacing the Dirac delta function in the standard multipole expansion [185] by a localized force envelope. The force-coupling method has been verified [49, 136, 135] and applied in

many suspension flows; for example, a sedimentation problem [51], bimodal suspensions [2], turbulent flows [224], and biological flows [108]. Since multi-body hydrodynamic interactions are accounted for by solving the Stokes equation, the computational cost of FCM depends on the choice of the Stokes solver. In a periodic domain, the long-range hydrodynamic interactions can be calculated in $O(N_p log N_p)$ operations using a Fourier spectral method, in which N_p is the number of particles. Dance & Maxey[51] performed the numerical simulations of particle sedimentation with up to 10,000 particles. The force-coupling method can be implemented with any existing flow solver by adding functions to integrate and distribute the force envelope. Recently, Liu *et al.* [131] showed that the force-coupling method can simulate suspensions of ellipsoidal particles by appropriately rescaling the force envelopes.

In the force-coupling method, the translational and angular velocities of a particle are estimated by the local average of the fluid velocity weighted by the corresponding force envelopes. This approach has a computational advantage by reducing the number of grid points necessary to resolve a particle. Once the resolution is fine enough to resolve the force envelope, FCM can accurately reproduce the far-field solution. Typically, it requires only $a/\Delta x \simeq 3$ to resolve a particle in which Δx is the grid spacing. This is less than other methods, such as the immersed boundary method or the lattice-Boltzmann simulations. On the other hand, it has a disadvantage that the near field solution is not correctly resolved. When two particles are close, the force-coupling method cannot reproduce the lubrication effects [135]. As a result, the force-coupling method has been used mainly for low volume fractions, $\phi < 0.1$.

Dance & Maxey [50] developed a method to incorporate the lubrication effects into the force-coupling method based on the exact solution of the viscous lubrication interactions of a particle-pair. They employed a predictor-corrector type approach. First, the far-field interaction is calculated by the standard FCM to estimate the lubrication force and then the lubrication force is used as a feedback force in the mobility formulation. By construction, their method can reproduce the exact particle velocities for a particle-pair interaction. At low volume fractions in which most lubrication interactions are from particle doublets, the 'lubrication barrier' would be sufficient [2]. However, it is difficult to generalize the approach to include multi-body interactions, which generally require the addition of lubrication interactions to a resistance formulation [63].

The main goal of this chapter is to develop an efficient method to incorporate the lubrication forces for general volume fractions into the force-coupling method. First, a brief review of the force-coupling method is given. For the particles near a wall, the force envelopes are modified to correctly account for particle-wall hydrodynamic interactions. A procedure to include an FCM quadrupole is proposed. We derive the discretized equations of FCM and show that the force-coupling method in Stokes flow can be expressed in terms of a mobility matrix problem. A new efficient and robust iterative scheme to calculate the stresslet is introduced. The lubrication correction method for the force-coupling method is developed by applying the pair-wise additivity approximation. The force-coupling procedure for Navier-Stokes suspensions is then discussed. The numerical methods used to solve the Stokes equations in a tri-periodic and a wall-bounded domain are explained. The numerical simulations of suspensions of monodisperse spheres in an infinite domain and a channel are performed to verify the present lubrication correction method.

2.2 Force-coupling method: Stokes flow

2.2.1 Review of the force-coupling method

The equation of the fluid motion with the force-coupling method is

$$\boldsymbol{\nabla} p(\boldsymbol{x}) = \mu \nabla^2 \boldsymbol{u}(\boldsymbol{x}) + \boldsymbol{f}(\boldsymbol{x}), \tag{2.1}$$

$$\boldsymbol{\nabla} \cdot \boldsymbol{u} = 0, \tag{2.2}$$

in which p is pressure, μ is viscosity of the fluid, $\boldsymbol{u}$ is fluid velocity. The force density $\boldsymbol{f}$ is defined as

$$f_i(\boldsymbol{x}) = \sum_{n=1}^{N_p} \left\{ F_i^n \Delta_M(\boldsymbol{x} - \boldsymbol{Y}^n) + G_{ij}^n \frac{\partial}{\partial x_j} \Delta_D(\boldsymbol{x} - \boldsymbol{Y}^n) \right\}, \tag{2.3}$$

where F_i and G_{ij} are the force monopole and force dipole moments, respectively. Δ_M and Δ_D are the FCM force envelopes defined as

$$\Delta_M(\boldsymbol{x}) = \frac{1}{(2\pi\sigma_M^2)^{3/2}} \exp\left(-\frac{\boldsymbol{x}^2}{2\sigma_M^2}\right), \tag{2.4}$$

$$\Delta_D(\boldsymbol{x}) = \frac{1}{(2\pi\sigma_D^2)^{3/2}} \exp\left(-\frac{\boldsymbol{x}^2}{2\sigma_D^2}\right). \tag{2.5}$$

The length scales σ_M and σ_D are chosen to satisfy the overall energy budget for the flow [135, 144],

$$\frac{a}{\sigma_M} = \sqrt{\pi}, \tag{2.6}$$

$$\frac{a}{\sigma_D} = \left(6\sqrt{\pi}\right)^{1/3}. \tag{2.7}$$

These expressions for the length scales ensure that the exact Stokes drag is obtained and further that corresponding degenerate force quadrupoles and the linear Faxen terms for finite particle size and local flow variations are estimated to good approximation with no additional terms.

Once $\boldsymbol{u}(\boldsymbol{x})$ is obtained, the velocity of each particle $\boldsymbol{V}^n(t)$ is found by the weighted volume integral of $\boldsymbol{u}(\boldsymbol{x})$ [144],

$$\boldsymbol{V}^n = \int \boldsymbol{u}(x)\Delta_M(\boldsymbol{x} - \boldsymbol{Y}^n)d^3\boldsymbol{x}. \tag{2.8}$$

Similarly, the angular velocity of each particle $\boldsymbol{\Omega}^n$ is calculated from

$$\Omega_i^n = \frac{1}{2}\int \epsilon_{ijk}\frac{\partial u_k}{\partial x_j}\Delta_D(\boldsymbol{x} - \boldsymbol{Y}^n)d^3\boldsymbol{x}. \tag{2.9}$$

In dynamic simulation, the location of a particle is determined by numerically integrating the equation of particle motion,

$$\frac{d\boldsymbol{Y}^n}{dt} = \boldsymbol{V}^n. \tag{2.10}$$

Here, we use the third-order Adam-Bashforth method to solve equation (2.10).

The monopole coefficient $\boldsymbol{F}^n$ is the force of the particle on the fluid, which is the sum of forces on the particle other than the hydrodynamic interaction, and include gravity, short-range inter-particle surface forces, magnetic forces, and random Brownian forces.

The dipole coefficient G_{ij} consists of symmetric and anti-symmetric parts. The anti-symmetric part T_{ij} is related to the torque exerted by the particle on the fluid,

$$T_{ij} = \frac{1}{2}\epsilon_{ijk}T_k^{ext}, \tag{2.11}$$

in which $\boldsymbol{T}^{ext}$ in turn denotes an external torque on the particle. The symmetric part S_{ij}

corresponds to a stresslet acting on the fluid. S_{ij} is found from the condition that the contribution of the stresslet to the total rate of work on the fluid is zero [135]. In other words, S_{ij} is chosen to satisfy the constraint,

$$E_{ij} = \frac{1}{2}\int \left(\frac{\partial u_i}{\partial x_j} + \frac{\partial u_j}{\partial x_i}\right) \Delta_D(\boldsymbol{x} - \boldsymbol{Y}^n(t)) d^3\boldsymbol{x} = 0, \tag{2.12}$$

for each particle. Since S_{ij} depends on the rate-of-strain, it has to be determined by an iterative method. Lomholt *et al.* [136] and Dance & Maxey [50] described steepest-decent iterative methods to accomplish this. In section 2.2.4 a conjugate gradient procedure to solve equation (2.12) efficiently is introduced.

2.2.2 Quadrupole expansion

In this section, we extend the force-coupling method to include a higher-order multipole. In Lomholt & Maxey [135], it is shown that the force-coupling method with force dipole gives a good approximation to the exact Stokes solution in uniform straining flows. As such, the force-coupling method can be used reliably for non-uniform flows, if the lengthscale of the spatial variation of the fluid velocity is large enough compared to the particle diameter that the strain rate can be assumed to be uniform on the particle scale. However, in some special cases (see, *e.g.*, chapter 9 of Keaveny [107]) or for large particles in a quadratic flow, a higher-order multipole needs to be considered.

2.2.2.1 Traceless quadrupole

Consider the Stokes equations with a singularity and its derivatives at the origin,

$$\boldsymbol{\nabla} p(\boldsymbol{x}) = \mu\nabla^2\boldsymbol{u}(\boldsymbol{x}) + \sum_{p=0}^{\infty} \boldsymbol{F}_{\xi_1\cdots\xi_p} \frac{\partial^p}{\partial x_{\xi_1}\cdots\partial x_{\xi_p}} \delta(\boldsymbol{x}). \tag{2.13}$$

The fluid field induced by the singularities can be obtained by the Green's function for Stokes flows and its derivatives. The Green's function for the Stokes equations, or so called the Oseen tensor, is given by

$$\mathcal{G}_{ij}(\boldsymbol{x}) = \left(\frac{\delta_{ij}}{r} + \frac{x_i x_j}{r^3}\right), \tag{2.14}$$

in which $r = |\boldsymbol{x}|$. The fundamental solution of the Stokes equations, so called Stokeslet, is given by

$$u_i(\boldsymbol{x}) = \frac{1}{8\pi\mu} G_{ij} F_j. \tag{2.15}$$

Then, the solution of (2.13) can be written as the sum of the Stokeslet and its derivatives,

$$u_i(\boldsymbol{x}) = \frac{1}{8\pi\mu} \sum_{p=0}^{\infty} F_j \, \xi_1 \cdots \xi_p \frac{\partial^p}{\partial x_{\xi_1} \cdots \partial x_{\xi_p}} \mathcal{G}_{ij}. \tag{2.16}$$

The flow field induced by an object in Stokes flows can be obtained by a combination of these singularity solutions. For example, a sphere moving in a quiescent flow is given by the sum of the Stokeslet and the degenerate quadrupole,

$$u_i(\boldsymbol{x}) = \left(1 + \frac{a^2}{6}\nabla^2\right) \frac{\mathcal{G}_{ij}}{8\pi\mu} F_j, \tag{2.17}$$

in which a is the particle radius.

Consider a sphere in an undisturbed flow ($\boldsymbol{u}^\infty$) given by

$$u_i^\infty = S_{ijk} x_j x_k, \tag{2.18}$$

in which the third-order tensor S_{ijk} is chosen to satisfy

$$\frac{\partial E_{ij}^\infty}{\partial x_k} = C. \tag{2.19}$$

Here, E_{ij}^∞ is the strain rate $E_{ij} = 1/2(\partial_j u_i + \partial_i u_j)$ and C is a constant. To satisfy the divergence-free ($\boldsymbol{\nabla} \cdot \boldsymbol{u}^\infty = 0$) and traceless ($\nabla^2 \boldsymbol{u}^\infty = 0$) conditions, the third-order tensor S_{ijk} should satisfy

$$\begin{aligned} S_{iij} &= S_{iji} = 0, \\ S_{ijj} &= 0. \end{aligned}$$

And, from the symmetry of the strain rate,

$$S_{ijk} = S_{ikj}.$$

The disturbance flow generated by a sphere in $\boldsymbol{u}^{\infty}$ is given by a traceless force quadrupole and a degenerate force sextupole,

$$u_i^D(\boldsymbol{x}) = \left(1 + \alpha\nabla^2\right) \frac{\mathcal{G}_{ij,\,kl}(r)}{8\pi\mu} Q_{jkl}, \tag{2.20}$$

in which Q_{jkl} denotes the quadrupole strength and α is a constant to be determined from the Faxén's law. The quadrupole is given by

$$\begin{aligned} \frac{\partial^2 \mathcal{G}_{ij}}{\partial x_k \partial x_l} &= \frac{1}{r^3}\left(-\delta_{ij}\delta_{kl} + \delta_{jk}\delta_{il} + \delta_{ik}\delta_{jl}\right) \\ &- \frac{3}{r^5}(-\delta_{ij}x_k x_l + \delta_{jk}x_i x_l + \delta_{ik}x_j x_l + \delta_{il}x_j x_k + \delta_{jl}x_i x_k + \delta_{kl}x_i x_j) \\ &+ \frac{15}{r^7} x_i x_j x_k x_l, \end{aligned} \tag{2.21}$$

and, similarly, the degenerate-sextupole is

$$\begin{aligned} \nabla^2 \frac{\partial^2 \mathcal{G}_{ij}}{\partial x_k \partial x_l} &= -\frac{6}{r^5}\left(\delta_{ij}\delta_{kl} + \delta_{jk}\delta_{il} + \delta_{ik}\delta_{jl}\right) \\ &+ \frac{30}{r^7}(\delta_{ij}x_k x_l + \delta_{jk}x_i x_l + \delta_{ik}x_j x_l + \delta_{il}x_j x_k + \delta_{jl}x_i x_k + \delta_{kl}x_i x_j) \\ &- \frac{210}{r^9} x_i x_j x_k x_l. \end{aligned} \tag{2.22}$$

As the sphere is not moving, the no-slip boundary condition on the sphere surface is $\boldsymbol{u}^D(r = a) = -\boldsymbol{u}^{\infty}(r = a)$. To match the no-slip boundary condition, the terms in $\boldsymbol{u}^D$ of which order is higher than those in $\boldsymbol{u}^{\infty}$ need to vanish, which in turn determines the constant α as $\alpha = a^2/14$, and so

$$u_i^D(\boldsymbol{x}) = \left(1 + \frac{a^2}{14}\nabla^2\right) \frac{\mathcal{G}_{ij,\,kl}}{8\pi\mu} Q_{jkl} \quad \text{for } r \geq a. \tag{2.23}$$

Matching the no-slip boundary condition, the quadrupole strength Q_{ijk} can be related to S_{ijk} as

$$\begin{aligned} &\frac{Q_{jkl}}{7a^3}\Big[(-10\delta_{ij}\delta_{kl} + 4\delta_{jk}\delta_{il} + 4\delta_{ik}\delta_{jl}) \\ &\quad - \frac{6}{a^2}(-6\delta_{ij}x_k x_l + \delta_{jk}x_i x_l + \delta_{ik}x_j x_l + \delta_{il}x_j x_k + \delta_{jl}x_i x_k + \delta_{kl}x_i x_j)\Big] \\ &\quad = -8\pi\mu S_{ijk} x_j x_k. \end{aligned} \tag{2.24}$$

Applying the divergence-free, traceless, and symmetry conditions yields

$$Q_{ijk} = -\frac{7}{3}\pi\mu a^5 S_{ijk}. \tag{2.25}$$

The corresponding Stokes equations with the *finite force* quadrupole may be written as

$$\frac{\partial p}{\partial x_i} = \mu\nabla^2 u_i + Q_{ijk}\frac{\partial^2 \Delta}{\partial x_j \partial x_k}, \tag{2.26}$$

in which

$$\Delta(r) = \frac{1}{(2\pi\sigma^2)^{3/2}}\exp\left(-\frac{r^2}{2\sigma^2}\right). \tag{2.27}$$

Here, the lengthscale σ is to be determined. Similar to the standard multipole expansion, the disturbed velocity given by the FCM quadrupole can be written as

$$u_i^D(\boldsymbol{x}) = \mathcal{G}_{ij,\,kl}^{FCM}(\boldsymbol{x})Q_{jkl}, \tag{2.28}$$

in which $\mathcal{G}_{ij}^{FCM}$ is the FCM Oseen tensor given by Maxey & Patel [144]. By differentiating the FCM Oseen tensor, the FCM force quadrupole is given as

$$\begin{aligned}\mathcal{G}_{ij,\,kl}^{FCM}(\boldsymbol{x}) = {} & \frac{1}{r}\delta_{ij}\delta_{kl}\frac{dA(r)}{dr} + (\delta_{ik}\delta_{jl} + \delta_{jk}\delta_{il})B(r) - \delta_{ij}\frac{x_k x_l}{r^2}\left[\frac{1}{r}\frac{dA(r)}{dr} - \frac{d^2A(r)}{dr^2}\right] \\ & + (\delta_{jk}x_i x_l + \delta_{ik}x_j x_l + \delta il x_j x_k + \delta_{jl}x_i x_k + \delta_{kl}x_i x_j)\frac{1}{r}\frac{dB(r)}{dr} \\ & - \frac{x_i x_j x_k x_l}{r^2}\left(\frac{1}{r}\frac{dB(r)}{dr} - \frac{d^2B(r)}{dr^2}\right).\end{aligned} \tag{2.29}$$

And,

$$\frac{dA}{dr} = -\frac{1}{8\pi\mu r^2}\left[\left(1+\frac{3}{\xi^2}\right)erf\left(\frac{\xi}{\sqrt{2}}\right) - \left(4\xi + \frac{6}{\xi}\right)\frac{\exp(-\xi^2/2)}{\sqrt{2\pi}}\right], \tag{2.30}$$

$$\frac{d^2A}{dr^2} = \frac{1}{4\pi\mu r^3}\left[\left(1+\frac{6}{\xi^2}\right)erf\left(\frac{\xi}{\sqrt{2}}\right) - \left(\frac{12}{\xi} + 6\xi + 2\xi^3\right)\frac{\exp(-\xi^2/2)}{\sqrt{2\pi}}\right], \tag{2.31}$$

$$B = \frac{1}{8\pi\mu r^3}\left[\left(1-\frac{3}{\xi^2}\right)erf\left(\frac{\xi}{\sqrt{2}}\right) + \frac{6}{\xi}\frac{\exp(-\xi^2/2)}{\sqrt{2\pi}}\right], \tag{2.32}$$

$$\frac{dB}{dr} = -\frac{1}{8\pi\mu r^4}\left[\left(3-\frac{15}{\xi^2}\right)erf\left(\frac{\xi}{\sqrt{2}}\right) + \left(\frac{30}{\xi} + 4\xi\right)\frac{\exp(-\xi^2/2)}{\sqrt{2\pi}}\right], \tag{2.33}$$

$$\frac{d^2B}{dr^2} = \frac{3}{2\pi\mu r^5}\left[\left(1-\frac{15}{2}\frac{1}{\xi^2}\right)erf\left(\frac{\xi}{\sqrt{2}}\right) + \left(\frac{15}{\xi} + 3\xi + \frac{1}{3}\xi^3\right)\frac{\exp(-\xi^2/2)}{\sqrt{2\pi}}\right], \tag{2.34}$$

in which $\xi = r/\sigma$. At $r = 0$, $\mathcal{G}^{FCM}_{ij,\,kl}$ has a finite value,

$$\mathcal{G}^{FCM}_{ij,\,kl}(0) = \frac{1}{30\pi\mu\sigma^3\sqrt{2\pi}}(\delta_{ik}\delta_{jl} + \delta_{jk}\delta_{il} - 4\delta_{ij}\delta_{kl}). \tag{2.35}$$

Considering that a traceless quadrupole does not contribute to the total rate-of-work, we have

$$\int \frac{\partial^2 u_i^{FCM}}{\partial x_j \partial x_k}\Delta(r)d^3\boldsymbol{x} = -2S_{ijk}. \tag{2.36}$$

From the Fourier transform of the Stokes equations (2.26), the fluid velocity can be written as

$$\hat{u}_i^{FCM}(\boldsymbol{k}) = -\frac{1}{\mu}\left(\delta_{ij} - \frac{k_i k_j}{k^2}\right)\frac{k_k k_l}{k^2}\widehat{\Delta}(\boldsymbol{k})Q_{jkl}, \tag{2.37}$$

where the hat denotes a Fourier coefficient, $\boldsymbol{k}$ is a wavenumber, *i.e.* $\widehat{\Delta}$ is

$$\widehat{\Delta}(\boldsymbol{k}) = \frac{1}{(2\pi)^3}\exp\left(-\frac{k^2\sigma^2}{2}\right). \tag{2.38}$$

Then,

$$\begin{aligned}\Gamma_{ijk} &= \int \frac{\partial^2 u_i^{FCM}}{\partial x_j \partial x_k}\Delta(r)d^3\boldsymbol{x} \\ &= \frac{Q_{pqr}}{(2\pi)^3\mu}\int\left(\delta_{ip} - \frac{k_i k_p}{k^2}\right)\frac{k_j k_k k_q k_r}{k^2}\exp(-k^2\sigma^2)d^3\boldsymbol{k}.\end{aligned} \tag{2.39}$$

Consider a 2-dimensional flow, such that

$$S_{111} = -S_{122}, \tag{2.40}$$

$$S_{122} = S_{212}. \tag{2.41}$$

Then,

$$\Gamma_{122} = \frac{Q_{111}}{(2\pi)^3\mu}\int\frac{k_2^2}{k^2}\left[k_1^2 - k_2^2 - \frac{1}{k^2}(k_1^4 - 3k_1^2k_2^2)\right]\exp(-k^2\sigma^2)d^3\boldsymbol{k}. \tag{2.42}$$

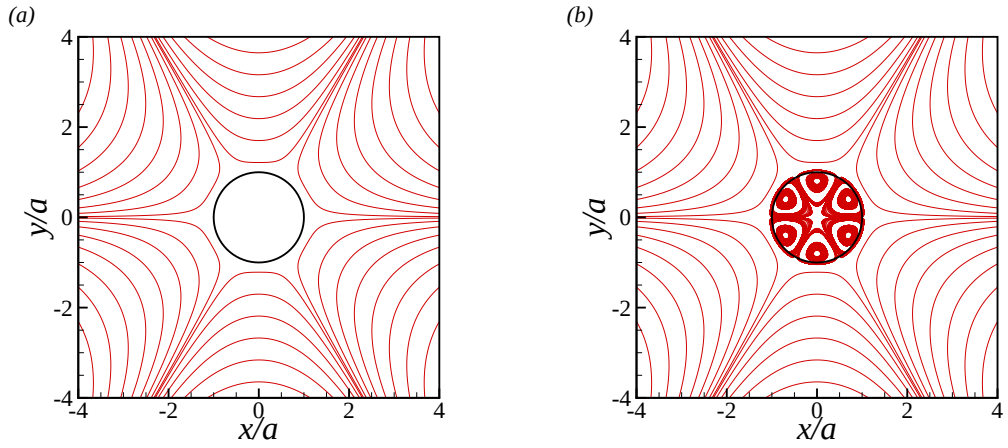

Figure 2.1: Streamlines of *(a)* exact solution and *(b)* FCM solution.

Direct integration of (2.42) gives

$$\Gamma_{122} = -\frac{1}{70}(\pi^{3/2}\sigma^5\mu)^{-1}Q_{111} = 2S_{111}. \tag{2.43}$$

The FCM lengthscale σ for force quadrupole can be computed by substituting (2.25) into (2.43),

$$\left(\frac{a}{\sigma}\right)^5 = 60\sqrt{\pi}. \tag{2.44}$$

To verify the result, the flow field induced by a sphere in a two-dimensional uniform viscous force field is computed from the FCM Green's function. The undisturbed field is given by

$$u_i^\infty = S_{ijk}x_j x_k, \tag{2.45}$$

$$\begin{aligned} S_{1jk} &= \begin{bmatrix} 1 & 0 & 0 \\ 0 & -1 & 0 \\ 0 & 0 & 0 \end{bmatrix}, \\ S_{2jk} &= \begin{bmatrix} 0 & -1 & 0 \\ -1 & 0 & 0 \\ 0 & 0 & 0 \end{bmatrix}, \\ S_{3jk} &= \mathbf{0}. \end{aligned} \tag{2.46}$$

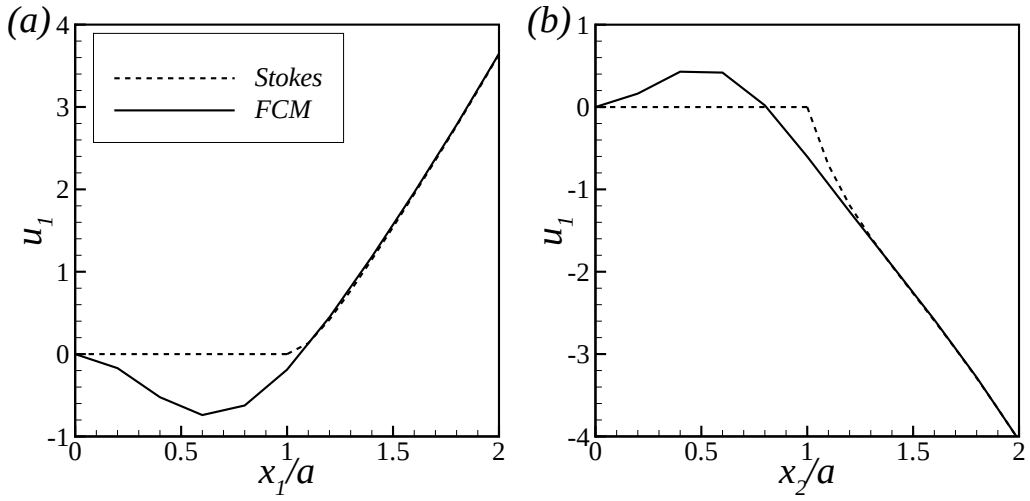

Figure 2.2: u_1 along *(a)* x_1 and *(b)* x_2 axes.

Figures 2.1 shows the streamline obtained from the exact and the FCM solutions. It is shown that the FCM solution agrees well with the exact solution. The flow velocity in x_1 direction is shown in 2.2. It is shown that FCM can reproduce the far-field solution almost exactly. However, similarly to the results in Lomholt & Maxey [135], there is some discrepancy between the FCM and exact solutions near the particle surface ($r < 1.25a$). Using a regularized multipole, FCM resolves a Faxén term only partially [144]. It seems that the error may be caused by the degenerate sextupole being resolved only partially.

In the case considered here, a single sphere in an infinite domain, it is straightforward to calculate the quadrupole strength analytically. However, in general, we need an iterative solver to compute multibody hydrodynamic interactions or in the case where S_{ijk} is not uniform. Here, we suggest an iterative procedure to find $\boldsymbol{Q}$.

We hope to find Q_{ijk} from the constraint

$$\int \left(\boldsymbol{\Gamma}^{FCM} + \boldsymbol{\Gamma}^{\infty}\right) \Delta(\boldsymbol{x}) d^3\boldsymbol{x} = 0, \tag{2.47}$$

in which the third-order tensor $\Gamma^{FCM}_{ijk} = \partial_j \partial_k u^{FCM}_i$. Define a linear operator $\mathfrak{I}_{jk}$,

$$\mathfrak{I}_{jk}\boldsymbol{Q} = \int \left(\frac{\partial^2}{\partial x_j \partial x_k} \mathfrak{S}\boldsymbol{Q}\right) \Delta(\boldsymbol{x}) d^3\boldsymbol{x}, \tag{2.48}$$

in which $\mathfrak{S}$ is a Stokes operator to compute the fluid velocity from the given FCM quadrupole.

Let $\boldsymbol{r}^k$ be a residual by k-th iteration,

$$\boldsymbol{r}^k = \mathfrak{I}\boldsymbol{Q}^k + \tilde{\boldsymbol{\Gamma}}^\infty, \tag{2.49}$$

in which $\tilde{\boldsymbol{\Gamma}}^\infty = \int \boldsymbol{\Gamma}^\infty \Delta d\boldsymbol{x}$. Assume $(k+1)$-th approximation can be obtained from the following relation,

$$\boldsymbol{Q}^{k+1} = \boldsymbol{Q}^k + \lambda \boldsymbol{r}^k, \tag{2.50}$$

in which λ is a constant. For the convergence of the sequence, we want to find λ minimizing a L_2-norm, $\|\mathfrak{I}\boldsymbol{Q}^{k+1} + \tilde{\boldsymbol{\Gamma}}^\infty\|^2$. λ can be found from

$$\begin{aligned} \frac{\partial}{\partial\lambda}\|\mathfrak{I}\boldsymbol{Q}^{k+1} + \tilde{\boldsymbol{\Gamma}}^\infty\|^2 &= \frac{\partial}{\partial\lambda}\|\mathfrak{I}(\boldsymbol{Q}^k + \lambda\boldsymbol{r}^k) + \tilde{\boldsymbol{\Gamma}}^\infty\|^2 = \frac{\partial}{\partial\lambda}\|(\mathfrak{I}\boldsymbol{Q}^k + \tilde{\boldsymbol{\Gamma}}^\infty) + \lambda\mathfrak{I}\boldsymbol{r}^k\|^2 \\ &= \frac{\partial}{\partial\lambda}\|\boldsymbol{r}^k + \lambda\mathfrak{I}\boldsymbol{r}^k\|^2. \end{aligned} \tag{2.51}$$

Hence,

$$\lambda = -\frac{\boldsymbol{r}^k \cdot \mathfrak{I}\boldsymbol{r}^k}{\mathfrak{I}\boldsymbol{r}^k \cdot \mathfrak{I}\boldsymbol{r}^k}, \tag{2.52}$$

and

$$\boldsymbol{Q}^{k+1} = \boldsymbol{Q}^k + \lambda\boldsymbol{r}^k, \tag{2.53}$$

$$\boldsymbol{r}^{k+1} = \mathfrak{I}\boldsymbol{Q}^{k+1} + \tilde{\boldsymbol{\Gamma}}^\infty = \mathfrak{I}(\boldsymbol{Q}^k + \lambda\boldsymbol{r}^k) + \tilde{\boldsymbol{\Gamma}}^\infty = \boldsymbol{r}^k + \lambda\mathfrak{I}\boldsymbol{r}^k. \tag{2.54}$$

Note that the iterative solver is essentially a steepest-decent method and the iteration converges only if the linear operator $\mathfrak{I}$ is positive (semi-)definite, which is true for the Stokes operator. So far, we have considered only the traceless quadrupole. The degenerate quadrupole case will be considered in 2.2.2.2. In the numerical tests, it is found that the required number of iteration is similar to that of the dipole.

2.2.2.2 Degenerate quadrupole

Consider a force-free and torque-free particle in a parabolic flow,

$$\boldsymbol{u}^\infty = (A(x_2^2 + x_3^2), 0, 0), \tag{2.55}$$

in which A is a constant. Assume a particle is placed at the origin $\boldsymbol{x} = (0,0,0)^T$. Since the flow is axisymmetric, it is convenient to use a cylindrical coordinate. Let u_r and u_θ be the radial and azimuthal components of u, respectively. Then,

$$\begin{cases} u_r^\infty = Ar^2 sin^2\theta cos\theta = \frac{1}{r^2 sin\theta}\frac{\partial \psi^\infty}{\partial \theta}, \\ u_\theta^\infty = -Ar^2 sin^3\theta = -\frac{1}{r sin\theta}\frac{\partial \psi^\infty}{\partial r}, \end{cases} \tag{2.56}$$

in which ψ^∞ is the streamfunction of $\boldsymbol{u}^\infty$. Solving (2.56) for ψ^∞ gives

$$\psi^\infty = \frac{1}{4} Ar^4 sin^4\theta. \tag{2.57}$$

Similarly, using the streamfunction, the Stokes equation for the disturbance velocity $\boldsymbol{u}^D$ reduces to [87]

$$E^4 \psi^D = 0, \tag{2.58}$$

in which E is an operator defined as

$$E^2 = \frac{\partial^2}{\partial r^2} + \frac{sin\theta}{r^2}\frac{\partial}{\partial \theta}\left(\frac{1}{sin\theta}\frac{\partial}{\partial \theta}\right). \tag{2.59}$$

The solution of (2.58) can be found by splitting into the homogeneous ψ_h^D and particular solutions ψ_p^D,

$$\begin{cases} E^2 \psi_h^D = 0, \\ E^2 \psi_p^D \neq 0. \end{cases} \tag{2.60}$$

As the streamfunction subjected to the operator E^2 represents the vorticity, ψ_h^D and ψ_p^D correspond to the flow by irrotational and rotational singularities in the multipole solution, respectively.

The general solution for ψ_h^D is given by

$$\psi_h^D(r,\xi) = \sum_{n=0}^{\infty} \left(A_n r^n + B_n r^{-n+1}\right) G_n(\xi), \tag{2.61}$$

in which A and B are constants, $\xi = cos\theta$, and $G_n(\xi)$ is the Gegenbauer function. The first

few terms of the Gegenbauer function are

$$\begin{aligned} G_2(\xi) &= \frac{1}{2}(1-\xi^2) = \frac{1}{2}sin^2\theta, \\ G_3(\xi) &= \frac{1}{2}\xi(1-\xi^2) = \frac{1}{2}cos\theta sin^2\theta, \\ G_4(\xi) &= \frac{1}{8}(1-\xi^2)(5\xi^2-1) = \frac{1}{8}sin^2\theta(4-5sin^2\theta), \\ G_5(\xi) &= \frac{1}{8}\xi(1-\xi^2)(7\xi^2-3) = \frac{1}{8}cos\theta sin^2\theta(4-7sin^2\theta). \end{aligned}$$

The solution for ψ_p^D is given by

$$\psi_p^D(r,\xi) = \sum_{n=2}^{\infty} \left(C_n r^{n+2} + D_n r^{-n+3}\right) G_n(\xi). \tag{2.62}$$

Therefore,

$$\psi^D(r,\xi) = \sum_{n=2}^{\infty} \left(A_n r^n + B_n r^{-n+1} + C_n r^{n+2} + D_n r^{-n+3}\right) G_n(\xi). \tag{2.63}$$

The coefficients A_n, B_n, C_n, and D_n in (2.63) can be determined by applying the no-slip boundary condition on the particle surface. In a cylindrical coordinate, the no-slip boundary conditions are

$$u_r^D + u_r^\infty = V_r \qquad \& \qquad u_\theta^D + u_\theta^\infty = V_\theta \qquad \text{on} \quad r = a, \tag{2.64}$$

in which the particle velocity $\boldsymbol{V} = (2a^2A/3, 0, 0)^T$. By comparing the order of the terms, it is obvious that terms other than $n = 2$ and 4 in (2.63) should vanish. And, as the velocity is zero at $r \to \infty$, all the terms with a positive exponent ($r^k,\ k \geq 0$) should be eliminated. Then,

$$\psi^D = B_2 r^{-1} G_2(\xi) + \left(B_4 r^{-3} + D_4 r^{-1}\right) G_4(\xi). \tag{2.65}$$

Applying the no-slip boundary condition,

$$\begin{aligned} B_2 &= \frac{4}{15}a^5 A, \\ B_4 &= -a^7 A, \qquad D_4 = \frac{7}{5}a^5 A. \end{aligned}$$

Comparing with the multipole solution, B_2, B_4, and D_4 terms represent, respectively, the degenerate quadrupole, the degenerate sextupole, and the quadrupole. Now, the fluid velocity is

$$\begin{aligned}
u_r = & \frac{4}{15}\left(\frac{a}{r}\right)^3 cos\theta a^2 A && \text{: degenerate quadrupole (D.Q)} \\
& +\frac{7}{10}\left(\frac{a}{r}\right)^3 cos\theta(2-5sin^2\theta)a^2 A && \text{: quadrupole (Q)} \\
& -\frac{1}{2}\left(\frac{a}{r}\right)^5 cos\theta(2-5sin^2\theta)a^2 A, && \text{: degenerate sextupole (D.S)}
\end{aligned} \tag{2.66}$$

$$\begin{aligned}
u_\theta = & \frac{2}{15}\left(\frac{a}{r}\right)^3 cos\theta a^2 A && \text{: D.Q} \\
& +\frac{7}{40}\left(\frac{a}{r}\right)^3 sin\theta(2-5sin^2\theta)a^2 A && \text{: Q} \\
& -\frac{3}{8}\left(\frac{a}{r}\right)^5 sin\theta(2-5sin^2\theta)a^2 A. && \text{: D.S}
\end{aligned} \tag{2.67}$$

In Cartesian coordinates,

$$\begin{aligned}
\tilde{u}_1 = & -\frac{1}{5}\left(1-3\frac{\tilde{x}_1^2}{r^2}\right)\left(\frac{a}{r}\right)^3 V_1 \\
& -\frac{21}{20}\left(1-3\frac{\tilde{x}_1^2}{r^2}+5\frac{\tilde{x}_1^2\tilde{x}_2^2}{r^4}-\frac{5}{4}\frac{\tilde{x}_2^4}{r^4}\right)\left(\frac{a}{r}\right)^3 V_1 \\
& +\frac{3}{4}\left(3-5\frac{\tilde{x}_1^2}{r^2}+5\frac{\tilde{x}_1^2\tilde{x}_2^2}{r^4}-\frac{15}{4}\frac{\tilde{x}_2^4}{r^4}\right)\left(\frac{a}{r}\right)^5 V_1,
\end{aligned} \tag{2.68}$$

$$\begin{aligned}
\tilde{u}_2 = & \frac{3}{5}\frac{\tilde{x}_1\tilde{x}_2}{r^2}\left(\frac{a}{r}\right)^3 V_1 \\
& -\frac{21}{20}\left(-3\frac{\tilde{x}_1\tilde{x}_2}{r^2}+\frac{25}{4}\frac{\tilde{x}_1\tilde{x}_2^3}{r^4}\right)\left(\frac{a}{r}\right)^3 V_1 \\
& +\frac{3}{4}\left(-5\frac{\tilde{x}_1\tilde{x}_2}{r^2}+\frac{35}{4}\frac{\tilde{x}_1\tilde{x}_2^3}{r^4}\right)\left(\frac{a}{r}\right)^5 V_1,
\end{aligned} \tag{2.69}$$

where the tilde denotes a variable in the plane of axisymmetry.

As the solution consists of the degenerate quadrupole, quadrupole, and degenerate sextupole, the fluid velocity may be written as

$$u_i = \nabla^2\frac{G_{ij}}{8\pi\mu}H_j + \left(1+\beta a^2\nabla^2\right)\frac{G_{ij,\,kl}}{8\pi\mu}Q_{jkl}, \tag{2.70}$$

in which β is a constant. By comparing (2.70) with (2.68 - 2.69),

$$u_i = \nabla^2 \frac{G_{ij}}{8\pi\mu} H_j + \left(1 + \frac{a^2}{14}\nabla^2\right) \frac{G_{ij,\,kl}}{8\pi\mu} Q_{jkl}, \tag{2.71}$$

$$H_1 = -\frac{8}{15}\pi\mu a^5 A = -\frac{4}{5}\pi\mu a^3 V_1, \quad H_2 = H_3 = 0, \tag{2.72}$$

$$\begin{aligned} Q_{1jk} &= \begin{bmatrix} 2\mathfrak{A} & 0 & 0 \\ 0 & -\mathfrak{A} & 0 \\ 0 & 0 & -\mathfrak{A} \end{bmatrix}, \\ Q_{2jk} &= \begin{bmatrix} 0 & -\mathfrak{A} & 0 \\ -\mathfrak{A} & 0 & 0 \\ 0 & 0 & 0 \end{bmatrix}, \\ Q_{3jk} &= \begin{bmatrix} 0 & 0 & -\mathfrak{A} \\ 0 & 0 & 0 \\ -\mathfrak{A} & 0 & 0 \end{bmatrix}. \end{aligned} \tag{2.73}$$

Here,

$$\mathfrak{A} = \frac{7}{15}\pi\mu a^5 A = \frac{7}{10}\pi\mu a^3 V_1.$$

Now, consider the velocity field by the FCM degenerate quadrupole ($\boldsymbol{u}^{DQ}$). Define

$$\Gamma_{ijk}^{DQ} = \int \frac{\partial^2 u_i^{DQ}}{\partial x_j \partial x_k} \Delta d^3\boldsymbol{x}. \tag{2.74}$$

From the convolution theorem,

$$\begin{aligned} \Gamma_{ijk}^{DQ} &= \frac{1}{(2\pi)^3} \int \left(\delta_{ip} - \frac{k_i k_p}{k^2}\right) \frac{k_j k_k}{\mu} \exp(-\sigma_{DQ}^2 k^2) d^3\boldsymbol{k} H_p \\ &= \tau_{ijkp} H_p, \end{aligned} \tag{2.75}$$

in which σ_{DQ} is the lengthscale of the FCM degenerate quadrupole and τ_{ijkp} is a fourth-order isotropic tensor. In general, a fourth-order isotropic tensor can be written as

$$\tau_{ijkp} = \alpha_1 \delta_{ij}\delta_{kp} + \alpha_2 \delta_{ik}\delta_{jp} + \alpha_3 \delta_{ip}\delta_{jk}, \tag{2.76}$$

in which α_i is the coefficient to be determined. First, from the divergence-free condition,

$$\Gamma^{DQ}_{111} + \Gamma^{DQ}_{212} + \Gamma^{DQ}_{313} = (\alpha_1 + 3\alpha_2 + \alpha_3)H_1 = 0, \tag{2.77}$$

and, from the symmetry ($\Gamma_{ijk} = \Gamma_{ikj}$), $\alpha_1 = \alpha_2$. Therefore, the fourth-order tensor reduces to

$$\tau_{ijkp} = \alpha\left(\delta_{ij}\delta_{kp} + \delta_{ik}\delta_{jp} - 4\delta_{ip}\delta_{jk}\right). \tag{2.78}$$

By comparing the direct integration of (2.75) and the coefficient of τ_{ijkp},

$$\begin{aligned}
\tau_{ijji} &= \frac{1}{(2\pi)^3}\int 2k^2\exp(-\sigma^2_{DQ}k^2)d^3\boldsymbol{k} = \frac{3}{8}(\mu\sigma^5_{DQ}\pi^{3/2})^{-1} && (2.79)\\
&= \alpha\left(\delta_{ij}\delta_{ij} + \delta_{ij}\delta_{ij} - 4\delta_{ii}\delta_{jj}\right) = -30\alpha,\\
\alpha &= -(80\mu\sigma^5_{DQ}\pi^{3/2})^{-1}. && (2.80)
\end{aligned}$$

Therefore,

$$\begin{aligned}
\Gamma^{DQ}_{1jk} &= \begin{bmatrix} -2\mathfrak{B} & 0 & 0 \\ 0 & -4\mathfrak{B} & 0 \\ 0 & 0 & -4\mathfrak{B} \end{bmatrix},\\
\Gamma^{DQ}_{2jk} &= \begin{bmatrix} 0 & \mathfrak{B} & 0 \\ \mathfrak{B} & 0 & 0 \\ 0 & 0 & 0 \end{bmatrix}, && (2.81)\\
\Gamma^{DQ}_{3jk} &= \begin{bmatrix} 0 & 0 & \mathfrak{B} \\ 0 & 0 & 0 \\ \mathfrak{B} & 0 & 0 \end{bmatrix},
\end{aligned}$$

in which $\mathfrak{B} = -(80\mu\sigma^5_{DQ}\pi^{3/2})^{-1}H_1$.

Similarly, for the FCM quadrupole,

$$\begin{aligned}
\Gamma^{Q}_{ijk} &= \frac{1}{(2\pi)^3}\int\left(\delta_{ip} - \frac{k_ik_p}{k^2}\right)\frac{k_jk_kk_qk_r}{\mu k^2}\exp(-\sigma^2_Qk^2)d^3\boldsymbol{k}Q_{pqr} && (2.82)\\
&= \tau_{ijkpqr}Q_{pqr}, && (2.83)
\end{aligned}$$

in which σ_Q is the lengthscale of the FCM quadrupole and τ_{ijkpqr} is a 6th-order isotropic

tensor. Although σ_Q is derived in the previous section, we will treat σ_Q as an unknown coefficient for now. A sixth-order isotropic tensor can be written as

$$\begin{aligned}
\tau_{ijkpqr} &= \delta_{ip}(\alpha_1\delta_{qj}\delta_{rk} + \alpha_2\delta_{qk}\delta_{rj} + \alpha_3\delta_{qr}\delta_{kj}) \\
&+ \delta_{iq}(\alpha_4\delta_{pj}\delta_{rk} + \alpha_5\delta_{pk}\delta_{rj} + \alpha_6\delta_{pr}\delta_{kj}) \\
&+ \delta_{ir}(\alpha_7\delta_{pj}\delta_{qk} + \alpha_8\delta_{pk}\delta_{qj} + \alpha_9\delta_{pq}\delta_{kj}) \\
&+ \delta_{ij}(\alpha_{10}\delta_{pk}\delta_{qr} + \alpha_{11}\delta_{pq}\delta_{kr} + \alpha_{12}\delta_{pr}\delta_{kq}) \\
&+ \delta_{ik}(\alpha_{13}\delta_{pj}\delta_{qr} + \alpha_{14}\delta_{pq}\delta_{jr} + \alpha_{15}\delta_{pr}\delta_{jq}),
\end{aligned} \tag{2.84}$$

in which α_i's are unknown coefficients. Again, applying symmetry and divergence-free conditions, the number of the unknown coefficients can be reduced to three;

$$\begin{aligned}
\tau_{ijkpqr} &= \alpha_1\delta_{ip}(\delta_{qj}\delta_{rk} + \delta_{qk}\delta_{rj}) \\
&+ \alpha_2[\delta_{pj}(\delta_{iq}\delta_{rk} + \delta_{ir}\delta_{qk}) + \delta_{pk}(\delta_{iq}\delta_{rj} + \delta_{ir}\delta_{qk}) - 2\delta_{ip}\delta_{kj}\delta_{qr}] \\
&+ \alpha_3[\delta_{qr}(\delta_{ij}\delta_{pk} + \delta_{ik}\delta_{pj}) - 4\delta_{ip}\delta_{kj}\delta_{qr}].
\end{aligned} \tag{2.85}$$

From the constraint,

$$\mathbf{\Gamma}^{\infty} + \mathbf{\Gamma}^{DQ} + \mathbf{\Gamma}^{Q} = \mathbf{0}, \tag{2.86}$$

we have

$$\Gamma^Q_{212} = 2(\alpha_1 + 2\alpha_2)Q_{122} = -\mathfrak{B}, \tag{2.87}$$

$$\Gamma^Q_{111} = -4(\alpha_1 + \alpha_2 - \alpha_3)Q_{122} = 2\mathfrak{B}, \tag{2.88}$$

which indicates $\alpha_2 = -\alpha_3$. Then, the sixth-order tensor becomes

$$\begin{aligned}
\tau_{ijkpqr} &= \alpha_1\delta_{ip}(\delta_{qj}\delta_{rk} + \delta_{qk}\delta_{rj}) \\
&+ \alpha_2[\delta_{pj}(\delta_{iq}\delta_{rk} + \delta_{ir}\delta_{qk}) + \delta_{pk}(\delta_{iq}\delta_{rj} + \delta_{ir}\delta_{qj}) - \delta_{qr}(\delta_{ij}\delta_{pk} + \delta_{ik}\delta_{pj}) \\
&+ 2\delta_{ip}\delta_{kj}\delta_{qr}].
\end{aligned} \tag{2.89}$$

Comparing with the direct integration of τ_{ijkpqr},

$$\begin{aligned}\tau_{ijkijk} &= \frac{1}{(2\pi)^3}\int 2\frac{k^2}{\mu}\exp(-\sigma_Q^2 k^2)d^3\boldsymbol{k} = \frac{3}{8}(\mu\sigma_Q^5\pi^{3/2})^{-1} \\ &= 36\alpha_1 + 36\alpha_2,\end{aligned} \tag{2.90}$$

and assuming $\sigma_{DQ} = \sigma_Q = \sigma$, the unknown coefficients α_1 and α_2 are

$$\begin{aligned}\alpha_1 &= \frac{46}{3360}(\mu\pi^{3/2}\sigma^5)^{-1}, \\ \alpha_2 &= -\frac{11}{3360}(\mu\pi^{3/2}\sigma^5)^{-1}.\end{aligned}$$

And,

$$\begin{aligned}\Gamma^Q_{1jk} &= \begin{bmatrix} 2\mathfrak{B} & 0 & 0 \\ 0 & -\mathfrak{B} & 0 \\ 0 & 0 & -\mathfrak{B} \end{bmatrix}, \\ \Gamma^Q_{2jk} &= \begin{bmatrix} 0 & -\mathfrak{B} & 0 \\ -\mathfrak{B} & 0 & 0 \\ 0 & 0 & 0 \end{bmatrix}, \\ \Gamma^Q_{3jk} &= \begin{bmatrix} 0 & 0 & -\mathfrak{B} \\ 0 & 0 & 0 \\ -\mathfrak{B} & 0 & 0 \end{bmatrix}.\end{aligned} \tag{2.91}$$

By comparing (2.81) with (2.91) and from (2.86), the lengthscale σ can be determined as

$$-5\mathfrak{B} = -2A, \tag{2.92}$$

$$\frac{a}{\sigma} = (60\pi^{1/2})^{1/5}. \tag{2.93}$$

It is shown that the σ for the degenerate quadrupole flow is the same with that for the traceless quadrupole flow.

The FCM and exact solutions are compared in figure 2.3. Figure 2.3 (a) shows u_1 in the x_1 direction and (b) is u_1 in the x_2 direction. It is shown that in both cases, the FCM solution approximates the far-field solution with a good accuracy. In $u_1(x_2)$, it is shown that the FCM solution underestimates the fluid velocity when $r/a \leq 1.25$.

As a final remark, in the standard FCM procedure [144], the particle velocity is obtained

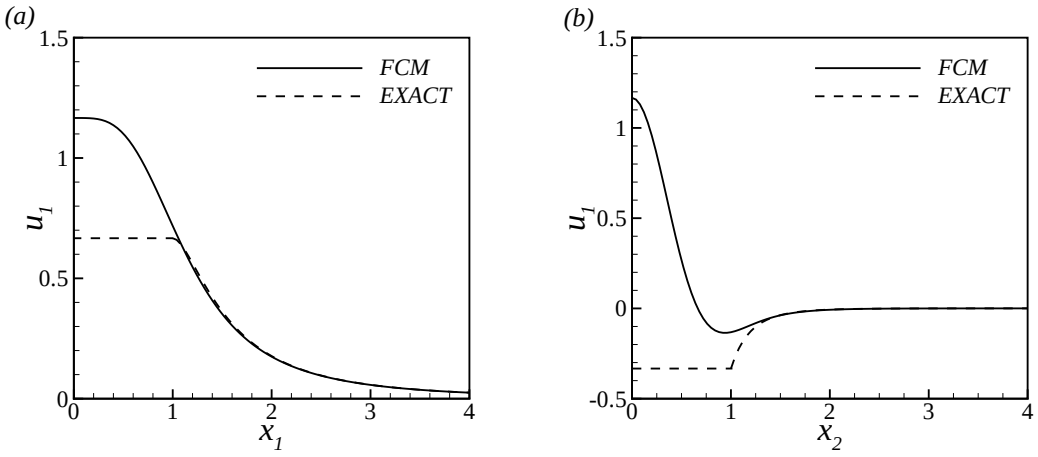

Figure 2.3: u_1 in *(a)* x_1 and *(b)* x_2 directions.

by a weight average, $\boldsymbol{V} = \int \boldsymbol{u}\Delta_M d^3\boldsymbol{x}$, in which Δ_M is the monopole envelope. As mentioned in the beginning of this section, the procedure works well if the particle diameter is small compared to the scale of the spatial variation of $\boldsymbol{u}$. However, if we include the degenerate quadrupole to resolve the parabolic flow, the standard procedure no longer works. Consider the FCM for a sphere in a parabolic flow,

$$0 = -\frac{\partial p}{\partial x_i} + \mu\nabla^2 u_i + H_i\nabla^2\Delta_{DQ} + \text{traceless Quadrupole.} \tag{2.94}$$

As the traceless quadrupole does not contribute to the translational motion of the particle, in the standard FCM procedure, the particle velocity is computed from

$$\begin{aligned}\int (u_i^{FCM} + u_i^{\infty})\Delta_M d^3\boldsymbol{x} &= -\frac{H_j}{(2\pi)^3\mu}\int\left(\delta_{ij} - \frac{k_i k_j}{k^2}\right)\exp\left(-k^2\frac{\sigma_{DQ}^2+\sigma_M^2}{2}\right)d^3\boldsymbol{k} \\ &+ \frac{3}{\pi}\tilde{V}_i\end{aligned} \tag{2.95}$$

in which $\tilde{\boldsymbol{V}}$ is the exact particle velocity. Then, the FCM particle velocity is

$$\boldsymbol{V} = -\frac{\boldsymbol{H}}{12\mu\left(\pi\frac{\sigma_{DQ}^2+\sigma_M^2}{2}\right)^{3/2}} + \frac{3}{\pi}\tilde{\boldsymbol{V}} = 1.282\tilde{\boldsymbol{V}}. \tag{2.96}$$

It is shown that the standard FCM procedure to compute the particle velocity results in a non-negligible error if the degenerate quadrupole is included. A more general approach to include higher-order multipoles is a subject of further investigation.

2.2.3 Modification of the FCM envelopes near a wall

For wall-bounded flows, (2.1) is solved numerically with the appropriate no-slip boundary conditions for rigid walls to obtain the incompressible Stokes flow field $\boldsymbol{u}$, which gives far-field hydrodynamic interactions. The force envelopes, Δ_M and Δ_D, while narrowly confined to each particle do extend beyond the physical size of the particle. As a result, it is possible that when a particle is close to a wall the envelope overlaps the boundary. Similarly, in evaluating the integrals for the particle velocity (2.8) or for the rate of strain (2.12) and the angular velocity (2.9) the range of integration goes outside of the physical flow domain. In previous simulations of wall-bounded flows based on FCM [51, 132, 133, 135], if a particle is close to a wall then the FCM envelope is truncated at the wall boundary in (2.1) and integration is confined to the physical flow domain.

For a particle in contact with a rigid boundary, the truncated volume in (2.8) is approximately 3.8% of the total and similarly for (2.12) is 1.4%. The effects of this truncation procedure can be included and accounted for at low volume fractions in the estimates of the particle-wall lubrication forces [50]. This procedure is self-consistent. However, it presents a minor problem for evaluating results directly related to an imposed external shear flow.

As an illustration, consider a flow bounded by a rigid wall at $x_2 = 0$ so that the flow domain $\boldsymbol{\Omega}^D$ is the semi-infinite region $\boldsymbol{\Omega}^D = (-\infty, \infty) \times (0, \infty) \times (-\infty, \infty)$ and the wall is located on the boundary $\partial\boldsymbol{\Omega}^D$. A particle in a linear shear flow $\boldsymbol{u}^\infty = (\dot{\gamma}x_2, 0, 0)^T$, in which $\dot{\gamma}$ is the shear rate, would usually give the result from FCM that

$$\boldsymbol{V}^\infty = \boldsymbol{u}^\infty(\boldsymbol{Y}) = \int\limits_{\boldsymbol{I}_n(\boldsymbol{Y})} \boldsymbol{u}^\infty(\boldsymbol{x})\Delta_M(\boldsymbol{x}-\boldsymbol{Y})d^3\boldsymbol{x}. \tag{2.97}$$

The domain of numerical integration is $\boldsymbol{I_n}(\boldsymbol{Y}) = \{\boldsymbol{x} : \boldsymbol{x} \in \mathbb{R}^3,\ |\boldsymbol{x}-\boldsymbol{Y}| < a\times n\}$, representing a sphere of larger radius na where n is a positive real number. In order to obtain full accuracy, n is usually chosen such that $n \geq 2.5$. If a particle is close to a wall such that $\boldsymbol{I}_n(\boldsymbol{Y}) \nsubseteq \boldsymbol{\Omega}^D$, then the FCM envelope is truncated at the wall boundary, i.e. the integration is performed only in $\boldsymbol{I}_n(\boldsymbol{Y}) \cap \boldsymbol{\Omega}^D$. This results in $\boldsymbol{V}^\infty \neq \boldsymbol{u}^\infty(\boldsymbol{Y})$.

As a remedy to this problem, the FCM envelope is modified for particles near a wall ($Y_2 < a \times n$) and an image envelope is introduced. That is for the force monopole term,

$$\Delta_M^{Wall}(\boldsymbol{x}-\boldsymbol{Y}) = \Delta_M(\boldsymbol{x}-\boldsymbol{Y}) - \Delta_M(\boldsymbol{x}-\boldsymbol{Y}^{Img}), \tag{2.98}$$

in which $\boldsymbol{Y}^{Img} = (Y_1, -Y_2, Y_3)^T$. Similarly, the dipole envelope is given as,

$$\Delta_D^{Wall}(\boldsymbol{x} - \boldsymbol{Y}) = \Delta_D(\boldsymbol{x} - \boldsymbol{Y}) + \Delta_D(\boldsymbol{x} - \boldsymbol{Y}^{Img}). \tag{2.99}$$

The modified wall envelopes ensure that

$$\boldsymbol{V}^{\infty} = \boldsymbol{u}^{\infty}(\boldsymbol{Y}) = \int\limits_{\boldsymbol{I}_n(\boldsymbol{Y}) \cap \boldsymbol{\Omega}^D} \boldsymbol{u}^{\infty}(\boldsymbol{x}) \Delta_M^{Wall}(\boldsymbol{x} - \boldsymbol{Y}) d^3\boldsymbol{x}, \tag{2.100}$$

and

$$E_{ij}^{\infty} = e_{ij}^{\infty}(\boldsymbol{Y}) = \int\limits_{\boldsymbol{I}_n(\boldsymbol{Y}) \cap \boldsymbol{\Omega}^D} e_{ij}^{\infty}(\boldsymbol{x}) \Delta_D^{Wall}(\boldsymbol{x} - \boldsymbol{Y}) d^3\boldsymbol{x}, \tag{2.101}$$

as well as ensuring that the particle angular velocity matches the fluid vorticity (2.9) for the imposed external flow. This modified procedure is also self-consistent. Coincidentally, the image envelope Δ_M^{Wall} would correspond to the lowest order image Stokeslet as given by [18], where they apply image methods to solve for Stokes flow in the presence of a rigid boundary. However, the reasons for the formulation of the wall-envelopes are different and the underlying numerical solution to (2.1) already ensures that the no-slip conditions are satisfied.

2.2.4 Discretized equation of FCM

Due to the linearity of the Stokes equation, there are linear relations between the force moments and the flow parameters [28, 110]. Finding the force moments from the prescribed flow parameters is called the resistance problem while in the mobility problem the flow parameters are the unknowns which are to be found from the given force moments. In this section, the semi-discretized equation of the force-coupling method is presented conceptually in the form of the grand mobility matrix and a more efficient conjugate gradient method to calculate S_{ij} is described.

For simplicity, let the computational domain $\boldsymbol{\Omega}^D$ be a cubic domain in $\mathbb{R}^3$. $\boldsymbol{\Omega}^D$ can be a bounded domain with some boundary conditions on $\partial\boldsymbol{\Omega}^D$ or an unbounded domain with periodic boundary conditions. We consider the fluid of a constant viscosity μ extends in the whole domain including the volume occupied by the particles and the fluid velocity and

pressure satisfy equations (2.1)–(2.2) in $\boldsymbol{\Omega}^D$.

In equation (2.8), $\boldsymbol{V}^n$ can be approximated by a Gaussian quadrature rule,

$$\boldsymbol{V}^n = \sum_{i=1}^{N_x}\sum_{j=1}^{N_y}\sum_{k=1}^{N_z} \boldsymbol{u}(\boldsymbol{x}^{i,j,k})\Delta_M(\boldsymbol{x}^{i,j,k} - \boldsymbol{Y}^n) w_i^x w_j^y w_k^z, \tag{2.102}$$

in which N_x, N_y, and N_z are, respectively, the number of grid points in the x_1, x_2, and x_3 directions (or x, y, z), $\boldsymbol{x}^{i,j,k}$ is the position vector of the (i,j,k)-th grid point, and w_i^α is the weight of the Gaussian quadrature in the α direction. In matrix form,

$$\boldsymbol{V} = \boldsymbol{D_M W u}, \tag{2.103}$$

in which the terms are

$\boldsymbol{V}$: $(3N_p)$ vector which contains the particle velocities

$$\boldsymbol{V} = \begin{bmatrix} \boldsymbol{V}_1 \\ \boldsymbol{V}_2 \\ \boldsymbol{V}_3 \end{bmatrix}, \quad \boldsymbol{V}_j = \begin{bmatrix} V_j^1 \\ V_j^2 \\ \vdots \\ V_j^{N_p} \end{bmatrix} \tag{2.104}$$

$\boldsymbol{u}$: $(3Ng)$ vector for the fluid velocity at each grid points ($Ng = N_x \times N_y \times N_z$).

$$\boldsymbol{u} = \begin{bmatrix} \boldsymbol{u}_1 \\ \boldsymbol{u}_2 \\ \boldsymbol{u}_3 \end{bmatrix}, \quad \boldsymbol{u}_j = \begin{bmatrix} u_j(\boldsymbol{x}^{1,1,1}) \\ \vdots \\ u_j(\boldsymbol{x}^{N_x,N_y,N_z}) \end{bmatrix} \tag{2.105}$$

$\boldsymbol{W}$: $(3Ng) \times (3Ng)$ diagonal matrix for the weighting coefficients of the Gaussian quadrature.

$$\boldsymbol{W} = \begin{bmatrix} \boldsymbol{w} & \boldsymbol{0} & \boldsymbol{0} \\ \boldsymbol{0} & \boldsymbol{w} & \boldsymbol{0} \\ \boldsymbol{0} & \boldsymbol{0} & \boldsymbol{w} \end{bmatrix}, \quad \boldsymbol{w} = \begin{bmatrix} w_1^x w_1^y w_1^z & 0 & \cdots & 0 \\ 0 & \ddots & & \vdots \\ \vdots & & \ddots & 0 \\ 0 & \cdots & 0 & w_{N_x}^x w_{N_y}^y w_{N_z}^z \end{bmatrix} \tag{2.106}$$

$\boldsymbol{D_M}$: $(3N_p) \times (3Ng)$ matrix of Δ_M at each grid points.

$$\begin{aligned} \boldsymbol{D_M} &= \begin{bmatrix} \boldsymbol{d} & \boldsymbol{0} & \boldsymbol{0} \\ \boldsymbol{0} & \boldsymbol{d} & \boldsymbol{0} \\ \boldsymbol{0} & \boldsymbol{0} & \boldsymbol{d} \end{bmatrix}, \\ \boldsymbol{d} &= \begin{bmatrix} \Delta_M(\boldsymbol{x}^{1,1,1} - \boldsymbol{Y}^1) & \cdots & \Delta_M(\boldsymbol{x}^{N_x,N_y,N_z} - \boldsymbol{Y}^1) \\ \vdots & & \vdots \\ \Delta_M(\boldsymbol{x}^{1,1,1} - \boldsymbol{Y}^{N_p}) & \cdots & \Delta_M(\boldsymbol{x}^{N_x,N_y,N_z} - \boldsymbol{Y}^{N_p}) \end{bmatrix} \end{aligned} \tag{2.107}$$

It is worthwhile to note that, because the force envelope is a rapidly decaying function, we can assume $\Delta_M(\boldsymbol{x} - \boldsymbol{Y}) = 0$ if $|\boldsymbol{x} - \boldsymbol{Y}| > 3a$, which makes $\boldsymbol{d}$ a sparse matrix. Hence, the matrix-matrix multiplication $\boldsymbol{D_M W u}$ is done in $O(N_p)$ operations.

Through linearity, the flow parameters can be represented by the sum of their components. First, the fluid velocity $\boldsymbol{u}$ generated by the given force monopole is

$$\boldsymbol{u} = \mathbb{S}\boldsymbol{D}_{\boldsymbol{M}}^T\boldsymbol{F}, \tag{2.108}$$

in which $\mathbb{S}$ is a $(3Ng) \times (3Ng)$ matrix determined by the choice of numerical scheme to solve the Stokes equations and $\boldsymbol{F}$ is the $3N_p$ vector containing the monopole coefficients of each particle.

$$\boldsymbol{F} = \begin{bmatrix} \boldsymbol{f_1} \\ \boldsymbol{f_2} \\ \boldsymbol{f_3} \end{bmatrix}, \quad \boldsymbol{f}_j = \begin{bmatrix} F_j^1 \\ \vdots \\ F_j^{N_p} \end{bmatrix} \tag{2.109}$$

In terms of these, the particle velocity $\boldsymbol{V}$ from the FCM monopole calculation is

$$\boldsymbol{V} = \boldsymbol{D_M W}\mathbb{S}\boldsymbol{D}_{\boldsymbol{M}}^T\boldsymbol{F} = \boldsymbol{M}_{FV}\boldsymbol{F}, \tag{2.110}$$

in which $\boldsymbol{M}_{FV}$ is the FCM mobility matrix relating the translational velocity to the force monopole. In the Stokes problem, the symmetric positive definiteness (SPD) of the mobility matrix can be proven by the reciprocal theorem [110]. The same property is preserved in FCM. It is trivial to show that the positive semi-definiteness of $\mathbb{S}$, which is true for many numerical schemes such as the spectral or the spectral element methods, implies the positive

semi-definiteness of $\boldsymbol{M}_{FV}$.

Secondly, the mobility matrix for the rate-of-strain (2.12) in response to the symmetric force dipole (stresslet) is similarly given by

$$\boldsymbol{M}_{SE} = -\boldsymbol{D}_D \boldsymbol{W} \mathbb{S} \boldsymbol{D}_D^T, \tag{2.111}$$

in which $\boldsymbol{D}_D$ is a $(5N_p) \times (3Ng)$ matrix to calculate the derivatives of the dipole Gaussian envelope $\Delta_D(\boldsymbol{x} - \boldsymbol{Y})$,

$$\begin{aligned} \boldsymbol{D_D} &= \begin{bmatrix} \boldsymbol{d_x} & \boldsymbol{0} & -\boldsymbol{d_z} \\ \boldsymbol{d_y} & \boldsymbol{d_x} & \boldsymbol{0} \\ \boldsymbol{d_z} & \boldsymbol{0} & \boldsymbol{d_x} \\ \boldsymbol{0} & \boldsymbol{d_y} & -\boldsymbol{d_z} \\ \boldsymbol{0} & \boldsymbol{d_z} & \boldsymbol{d_y} \end{bmatrix}, \\ \boldsymbol{d_x} &= \begin{bmatrix} \frac{\partial}{\partial x}\Delta_D(\boldsymbol{x}^{1,1,1} - \boldsymbol{Y}^1) & \cdots & \frac{\partial}{\partial x}\Delta_D(\boldsymbol{x}^{N_x,N_y,N_z} - \boldsymbol{Y}^1) \\ \vdots & & \vdots \\ \frac{\partial}{\partial x}\Delta_D(\boldsymbol{x}^{1,1,1} - \boldsymbol{Y}^{N_p}) & \cdots & \frac{\partial}{\partial x}\Delta_D(\boldsymbol{x}^{N_x,N_y,N_z} - \boldsymbol{Y}^{N_p}) \end{bmatrix}. \end{aligned} \tag{2.112}$$

Here, a derivative of $\boldsymbol{u}$ is calculated by

$$\int \frac{\partial u_i}{\partial x_j} \Delta_D(\boldsymbol{x} - \boldsymbol{Y}) d^3\boldsymbol{x} = -\int u_i \frac{\partial}{\partial x_j} \Delta_D(\boldsymbol{x} - \boldsymbol{Y}) d^3\boldsymbol{x}. \tag{2.113}$$

Equation (2.113) holds when either $\boldsymbol{u}$ or Δ_D has compact support in $\boldsymbol{\Omega}^D$. In a bounded domain, although Δ_D is not compact in $\boldsymbol{\Omega}^D$, $\boldsymbol{u}$ vanishes on $\partial\boldsymbol{\Omega}^D$. Therefore, equation (2.113) holds also for the bounded domain.

Instead of calculating all 9 components of the rate of strain E_{ij}, only 5 independent components are evaluated

$$\tilde{\boldsymbol{E}} = \begin{bmatrix} \boldsymbol{E}_{11} - \boldsymbol{E}_{33} \\ 2\boldsymbol{E}_{12} \\ 2\boldsymbol{E}_{13} \\ \boldsymbol{E}_{22} - \boldsymbol{E}_{33} \\ 2\boldsymbol{E}_{23} \end{bmatrix}. \tag{2.114}$$

Similarly, let $\boldsymbol{D_T}$ be a $(3N_p) \times (3Ng)$ matrix whose entries are

$$\boldsymbol{D_T} = \frac{1}{2}\begin{bmatrix} \mathbf{0} & \boldsymbol{d_z} & -\boldsymbol{d_y} \\ -\boldsymbol{d_z} & \mathbf{0} & \boldsymbol{d_x} \\ \boldsymbol{d_y} & -\boldsymbol{d_x} & \mathbf{0} \end{bmatrix}. \tag{2.115}$$

Thirdly, the mobility matrix for the angular velocity of particles in response to torque is given as

$$\boldsymbol{M}_{T\Omega} = \boldsymbol{D_T}\boldsymbol{W}\mathbb{S}\boldsymbol{D_T^T}. \tag{2.116}$$

The definitions of the other mobility matrices are as follows:

$$\boldsymbol{M}_{TV} = \boldsymbol{D_M}\boldsymbol{W}\mathbb{S}\boldsymbol{D_T^T},\ \boldsymbol{M}_{SV} = \boldsymbol{D_M}\boldsymbol{W}\mathbb{S}\boldsymbol{D_D^T},\ \boldsymbol{M}_{S\Omega} = \boldsymbol{D_T}\boldsymbol{W}\mathbb{S}\boldsymbol{D_D^T}. \tag{2.117}$$

Consistent with reciprocal theorem, the FCM mobility matrices have the following symmetry relations,

$$\boldsymbol{M}_{TV} = \boldsymbol{M}_{F\Omega}^T,\quad \boldsymbol{M}_{SV} = -\boldsymbol{M}_{FE}^T,\quad \boldsymbol{M}_{S\Omega} = -\boldsymbol{M}_{TE}^T. \tag{2.118}$$

Applying constraints for the stresslet coefficients (2.12), the FCM grand mobility matrix $\boldsymbol{M}^{FCM}$ is constructed as

$$\begin{bmatrix} \boldsymbol{V} - \boldsymbol{V}^\infty \\ \boldsymbol{\Omega} - \boldsymbol{\Omega}^\infty \\ -\tilde{\boldsymbol{E}}^\infty \end{bmatrix} = \boldsymbol{M}^{FCM}\begin{bmatrix} \boldsymbol{F} \\ \boldsymbol{T} \\ \boldsymbol{S} \end{bmatrix} = \begin{bmatrix} \boldsymbol{M}_{FV} & \boldsymbol{M}_{TV} & \boldsymbol{M}_{SV} \\ \boldsymbol{M}_{F\Omega} & \boldsymbol{M}_{T\Omega} & \boldsymbol{M}_{S\Omega} \\ \boldsymbol{M}_{FE} & \boldsymbol{M}_{TE} & \boldsymbol{M}_{SE} \end{bmatrix}\begin{bmatrix} \boldsymbol{F} \\ \boldsymbol{T} \\ \boldsymbol{S} \end{bmatrix}, \tag{2.119}$$

in which a sub-matrix $\boldsymbol{M}_{AB}$ of $\boldsymbol{M}^{FCM}$ is a mobility matrix to calculate a value B from a given coefficient A. $\boldsymbol{\Omega}$ and $\boldsymbol{T}$ are $(3N_p)$ vectors containing the angular velocity and torques, respectively. $\boldsymbol{S}$ is a $(5N_p)$ vector of the 5 independent stresslet coefficients, S_{11}, S_{12}, S_{13}, S_{22}, S_{23}. $\boldsymbol{V}^\infty$ and $\boldsymbol{\Omega}^\infty$ are, respectively, the translational and angular velocities by imposed field. $\tilde{\boldsymbol{E}}^\infty$ is the rate-of-strain vector by the imposed field. Note that the FCM grand mobility matrix in equation (2.119) is not symmetric positive semi-definite, as may be seen from equation (2.118). To make it SPD, the signs of the third row need to be changed.

Although FCM is formulated here in matrix form, in the actual computation, the grand

mobility matrix need not be constructed. The computation consists of three steps:

1. Calculate the force density at each grid point.

$$\boldsymbol{z} = \boldsymbol{D}_{\boldsymbol{M}}^{T}\boldsymbol{F} + \boldsymbol{D}_{\boldsymbol{T}}^{T}\boldsymbol{T} + \boldsymbol{D}_{\boldsymbol{D}}^{T}\boldsymbol{S}. \tag{2.120}$$

   The number of operations in this step is $O(N_p)$.

2. Solve the Stokes equation.

$$\boldsymbol{u} = \mathbb{S}\boldsymbol{z}. \tag{2.121}$$

   If the computational domain is periodic in all 3 directions, a Fourier-spectral method can be used to solve the Stokes equation. Then, the Stokes equation can be solved in $O(Ng\log(Ng))$ operations. If the domain size is increased keeping the volume fraction constant, N_p increases linearly in proportion to Ng. Hence, the number of operations in this step is $O(N_p\log(N_p))$.

3. Finally, $\boldsymbol{V}$ and $\boldsymbol{\Omega}$ are computed by integrating $\boldsymbol{u}$ (equations 2.8, 2.9), which requires $O(N_p)$ operations.

As a whole, the computational cost of FCM is $O(N_p\log(N_p))$.

A key aspect of solving the flow problem is the determination of the stresslet coefficients. In equation (2.119), $\boldsymbol{F}$ and $\boldsymbol{T}$ are known while $\boldsymbol{S}$ is to be determined from the constraints for dipole moments. In other words,

$$-\tilde{\boldsymbol{E}}^{\infty} - \boldsymbol{M}_{FE}\boldsymbol{F} - \boldsymbol{M}_{TE}\boldsymbol{T} = \boldsymbol{M}_{SE}\boldsymbol{S} \tag{2.122}$$

must be solved to obtain $\boldsymbol{S}$. Previously, Dance & Maxey[50] suggested a steepest-decent method to solve equation (2.122). At low volume fractions, this iterative method converges within a few iterations. However, it is found that the method converges very slowly at high volume fractions [37]. As it is shown in equation (2.111) that $-\boldsymbol{M}_{SE}$ is SPD, a conjugate gradient method can be used to solve the system [56]. The solution procedures are as follows:

1. Solve the Stokes equation with $\boldsymbol{F}$, $\boldsymbol{T}$ and an initial estimate $\boldsymbol{S}^0$ to calculate the

residual $\boldsymbol{r}^0$ and a vector $\boldsymbol{p}^0$.

$$\begin{aligned}\boldsymbol{r}^0 &= \tilde{\boldsymbol{E}}^\infty + \boldsymbol{D}_D \boldsymbol{W} \mathbb{S} (\boldsymbol{D}_M^T \boldsymbol{F} + \boldsymbol{D}_T^T \boldsymbol{T} + \boldsymbol{D}_D^T \boldsymbol{S}^0), \\ \boldsymbol{p}^0 &= \boldsymbol{r}^0.\end{aligned}$$

2. Solve the Stokes equation with $\boldsymbol{p}$ as a dipole coefficient,

$$\boldsymbol{\zeta}^k = -\boldsymbol{D}_D \boldsymbol{W} \mathbb{S} \boldsymbol{D}_D^T \boldsymbol{p}^k.$$

3. Update $\boldsymbol{S}$, $\boldsymbol{r}$, and $\boldsymbol{p}$ using the standard conjugate gradient procedure. Repeat the process until converges, i.e. $||\boldsymbol{r}|| < \delta$ for a tolerance δ.

$$\begin{aligned}\alpha^k &= \boldsymbol{r}^k \cdot \boldsymbol{r}^k / \boldsymbol{\zeta}^k \cdot \boldsymbol{p}^k, \\ \boldsymbol{S}^{k+1} &= \boldsymbol{S}^k + \alpha^k \boldsymbol{p}^k, \\ \boldsymbol{r}^{k+1} &= \boldsymbol{r}^k - \alpha^k \boldsymbol{\zeta}^k, \\ \beta^k &= \boldsymbol{r}^{k+1} \cdot \boldsymbol{r}^{k+1} / \boldsymbol{r}^k \cdot \boldsymbol{r}^k, \\ \boldsymbol{p}^{k+1} &= \boldsymbol{r}^{k+1} + \beta^k \boldsymbol{p}^k. \end{aligned} \tag{2.123}$$

4. Once converged, $\boldsymbol{V}$ and $\boldsymbol{\Omega}$ are found from equation (2.119).

In that the particle velocity is calculated by solving the Stokes equation instead of constructing the grand mobility matrix, the force-coupling method is a matrix-free method to solve the mobility problem. Representing the force-coupling method as a matrix-free method gives more options to improve the method. For example, it was observed that in the bimodal suspensions finding $\boldsymbol{S}$ takes more iterations than in the mono-disperse suspensions to reach a converged result[2, 37]. In the limit of a dilute suspension, $\boldsymbol{M}_{SE}$ is a diagonal matrix such that

$$S_{ij}^n = \frac{20}{3} \pi \mu a_n^3 E_{ij}^n, \tag{2.124}$$

in which a_n is the radius of the particle n. Due to the factor a_n^3 in the diagonals of $\boldsymbol{M}_{SE}$, the condition number of $\boldsymbol{M}_{SE}$ will increase approximately as the cube of the ratio of the

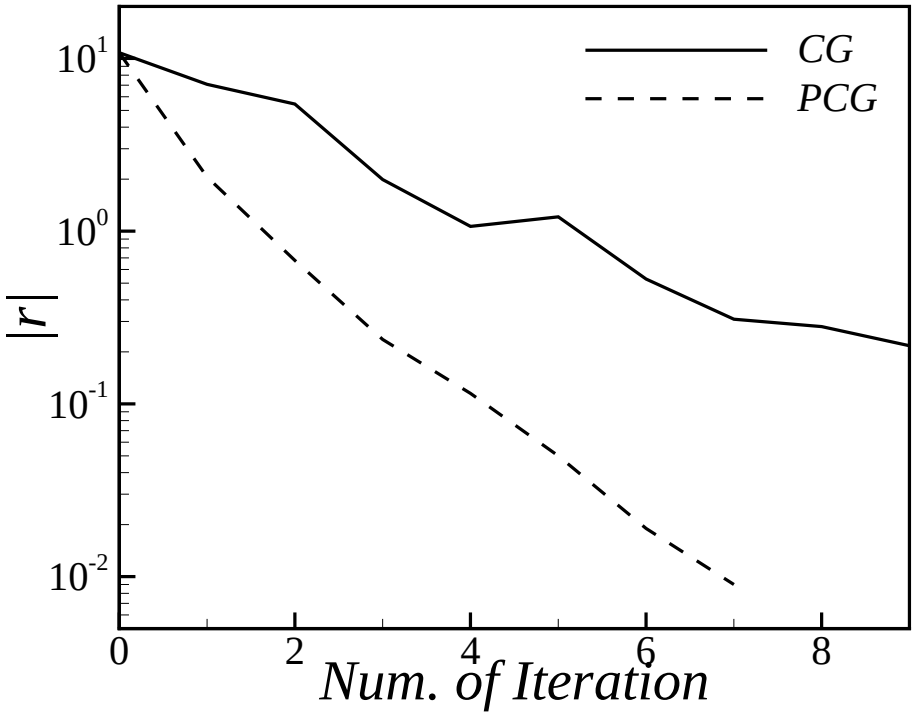

Figure 2.4: The residual 2-norm history for bi-disperse suspension.

radius of the largest particle to the radius of the smallest particle, $\mathcal{K}(\boldsymbol{M}_{SE}) \sim (a_L/a_S)^3$, which makes it difficult to invert $\boldsymbol{M}_{SE}$ using CG even at low volume fractions. In this case, a preconditioned conjugate gradient method (PCG) is more effective [56].From the result in the dilute limit, we can choose the preconditioner as a diagonal matrix of which elements are $3/20\pi\mu a_n^3$. Figure 2.4 shows the residual L_2-norm history for a bimodal suspension in a Poiseuille flow. The size ratio (a_L/a_S) is 2 and the volume fractions of large and small particles are 9% ($N_p = 64$) and 1% ($N_p = 57$), respectively. The particles are randomly distributed. As expected, PCG converges faster than CG.

2.3 Lubrication correction

2.3.1 General formulation

$\boldsymbol{M}^{FCM}$ resolves terms up to the dipole moments and the many-body interactions are naturally resolved by solving the Stokes equation. However, due to the lack of high-order terms, the force-coupling method cannot fully resolve the particle-particle interaction when the

separation distance between two nearby particles is small [135, 144].

Dance & Maxey [50] developed an efficient lubrication model by comparing the exact resistance relations to the numerical resistance relations of FCM for particle-pair and particle-wall interactions. The lubrication model is suited to dilute system in which most lubrication interactions come from particle doublets. To account for the multi-body lubrication interactions, the lubrication force estimated by the sum of each particle-pair interactions is added to the mobility problem as a feedback force. However, it turned out that simply adding the lubrication force to the mobility problem in a pairwise manner is not enough to resolve the many-body hydrodynamic interactions accurately [50, 63].

Since Durlofsky *et al.* [63] suggested a lubrication approximation scheme for their Stokesian Dynamics simulation, their approach has been successfully applied in many subsequent SD simulations [24, 197, 198] as well as in other simulation methods [36, 121, 162]. Instead of adding high-order multipole moments in the resistance matrix, they added the near field interaction to the inverse of the grand mobility matrix in a pairwise manner as an approximation to the exact grand resistance matrix. The near field resistance function is calculated by subtracting the two-body SD resistance matrix ($\boldsymbol{R}_2^{SD}$) from the exact one ($\boldsymbol{R}_2$) obtained from the lubrication theory. Considering that $\boldsymbol{L} = \boldsymbol{R}_2 - \boldsymbol{R}_2^{SD}$ contains the contributions from only high-order multipole moments which decay rapidly in space, the pairwise additivity of the lubrication correction is a reasonable approximation. In this section, we develop the lubrication correction method for the force-coupling method based on the pairwise addition of the lubrication matrix.

The FCM resistance relation is

$$\left(\boldsymbol{M}^{FCM}\right)^{-1} \begin{bmatrix} \mathcal{V} - \mathcal{V}^{\infty} \\ -\tilde{\boldsymbol{E}}^{\infty} \end{bmatrix} = \begin{bmatrix} \mathcal{F} \\ \boldsymbol{S} \end{bmatrix}, \tag{2.125}$$

in which

$$\mathcal{V} = \begin{bmatrix} \boldsymbol{V} \\ \boldsymbol{\Omega} \end{bmatrix}, \quad \mathcal{F} = \begin{bmatrix} \boldsymbol{F} \\ \boldsymbol{T} \end{bmatrix}. \tag{2.126}$$

Following [63], the resistance matrix with the lubrication correction is

$$\left(\left(\boldsymbol{M}^{FCM}\right)^{-1}+\boldsymbol{L}\right)\begin{bmatrix}\mathcal{V}-\mathcal{V}^{\infty}\\ -\tilde{\boldsymbol{E}}^{\infty}\end{bmatrix}=\begin{bmatrix}\mathcal{F}\\ \boldsymbol{S}\end{bmatrix}, \tag{2.127}$$

in which the lubrication correction matrix $\boldsymbol{L}$ is

$$\boldsymbol{L}=\begin{bmatrix}\boldsymbol{R}^{L}_{VF} & \boldsymbol{R}^{L}_{\Omega F} & \boldsymbol{R}^{L}_{EF}\\ \boldsymbol{R}^{L}_{VT} & \boldsymbol{R}^{L}_{\Omega T} & \boldsymbol{R}^{L}_{ET}\\ \boldsymbol{R}^{L}_{VS} & \boldsymbol{R}^{L}_{\Omega S} & \boldsymbol{R}^{L}_{ES}\end{bmatrix}. \tag{2.128}$$

$\boldsymbol{R}_{AB}$ is the resistance matrix to calculate B from given A and $\boldsymbol{R}^{L}$ is the difference between the exact two-body resistance matrix and the FCM resistance matrix, $\boldsymbol{R}^{L}=\boldsymbol{R}_{2B}-\boldsymbol{R}^{FCM}_{2B}$. Let

$$\mathcal{R}=\begin{bmatrix}\boldsymbol{R}^{L}_{VF} & \boldsymbol{R}^{L}_{\Omega F}\\ \boldsymbol{R}^{L}_{VT} & \boldsymbol{R}^{L}_{\Omega T}\end{bmatrix}. \tag{2.129}$$

Multiplying $\boldsymbol{M}^{FCM}$ on both sides of equation (2.127) and rearranging give

$$\begin{bmatrix}\boldsymbol{M}_{\mathcal{F}\mathcal{V}}\mathcal{F}^{tot}\\ -\boldsymbol{M}_{\mathcal{F}E}\mathcal{F}^{tot}-\tilde{\boldsymbol{E}}^{\infty}\end{bmatrix}=\begin{bmatrix}\boldsymbol{I}+\boldsymbol{M}_{\mathcal{F}\mathcal{V}}\mathcal{R} & -\boldsymbol{M}_{S\mathcal{V}}\\ -\boldsymbol{M}_{\mathcal{F}E}\mathcal{R} & \boldsymbol{M}_{SE}\end{bmatrix}\begin{bmatrix}\mathcal{V}-\mathcal{V}^{\infty}\\ \boldsymbol{S}^{tot}\end{bmatrix}, \tag{2.130}$$

in which

$$\mathcal{F}^{tot} = \mathcal{F}+R^{L}_{E\mathcal{F}}\boldsymbol{E}^{\infty}, \tag{2.131}$$

$$\boldsymbol{S}^{tot} = \boldsymbol{S}+R^{L}_{ES}\boldsymbol{E}^{\infty}-R^{L}_{\mathcal{V}S}(\mathcal{V}-\mathcal{V}^{\infty}). \tag{2.132}$$

Note that the dipole coefficient $\boldsymbol{S}^{tot}$ obtained by solving equation (2.130) is different from the stresslet of the particle $\boldsymbol{S}$.

Equation (2.130) is not SPD. So that a GMRES or Bi-conjugate gradient method is required to solve the system. However, often these converge slowly or in some cases the convergence is not even guaranteed. Instead, in order to make the matrix SPD, equation (2.130) is solved for $\mathcal{F}^{lub}=\mathcal{R}(\mathcal{V}-\mathcal{V}^{\infty})$ instead of $\mathcal{V}-\mathcal{V}^{\infty}$. Rewriting equation (2.130)

yields

$$\begin{bmatrix} \boldsymbol{M}_{\mathcal{FV}}\mathcal{F}^{tot} \\ \boldsymbol{M}_{\mathcal{FE}}\mathcal{F}^{tot} + \tilde{\boldsymbol{E}}^{\infty} \end{bmatrix} = \begin{bmatrix} \mathcal{R}^{-1} + \boldsymbol{M}_{\mathcal{FV}} & -\boldsymbol{M}_{S\mathcal{V}} \\ \boldsymbol{M}_{\mathcal{FE}} & -\boldsymbol{M}_{SE} \end{bmatrix} \begin{bmatrix} \mathcal{F}^{lub} \\ \boldsymbol{S}^{tot} \end{bmatrix}. \tag{2.133}$$

The signs in the second row are changed to make the matrix symmetric.

The resistance relation for the force and torque of a particle pair is

$$\begin{bmatrix} \boldsymbol{F}^1 \\ \boldsymbol{F}^2 \\ \boldsymbol{T}^1 \\ \boldsymbol{T}^2 \end{bmatrix} = \mu \begin{bmatrix} \boldsymbol{A}^{11} & \boldsymbol{A}^{12} & \boldsymbol{B}^{11} & -\boldsymbol{B}^{12} & \boldsymbol{G}^{11} & -\boldsymbol{G}^{12} \\ \boldsymbol{A}^{12} & \boldsymbol{A}^{11} & \boldsymbol{B}^{12} & -\boldsymbol{B}^{11} & \boldsymbol{G}^{12} & -\boldsymbol{G}^{11} \\ (\boldsymbol{B}^{11})^T & (\boldsymbol{B}^{12})^T & \boldsymbol{C}^{11} & \boldsymbol{C}^{12} & \boldsymbol{H}^{11} & \boldsymbol{H}^{12} \\ -(\boldsymbol{B}^{12})^T & -(\boldsymbol{B}^{11})^T & \boldsymbol{C}^{12} & \boldsymbol{C}^{11} & \boldsymbol{H}^{12} & \boldsymbol{H}^{11} \end{bmatrix} \begin{bmatrix} \boldsymbol{V}^1 - \boldsymbol{V}^{\infty}(\boldsymbol{Y}^1) \\ \boldsymbol{V}^2 - \boldsymbol{V}^{\infty}(\boldsymbol{Y}^2) \\ \boldsymbol{\Omega}^1 - \boldsymbol{\Omega}^{\infty}(\boldsymbol{Y}^1) \\ \boldsymbol{\Omega}^2 - \boldsymbol{\Omega}^{\infty}(\boldsymbol{Y}^2) \\ -\boldsymbol{E}^{\infty} \\ -\boldsymbol{E}^{\infty} \end{bmatrix}. \tag{2.134}$$

Exploiting the axisymmetry of the two sphere configuration, the resistance tensors can be written in terms of several scalar functions. Following the notation in Kim & Karrila [110],

$$\begin{aligned} A_{ij}^{\alpha\beta}/6\pi a &= X_{\alpha\beta}^{A} d_i d_j + Y_{\alpha\beta}^{A}(\delta_{ij} - d_i d_j), \\ B_{ij}^{\alpha\beta}/6\pi a^2 &= Y_{\alpha\beta}^{B} \epsilon_{jik} d_k, \\ C_{ij}^{\alpha\beta}/8\pi a^3 &= X_{\alpha\beta}^{C} d_i d_j + Y_{\alpha\beta}^{C}(\delta_{ij} - d_i d_j), \\ G_{kij}^{\alpha\beta}/6\pi a^2 &= X_{\alpha\beta}^{G}(d_i d_j - \frac{1}{3}\delta_{ij}) d_k + Y_{\alpha\beta}^{G}(d_i \delta_{jk} + d_j \delta_{ik} - 2 d_i d_j d_k), \\ H_{kij}^{\alpha\beta}/8\pi a^3 &= Y_{\alpha\beta}^{H}(\epsilon_{ikl} d_l d_j + \epsilon_{jkl} d_l d_i), \end{aligned}$$

in which $\boldsymbol{d} = \boldsymbol{r}/|\boldsymbol{r}|$ and $\boldsymbol{r} = \boldsymbol{Y}^{\beta} - \boldsymbol{Y}^{\alpha}$. The analytic forms of the scalar functions are given in [50, 101, 110].

To calculate the FCM resistance function, first the two-particle mobility matrices for various configurations and separation distances were constructed from the FCM Oseen operator given in [135, 144]. Then, the mobility matrices were inverted to obtain the values of the resistance functions for each separation distance. Finally, the resistance functions

Table 2.1: FCM resistance functions for a particle pair

	C_0	C_1	C_2	C_3	C_4
X_{11}^A	2.3593	−2.6950	3.4626	−2.6058	0.8310
X_{12}^A	−1.7187	2.7545	−3.4658	2.6047	−0.8308
X_{11}^C	1.0151	−0.0419	0.0576	−0.0426	0.0132
X_{12}^C	−0.1241	0.1783	−0.1524	0.0816	−0.0205
X_{11}^G	0.9670	−2.0276	2.4960	−1.7932	0.5540
X_{12}^G	−1.1651	2.0898	−2.5005	1.7946	−0.5563
Y_{11}^A	1.3351	−0.6292	0.7689	−0.5602	0.1754
Y_{12}^A	−0.6114	0.7157	−0.7830	0.5571	−0.1737
Y_{11}^B	−0.1998	0.4427	−0.5613	0.4066	−0.1256
Y_{12}^B	0.3532	−0.5293	0.5749	−0.3972	0.1238
Y_{11}^C	1.1253	−0.3090	0.3944	−0.2779	0.0832
Y_{12}^C	0.0965	−0.1827	0.2050	−0.1378	0.0409
Y_{11}^G	0.0816	−0.2134	0.2889	−0.2144	0.0668
Y_{12}^G	−0.1111	0.2423	−0.2936	0.2065	−0.0630
Y_{11}^H	0.0165	−0.0669	0.1117	−0.0909	0.0294
Y_{12}^H	0.1695	−0.2605	0.2386	−0.1362	0.0361

were found by a non-singular asymptotic matching,

$$R = C_0 + C_1\epsilon + C_2\epsilon^2 + C_3\epsilon^3 + C_4\epsilon^4, \tag{2.135}$$

in which ϵ is the separation distance between two particles, $a\epsilon = |\boldsymbol{r}| - 2a$. Coefficients of the polynomials are given in table 2.1.

An example of the FCM resistance function is shown in figure 2.5. X_{11}^A is a resistance function relating the force and the translational velocity for the translational motion along the sphere-sphere axis [110]. The corresponding values of X_{11}^A for the force-torque-stresslet version of SD (SD-FTS) is obtained from [96]. For this resistance function, it is shown that the force-coupling method shows the similar far field approximation with SD-FTS. It is shown that FCM resistance function is almost indistinguishable from the exact resistance function when $r/a > 2.5$. Hence, the cut-off distance for the lubrication interaction is set to $r_c = 2.8a$.

Solving equation (2.133) using a conjugate gradient method requires inner and outer conjugate gradient solvers to invert both $\mathcal{R}$ and the full system simultaneously. However, due to the large condition number, it is not trivial to compute $\mathcal{R}^{-1}$ using an iterative solver. For example, in a squeezing configuration of a particle pair, only the resistance function

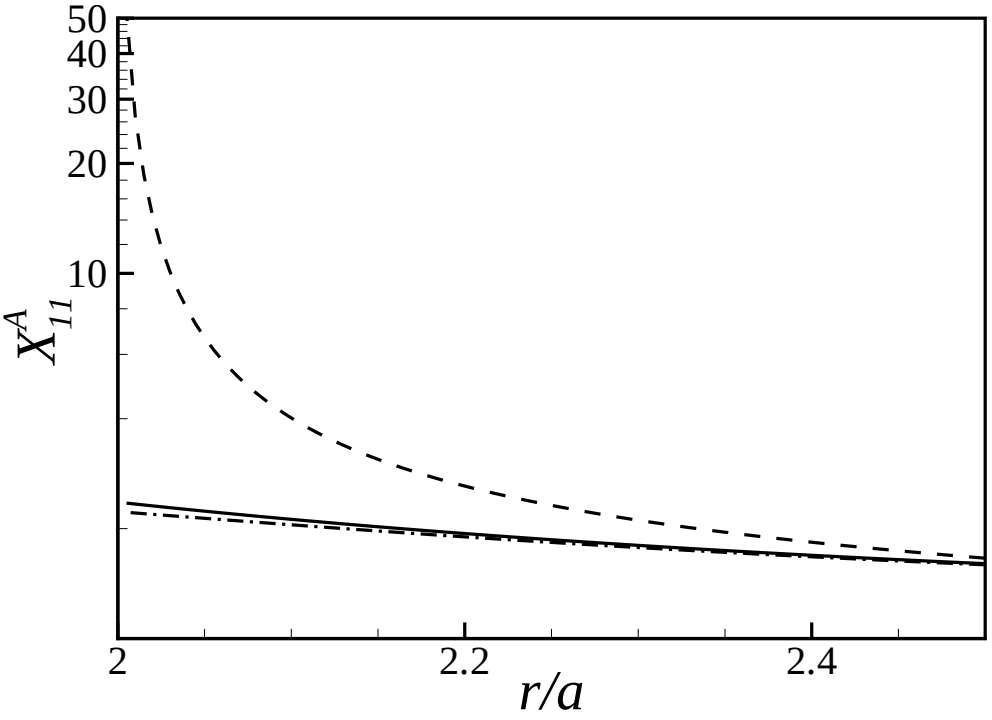

Figure 2.5: The resistance function X_{11}^A of the exact solution (dashed line), FCM (solid line), and SD-FTS (dash-dot line).

X^A is considered

$$\begin{bmatrix} F_{\parallel}^1 \\ F_{\parallel}^2 \end{bmatrix} = 6\pi\mu a \begin{bmatrix} X_{11}^A & X_{12}^A \\ X_{12}^A & X_{11}^A \end{bmatrix} \begin{bmatrix} V_{\parallel}^1 \\ V_{\parallel}^2 \end{bmatrix}. \tag{2.136}$$

The leading-order singular term in X^A is $1/\epsilon$ and the difference between diagonal (X_{11}^A) and off-diagonal (X_{12}^A) terms are $O(10^{-3})$, which makes the condition number of the matrix $\mathcal{K}(\mathcal{R}) \sim 1/\epsilon \times 10^3$ for ϵ small. Even when $\epsilon = 10^{-3}$, $\mathcal{K}(\mathcal{R})$ is $O(10^6)$. At high volume fractions, $\mathcal{K}(\mathcal{R})$ becomes too large for the matrix to be inverted using the standard conjugate gradient method.

Here, we present a preconditioned conjugate gradient method in which $\mathcal{R}^{-1}$ is calculated recursively without an iterative solver. Let $\boldsymbol{P}$ be a preconditioner for equation (2.133) defined as

$$\boldsymbol{P}^{-1} = \begin{bmatrix} \mathcal{R} & \boldsymbol{0} \\ \boldsymbol{0} & \kappa \boldsymbol{I} \end{bmatrix}, \tag{2.137}$$

in which κ is a scale factor, $\kappa = \frac{20}{3}\pi\mu a^3$. The procedure is as follows

1. *Initialization*:

   Initialize vectors $\boldsymbol{r}, \boldsymbol{\psi}$, and $\boldsymbol{\phi}$ from an initial estimate $\mathcal{F}^0 = \mathcal{R}\mathcal{V}^0$ and $\boldsymbol{S}^0$.

$$\begin{bmatrix} \boldsymbol{r}_f^0 \\ \boldsymbol{r}_s^0 \end{bmatrix} = \begin{bmatrix} \boldsymbol{M}_{\mathcal{F}\mathcal{V}}(\mathcal{F}^{tot} - \mathcal{F}^0) + \boldsymbol{M}_{S\mathcal{V}}\boldsymbol{S}^0 - \mathcal{V}^0 \\ \boldsymbol{M}_{\mathcal{F}E}(\mathcal{F}^{tot} - \mathcal{F}^0) + \boldsymbol{M}_{SE}\boldsymbol{S}^0 + \tilde{\boldsymbol{E}}^{\infty} \end{bmatrix}, \tag{2.138}$$

$$\begin{bmatrix} \psi_f^0 \\ \psi_s^0 \end{bmatrix} = \boldsymbol{P}^{-1}\boldsymbol{r}^0 = \begin{bmatrix} \mathcal{R}\boldsymbol{r}_f^0 \\ \kappa \boldsymbol{r}_s^0 \end{bmatrix}, \tag{2.139}$$

$$\boldsymbol{\phi}^0 = \boldsymbol{\psi}^0. \tag{2.140}$$

2. *Iteration*:

For $n = 0,\ 1,\ \cdots$

$$\begin{aligned}
\alpha^n &= \frac{\boldsymbol{\psi}^n \cdot \boldsymbol{r}^n}{\boldsymbol{\phi}^n \cdot \boldsymbol{A}\boldsymbol{\phi}^n} && (2.141)\\
\begin{bmatrix}\mathcal{F}^{n+1}\\ \boldsymbol{S}^{n+1}\end{bmatrix} &= \begin{bmatrix}\mathcal{F}^{n}\\ \boldsymbol{S}^{n}\end{bmatrix} + \alpha^n \begin{bmatrix}\phi_f^n\\ \phi_s^n\end{bmatrix} && (2.142)\\
\boldsymbol{r}^{n+1} &= \boldsymbol{r}^n - \alpha^n \boldsymbol{A}\boldsymbol{\phi}^n && (2.143)\\
\boldsymbol{\psi}^{n+1} &= \boldsymbol{P}^{-1}\boldsymbol{r}^{n+1} && (2.144)\\
\beta^n &= \frac{\boldsymbol{\psi}^{n+1} \cdot \boldsymbol{r}^{n+1}}{\boldsymbol{\psi}^n \cdot \boldsymbol{r}^n} && (2.145)\\
\boldsymbol{\phi}^{n+1} &= \boldsymbol{\psi}^{n+1} + \beta^n \boldsymbol{\phi}^n && (2.146)
\end{aligned}$$

where

$$\boldsymbol{A} = \begin{bmatrix}\mathcal{R}^{-1} + \boldsymbol{M}_{\mathcal{F}\mathcal{V}} & -\boldsymbol{M}_{S\mathcal{V}}\\ \boldsymbol{M}_{\mathcal{F}E} & -\boldsymbol{M}_{SE}\end{bmatrix}. \qquad (2.147)$$

3. Repeat step 2 until $||\boldsymbol{r}^{n+1}||^2 \leq \delta$ for a tolerance level δ.

In step 2, $\boldsymbol{A}\boldsymbol{\phi}^n$ involves computing $\mathcal{R}^{-1}\phi_f^n$. From the initialization step, it is obvious that

$$\mathcal{R}^{-1}\phi_f^0 = \mathcal{R}^{-1}\psi_f^0 = \boldsymbol{r}_f^0. \qquad (2.148)$$

Similarly, for $n \geq 1$, there is a general recursive solution,

$$\begin{aligned}
\mathcal{R}^{-1}\phi_f^n &= \mathcal{R}^{-1}(\psi_f^n + \beta^{n-1}\phi_f^{n-1}) = \boldsymbol{r}_f^n + \beta^{n-1}(\mathcal{R}^{-1}\phi_f^{n-1})\\
&= \boldsymbol{r}_f^n + \sum_{i=0}^{n-1}\left(\prod_{j=i}^{n-1}\beta^j\right)\boldsymbol{r}_f^i. && (2.149)
\end{aligned}$$

Once $\mathcal{F}^{lub}$ is found, $\mathcal{V}$ can be computed from either

$$\mathcal{V} = \mathcal{R}^{-1}\mathcal{F}^{lub}, \qquad (2.150)$$

or

$$\mathcal{V} = \mathcal{V}^{\infty} + \boldsymbol{M}_{\mathcal{F}\mathcal{V}}(\mathcal{F}^{tot} - \mathcal{F}^{lub}) + \boldsymbol{M}_{S\mathcal{V}}\boldsymbol{S}^{tot}. \qquad (2.151)$$

Note that at low volume fractions, there are many particles which do not have particles in their neighborhood. In that case, the number of degrees of freedom of equation (2.150) is $6 \times N_c$ and not $6 \times N_p$, in which N_c denotes the number of particles which have at least one particle within the cut-off distance ($r_c = 2.8a$). Therefore, to calculate $\mathcal{V}$ for those particles which do not have any neighboring particles, we need to solve equation (2.151).

2.3.2 Particle-wall lubrication correction

Close to a rigid, no-slip boundary, additional viscous lubrication corrections are required for the motion of a particle relative to the wall boundary. This modification for FCM is given by [50] in the simpler context of dilute suspensions. We summarize briefly, and with more general notation, the steps for adding these corrections in the resistance matrix.

The resistance relation of a single particle moving in a flow near a wall is

$$\begin{bmatrix} \boldsymbol{F} \\ \boldsymbol{T} \end{bmatrix} = \mu \begin{bmatrix} \boldsymbol{A} & \boldsymbol{B} & \boldsymbol{G} \\ \boldsymbol{B}^T & \boldsymbol{C} & \boldsymbol{H} \end{bmatrix} \begin{bmatrix} \boldsymbol{V} - \boldsymbol{V}^{\infty}(\boldsymbol{Y}) \\ \boldsymbol{\Omega} - \boldsymbol{\Omega}^{\infty}(\boldsymbol{Y}) \\ -\boldsymbol{E}^{\infty} \end{bmatrix}. \tag{2.152}$$

Following the notation in [110], the resistance tensors are

$$\begin{aligned} A_{ij}/6\pi a &= X^A d_i d_j + Y^A(\delta_{ij} - d_i d_j), \\ B_{ij}/6\pi a^2 &= Y^B \epsilon_{jik} d_k, \\ C_{ij}/8\pi a^3 &= X^C d_i d_j + Y^C(\delta_{ij} - d_i d_j), \\ G_{kij}/6\pi a^2 &= Y^G(d_i \delta_{jk} + d_j \delta_{ik} - 2 d_i d_j d_k), \\ H_{kij}/8\pi a^3 &= Y^H(\epsilon_{ikl} d_l d_j + \epsilon_{jkl} d_l d_i), \end{aligned}$$

in which $\boldsymbol{d}$ is the unit vector from the particle center to a wall. The exact values for the various wall resistance functions are summarized in Appendix A, where they are given as asymptotic series in the gap width $a\epsilon$ between the particle and the wall.

Second, the non-singular estimates of the corresponding wall resistance functions from FCM are determined numerically for a single particle. This computation is done in the domain $\boldsymbol{\Omega}^D = (0, L_x) \times (0, L_y) \times (0, L_z)$, where periodic boundary conditions are applied in the x_1 and x_3 directions with the no-slip boundary conditions ($\boldsymbol{u} = 0$) on $x_2 = 0$ and L_y. A Fourier spectral method is used in the horizontal (x_1, x_3) directions and a spectral element

Table 2.2: Particle-wall FCM resistance functions

	C_0	C_1	C_2	C_3	C_4
X^A	8.1108	-26.117	62.532	-84.151	46.472
Y^A	2.3514	-3.6192	8.5516	-13.557	9.8027
Y^B	-0.2295	1.2393	-3.7731	6.6984	-5.0789
X^C	1.1239	-0.3084	0.3610	-0.1688	-0.0030
Y^C	1.4205	-1.4217	3.0026	-4.1003	2.6037
Y^G	0.5629	-1.7656	4.0292	-6.1515	4.3758
Y^H	-0.0447	-0.1588	1.0918	-2.3320	1.7748

method is employed in the vertical direction (x_2). Details of the numerical method are given in 2.5.2. In order to estimate the FCM resistance functions, the numerical simulations were performed in a large channel, $L_x/a = L_y/a = L_z/a = 60$, so as to minimize the effects of the periodicity and the presence of the upper wall. A sphere is located at $L_x/a = L_z/a = 30$. The hydrodynamic drag and torque were computed, varying the distance from the lower wall for the different configurations of particle motion or flow. The results were then matched to a regular asymptotic expansion for the FCM resistance function for small values of the gap $a\epsilon$ between the particle and the lower wall;

$$R = C_0 + C_1\epsilon + C_2\epsilon^2 + C_3\epsilon^3 + C_4\epsilon^4.$$

The coefficients are shown in table 2.2. The particle-wall resistance function X^C is finite at the wall, $\epsilon = 0$, and is matched satisfactorily by the FCM result so that in practice, special treatment of this term is not necessary.

The lubrication correction is implemented in the same way as described in 2.3.1. First, $\mathcal{R}$ is constructed by summing all the particle-pair interactions. Since the lubrication force arises from the relative motion between particles, $\mathcal{R}_{2B}$ is written in the relative velocity formulation [34, 162]. Then, the resistance tensors for the particle-wall lubrication are added to $\mathcal{R}$.

2.3.3 Fictitious inertia for dynamic simulation

In section 2.3.1, we have shown that the lubrication force can be computed without inverting the resistance matrix $\mathcal{R}$. There are two formulae to compute $\mathcal{V}$ (2.150) and (2.151) and the difference in $\mathcal{V}$ calculated by between two formulae are negligibly small; usually less

than 0.1%. In practice, (1) solving (2.150) can be much faster than (2.151), as it consists of only matrix-vector multiplications, and (2) it was found that the preconditioned conjugate gradient solver converges faster when the velocity obtained by (2.150) is used as an initial estimate. Yet, inverting the ill-conditioned matrix $\mathcal{R}$ is not an easy task. Here, we introduces a fictitious inertia to the force balance equation (2.127) to accelerate the convergence for dynamic simulations.

Adding fictitious particle accelerations on both sides of (2.127) yield

$$\left(\left(\boldsymbol{M}^{FCM}\right)^{-1}+\boldsymbol{L}\right)\begin{bmatrix}\tilde{\mathcal{V}}\\ -\tilde{\boldsymbol{E}}^{\infty}\end{bmatrix}+\begin{bmatrix}\lambda\frac{d}{dt}\tilde{\mathcal{V}}\\ \boldsymbol{0}\end{bmatrix}=\begin{bmatrix}\mathcal{F}\\ \boldsymbol{S}\end{bmatrix}+\begin{bmatrix}\lambda\frac{d}{dt}\tilde{\mathcal{V}}\\ \boldsymbol{0}\end{bmatrix}, \tag{2.153}$$

in which $\tilde{\mathcal{V}}=\mathcal{V}-\mathcal{V}^{\infty}$ and λ is a constant. Simply, we can use an implicit time discretization for the acceleration term on L.H.S and an explicit discretization for the acceleration on R.H.S. If a second order temporal discretization is used,

$$\begin{aligned}&\left(\left(\boldsymbol{M}^{FCM}\right)^{-1}+\boldsymbol{L}\right)^{n+1}\begin{bmatrix}\tilde{\mathcal{V}}\\ -\tilde{\boldsymbol{E}}^{\infty}\end{bmatrix}^{n+1}+\frac{\lambda}{2\delta t}\begin{bmatrix}\tilde{\mathcal{V}}^{n+1}-\tilde{\mathcal{V}}^{n-1}\\ \boldsymbol{0}\end{bmatrix}=\\ &\begin{bmatrix}\mathcal{F}\\ \boldsymbol{S}\end{bmatrix}^{n+1}+\frac{\lambda}{2\delta t}\begin{bmatrix}3\tilde{\mathcal{V}}^{n}-4\tilde{\mathcal{V}}^{n-1}+\tilde{\mathcal{V}}^{n-2}\\ \boldsymbol{0}\end{bmatrix}.\end{aligned} \tag{2.154}$$

If we assume $\mathcal{V}$ is smooth in time, it is trivial to show that the error caused by the fictitious inertia is $O(\lambda\delta t^2)$. As the time step δt in the simulations of concentrated suspensions is usually very small $\delta t \sim 10^{-3}/\dot{\gamma}$ – $10^{-4}/\dot{\gamma}$, the error due to the fictitious inertia is many times less than the tolerance of the conjugate gradient solver. It is also found that, in practice, it is sufficient to choose the coefficient $\lambda \sim O(\delta t)$, which makes the error even smaller $\sim O(\delta t^3)$.

Choosing $\lambda = 2\alpha\delta t$ and rearranging (2.154), the final equation for the lubrication force is

$$\begin{bmatrix}\boldsymbol{M}_{\mathcal{F}\mathcal{V}}\mathcal{F}'\\ \boldsymbol{M}_{\mathcal{F}E}\mathcal{F}'+\tilde{\boldsymbol{E}}^{\infty}\end{bmatrix}=\begin{bmatrix}(\mathcal{R}+\alpha\boldsymbol{I})^{-1}+\boldsymbol{M}_{\mathcal{F}\mathcal{V}} & -\boldsymbol{M}_{S\mathcal{V}}\\ \boldsymbol{M}_{\mathcal{F}E} & -\boldsymbol{M}_{SE}\end{bmatrix}\begin{bmatrix}\mathcal{F}^{lub}\\ \boldsymbol{S}^{tot}\end{bmatrix}, \tag{2.155}$$

in which α is an arbitrary constant of $O(1)$, $\boldsymbol{I}$ is the identity matrix, and

$$\mathcal{F}' = \mathcal{F}^{tot} + \alpha(3\mathcal{V}^n - 3\mathcal{V}^{n-1} + \mathcal{V}^{n-2}). \tag{2.156}$$

Once $\mathcal{F}^{lub}$ is computed, the particle velocities are computed from

$$\mathcal{V} = (\mathcal{R} + \alpha \boldsymbol{I})^{-1} \mathcal{F}^{lub}. \tag{2.157}$$

Equation (2.155) can be solved by the same preconditioned conjugate gradient procedure as for (2.133).

2.4 Solution procedure for finite-inertia suspensions

The force-coupling method was developed for Stokes flows [144, 135]. Nevertheless, it has been verified and successfully employed for finite-Reynolds-number and turbulent flows [136, 39, 211, 225, 228]. Although the FCM with both the mono- and dipole forces has been used for Navier-Stokes flows, the solution procedure has not been clearly shown in any of the previous papers. In this section, the force-coupling procedure for the Navier-Stokes equations with the lubrication correction shown in section 2.3.1 is described.

The Navier-Stokes equations with the force-coupling method are

$$\boldsymbol{\nabla} \cdot \boldsymbol{u} = 0 \tag{2.158}$$

$$\begin{aligned} \rho_f \frac{\partial \boldsymbol{u}}{\partial t} &= -\boldsymbol{\nabla} p - \rho_f (\boldsymbol{u} \cdot \boldsymbol{\nabla}) \boldsymbol{u} + \mu \nabla^2 \boldsymbol{u} \\ &+ \sum_k^{N_p} \boldsymbol{F}_k \Delta_M(\boldsymbol{x} - \boldsymbol{Y}_k) + (\boldsymbol{G}_k \cdot \boldsymbol{\nabla}) \Delta_D(\boldsymbol{x} - \boldsymbol{Y}_k), \end{aligned} \tag{2.159}$$

in which ρ_f is the density of the fluid and N_p is the total number of particles. From the equation of motion of particles, the monopole strength $\boldsymbol{F}$ is given by

$$\boldsymbol{F} = -(m_p - m_f) \left(\frac{d\boldsymbol{V}}{dt} - g \right) - \boldsymbol{F}^{lub} + \boldsymbol{F}^P, \tag{2.160}$$

where $\boldsymbol{g}$ is the gravitational acceleration, $\boldsymbol{F}^P$ is the interparticle force, m_p is the mass of the suspended particle, and m_f denotes the mass of fluid which occupies the same volume of the suspended particle. In the case of suspensions of neutrally buoyant particles, the first

term on R.H.S of (2.160) is zero. However, to construct a well-conditioned system, we will leave the particle acceleration term for now and disregard the gravitational acceleration.

To solve the Navier-Stokes equations, usually a semi-implicit temporal discretization is employed; the viscous terms are treated implicitly and an explicit scheme is used for the non-linear terms. Using the Adam-Bashforth family schemes, a semi-discretized equation of (2.159) can be written as,

$$\begin{aligned}\rho_f \frac{\boldsymbol{u}^{n+1}-\boldsymbol{u}^n}{\delta t} &= -\boldsymbol{\nabla} p^{n+1} - \sum_{i=1}^{J_e} \alpha_i \boldsymbol{H}^{n+1-i} + \mu \sum_{i=0}^{J_i} \beta_i (\nabla^2 \boldsymbol{u})^{n+1-i} \\ &+ \sum_{k}^{N_p} \boldsymbol{F}_k \Delta_M(\boldsymbol{x}-\boldsymbol{Y}_k) + (\boldsymbol{G}_k \cdot \boldsymbol{\nabla}) \Delta_D(\boldsymbol{x}-\boldsymbol{Y}_k), \end{aligned} \tag{2.161}$$

in which the coefficients α_i and β_i and the order of explicit J_e and implicit discretization J_i depend on the choice of the scheme, $\boldsymbol{H}$ is the nonlinear term ($H_i = -\rho u_j \partial_j u_i$). We have not specified a scheme for the force-coupling terms, yet. Note that, the Nabla operators – the gradient and Laplacian operators in the nonlinear and viscous terms, respectively – need to be included in the temporal discretization. In a fixed computational domain, it is obvious that $\nabla^{n+1} = \nabla^n$. However, in a coordinate system deforming with time (see section 2.5.1), care should be taken on treating the Nabla operator as $\nabla^n u^n \neq \nabla^{n+1} u^n$.

The dipole term consists of the couplet and stresslet. When there is no external torque, the couplet is only due to the lubrication torque given in section 2.3.1. The stresslet acts as a constraint to satisfy the kinetic energy balance that the contribution to the total rate of work is zero, which corresponds to the rigidity constraint given in (2.12) and (2.122). The monopole coefficient includes the lubrication force, which is proportional to the velocity of the particle $\mathcal{RV}$. As the lubrication force is proportional to $\sim 1/\epsilon$, in concentrated suspensions, the system becomes numerically too stiff to use an explicit method. Here, we use a fully implicit scheme for the FCM force terms. Then, then the FCM force terms in (2.161) are

$$\sum_{k}^{N_p} \boldsymbol{F}_k^{n+1} \Delta_M(\boldsymbol{x}-\boldsymbol{Y}_k^{n+1}) + (\boldsymbol{G}_k^{n+1} \cdot \boldsymbol{\nabla}) \Delta_D(\boldsymbol{x}-\boldsymbol{Y}_k^{n+1}). \tag{2.162}$$

Here, the monopole force consists of the interparticle force, lubrication force, and particle accelerations. The interparticle force only depends on the configuration of the particles at

$t = (n+1)\delta t$, which can be easily evaluated. To obtain the lubrication force implicitly, we need to invert the FCM resistance matrix as done in section 2.3.1. This will be explained in detail later in this section. To make the resistance matrix well conditioned, the particle acceleration term is separated into two parts,

$$-(m_p - m_f)\left(\frac{d\boldsymbol{V}}{dt}\right)^{n+1} = m_f \frac{\boldsymbol{V}^n - \boldsymbol{V}^{n-1}}{\delta t} - m_p \frac{\boldsymbol{V}^{n+1} - \boldsymbol{V}^n}{\delta t}. \tag{2.163}$$

Even for neutrally-buoyant particles ($m_f = m_p$), we will treat the first and the second terms on R.H.S separately, similarly to the fictitious inertia in the previous section.

The solution procedure of the semi-discretized equation (2.161) is as follows

1. Move the particles to the new location using an explicit scheme,

$$\boldsymbol{Y}^{n+1} = \boldsymbol{Y}^n + \sum_{i=0}^{J} \xi_i \boldsymbol{V}^{n-i},$$

   in which ξ_i is a coefficient of the explicit scheme used.

2. Calculate the force envelopes and the interparticle forces at $t = (n+1)\delta t$.

3. Calculate an intermediate velocity from the explicit terms,

$$\begin{aligned}\hat{\boldsymbol{u}} = \boldsymbol{u}^n \quad &+ \quad \frac{\delta t}{\rho_f}\Bigg(\sum_{i=1}^{J_e} \alpha_i \boldsymbol{H}^{n+1-i} + \mu \sum_{i=1}^{J_i} \beta_i (\nabla^2 \boldsymbol{u})^{n+1-i} \\ &+ \quad \sum_{k}^{N_p} \left[m_f \frac{\boldsymbol{V}_k^n - \boldsymbol{V}_k^{n-1}}{\delta t} + \boldsymbol{F}_k^P \right] \Delta_M(\boldsymbol{x} - \boldsymbol{Y}_k^{n+1}) \Bigg).\end{aligned}$$

4. Compute an intermediate pressure from the continuity equation,

$$\begin{aligned}\nabla^2 p^* &= -\rho_f \boldsymbol{\nabla} \cdot \left(\frac{\hat{\boldsymbol{u}}}{\delta t}\right), \\ \tilde{\boldsymbol{u}} &= \hat{\boldsymbol{u}} - \frac{\delta t}{\rho_f} \boldsymbol{\nabla} p^*.\end{aligned}$$

   Note that the Nabla operators are for $t = (n+1)\delta t$. After this step, the intermediate velocity $\tilde{\boldsymbol{u}}$ satisfies the divergence-free condition.

5. Compute $\boldsymbol{u}^{n+1}$ by solving

$$\left(\frac{\rho_f}{\delta t} - \mu\beta_0\nabla^2\right)\boldsymbol{u}^{n+1} = \frac{\rho_f}{\delta t}\tilde{\boldsymbol{u}} - \boldsymbol{\nabla}p^{**} + \boldsymbol{f},$$

in which

$$\begin{aligned}
\nabla^2 p^{**} &= \boldsymbol{\nabla}\cdot\boldsymbol{f}, \\
\boldsymbol{f} &= \sum_k^{N_p} -\left[\frac{m_p}{\delta t}(\boldsymbol{V}_k^{n+1} - \boldsymbol{V}_k^n) + \boldsymbol{F}_k^{lub}\right]\Delta_M(\boldsymbol{x} - \boldsymbol{Y}_k^{n+1}) \\
&\quad + (\boldsymbol{G}_k^{n+1}\cdot\boldsymbol{\nabla})\Delta_D(\boldsymbol{x} - \boldsymbol{Y}_k^{n+1}).
\end{aligned}$$

In the last step of the force-coupling procedure, the FCM terms on the R.H.S. are functions of $\boldsymbol{u}$ at $t = (n+1)\delta$ and, hence, an iterative solver is necessary to solve the equation. The equation of $\boldsymbol{u}^{n+1}$ in the last step is elliptic and the only difference compared to the Stokes equations is that the Laplacian operator in the Stokes equations is replaced by a Helmholtz operator. Hence, a preconditioned conjugate gradient procedure similar to the one shown in sections 2.3.1 and 2.3.3 can be used. In fact, the equation in the last step is easier to solve than the Stokes equations, as a spatial discretization of the Helmholtz operator often results in a better conditioned matrix than that of the Laplacian operator.

In a matrix form, the final equation becomes

$$\begin{bmatrix} \boldsymbol{M}_{\mathcal{F}\mathcal{V}}\mathcal{F}' \\ \boldsymbol{M}_{\mathcal{F}E}\mathcal{F}' + \boldsymbol{E}^{\infty} \end{bmatrix} + \begin{bmatrix} \tilde{\mathcal{V}} \\ \tilde{\boldsymbol{E}} \end{bmatrix} = \begin{bmatrix} (\mathcal{R} + \frac{1}{\delta t}\boldsymbol{\Lambda})^{-1} + \boldsymbol{M}_{\mathcal{F}\mathcal{V}} & -\boldsymbol{M}_{S\mathcal{V}} \\ \boldsymbol{M}_{\mathcal{F}E} & -\boldsymbol{M}_{SE} \end{bmatrix} \begin{bmatrix} \mathcal{F}^{lub} \\ \boldsymbol{S}^{n+1} \end{bmatrix}, \tag{2.164}$$

in which $\mathcal{F}' = \mathcal{F}^{tot} + (1/\delta t)\boldsymbol{\Lambda}\mathcal{V}^n$, $\boldsymbol{\Lambda}$ is the diagonal matrix for the mass and moment of inertia of the particle. $\tilde{\mathcal{V}}$ and $\tilde{\boldsymbol{E}}$ are, respectively, the velocities and strain rate estimated from the intermediate velocity $\tilde{\boldsymbol{u}}$. The particle stresslet can be computed by (2.132), replacing $\boldsymbol{S}^{tot}$ by $\boldsymbol{S}^{n+1}$. Note that the mobility matrix corresponds to solving the Helmholtz equation, not the Laplace equation in the Stokes flows. In Stokes flows, the particle velocity is calculated by inverting the resistance matrix, as we are only interested in the motion of the particles. However, in Navier-Stokes flows, the flow field at $t = (n+1)\delta t$ is necessary to compute the nonlinear terms. So, we need to first compute $\boldsymbol{u}^{n+1}$ from $\mathcal{F}^{lub}$ and $\boldsymbol{S}^{n+1}$ and, then, estimate $\mathcal{V}^{n+1}$ by the weighted integration of $\boldsymbol{u}^{n+1}$ as shown in (2.8, 2.9).

As a final remark, the overall temporal accuracy of the scheme given in this section is $\sim O(\delta t)$, as usual in other schemes to simulate concentrated suspensions [162]. Because the time step size δt is usually very small in the simulations of concentrated suspensions, $\delta t \sim 10^{-3}/\dot{\gamma}$, the first order accuracy seems not be an issue in resolving essential dynamics of suspension flows. Nevertheless, we propose a higher-order temporal discretization. Usually, in a semi-implicit method, the Crank-Nicolson method is used for the implicit terms. However, as we want to keep the stresslet term as a constraint at $t = (n+1)\delta t$, a backward multi-step method would be more appropriate for our purpose. The stiffly-stable scheme proposed by Karniadakis *et al.* [103] for the Navier-Stokes equations would be a reasonable choice for the time integration. Using the stiffly-stable scheme, the semi-discretized equation is given as

$$\rho_f \frac{\gamma_0 \boldsymbol{u}^{n+1} - \sum_{q=0}^{J_i-1} \alpha_q \boldsymbol{u}^{n-q}}{\delta t} = -\boldsymbol{\nabla} p^{n+1} - \sum_{i=0}^{J_e-1} \beta_i \boldsymbol{H}^{n-i} + \mu \nabla^2 \boldsymbol{u}^{n+1} + \boldsymbol{f}^{n+1}, \qquad (2.165)$$

in which

$$\begin{aligned} \boldsymbol{f}^{n+1} &= \sum_{k}^{N_p} \left[m_f \left(\frac{d\boldsymbol{V}_k}{dt} \right)^{n+1} - m_p \left(\frac{d\boldsymbol{V}_k}{dt} \right)^{n+1} - \boldsymbol{F}_k^{lub} + \boldsymbol{F}^P \right] \Delta_M(\boldsymbol{x} - \boldsymbol{Y}_k^{n+1}) \\ &+ (\boldsymbol{G}_k^{n+1} \cdot \boldsymbol{\nabla}) \Delta_D(\boldsymbol{x} - \boldsymbol{Y}_k^{n+1}). \end{aligned} \qquad (2.166)$$

The particle acceleration terms can be treated as before, but using a high-order polynomial. The pressure is calculated by using the same splitting procedure shown in the first-order scheme. In a tri-periodic domain, the pressure can be computed by an algebraic equation in the Fourier space. However, in a wall bounded domain, the pressure boundary condition needs to be treated carefully. See Karniadakis & Sherwin [104] for high-order pressure boundary conditions. The coefficients γ_0, α_i, and β_i can be found in Karniadakis *et al.* [103] and Karniadakis & Sherwin [104]. Even though the higher-order formulation is shown for an arbitrary order, generally it is not recommended to use more than the second-order scheme. First, as shown by Dahlquist [48], the scheme is A-stable only up to second order and, second, in a wall-bounded domain, the accuracy of the solver is anyway limited by the pressure boundary condition.

2.5 Flow solvers

2.5.1 Tri-periodic domain

One of the simplest and yet most interesting non-colloidal suspension flows is homogeneous suspensions in a linear shear flow in an infinite domain. To model such an infinite domain, usually a tri-periodic domain is used in numerical simulations. It should be noted that, when a periodic boundary condition is used, it is assumed that the dimension of the domain in the periodic direction $\mathcal{L}$ is sufficiently large that the Eulerian correlation of the variables of interest decays before $\mathcal{L}/2$. In other words, an integral lengthscale l should be much smaller than $\mathcal{L}/2$.

One of the difficulties in imposing the periodic boundary condition in a tri-periodic domain is that the periodic image of a variable is a function of the time in shear flow. That is, $f(x_1, x_2, x_3) = f(x_1 + n_1 H_1 + n_2 H_2 \dot{\gamma} t, x_2 + n_2 H_2, x_3 + n_3 H_3)$, in which $x_1,\ x_2$, and x_3 denote, respectively, the velocity, velocity-gradient, and vorticity directions, H_i is the size of the domain in $i-$direction, $n_1,\ n_2$, and n_3 are arbitrary constants, and $\dot{\gamma}$ is the shear rate. Lees & Edward [125] devised a bi-periodic domain concept to account for this time dependence, which is the celebrated 'Lees-Edward' boundary condition. To solve the Navier-Stokes equations in such a tri-periodic domain with an imposed strain-rate, Rogallo [183] proposed a moving coordinate system, in which a coordinate system is linearly related with an inertial frame of reference. In this section, we show a Fourier spectral method to solve the Stokes equations with the force-coupling method in the moving coordinate system.

Following Rogallo [183], the moving coordinate system is defined as,

$$X_i = B_{ij} x_j, \tag{2.167}$$

in which $\boldsymbol{X}$ is the coordinate system deforming with the imposed strain-rate, $\boldsymbol{x}$ is the frame of reference, and $\boldsymbol{B}$ is a second order tensor. In the case of linear shear flow, $\boldsymbol{B}$ is

$$\boldsymbol{B} = \begin{bmatrix} 1 & -\dot{\gamma} t & 0 \\ 0 & 1 & 0 \\ 0 & 0 & 1 \end{bmatrix}. \tag{2.168}$$

Then, the Stokes equations in the moving coordinate system are

$$B_{ji}\frac{\partial p}{\partial X_j} = \mu B_{kj}B_{lj}\frac{\partial^2 u_i}{\partial X_k \partial X_l} + f_i(\boldsymbol{X}), \tag{2.169}$$

or

$$\frac{\partial p}{\partial X_1} = \mu\nabla'^2 u_1 + f_1, \tag{2.170}$$

$$-T\frac{\partial p}{\partial X_1} + \frac{\partial p}{\partial X_2} = \mu\nabla'^2 u_2 + f_2, \tag{2.171}$$

$$\frac{\partial p}{\partial X_3} = \mu\nabla'^2 u_3 + f_3, \tag{2.172}$$

where T is the strain $T = \dot{\gamma}t$ and

$$\nabla'^2 = [1+T^2]\frac{\partial^2}{\partial X_1^2} + \frac{\partial^2}{\partial X_2^2} + \frac{\partial^2}{\partial X_3^2} - 2T\frac{\partial^2}{\partial X_1 \partial X_2}.$$

Now, the periodic boundary conditions for a cubic domain $\mathcal{D} = [0, H_1] \times [0, H_2] \times [0, H_3]$ are

$$\begin{aligned}
\boldsymbol{u}(0, X_2, X_3) &= \boldsymbol{u}(H_1, X_2, X_3) \qquad \forall (X_2, X_3) \in [0, H_2] \times [0, H_3], \\
\boldsymbol{u}(X_1, 0, X_3) &= \boldsymbol{u}(X_1, H_2, X_3) \qquad \forall (X_1, X_3) \in [0, H_1] \times [0, H_3], \\
\boldsymbol{u}(X_1, X_2, 0) &= \boldsymbol{u}(X_1, X_2, H_3) \qquad \forall (X_1, X_2) \in [0, H_1] \times [0, H_2].
\end{aligned}$$

The FCM force $\boldsymbol{f}$ in equation (2.169) is

$$f_i(\boldsymbol{X}) = \sum_{n=1}^{N_p} \left[F_i^n \Xi_M(\boldsymbol{X} - \boldsymbol{Y}^n) + G_{ij}^n B_{kj} \frac{\partial}{\partial X_k} \Xi_D(\boldsymbol{X} - \boldsymbol{Y}^n) \right], \tag{2.173}$$

in which Ξ and $\boldsymbol{Y}$ are, respectively, the FCM envelope and the position vector of the particle center in the moving coordinate system. The FCM envelope in the moving coordinate system is

$$\Xi(\Delta\boldsymbol{X}) = \frac{1}{(2\pi\sigma)^{3/2}} \exp\left[-\frac{(\Delta X_1 + T\Delta X_2)^2 + \Delta X_2^2 + \Delta X_3^2}{2\sigma^2} \right],$$

and its derivatives can be computed by

$$\begin{aligned}
\frac{\partial \Xi}{\partial X_1} &= \left(-\frac{\Delta X_1 + T\Delta X_2}{\sigma^2}\right)\Xi(\Delta \boldsymbol{X}),\\
\frac{\partial \Xi}{\partial X_2} &= -\frac{1}{\sigma^2}\left[(\Delta X_1 + T\Delta X_2)T + \Delta X_2)\right]\Xi(\Delta \boldsymbol{X}),\\
\frac{\partial \Xi}{\partial X_3} &= -\frac{\Delta X_3}{\sigma^2}\Xi(\Delta \boldsymbol{X}),
\end{aligned}$$

in which $\Delta \boldsymbol{X} = \boldsymbol{X} - \boldsymbol{Y}$.

The relation between the strain-rate tensor E_{ij} computed in $\boldsymbol{X}$ and that in the laboratory frame e_{ij} is

$$\begin{aligned}
e_{11} &= E_{11},\\
e_{12} &= E_{12} - T\frac{\partial u_1}{\partial X_1},\\
e_{13} &= E_{13},\\
e_{22} &= E_{22} - T\frac{\partial u_2}{\partial X_1},\\
e_{23} &= E_{23} - \frac{T}{2}\frac{\partial u_3}{\partial X_1},\\
e_{33} &= E_{33}.
\end{aligned}$$

Similarly, the vorticities in the moving coordinate $\boldsymbol{\Omega}$ and in the laboratory frame $\boldsymbol{\omega}$ are

$$\begin{aligned}
\omega_1 &= \Omega_1 - T\frac{\partial u_3}{\partial X_1},\\
\omega_2 &= \Omega_2,\\
\omega_3 &= \Omega_3 + T\frac{\partial u_1}{\partial X_1}.
\end{aligned}$$

The fluid velocity can be decomposed into the mean and fluctuating components,

$$\boldsymbol{u} = \boldsymbol{U} + \boldsymbol{u}', \tag{2.174}$$

in which $\boldsymbol{U} = \dot{\gamma} x_2$. The mean momentum equation can be obtained by substituting (2.174) into the Stokes equations in the frame of reference and averaging over the domain,

$$\left\langle \frac{\partial p}{\partial x_i} \right\rangle = \mu \langle \nabla^2 U_i + \nabla^2 u_i' \rangle + \langle f_i \rangle. \tag{2.175}$$

It is obvious that the second-order derivative terms on R.H.S of (2.175) disappear in the

mean momentum equation. The dipole terms in $\boldsymbol{f}$ also disappears in the mean momentum equation because $\int \partial\Xi/\partial x_j d^3\boldsymbol{x} = 0$. In the case of neutrally buoyant particles, the volume average of the monopole force should be zero. However, if the suspended particles are denser or lighter than the fluid, there is a mean monopole force, which corresponds to the density difference times gravity, to satisfy the mean momentum equation, the net force should be supported by the mean pressure gradient in (2.175). In the Fourier spectral method, we solve only for the fluctuating components and this process is taken care of by setting the mean component (zero wavenumber component) to be zero.

Expanding functions in a truncated Fourier series and using Galerkin projection, the Stokes equations in (2.170–2.172) become

$$ik_1\hat{p} = -\mu[|\boldsymbol{k}|^2 + T^2k_1^2 - 2Tk_1k_2]\hat{u}_1 + \hat{f}_1, \tag{2.176}$$

$$i(k_2 - Tk_1)\hat{p} = -\mu[|\boldsymbol{k}|^2 + T^2k_1^2 - 2Tk_1k_2]\hat{u}_2 + \hat{f}_2, \tag{2.177}$$

$$ik_3\hat{p} = -\mu[|\boldsymbol{k}|^2 + T^2k_1^2 - 2Tk_1k_2]\hat{u}_3 + \hat{f}_3, \tag{2.178}$$

in which $\hat{\psi}$ denotes a Fourier coefficient of a function ψ,

$$\psi(\boldsymbol{X}) = \sum \hat{\psi}(\boldsymbol{k}) \exp(i\boldsymbol{k}\cdot\boldsymbol{X}), \tag{2.179}$$

and $\boldsymbol{k}$ is wavenumber; $k_i = 2\pi n/H_i$, n is an integer. Define $K_i = B_{ji}k_j$. Then, (2.176 – 2.178) can be written as

$$iK_i\hat{p} = -\mu|\boldsymbol{K}|^2\hat{u}_i + \hat{f}_i. \tag{2.180}$$

The pressure in (2.180) can be eliminated by taking divergence of (2.180) and applying the continuity equation, $\boldsymbol{K}\cdot\hat{\boldsymbol{u}} = 0$. Then, the fluid velocity is computed from

$$\hat{u}_i = \frac{1}{\mu|\boldsymbol{K}|^2}\left[\delta_{ij} - \frac{K_iK_j}{|\boldsymbol{K}|^2}\right]\hat{f}_j. \tag{2.181}$$

Because the FCM envelopes are analytical, in theory, $\hat{\boldsymbol{f}}$ can be computed in the Fourier space as in the Fourier-Galerkin method. However, in practice, due to the load balancing problem between processors in parallel computing, a pseudo-spectral approach, in which $\boldsymbol{f}$ is computed in the physical space and then transformed into the Fourier space, is used.

In the moving coordinate system, as the deformation of the computational mesh gets larger, more grid points are needed to integrate the force envelope with the same accuracy as for a non-deformed mesh system. To prevent this problem, remeshing is performed at every $T = 0.5H_1/H_2$. This is done by setting $T = -0.5H_1/H_2$ at $T = 0.5H_1/H_2$. For details about the remeshing, see [183].

2.5.2 Bounded domain

Suspensions in a confined flow is of great interest due to its relevance to many engineering processes. However, the dynamics of concentrated suspensions under a confinement is a virtually unexplored field. Here, we consider suspensions in a simple, yet important geometry; namely, a suspension flow bounded two parallel walls. We will briefly review a hybrid spectral/spectral-element method to solve the Stokes equations in a channel geometry.

Consider a cubic domain $\mathcal{D} = (0, H_x) \times (0, H_y) \times (0, H_z)$. The computational domain is bounded by two parallel walls located at $x_2 = 0$ and $x_2 = H_y$ and assumed to be periodic in the horizontal directions $(x_1,\ x_3)$. Hence, the boundary conditions are

$$\begin{aligned}
\boldsymbol{u}(0, x_2, x_3) &= \boldsymbol{u}(H_x, x_2, x_3) \qquad \forall (x_2, x_3) \in (0, H_y) \times (0, H_z), \\
\boldsymbol{u}(x_1, x_2, 0) &= \boldsymbol{u}(x_1, x_2, H_z) \qquad \forall (x_1, x_2) \in (0, H_x) \times (0, H_y), \\
\boldsymbol{u}(x_1, 0, x_3) &= (V_{low}, 0, 0)^T \qquad \forall \boldsymbol{x} \in \partial\mathcal{D}_{low}, \\
\boldsymbol{u}(x_1, H_y, x_3) &= (V_{upp}, 0, 0)^T \qquad \forall \boldsymbol{x} \in \partial\mathcal{D}_{upp},
\end{aligned}$$

in which $\mathcal{D}_{low}$ and $\mathcal{D}_{upp}$ are, respectively, the Dirichlet boundaries at $x_2 = 0$ and H_y. Here, the walls are assumed to be mobile only in the x_1 direction and V_{low} and V_{upp} are the velocities of the lower and upper walls, respectively. In a Couette flow, the nominal shear rate $\dot{\gamma}$ is set by the Dirichlet boundary condition, $\dot{\gamma} = (V_{upp} - V_{low})/H_y$. However, in practice, owing to the linearity of the Stokes equations, only the disturbance velocity field by hydrodynamic interaction between particles needs to be computed and the final solution can be obtained simply by superposing the undisturbed velocity field. Hence, in solving the Stokes equations, the homogeneous boundary condition is used for the Dirichlet boundaries. That is, V_{low} and V_{upp} are set to zero.

The variational formulation of the Stokes equations is to find $(\boldsymbol{u}, p) \in \mathcal{X} \times \mathcal{M}$, such that

$$-(p, \nabla \boldsymbol{v}) + (\nabla \boldsymbol{v}, \mu \nabla \boldsymbol{u}) = (\boldsymbol{v}, \boldsymbol{f}),\ \forall \boldsymbol{v} \in \mathcal{X}, \tag{2.182}$$

$$(q, \nabla \cdot \boldsymbol{u}) = 0,\ \forall q \in \mathcal{M}, \tag{2.183}$$

in which $(\cdot, \cdot)$ is an inner product $(f, g) = \int_{\mathcal{D}} f g d\mathcal{D}$ and the appropriate function spaces for $\boldsymbol{u}$ and p are $\mathcal{X} = \mathcal{H}_0^1(\mathcal{D})$ and $\mathcal{M} = \mathcal{L}_0^2(\mathcal{D})$, respectively. Here, $\mathcal{H}_0^1(\mathcal{D})$ is a space of functions which are in the Sobolev space $\mathcal{H}^1$ and vanish at $\partial\mathcal{D} = \partial\mathcal{D}_{low} \bigcup \partial\mathcal{D}_{upp}$ and $\mathcal{L}_0^2(\mathcal{D})$ is a space of functions which are in $L^2(\mathcal{D})$ with zero average ($\int_{\mathcal{D}} f d\mathcal{D} = 0$). Note that, due to the *inf-sup* condition, different spaces are used for velocity and pressure. See [8, 29, 140] for details about the *inf-sup* condition.

A Fourier spectral method is used in x_1 and x_3 directions and the spectral element method is used in x_2 direction. Expanding the variables in Fourier series in x_1 and x_3 directions, the weak form of the Stokes equations (2.182 – 2.183) for each wavenumber $(k_1, k_3) \in (-\infty, \infty) \times (-\infty, \infty)$ are

$$ik_1(\hat{p}, \phi) + \mu(d_y \hat{u}_1, d_y \phi) + \mu k^2 (\hat{u}_1, \phi) = (\hat{f}_1, \phi), \tag{2.184}$$

$$-(\hat{p}, d_y \phi) + \mu(d_y \hat{u}_2, d_y \phi) + \mu k^2 (\hat{u}_2, \phi) = (\hat{f}_2, \phi), \tag{2.185}$$

$$ik_3(\hat{p}, \phi) + \mu(d_y \hat{u}_3, d_y \phi) + \mu k^2 (\hat{u}_3, \phi) = (\hat{f}_3, \phi), \tag{2.186}$$

$$(ik_1 \hat{u}_1 + d_y \hat{u}_2 + ik_3 \hat{u}_3, \psi) = 0, \tag{2.187}$$

in which $\hat{}$ denotes the Fourier coefficient, $d_y = d/dy$, and ϕ and q are test functions for the velocity and pressure, respectively. For the spectral element discretization, $\mathcal{D}$ is partitioned into several elements. Let $\mathcal{I}_i$ be the interval in the $i-$direction, such that $\mathcal{D} = \mathcal{I}_1 \times \mathcal{I}_2 \times \mathcal{I}_3$. The interval $\mathcal{I}_2$ is partitioned into the union of disjoint intervals, such as

$$\overline{\mathcal{I}_2} = \bigcup_{e=1}^{K} \overline{\mathcal{I}_2^e}, \tag{2.188}$$

in which $\mathcal{I}_2^e = (y_{e-1}, y_e)$ and $0 = y_0 < y_1 < \cdots < y_{K-1} < y_K = H_y$. Then, the proper spaces for the spectral element discretization are

$$\hat{\boldsymbol{u}} \in \mathcal{X}_h(\mathcal{I}_2) = \mathcal{H}_0^1(\mathcal{I}_2) \cap \mathcal{P}_{N,K}(\mathcal{I}_2), \tag{2.189}$$

$$\hat{p} \in \mathcal{M}_h(\mathcal{I}_2) = \mathcal{L}^2(\mathcal{I}_2) \cap \mathcal{P}_{N-2,K}(\mathcal{I}_2). \tag{2.190}$$

Here, $\mathcal{P}_{n,K}(\mathcal{I}) = \{\psi \in \mathcal{L}^2(\mathcal{I}); \psi|_{\mathcal{I}_k} \in \mathcal{P}_n(\mathcal{I}_k), k = 1, \cdots, K\}$ and $\mathcal{P}_n(\mathcal{I}_k)$ is the space of all polynomials of which degree is less than or equal to n.

In the spectral element method, a variable can be written as

$$g(x) = \sum_{i=0}^{N_{dof}-1} \tilde{g}^i \Phi^i(x) = \sum_{e=1}^{K} \sum_{p=0}^{N} \tilde{g}^{e,p} \phi_p^e(\xi), \tag{2.191}$$

in which $\tilde{g}$ is the expansion coefficient, Φ and ϕ_p^e are, respectively, the global and local modes, N_{dof} is the total number of the degree of freedom, and ξ is the local coordinate in the standard element $\mathcal{I}^{st} = (-1, 1)$. The local coordinate for an element e is simply

$$\xi = 2\frac{x_2 - y_{e-1}}{y_e - y_{e-1}} - 1, \; x_2 \in \mathcal{I}_2^e. \tag{2.192}$$

Here, we use the modal polynomial expansion. Hence, $\tilde{g}^{e,p}$ is the coefficient of the mode ϕ_p^e, not the physical value of $g(x)$ at a collocation point. The modal expansion basis $\phi_p^e(\xi)$ can be found in Karniadakis & Sherwin [104].

In an element $\mathcal{I}_2^e$, the inner products in (2.184 – 2.185) are computed by using a Gaussian quadrature. Here, we use the Gauss-Lobatto-Legendre (GLL) quadrature. The GLL quadrature is exact for a polynomial $\phi \in \mathcal{P}_{2Q-3}$, in which Q is the order of the GLL quadrature. The local operations of some of the inner products in (2.184 – 2.186) are given by,

$$\begin{aligned}
(\hat{u}, \phi_j^e) &= \int_{-1}^{1} \left[\sum_{i=0}^{N} \tilde{u}^{e,i} \phi_i^e(\xi) \right] \phi_j^e(\xi) \mathcal{J}^e d\xi \\
&= \mathcal{J}^e \sum_{i=0}^{N} \tilde{u}^{e,i} \left[\sum_{q=0}^{Q-1} \phi_i^e(\xi_q) \phi_j^e(\xi_q) w_q \right], \qquad (2.193) \\
(d_y \hat{u}, d_y \phi_j^e) &= \int_{-1}^{1} \frac{d}{d\xi} \left[\sum_{i=0}^{N} \tilde{u}^{e,i} \phi_i^e(\xi) \right] \frac{d\phi_j^e(\xi)}{d\xi} \mathcal{J}^{e-1} d\xi \\
&= \mathcal{J}^{e-1} \sum_{i=0}^{N} \tilde{u}^{e,i} \left[\sum_{q=0}^{Q-1} \left(\frac{d\phi_i^e}{d\xi} \right)_{\xi_q} \left(\frac{d\phi_j^e}{d\xi} \right)_{\xi_q} w_q \right], \qquad (2.194) \\
(\hat{p}, \phi_j^e) &= \int_{-1}^{1} \left[\sum_{i=0}^{M} \tilde{p}^{e,i} \psi_i^e(\xi) \right] \phi_j^e(\xi) \mathcal{J}^e d\xi \\
&= \mathcal{J}^e \sum_{i=0}^{M} \tilde{p}^{e,i} \left[\sum_{q=0}^{Q-1} \psi_i^e(\xi_q) \phi_j^e(\xi_q) w_q \right], \qquad (2.195)
\end{aligned}$$

in which ξ_q is the q-th GLL quadrature point, w_q is the weight of the GLL quadrature, ϕ^e and ψ^e are, respectively, the local basis functions for velocity and pressure, N, M are the orders of ϕ and ψ, respectively ($M = N-1$). The Jacobian $\mathcal{J}$ is simply $\mathcal{J} = (y_{e-1} - y_e)/2$. Similarly, a local operation in (2.187) is

$$(\hat{u}, \psi_j^e) = \mathcal{J}^e \sum_{i=0}^{N} \tilde{u}^{e,i} \left[\sum_{q=0}^{Q-1} \phi_i^e(\xi_q) \psi_j^e(\xi_q) w_q \right]. \tag{2.196}$$

In the modal expansion, we can choose N different from Q and the velocity and pressure share the same quadrature points. Considering the accuracy of the GLL quadrature rule, we use $N \leq Q-2$. A global operation can be easily constructed from the sum of the corresponding local operations shown above.

In a matrix form, (2.184 – 2.185) can be written as

$$ik_1 \tilde{\boldsymbol{M}} \boldsymbol{P} + \mu(\boldsymbol{L} + k\boldsymbol{M})\boldsymbol{U}_1 = \boldsymbol{B}\boldsymbol{W}\boldsymbol{F}_1, \tag{2.197}$$

$$-\tilde{\boldsymbol{D}} \boldsymbol{P} + \mu(\boldsymbol{L} + k\boldsymbol{M})\boldsymbol{U}_2 = \boldsymbol{B}\boldsymbol{W}\boldsymbol{F}_2, \tag{2.198}$$

$$ik_3 \tilde{\boldsymbol{M}} \boldsymbol{P} + \mu(\boldsymbol{L} + k\boldsymbol{M})\boldsymbol{U}_3 = \boldsymbol{B}\boldsymbol{W}\boldsymbol{F}_3, \tag{2.199}$$

in which $\boldsymbol{U}$ and $\boldsymbol{P}$ are vectors of the global modal coefficients of velocity and pressure, respectively, and $\boldsymbol{F}$ is a vector of the force $\hat{\boldsymbol{f}}$ at each grid points. The dimensions of $\boldsymbol{U}$, $\boldsymbol{P}$, and $\boldsymbol{F}$ are $((N-1)K+1)$, $((M-1)K+1)$ and $((Q-1)K+1)$, respectively. $\boldsymbol{B}$ is a matrix which contains ϕ at each grid points and, similarly, let $\tilde{\boldsymbol{B}}$ be the matrix for ψ. That is, in a local element e,

$$\begin{aligned} \boldsymbol{B}_{ij}^e &= \phi_i^e(\xi_j), \quad \text{for } 0 \leq i \leq N \ \& \ 0 \leq j \leq Q-1, \\ \tilde{\boldsymbol{B}}_{ij}^e &= \psi_i^e(\xi_j), \quad \text{for } 0 \leq i \leq M \ \& \ 0 \leq j \leq Q-1. \end{aligned}$$

Let $\boldsymbol{d}$ and $\tilde{\boldsymbol{d}}$ be the matrices of the derivatives of ϕ and ψ at each quadrature points, respectively;

$$\begin{aligned} \boldsymbol{d}_{ij}^e &= \frac{1}{\mathcal{J}^e} \left(\frac{d\phi_i^e}{d\xi} \right)_{\xi_j}, \quad \text{for } 0 \leq i \leq N \ \& \ 0 \leq j \leq Q-1, \\ \tilde{\boldsymbol{d}}_{ij}^e &= \frac{1}{\mathcal{J}^e} \left(\frac{d\psi_i^e}{d\xi} \right)_{\xi_j}, \quad \text{for } 0 \leq i \leq M \ \& \ 0 \leq j \leq Q-1. \end{aligned}$$

$\boldsymbol{W}$ is a diagonal matrix of the weights of GLL quadrature,

$$\boldsymbol{W}_{ij}^{e} = \mathcal{J}^{e}\delta_{ij}w_{i}^{e}, \quad \text{for } 0 \leq i,j \leq Q-1.$$

Then, the matrices in (2.197 – 2.199) can be written as

$$\begin{aligned}
\boldsymbol{M}^{e} &= \boldsymbol{B}^{e}\boldsymbol{W}^{e}\boldsymbol{B}^{eT}, \\
\boldsymbol{L}^{e} &= \boldsymbol{d}^{e}\boldsymbol{W}^{e}\boldsymbol{d}^{eT}, \\
\tilde{\boldsymbol{M}}^{e} &= \boldsymbol{B}^{e}\boldsymbol{W}^{e}\tilde{\boldsymbol{B}}^{eT}, \\
\tilde{\boldsymbol{D}}^{e} &= \boldsymbol{B}^{e}\boldsymbol{W}^{e}\tilde{\boldsymbol{d}}^{eT}.
\end{aligned}$$

Assembling local matrices to build a global matrix is straightforward. For details about constructing a global matrix, see Karniadakis & Sherwin [104].

The continuity equation (2.187) can be written as

$$ik_1\tilde{\boldsymbol{M}}^{T}\boldsymbol{U}_1 + \tilde{\boldsymbol{B}}\boldsymbol{W}\boldsymbol{d}^{T}\boldsymbol{U}_2 + ik_3\tilde{\boldsymbol{M}}^{T}\boldsymbol{U}_3 = 0. \tag{2.200}$$

Define a Helmholtz operator as $\boldsymbol{H} = \boldsymbol{L} + k\boldsymbol{M}$. Rearranging (2.197–2.199) and substituting into (2.200) yield

$$\begin{aligned}
(\widehat{\boldsymbol{D}}\boldsymbol{H}^{-1}\tilde{\boldsymbol{D}} + k^2\tilde{\boldsymbol{M}}^{T}\boldsymbol{H}^{-1}\tilde{\boldsymbol{M}})\boldsymbol{P} &= -[ik_1\tilde{\boldsymbol{M}}^{T}\boldsymbol{H}^{-1}\boldsymbol{B}\boldsymbol{W}\boldsymbol{F}_1 + \widehat{\boldsymbol{D}}\boldsymbol{H}^{-1}\boldsymbol{B}\boldsymbol{W}\boldsymbol{F}_2 \\
&\quad + ik_3\tilde{\boldsymbol{M}}^{T}\boldsymbol{H}^{-1}\boldsymbol{B}\boldsymbol{W}\boldsymbol{F}_3],
\end{aligned} \tag{2.201}$$

in which $\widehat{\boldsymbol{D}} = \tilde{\boldsymbol{B}}\boldsymbol{W}\boldsymbol{d}^{T}$. In (2.201), the pressure is decoupled from the velocity. Note that $\boldsymbol{P}$ calculated by (2.201) can be thought as a Lagrangian multiplier to satisfy the incompressibility and is different from the physical pressure.

In the Uzawa algorithm, first the pressure is computed from (2.201) and, then, the fluid velocity are calculated from (2.197 – 2.199) by using $\boldsymbol{P}$ obtained in the first step. A preconditioned conjugate gradient solver to solve (2.201) is explained in [104, 140].

2.6 Verification

In the force-coupling method, there are three major parameters, which determine the numerical accuracy. First, as the far-field interaction is computed by solving the Stokes equa-

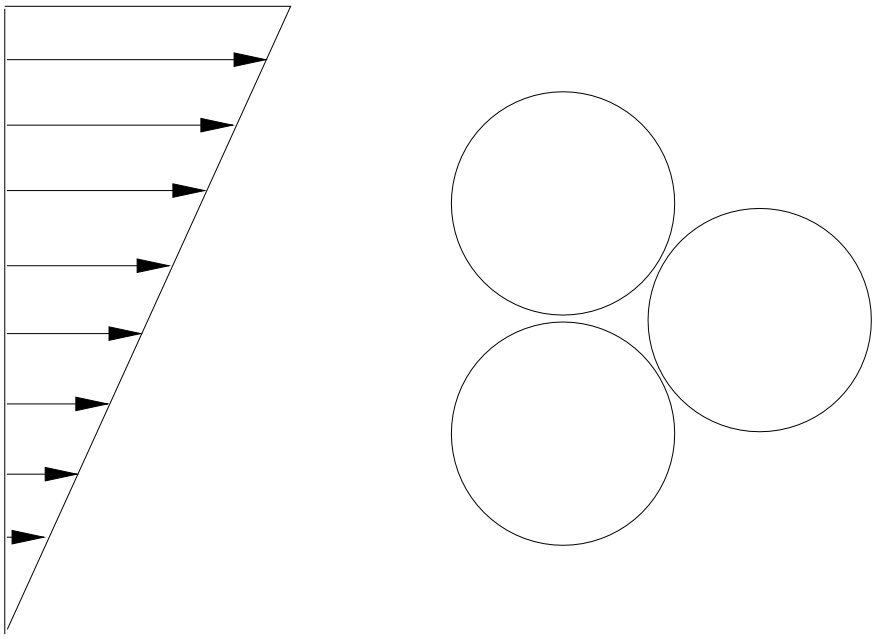

Figure 2.6: Configuration of the test problem.

tions in the force-coupling method, naturally the order of accuracy of the Stokes solver plays an important role in the accuracy of the solution. Second, for the computational efficiency, the force envelopes are distributed and integrated only in a small domain defined as $I_n(\boldsymbol{Y}) = \{\boldsymbol{x} | \boldsymbol{x} \in \mathbb{R}^3, |\boldsymbol{x} - \boldsymbol{Y}| < a \times n\}$ for a positive real constant n. Lastly, the grand-mobility matrix of LC-FCM is inverted by using a preconditioned conjugate gradient (PCG) solver. Hence, the tolerance level of PCG also affects the accuracy of the solution. In this section, we test the effects of these numerical parameters on the convergence of the solution.

2.6.1 Periodic domain

We test LC-FCM in a tri-periodic domain. The Stokes equations are solved by using the Fourier spectral method. For a particle-pair interaction problem, PCG converges to the tolerance $< O(10^{-10})$ within one or two iterations. So, we choose a three-particle interaction in a shear flow for a test problem. The three particles are seeded as a equilateral triangle in

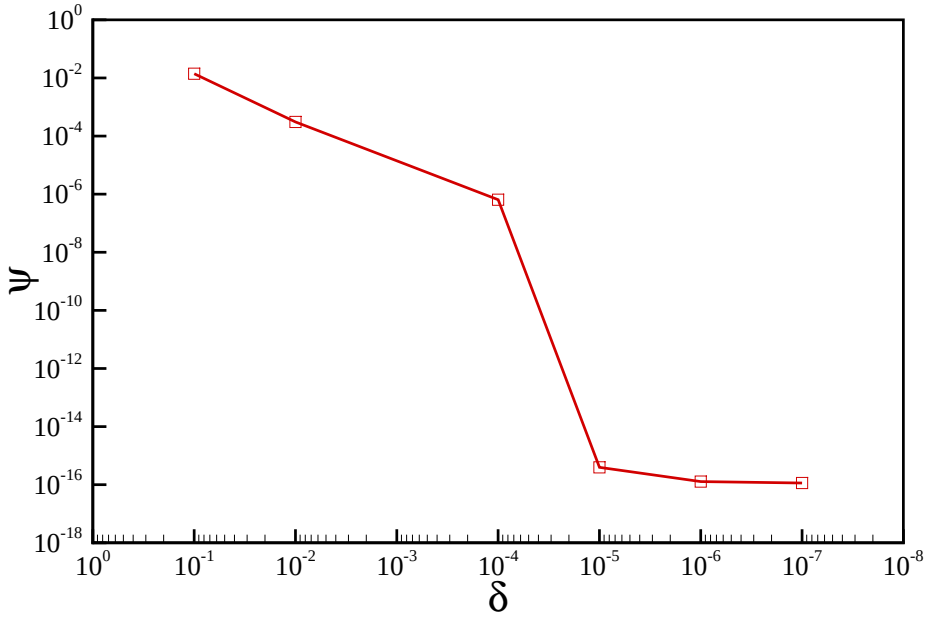

Figure 2.7: Effects of the tolerance level of the preconditioned conjugate gradient solver to the accuracy.

the shear plan as shown in figure 2.6. The distance between the particles is $2.01a$. The ratio of the length of the computational domain to the particle radius is fixed, $L/a = 25.133$.

First, the effects of the tolerance level of PCG δ is shown in figure 2.7. For the reference solution, LC-FCM is solved for the grid size $a/\Delta x = 10.186$, the tolerance level $\delta = 10^{-8}$, and the domain I_4. The error Ψ is defined as

$$\Psi = \left(\sum_{i=1}^{3} |\boldsymbol{V}^i - \boldsymbol{V}^i_{ref}|^2 \Big/ \sum_{i=1}^{3} |\boldsymbol{V}^i_{ref}|^2 \right)^{1/2}, \tag{2.202}$$

in which $\boldsymbol{V}_{ref}$ is the reference solution. For $10^{-4} \leq \delta \leq 10^{-1}$, Ψ decreases faster than $\sim \delta$, indicating that the tolerance level is an effective control for the error. Then, Ψ quickly drops to the machine accuracy for $\delta < 10^{-4}$. For $\delta > 10^{-4}$, the error Ψ is at least one order of magnitude smaller than δ. In the simulations of concentrated suspensions, we usually choose $\delta = 10^{-2} \sim 10^{-3}$.

Figure 2.8 shows show the effects of I_n on the accuracy of the solution. The reference solution is obtained by setting $a/\Delta x = 10.186$, $\delta = 10^{-6}$, and the domain size $n = 5$. It is shown that Ψ exhibits an exponential decay. The exponential decay of Ψ is expected as

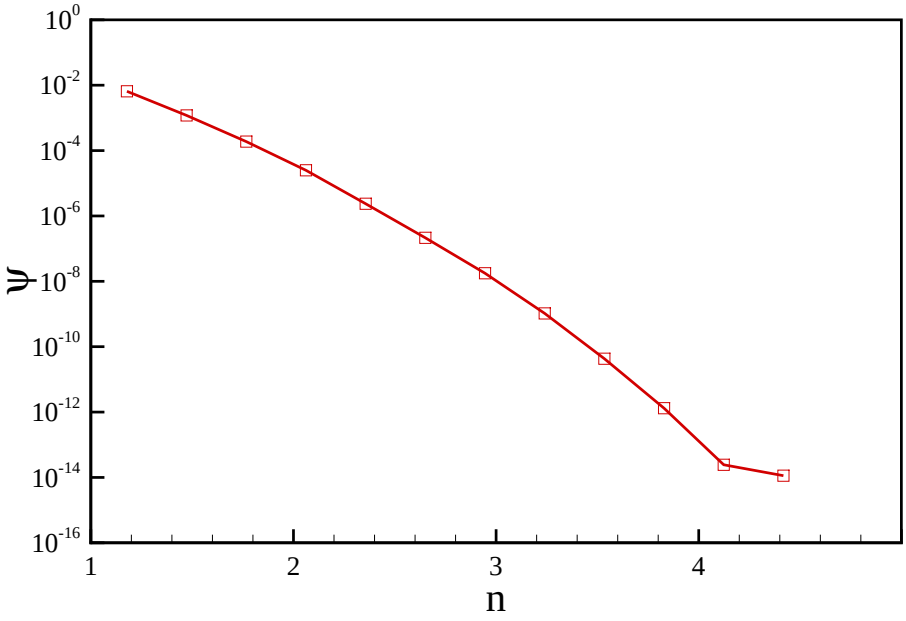

Figure 2.8: Effects of the integration width to the accuracy.

the regularized multipoles are Gaussian functions. Based on this result, the domain size is chosen between $n = 2.5 \sim 3.0$ in most of the computations in this thesis.

Finally, we show the effects of the grid resolution on the numerical accuracy. Here, the reference solution is obtained for $a/\Delta x = 10.186$, $\delta = 10^{-6}$, and the domain size $n = 4$. Figure 2.9 shows the spectral convergence of LC-FCM, which is expected as a Fourier spectral solver is employed. This result indicates that the numerical error is negligible in LC-FCM, as long as the particle radius is bigger than $3\Delta x$.

2.6.2 Channel flow

The angular velocity of a sphere moving parallel to a wall under the influence of an external force is given as

$$\frac{a\Omega}{V} = \frac{3}{4}\frac{Y^B}{Y^C}, \tag{2.203}$$

in which Y^B and Y^C are resistance functions for the particle-wall hydrodynamic interaction. The resistance functions are given in Dance & Maxey [50] for a very small gap $a\epsilon$ between the sphere and the wall. Here, we compare the numerical results obtained for a single sphere

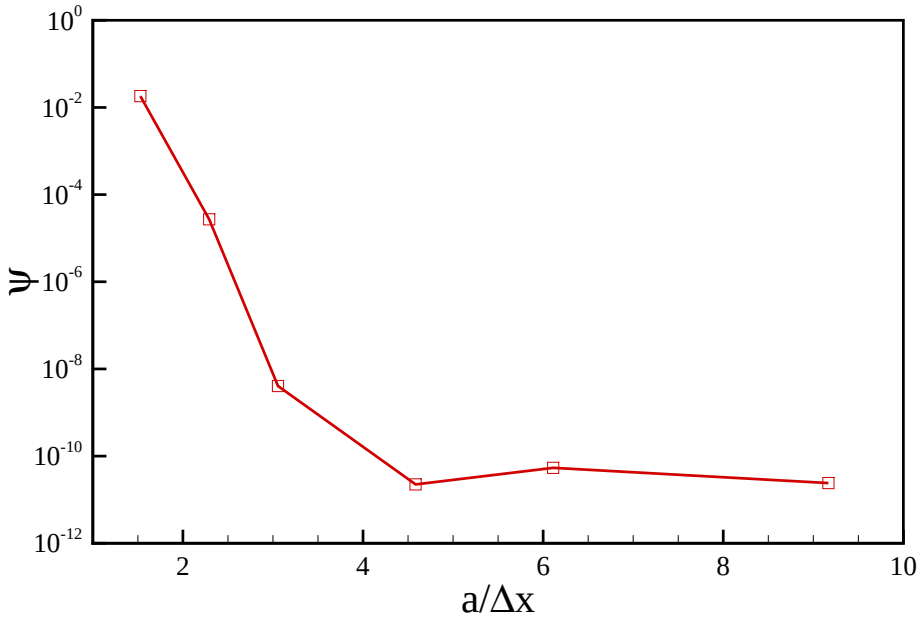

Figure 2.9: Convergence of LC-FCM as a function of the grid resolution.

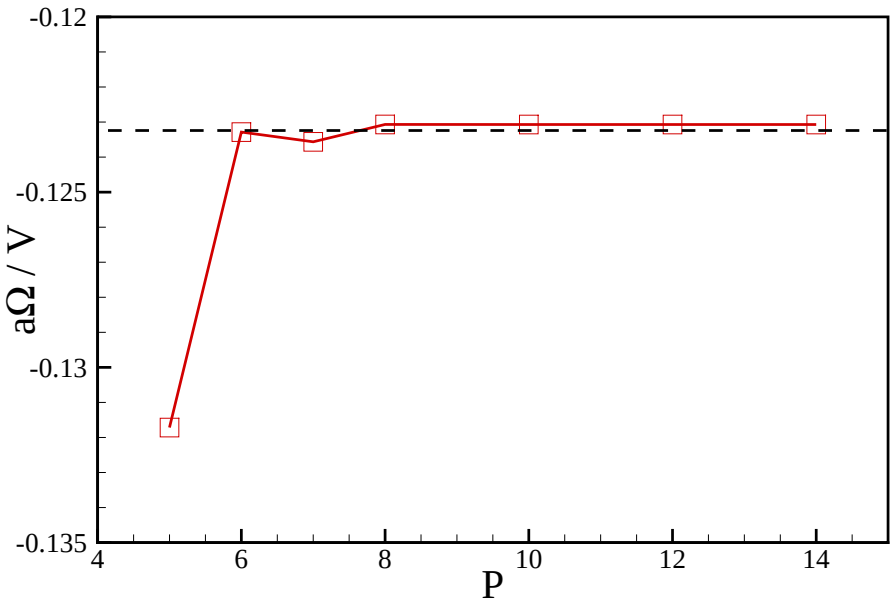

Figure 2.10: The ratio of the angular velocity to the translational velocity as a function of the maximum order of the polynomial in each elements. The dash line is the analytical solution from Dance & Maxey [50].

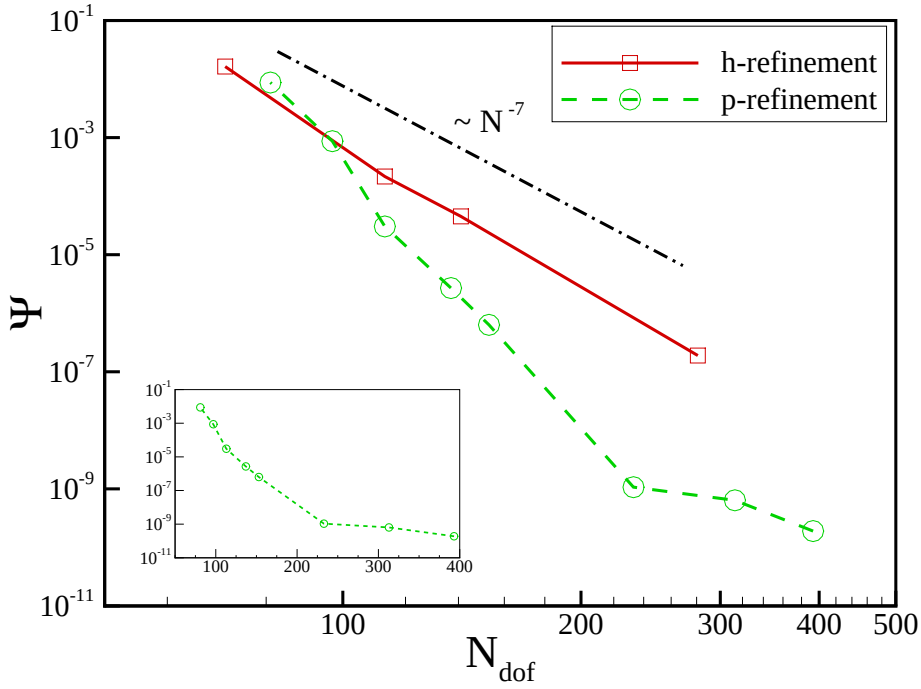

Figure 2.11: Convergence of $h-$type and $p-$type refinement. Inset shows the convergence of $p-$type refinement in a log-linear plot.

moving in a channel to the analytical solution given in [50]. The particle is located very close to the lower wall, $Y_2/a = 1.01$. To reduce the effect of the periodicity and the upper wall, the computational domain is chosen as $H_x \times H_y \times H_z = 40a \times 60a \times 40a$. The length of the element in the vertical direction is fixed, $L^e = 2a$, and the maximum order of the polynomial P is changed to test the convergence. The numbers of Fourier modes in the horizontal directions are fixed, $N_x \times N_x = 256 \times 256$. In figure 2.10, it is shown that the numerical solution converges as P increases. The difference between the analytical solution and the numerical solution for $P = 14$ is about 1.6×10^{-4}. It is worth noting that the analytical solutions are obtained by using an asymptotic expansion in ϵ and the solutions are supplemented by $O(1)$ corrections, which are obtained by fitting to numerical data. As the resistance functions in the literature have $O(\epsilon)$ errors and $O(1)$-correction terms are shown only up to four significant digits.

Finally, so as to check the convergence of the spectral element solver, LC-FCM solutions for a particle pair in a Couette flow are obtained by changing the number of degree of freedom N_{dof} in the wall-normal direction. In this numerical test, two particles are located

at the same wall-normal location $Y_2/a = 1.01$ and separated in the $x-$direction by $2.01a$. The upper wall is moving with the velocity $V_{upp} = \dot{\gamma} H_y$ for the shear rate $\dot{\gamma} = 1$. The dimensions of the computational domain and the resolution in the horizontal directions are the same as the one-sphere simulation shown above. The reference solution is obtained for $L^e = 6a$ with $P = 60$. In $p-$type refinement, L^e is fixed and P is changed from 11 to 50, while $h-$type refinement is performed by fixing $P = 7$ and changing L^e from 1 to 4. The $h-$type refinement exhibits an algebraic convergence $\sim N_{dof}^{-7}$ and the $p-$type refinement shows a much faster convergence close to the spectral convergence. The exponential decrease of Ψ is clearly shown in the inset of figure 2.11 for $N_{dof} < 300$.

2.7 Validation

2.7.1 Results I: particles in an infinite domain

To verify the lubrication correction method developed in section 2.3, several numerical simulations of spheres in an infinite domain are performed. The FCM mobility matrix is constructed by using the FCM Oseen tensors derived in Lomholt & Maxey [135].

2.7.1.1 Chain of particles settling under gravity

First, consider two horizontally separated spheres settling under gravity (see inset of figure 2.12). The hydrodynamic interaction induces counter-rotation of the particle pair. Near contact, the counter-rotation is frozen by the lubrication forces. The angular velocity calculated from the present lubrication correction (FCM-LUB) and FCM with just monopole and dipole terms (FCM-MD) are shown in figure 2.12. It is shown that the present lubrication correction method can reproduce the angular velocity with good accuracy when $r/a < 2.25$. At $r = 2.1$, the angular velocity obtained by Ganatos *et al.* [74] is 0.137 and the present method gives 0.139. For the resistance functions that have a leading-order $\log \epsilon$ singularity (Y^A, Y^B, Y^C, Y^G, and Y^H), the near-field form is used only when $\epsilon < 0.05$ and the far-field form is used for $0.05 < \epsilon < 0.8$. The exact resistance functions can be found in [50, 101, 110].

In a second example, the settling of a horizontal chain of seven spheres is calculated using FCM-LUB. The configuration of the particles is illustrated in figure 2.13 with the relative gap between the particles $\epsilon = 0.005$. The drag coefficient λ and angular velocity Ω for

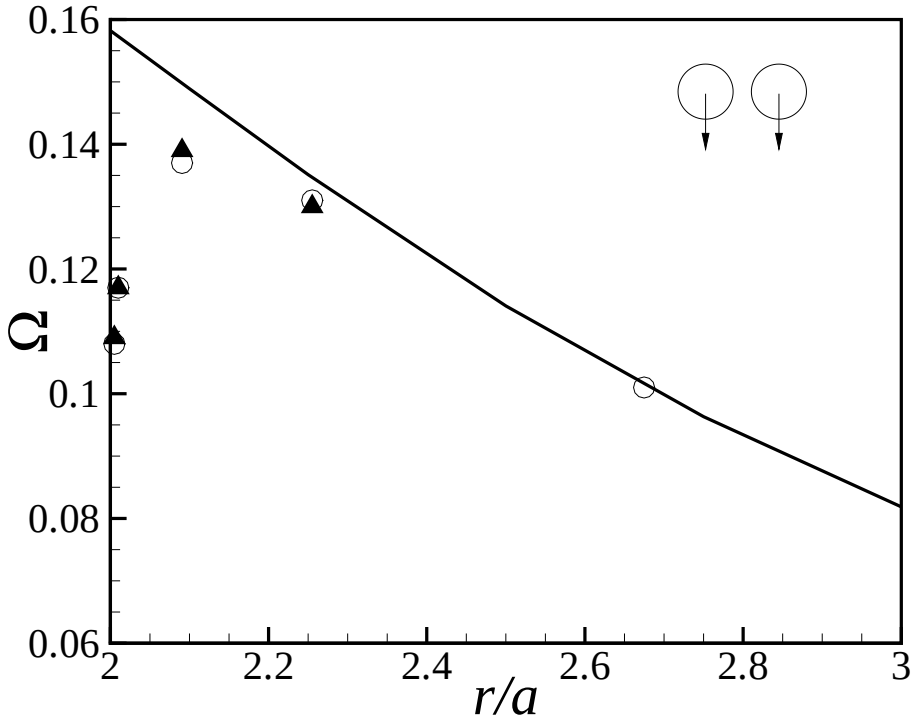

Figure 2.12: Comparison of angular velocity for a pair of equal spheres with horizontal separation. ∘, Ganatos *et al.* (1978); ▲, FCM-LUB; –, FCM-MD.

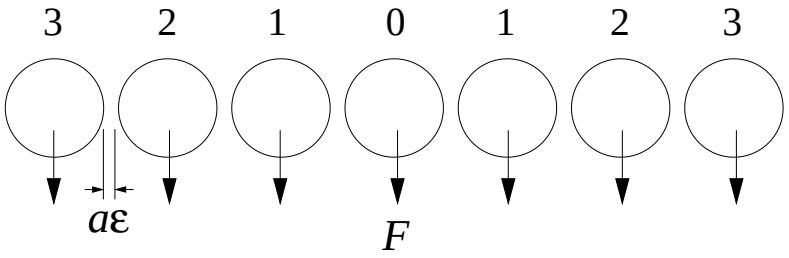

Figure 2.13: Illustration of the horizontal chain of 7 spheres.

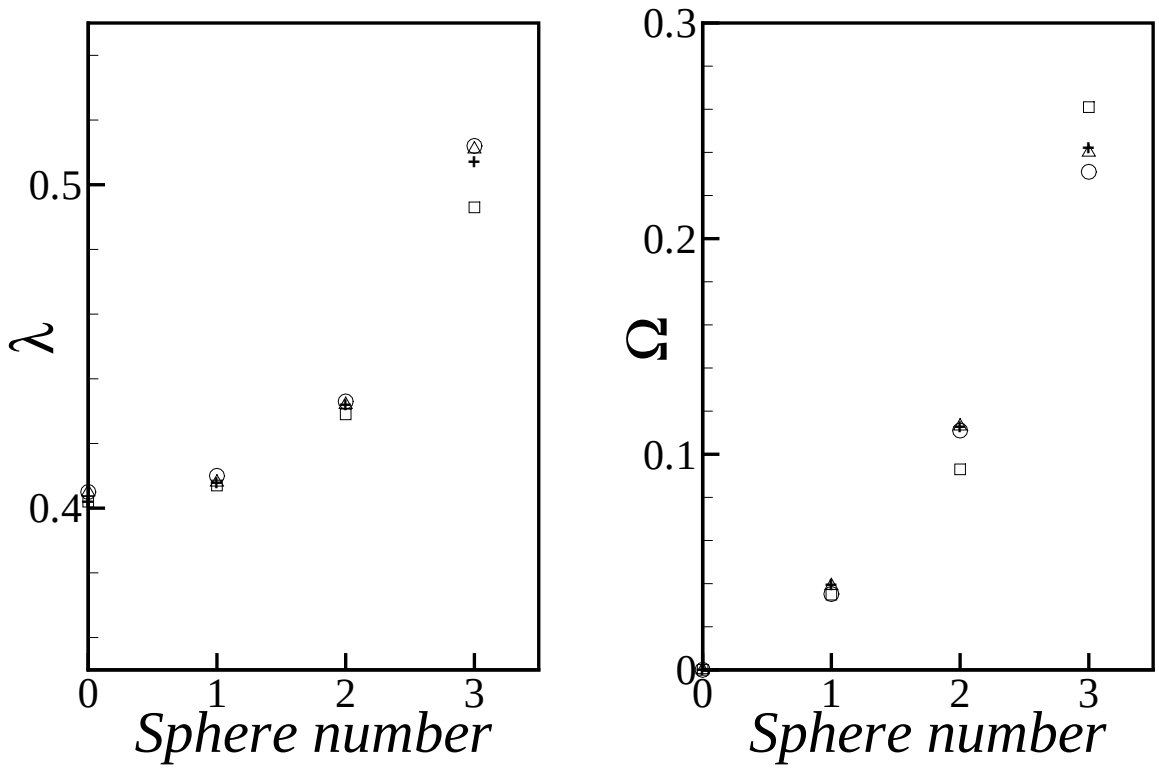

(a) (b)

Figure 2.14: Comparison of (a) the drag coefficient $\lambda = F/6\pi\mu aU$ and (b) angular velocity. ∘, Ganatos *et al.* (1978); △, Durlofsky *et al.* (1987); +, FCM-LUB; □, Dance & Maxey (2003).

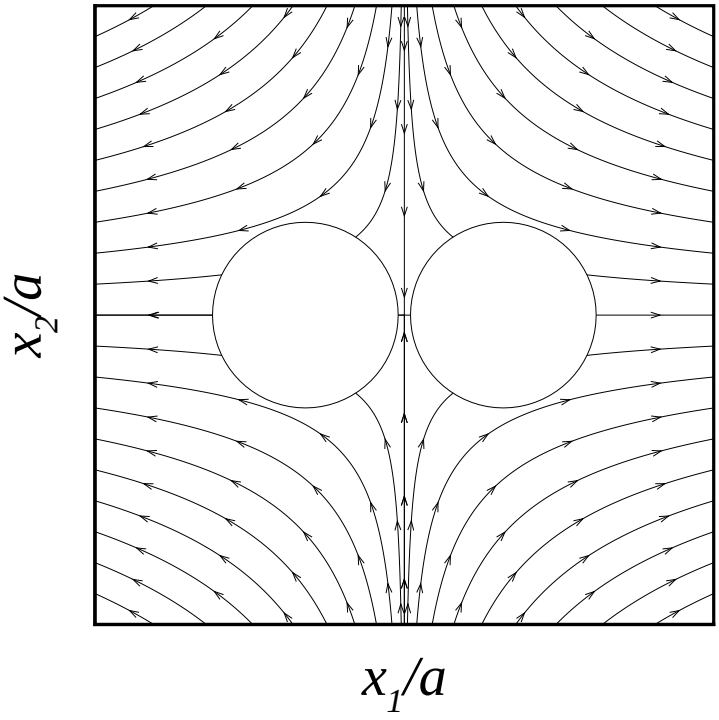

Figure 2.15: Illustration of a particle-pair in a pure straining flow.

each particle are compared to those obtained by Ganatos *et al.* [74] and FTS-SD[63]. The results are shown in figure 2.14. FCM with the present lubrication correction shows similar accuracy as FTS-SD. For the drag coefficient the maximum difference of λ between FCM-LUB and [74] is about 1%. The lubrication model of Dance & Maxey [50] shows relatively larger error, particularly for the particle 3. It was noted that the error at particle 3 may come from the pair-wise addition of the lubrication force in the mobility problem. This is consistent with the argument of Durlofsky *et al.* [63] that adding lubrication correction terms to the resistance matrix in a pair-wise manner and inverting the resistance matrix to solve the mobility problem better resolves many-body interactions as compared to adding the lubrication forces to the mobility problem.

2.7.1.2 Particles in a pure straining field

The interactions of a particle-pair in a linear flow field can be evaluated analytically and there are many solutions available in the literature [15, 14, 110], which are suitable for benchmarking a numerical scheme. In this section, the numerical computations for a pair

Table 2.3: Relative velocity of two spheres in a straining flow when $E = 1$.

ϵ	B&G	FCM
0.01	0.08195	0.07647
0.005	0.04087	0.03931
0.001	0.008158	0.008071

of force-free and torque-free spheres in a pure straining flow are performed and the results are compared with the analytical solutions.

Consider a particle pair in a uniform straining flow (see figure 2.15),

$$E_{ij}^{\infty} = E\delta_{ij11} - \frac{1}{2}E(\delta_{ij22} + \delta_{ij33}), \tag{2.204}$$

$$u_i^{\infty} = E_{ij}^{\infty} x_j, \tag{2.205}$$

in which δ_{ijkl} is 1 if all the indices are the same and 0 otherwise. Batchelor & Green (B&G) [14] solved this problem analytically by using bispherical harmonics. When $r_i = r\delta_{i1}$ and ϵ is small, the relative velocity and stresslet in B&G are

$$V_r = (1 - A(r))Er, \tag{2.206}$$

$$S_{11} = \frac{20}{3}\pi\mu a^3 E\left(1 + K + \frac{4}{3}L + \frac{2}{3}M\right), \tag{2.207}$$

in which

$$A(r) = 1 - 4.077\epsilon + O(\epsilon^{3/2}), \tag{2.208}$$

$$\frac{3}{2}K + 2L + M = 1.366 + O(\epsilon). \tag{2.209}$$

The relative velocities from B&G and FCM-LUB are shown in Table 2.3. At $\epsilon = 10^{-2}$, the error is about 7%. However, due to the $O(\epsilon^{3/2})$ error of $A(r)$ in B&G, it is difficult to assess the error of numerical method at this separation distance. As ϵ decreases, the difference between B&G and the present simulation becomes smaller. When $\epsilon = 10^{-3}$, the difference between B&G and FCM-LUB is about 1%.

The stresslet of a sphere is calculated from equation (2.132),

$$\boldsymbol{S} = \boldsymbol{S}^{tot} - R_{ES}^{L}\boldsymbol{E}^{\infty} + R_{\mathcal{V}S}^{L}(\mathcal{V} - \mathcal{V}^{\infty}), \tag{2.210}$$

Table 2.4: FCM resistance functions (X^M, Y^M, Z^M)

	C_0	C_1	C_2	C_3	C_4
X_{11}^M	−1.4235	0.9133	−1.0670	0.7197	−0.2120
X_{12}^M	−0.5911	0.9453	−0.9702	0.6307	−0.1852
Y_{11}^M	−1.0787	0.1991	−0.2617	0.1902	−0.0584
Y_{12}^M	0.0806	0.0370	−0.1294	0.0990	−0.0283
Z_{11}^M	−1.0035	0.0145	−0.0253	0.0221	−0.0075
Z_{12}^M	0.0593	−0.1281	0.1400	−0.0855	0.0229

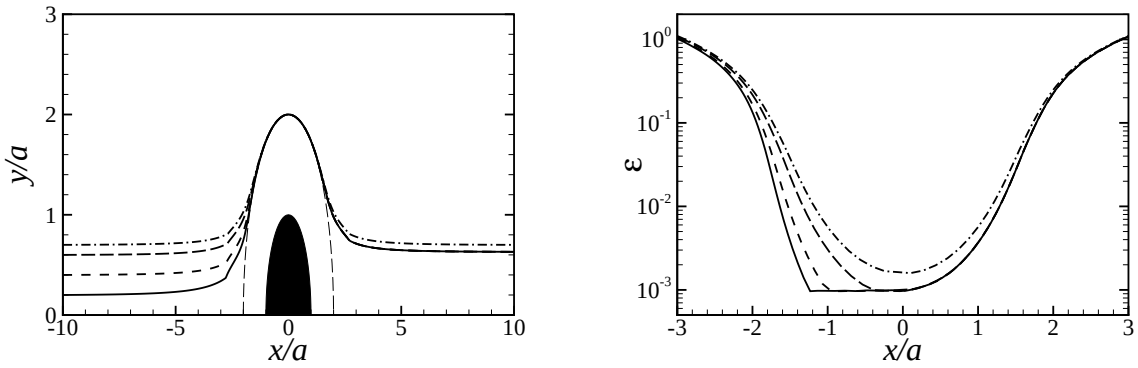

(a) (b)

Figure 2.16: (a) Relative trajectory of the centers of two equal spheres and (b) separation distances for different initial positions, Δy^I. The length scale of the contact force $R_{ref} = 2.001a$. From top to bottom: $\Delta y^I = 0.7$, 0.6, 0.4, and 0.2

in which $R_{\mathcal{V}S}^L = -(R_{E\mathcal{F}}^L)^T$. $\boldsymbol{S}^{tot}$ is obtained by solving the equation (2.130). To estimate $\boldsymbol{S}$, the fourth-order tensor R_{ES}^L needs to be constructed. The FCM resistance functions X^M, Y^M, and Z^M are given in table 2.4.

The stresslet given in B&G is

$$S_{11} = 40.017a^3E + O(\epsilon). \tag{2.211}$$

Using the lubrication correction, FCM gives $S_{11} = 39.226a^3E$ and $39.582a^3E$ when $\epsilon = 0.01$ and 0.005, respectively. As expected, the results get closer to B&G as ϵ decreases, and the differences are consistent with an $O(\epsilon)$ scaling.

Table 2.5: Upstream Δy^I and downstream center-to-center distances Δy^F for $R_{ref} = 2.001$.

$\Delta y^I/a$	$\Delta y^F/a$
0.2	0.631
0.4	0.631
0.6	0.631
0.7	0.700
0.8	0.800

2.7.1.3 Relative motion of a particle pair in a linear shear flow

If the surface of spheres are perfectly smooth and the interaction between a particle-pair is from purely hydrodynamics, the trajectories of the particle-pair should be time reversible as a consequence of the linearity of the Stokes equations. Consider a particle-pair in a shear flow, $u_1^\infty(y) = \dot{\gamma} y$, in which $\dot{\gamma}$ is a shear rate, with the initial center-to-center distances $\Delta x^I = \delta_x$, $\Delta y^I = \delta_y$, and $\Delta z^I = \delta_z$. Then, at the downstream location $\Delta x^F = -\delta_x$, the center-to-center distances in $y-$ and $z-$directions should be $\Delta y^F = \delta_y$ and $\Delta z^F = \delta_z$. If δ_y and δ_z are small, the minimum separation distance during a tumbling motion of the particle pair can be very small. Da Cunha & Hinch [47] observed that for $\delta_x/a = 10$, $\delta_y/a = \delta_z/a = 0.1$, the minimum separation is $4.75 \times 10^{-5} a$. In a physical systems, however, the surface roughness of particles breaks the reversibility, resulting in a net drift after the "collision". Smart & Leighton [200] measured the surface roughness of particles ranging from 43 to 6350 μm in diameter and found these to be the order of 10^{-2} to $10^{-3} a$.

Corresponding numerical simulations of a particle-pair in a linear shear flow are performed. $\delta_x/a = -10$ and $\delta_z/a = 0$ are used for all simulations. The time advancement was carried out by using a fourth-order Adam-Bashforth method with time step size $dt = 10^{-3}$. To prevent any overlap, an elastic contact force proposed by Dance *et al.* [49] is used. The contact force to the j-th particle by the i-th particle is given by

$$\boldsymbol{F}^{ij} = \begin{cases} -F_{ref} \left(\frac{R_{ref}^2 - |\boldsymbol{r}|^2}{R_{ref}^2 - 4a^2} \right)^2 \frac{\boldsymbol{r}}{|\boldsymbol{r}|} & \text{if } |\boldsymbol{r}| < R_{ref} \\ 0 & \text{otherwise,} \end{cases} \tag{2.212}$$

in which $\boldsymbol{r} = \boldsymbol{Y}^i - \boldsymbol{Y}^j$. Although in most numerical simulations a contact force is used to prevent the overlapping of particles as a result of finite dt, physically the use of a contact force is to model the surface roughness of particles [47].

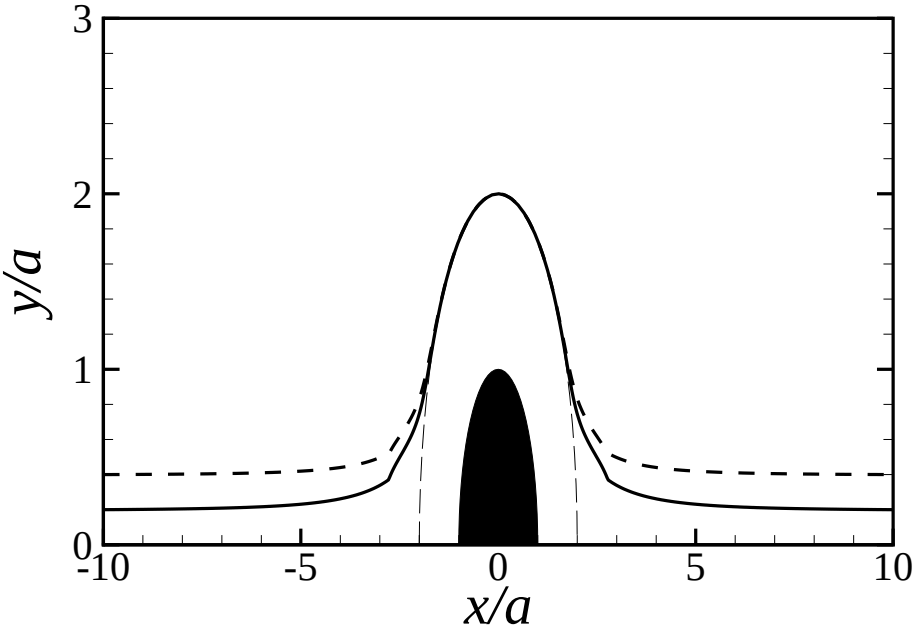

Figure 2.17: Relative trajectory of the centers of two equal spheres for different initial positions, Δy^I. The length scale of the contact force is $R_{ref} = 2.0001a$. From top to bottom: $\Delta y^I = 0.4$ and 0.2

Figure 2.16 shows the relative trajectories and the separation distances of the two equal spheres in the shear flow for $\Delta y^I/a = 0.2$, 0.4, 0.6, and 0.7 when $R_{ref} = 2.001$. When $\Delta y^I/a = 0.7$, the minimum separation is $\epsilon_{min} \simeq 0.0015$. Since the contact force is not activated, the trajectory shows the fore-after symmetry. For $\Delta y^I/a \leq 0.6$, it is observed that the symmetry is broken and there is a net displacement in the vertical direction. From the table 2.5, it can be deduced that Δy^F will be the same if $\Delta y^I/a < 0.631$. Using a traction-corrected boundary element method, Ingber *et al.* [97] observed that $\Delta y^F/a = 0.71$ for $\Delta y^I/a < 0.71$, when the surface roughness of a particle is $5 \times 10^{-4}a$. In their simulation, the minimum separation was $\epsilon_{min} = 1.03 \times 10^{-3}$. If $\epsilon < \epsilon_{min}$, the normal motion of a particle pair is restricted. On the other hand, in the present simulation, the contact force is activated when $\epsilon < 10^{-3}$ and $\epsilon_{min} \simeq 0.97 \times 10^{-3}$, which may contribute to the quantitative difference.

The relative trajectories for $R_{ref} = 2.0001$ is illustrated in figure 2.17. It is observed

that $\epsilon_{min} = 1.007783 \times 10^{-4}$ for $\Delta y^I/a = 0.2$. Since $\epsilon_{min} > R_{ref}$, the contact force is not used and the trajectories are symmetric.

2.7.2 Results II: homogeneous suspensions in an periodic domain

Here, the numerical simulation of concentrated suspensions in a periodic cell are illustrated. Three problems are considered; a simple cubic lattice of neutrally buoyant particles, high-frequency dynamic viscosity, and sheared suspensions of non-colloidal particles. The Fourier-spectral method shown in 2.5.1 is used to solve the Stokes equations. The length of the computational domain is kept constant, 2π, in all directions. The number of Fourier modes is determined by the particle radius. In FCM, as long as the force envelope is resolved the numerical result is insensitive to Δx. The computational resolution is kept $a/\Delta x \simeq 3$. The lubrication correction is used when the distance between particle centers is less than $2.8a$.

2.7.2.1 Rheology of particles in a periodic cell

Nunan & Keller [166] showed that the bulk deviatoric stress tensor σ_{ij} is related through the effective viscosity tensor μ^*_{ijkl} to shear rate $\dot{\gamma}$ as

$$\sigma_{ij} = 2\mu^*_{ijkl}\dot{\gamma}_{kl}, \tag{2.213}$$

in which $\dot{\gamma}_{kl}$ denotes the shear rate. For a cubic lattice of spheres, the effective viscosity tensor is given by [166],

$$\mu^*_{ijkl} = \frac{1}{2}\mu(1+\beta)(\delta_{ik}\delta_{jl} + \delta_{il}\delta_{jk} - \frac{2}{3}\delta_{ij}\delta_{kl}) + \mu(\alpha-\beta)(\delta_{ijkl} - \frac{1}{3}\delta_{ij}\delta_{kl}), \tag{2.214}$$

in which α and β are functions of the volume fraction. In the case of pure-straining flow, the effective viscosity tensor is a function of α only, while in the linear shear flow only β survives.

Figure 2.18 shows α and β for the simple cubic lattice of neutrally buoyant particles. FCM results are compared with the low volume fraction asymptotic solution given in [166] and the high volume fraction asymptotic result by Hoffman [90]. At low ϕ where far-field interaction plays the major role, the distance between particles are larger than the cut-off

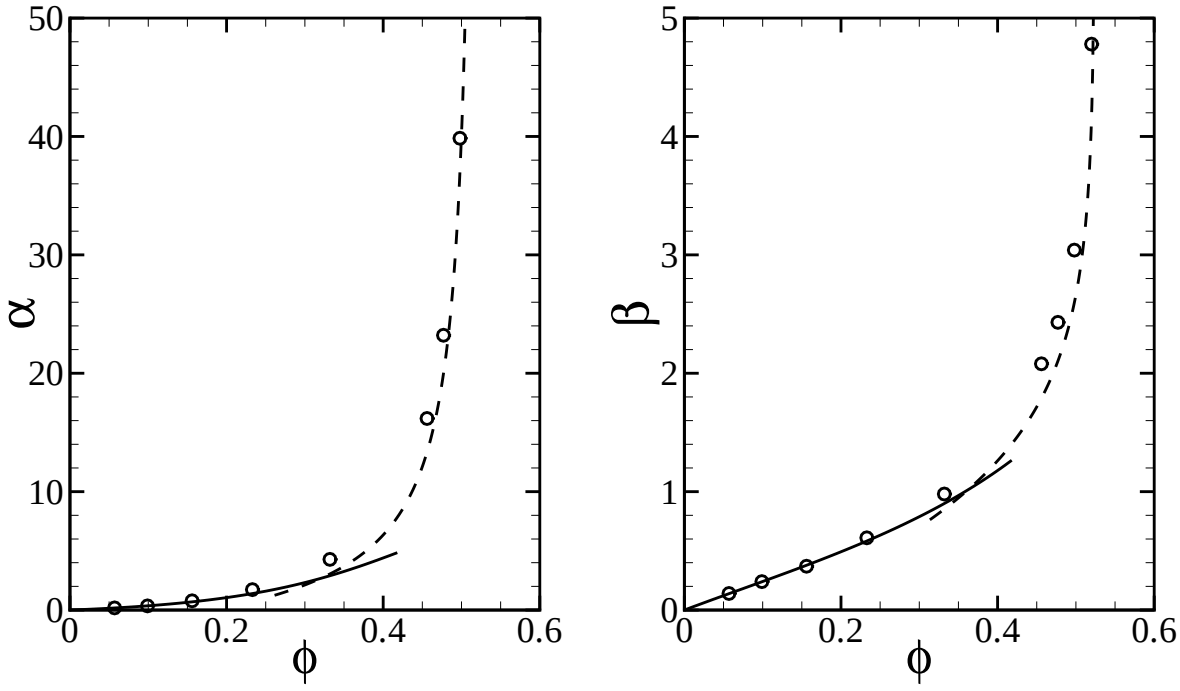

(a) (b)

Figure 2.18: The effective viscosity functions (a) α and (b) β in the functions of the volume fraction ϕ for the simple cubic lattice. The circle indicates FCM results. The dashed and solid lines are, respectively, the high and low concentration asymptotic solutions.

Table 2.6: Simulation parameters of the random static simulations

ϕ	0.1	0.2	0.3	0.35	0.4	0.45	0.5
a	0.35	0.35	0.35	0.35	0.38	0.395	0.409
N_p	138	276	414	483	432	432	432

distance of the lubrication correction and FCM-MD alone can reproduce the asymptotic solution. In the intermediate region, FCM-LUB predicts slightly higher effective viscosity, which is also observed in SD simulations [196]. However, the difference with the asymptotic results becomes smaller and smaller as $\phi \to \phi_{max}$.

2.7.2.2 High-frequency dynamic viscosity

The high-frequency dynamic viscosity μ^* is evaluated using the Monte Carlo approach. For each volume fraction ϕ, the shear viscosity is obtained by averaging over 1000 different random particle configurations. When $\phi \leq 0.35$, the random configuration can be achieved by using a uniform random number generator. For $\phi > 0.35$, body centered cubes are used initially to locate particles. Then, small random perturbations are introduced to generate the random configurations. The minimum distance between particles is kept larger than $10^{-5}a$. The contact force is not used for the Monte Carlo simulation. The simulation parameters are listed in table 2.6. The number of grid points are 64^3 for all static simulations. In figure 2.19, μ^* computed by the present FCM is compared with the empirical formula by Krieger & Dougherty [115], analytical results by Batchelor & Green (B&G) [14], and the multipole-moment simulation by Ladd [121], which is used as the reference. The Stokes-Einstein estimate is obtained in the dilute regime and B&G made ϕ^2 correction in the semi-dilute regime.

1. Stokes-Einstein estimate:

$$\mu^*/\mu = 1 + \frac{5}{2}\phi. \tag{2.215}$$

2. Batchelor & Green (1972):

$$\mu^*/\mu = 1 + \frac{5}{2}\phi + 5.2\phi^2. \tag{2.216}$$

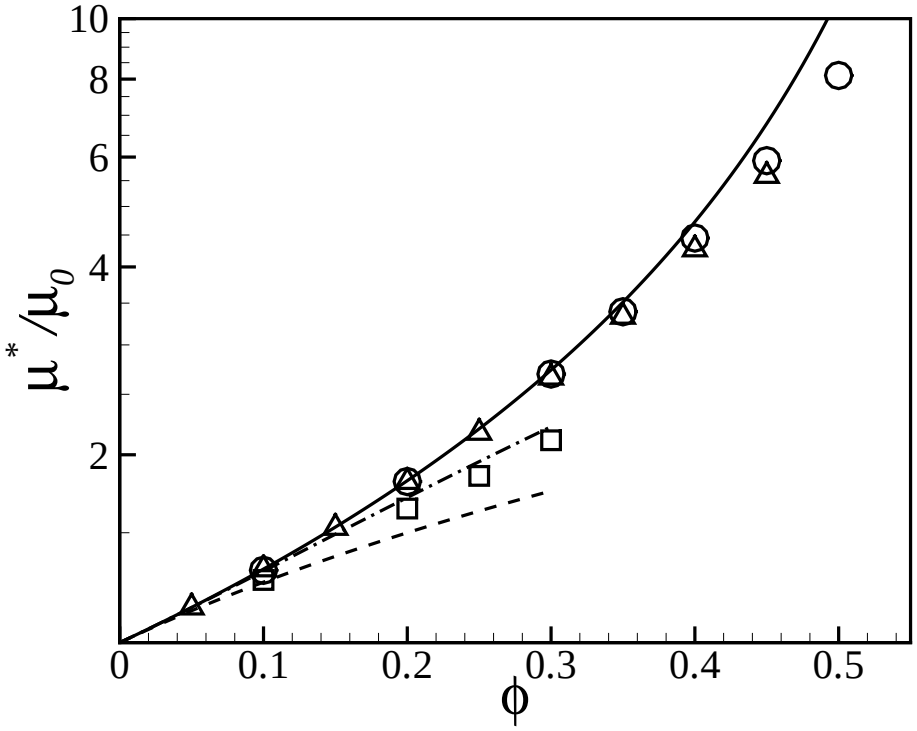

Figure 2.19: Shear viscosity in terms of volume fraction. Solid line, Krieger & Dougherty (1959); dashed line, Stokes-Einstein estimate; dash-dot line, Batchelor & Green (1972); △, Ladd (1990); ○, FCM-LUB; □, FCM-MD.

Table 2.7: Simulation parameters of the dynamic simulations

ϕ	Ng	N_p	a	Δt
0.3	128^3	4337	0.16	2×10^{-3}
0.4	96^3	1458	0.2532	2×10^{-3}

The empirical formula by Krieger & Dougherty is given by

$$\mu^*/\mu = \left(1 - \frac{\phi}{\phi_m}\right)^{-[\eta]\phi_m}, \tag{2.217}$$

in which ϕ_m is the maximum random packing volume fraction and $[\eta]$ is a rheological fitting parameter. Following Stickel & Powell[203], $[\eta] = \frac{5}{2}$ and $\phi_m = 0.63$ are used. It is observed that, the FCM-MD result is close to B&G. Since FCM-MD is a far-field approximation, it can reproduce the semi-dilute solution. At high ϕ, the deviation from the exact values becomes larger. It is shown that FCM-LUB gives accurate results. Although FCM-LUB predicts slightly higher μ^* compared to [121] when $\phi > 0.4$, the difference is about 5% at $\phi = 0.45$.

2.7.2.3 Sheared suspensions

Dynamic simulations are performed for $\phi = 0.3$ and 0.4. For the comparison with the prior simulation results [198], a conservative, short-range contact force of the exponential form

$$\boldsymbol{F}_p^{ij} = -F_{ref}\frac{\tau e^{-\tau\epsilon}}{1 - e^{-\tau\epsilon}}\boldsymbol{d} \tag{2.218}$$

is used. For all dynamic simulations, $\tau = 100$ and $F_{ref}\tau = 6\pi\mu\dot{\gamma}a^2$. Using these parameters, it is observed that the minimum values of ϵ are about 0.001 and 0.0005 at $\phi = 0.3$ and 0.4, respectively. Table 2.7 shows the simulation parameters used to compute the statistics.

We define a mean-square residual as

$$||\boldsymbol{R}||_M^2 = \frac{1}{N_p}\left(\sum_{i=1}^{6N_p}|r_{f,i}|^2 + \sum_{i=1}^{5N_p}|r_{s,i}|^2\right), \tag{2.219}$$

in which $\boldsymbol{r}_f$ and $\boldsymbol{r}_s$ are the residuals of $\mathcal{F}^{lub}$ and $\boldsymbol{S}^{tot}$, respectively. The tolerance level δ is chosen as $10^{-3} \sim 10^{-4}$ to ensure that the error of the particle velocity is $O(10^{-3} \sim 10^{-4})$.

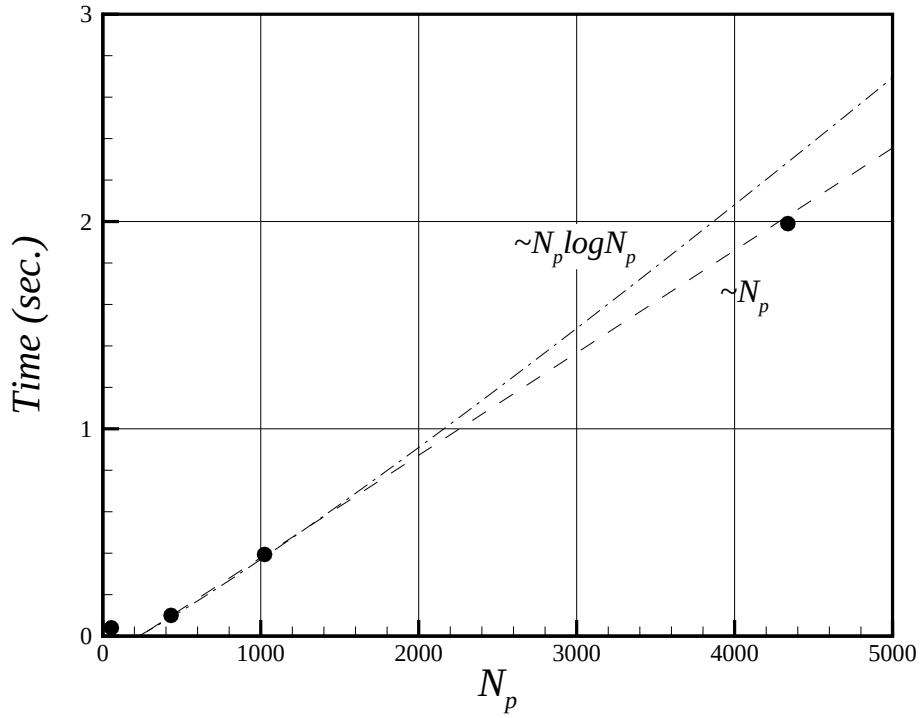

Figure 2.20: Computation time of one time step for $\phi = 0.3$.

Using the particle velocities in the previous time step as an initial estimate, the system is solved in under $7 \sim 8$ iterations. In the concentrated suspensions, due to the complex multi-body hydrodynamic interactions and the elastic contact forces, the trajectories of particles exhibit chaotic motions, which contributes to the random fluctuation of macroscopic variables such as the particle stresses. As a result, a small error in the calculation of the particle velocities is indistinguishable from the statistical noise so that setting very low tolerances does not add to the overall accuracy of a simulation. However, if the tolerance level is set too large, overlap of particles can happen as ϵ is small.

The simulations were performed on a 2.6GHz AMD Opteron Linux cluster. The computation time for one time step is shown in figure 2.20. All the computations were done using 16 processors and the computation time is the average over $500dt$. It is observed that the computation time is scaled as $\sim N_p$ rather than $\sim N_p logN_p$. This N_p-scaling is the result of the large operation counts in the numerical integration of the force envelope and the distribution of the force monopole and dipole to the computational mesh. For example, at $\phi = 0.3$ (table 2.7), the number of operations of the Stokes solver using a Fourier-spectral

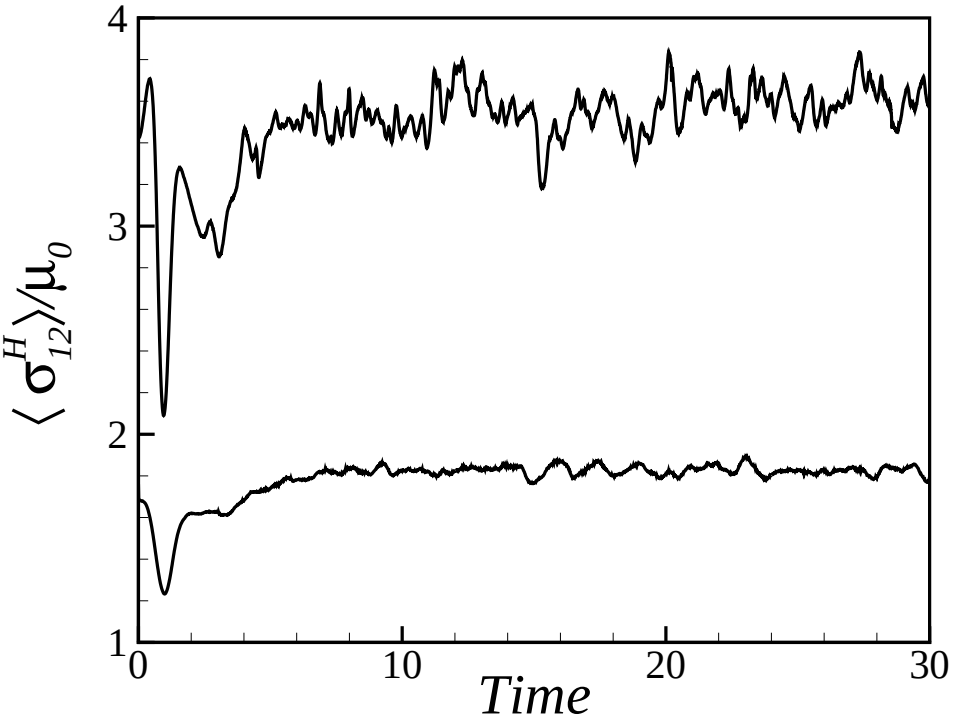

Figure 2.21: Time history of the deviatoric stress tensor. The top and bottom curves correspond, respectively, to $\phi = 0.4$ and 0.3.

method is $O(10^7)$ while the numerical integrations to calculate $\boldsymbol{V}$ and $\boldsymbol{E}$ take $O(10^8)$ operations. This gather and scatter processes take about 60% of the total computation time while the Stokes solver is about 15%. About 15% of the total computation time is spent on the communications between processors. In the present implementation, MPI collective communications are used in the FFT and gather-scatter processes. By changing the collective communications to non-blocking communications and overlapping with computations, further speed-up can be achieved.

Figure 2.21 shows the time history of the deviatoric stress tensor by hydrodynamic interactions;

$$\langle \boldsymbol{\sigma}^H \rangle = \frac{N_p}{V} \langle \boldsymbol{S} \rangle, \tag{2.220}$$

in which V is the volume of the sampling domain, in this case the computational domain, and $\langle \cdot \rangle$ denotes ensemble average. Time is normalized by the shear rate, $\dot{\gamma}$. Initial configurations

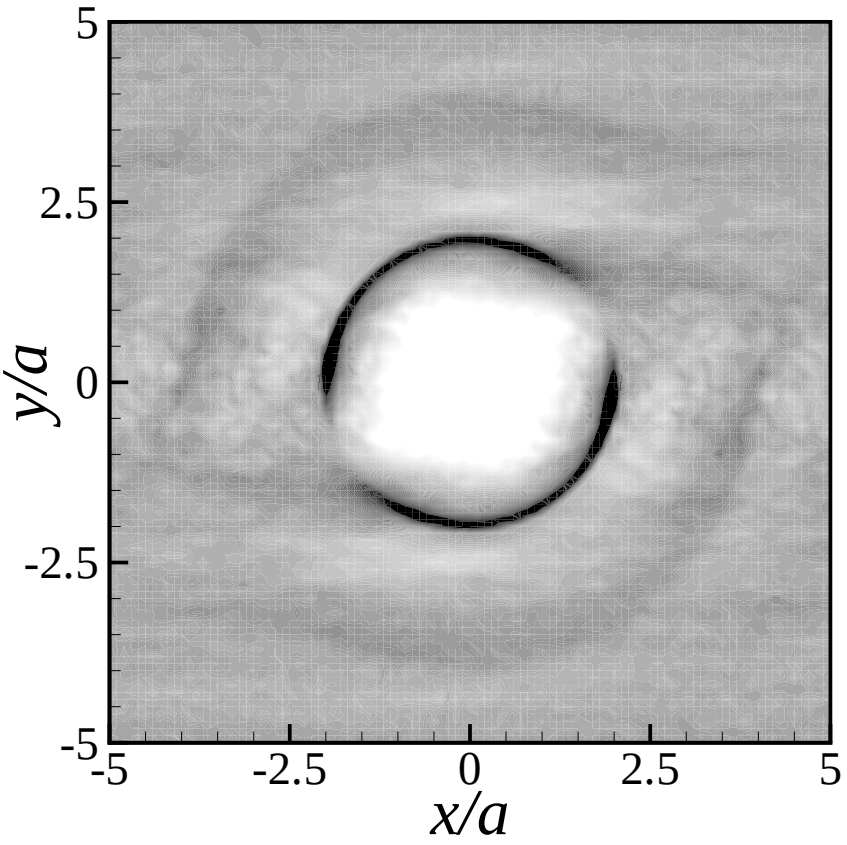

Figure 2.22: Projection of the pair-distribution function onto the $x - y$ plane. The darker the contour, the higher the probability is.

were generated from the body centered cubes with small random perturbations. σ_{12}^H drops sharply at first and starts increasing after $\dot{\gamma}t \simeq 1$ as the microstructure develops in response to the shear flow. To remove the effect of this initial transition, only data for $\dot{\gamma}t > 20$ are used to estimate the statistics.

Figure 2.22 shows the pair-distribution function projected onto the $x - y$ plane for $\phi = 0.4$, in which x and y denote the flow and the velocity gradient directions, respectively. In Stokes flow with perfectly smooth hard sphere suspensions, the pair-distribution function should be symmetric due to the reversibility of Stokes equation. However, as shown in figure 2.16, the net displacement caused by the contact force breaks the fore-after symmetry and the probability of finding another particle in the extensive strain direction becomes smaller than the compressible strain direction. The result for the pair-distribution function is consistent with that of Sierou & Brady [197].

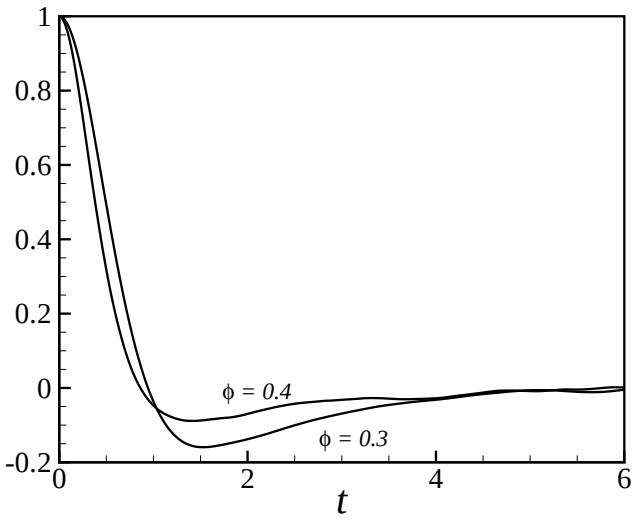

(a)

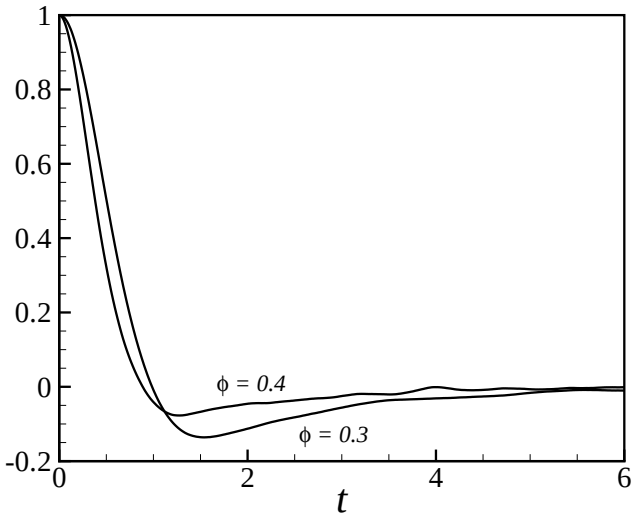

(b)

Figure 2.23: Velocity auto-correlation functions: (a) $\rho^{V_2}(t)$ and (b) $\rho^{V_3}(t)$ for $\phi = 0.3$ and 0.4.

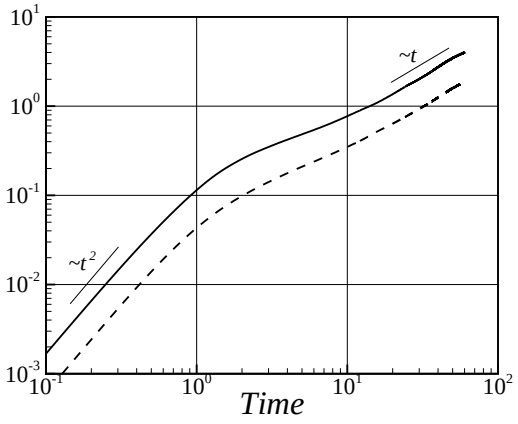

(a)

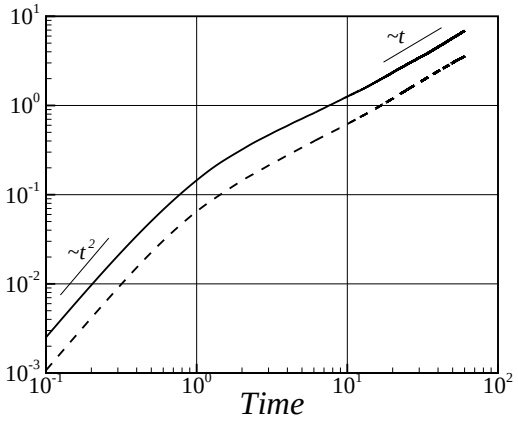

(b)

Figure 2.24: Mean squared displacement normalized by a^2 in the velocity gradient (solid line) and the vorticity directions (dashed line): (a) $\phi = 0.3$ and (b) $\phi = 0.4$.

A key element for the shear-induced random dispersion of particles in a suspension is the velocity auto-correlation, which is defined as

$$\rho^{V_i}(\tau) = \frac{\langle V_i(t) V_i(t+\tau) \rangle}{\langle V_i(t)^2 \rangle}. \tag{2.221}$$

Figure 2.23 shows the velocity auto-correlation for two volume fractions, $\phi = 0.3$ and 0.4. At the larger volume fraction, the velocity auto-correlation decays faster and the magnitude of the negative peak decreases, which is consistent with the earlier results of [58].

Figure 2.24 shows the mean squared displacement normalized by a^2,

$$\sigma_{Xi}(t) = \frac{\langle (Y_i(t) - Y_i(0))^2 \rangle}{a^2}. \tag{2.222}$$

It is well known that at short times in which the particle motion is strongly correlated with the initial configuration σ_X increases as $\sim t^2$, while at longer times a steady behavior is established and σ_X shows linear growth with time,

$$\sigma_{Xi}(t) \sim \quad \langle V_i^2 \rangle t^2, \qquad t \ll T_{Li}, \tag{2.223}$$

$$\sigma_{Xi}(t) \sim \quad 2\langle V_i^2 \rangle T_{Li} t, \qquad t \gg T_{Li}, \tag{2.224}$$

in which T_{Li} is the integral timescale in i-direction,

$$T_{Li} = \int_0^\infty \rho^{V_i}(s) ds. \tag{2.225}$$

The diffusivity D_i is given as

$$D_i = \langle V_i^2 \rangle T_{Li}. \tag{2.226}$$

The diffusivity can be estimated by two methods. One is from the integral of the velocity autocorrelation function, as shown in equation (2.226) and the other is by estimating the long-term slope of σ_X, which should yield the same results. Table 2.8 shows the diffusion coefficients evaluated from equation (2.226). The agreement with the previous simulations [198] is quite good.

There is a large scatter in the diffusion coefficients in the literature due to the variation in experimental conditions. In [198], it is found that the diffusion coefficients from SD simulations are almost half of the experimental results. In the experiments, several poorly quantified features, such as surface roughness, surfactant or steric forces, and residual Brownian forces, strongly affect the motion close to contact. In the numerical simulations, the contact force is used to model these effects. Using the contact force (2.212) with large cut-off distance ($R_{ref} = 2.2$), Abbas *et al.* [2] could obtain the diffusion coefficients similar to the experimental results. On the other hand, when using the lubrication model by Dance & Maxey [50], the diffusion coefficients were only about 2/3 of those with the large contact forces. Although there are many studies on the role of contact forces on suspensions

Table 2.8: Diffusion coefficients in y and z directions

ϕ	D_y	D_z
0.3	0.030	0.016
0.4	0.059	0.037

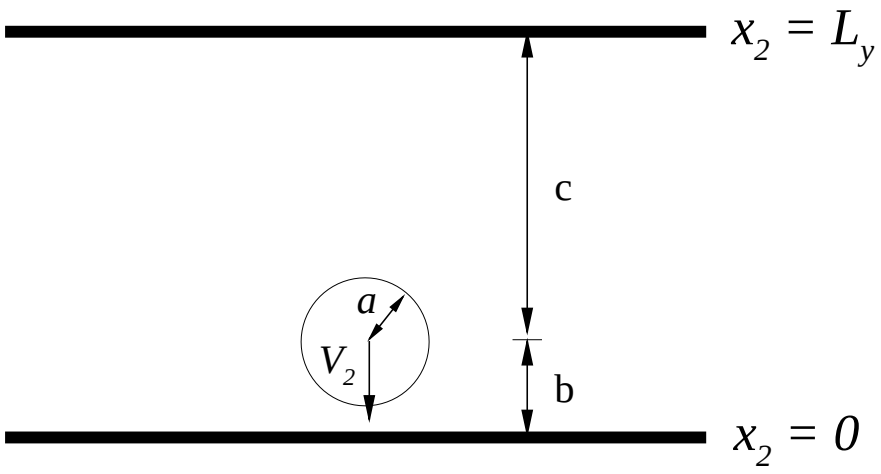

Figure 2.25: Geometry for a sphere placed between two walls.

[2, 47, 58, 97, 152], the choice of a contact force to represent the underlying physics correctly is still an open question.

2.7.3 Results III: single particle in a channel

We first illustrate the methods described in the previous sections by applying them to the motion of a single particle in a channel bounded by two parallel planar walls. The first example is of a spherical particle moving perpendicular to the walls under the action of an external force but in the absence of any other flow. The configuration of the channel geometry is shown in figure 2.25. Numerical results for the non-dimensional resistance

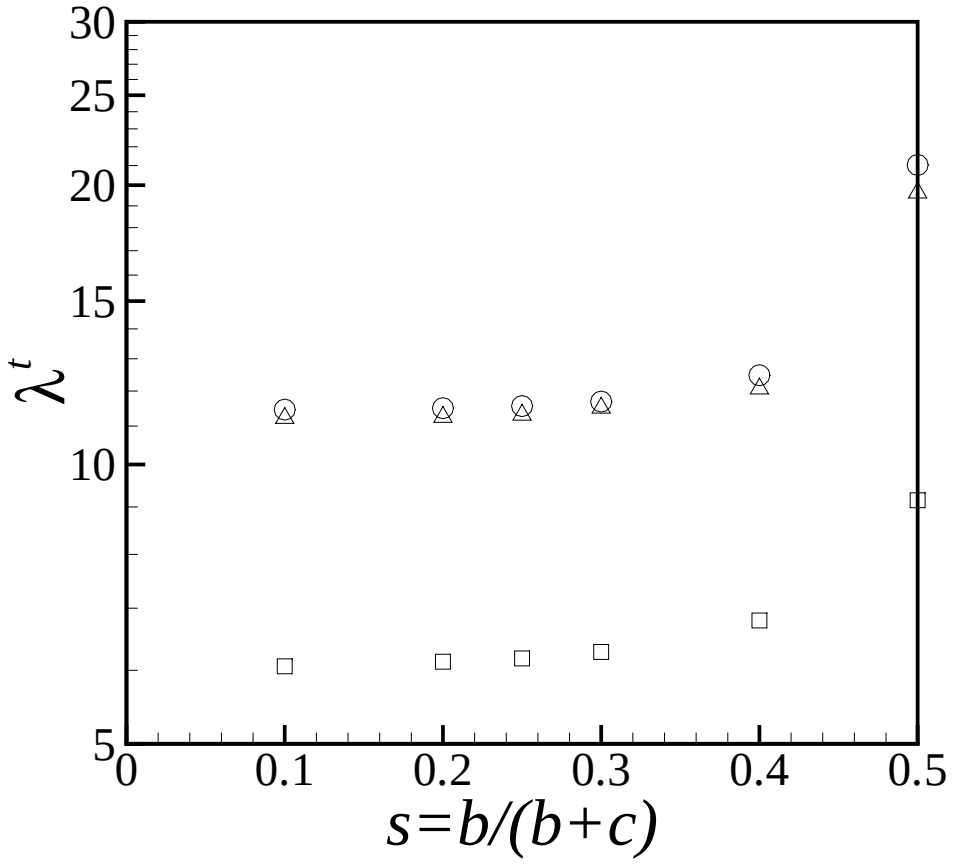

Figure 2.26: Drag coefficient λ^t from ◯, Ganatos *et al.* (1980); △, FCM with wall lubrication; □, FCM with monopole and dipole.

coefficient λ^t, defined by

$$\lambda^t = \frac{F_2}{6\pi\mu a V_2}, \tag{2.227}$$

have been obtained previously by [75] using a series solution and boundary collocation scheme for a channel with infinite planar walls. The corresponding FCM simulations are performed for a periodic channel, where $L_x/a = L_z/a = 60$. The height of the channel L_y is varied according to the parameter $s = b/(b+c)$ used by [75]. The gap between the particle and the wall is $0.1a$ so that $b/a = 1.1$.

A comparison of the results for λ^t from the two different approaches is shown in figure 2.26. Also shown are the values from FCM without the lubrication correction, which are roughly half the total for λ^t. This configuration is the most challenging to calculate with FCM, the gap being larger than at which near-field lubrication forces would dominate, and tests the matching procedure for the near-field and far-field conditions. In general the agreement of the results is very good, with differences of 2% or less for the most part. For the larger values of s the discrepancies are larger. For $s = 0.5$, the channel height is only $2.2a$ and the calibration procedures used to obtain the FCM wall resistance functions, which were based on widely separated channel walls are no longer appropriate.

The second example is for the translational velocity of a force-free and torque-free sphere in a Couette flow. The computational domain here is $L_x = 30$, $L_z = 20$ and $L_y = 10$ and the particle radius $a = 1$. The upper wall is moving in the x_1 direction with the velocity $V_{upp} = -1.0$, while the lower wall velocity is $V_{low} = 1.0$. Figure 2.27 shows the translational velocity of a sphere centered at various y locations, close to the upper wall at $y = 10$. The FCM results are compared with the boundary collocation results of [76] and the SD simulation by [199]. The results in [76] are used as the reference. In the FCM simulations, the lubrication corrections are used when $y/a > 8.8$, that is when the gap between the particle and the wall is less than $0.2a$. In the region where the far field solution plays the dominant role, the FCM results match those of [76] without any corrections. In the near-wall region, FCM gives more accurate results than the SD results reported in [199]. In the latter, a rigid wall was represented as a layer of fixed spherical "wall particles" rather than a smooth wall with no-slip boundary conditions. Further, the domain size was smaller, with periodic dimensions $L_x/a = L_z/a = 14$.

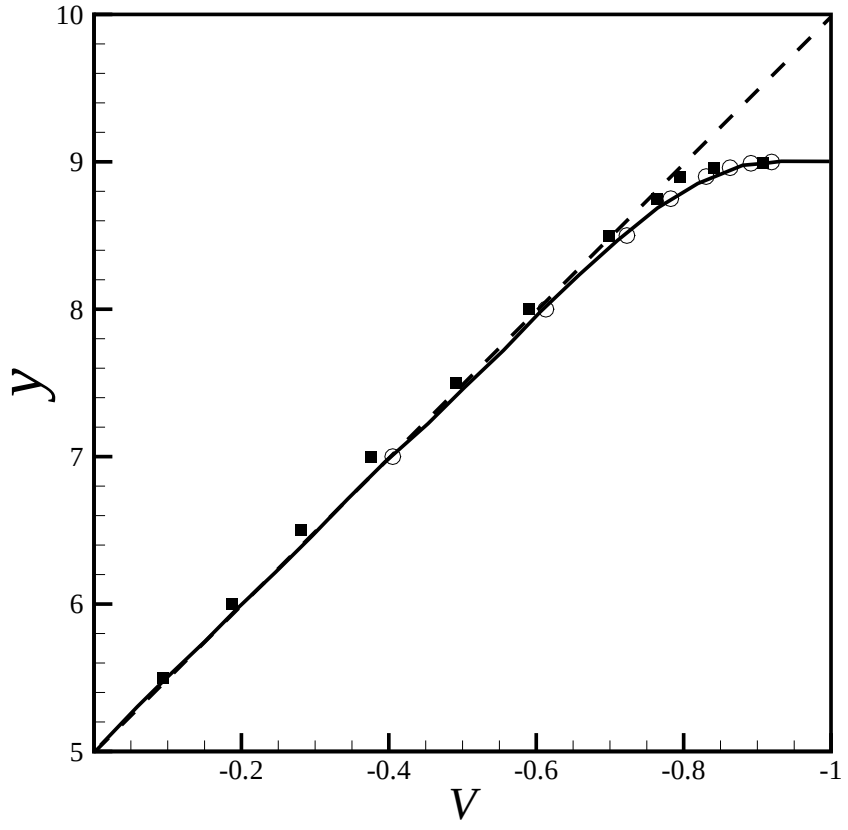

Figure 2.27: Translational velocity of a sphere V in a Couette flow: Solid line, Ganatos *et al.* (1982); ■, Singh & Nott (2000); ◯, present FCM.

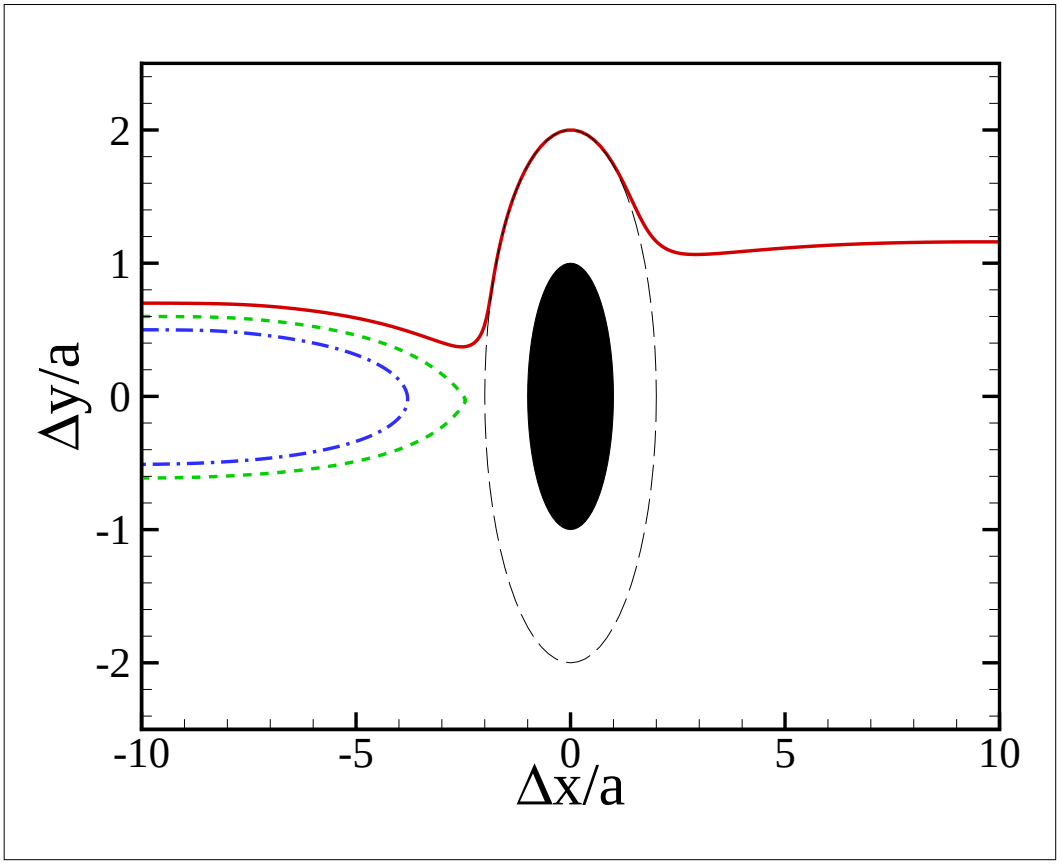

Figure 2.28: Relative trajectories in the $x-y$ plane for a particle pair in a linear shear flow at $Re_p = 1.0$. The initial vertical separation distances are $\Delta y/a = 0.5$ (dash-dot), 0.6 (dashed), and 0.7 (solid).

2.7.4 Results IV: a particle pair under a finite fluid inertia

In the limit of vanishing Reynolds number, the relative trajectory of a pair of equal-size particles in a linear shear flow can have only two types of trajectories, open or closed trajectory, depending on the initial relative position of the particles [15]. Kulkarni & Morris [118] have shown that, at finite Reynolds numbers, the topology of the relative trajectory changes from that of the Stokes flow. Using the lattice-Boltzmann simulations, they found reversing and spiralling trajectories in addition to the open trajectory of Stokes flow suspensions. Here, we used the force-coupling method to reproduce the lattice-Boltzmann simulations of Kulkarni & Morris [118].

Figure 2.28 shows the relative trajectory of a particle pair in the shear plane, *i.e.* the separation distance in the vorticity direction $\Delta z/a = 0$. The particle trajectories are computed for the particle-scale Reynolds number $Re_p = \frac{\rho\dot{\gamma}a^2}{\mu} = 1.0$. The initial separation

distance in the velocity direction is fixed, $\Delta x/a = 10$, while the vertical separation distances are changed from $\Delta y/a = 0.5$ to 0.7. It is found that the topology changes from the reversing to open trajectories as $\Delta y/a$ changes from 0.6 to 0.7. In [118], they found that the bifurcation point is about 0.6 for $Re_p = 1.0$. Considering the difference in the numerical set-up, LBM simulation of a wall-bounded channel in [118] versus FCM in tri-periodic domain in the present study, the agreement in the bifurcation point is satisfactory.

For the second example, we show the spiralling trajectory. The initial separation distance is fixed as $(\Delta x/a, \Delta y/a, \Delta z/a) = (-0.01, 0.005, 2.8)$ and the Reynolds numbers are changed from $Re_p = 0.1$ to 0.5. Figure 2.29 shows the relative trajectories in the $x - z$ direction. It is seen that the particle moves towards the reference particle at the origin showing an oscillatory motion in the $x-z$ plane. The spiralling trajectory observed in the present study is qualitatively consistent with those in Kulkarni & Morris [118]. Note that the spiralling trajectory is caused by the secondary flow and, hence, accurate representation of the no-slip boundary on the particle surface is important in resolving the dynamics. In the force-coupling method, a particle is represented by a "smooth" Guassian profile, instead of having a sharp no-slip boundary, which results in an underestimation of the non-linear interaction. As a result, the timescale of the spiralling trajectory in FCM is about $O(10^3)$ in contrast to $O(10^2)$ of the lattice-Boltzmann simulation [118]. In the previous lattice-Boltzmann simulations, the particle surface is represented by a staggered non-smooth surface. As the timescale of the multi-particle interaction is usually $O(1)$ or smaller in concentrated suspensions, the detailed mechanism of this spiralling trajectory is not expected to play an important role. A more detailed discussion of a secondary flow induced by the non-linear interaction is given in Chapter 5.

2.8 Conclusions

In this chapter, the lubrication-corrected FCM (LC-FCM) has been derived for the inclusion of lubrication forces between particles in the simulation of viscous suspensions using the force-coupling method. These forces are evaluated on the basis of pairwise additions to the resistance formulation, the inverse of the natural mobility formulation provided by FCM. This provides a more reliable estimate of lubrication interactions for concentrated suspensions than using pairwise addition to the mobility problem. Efficient and robust

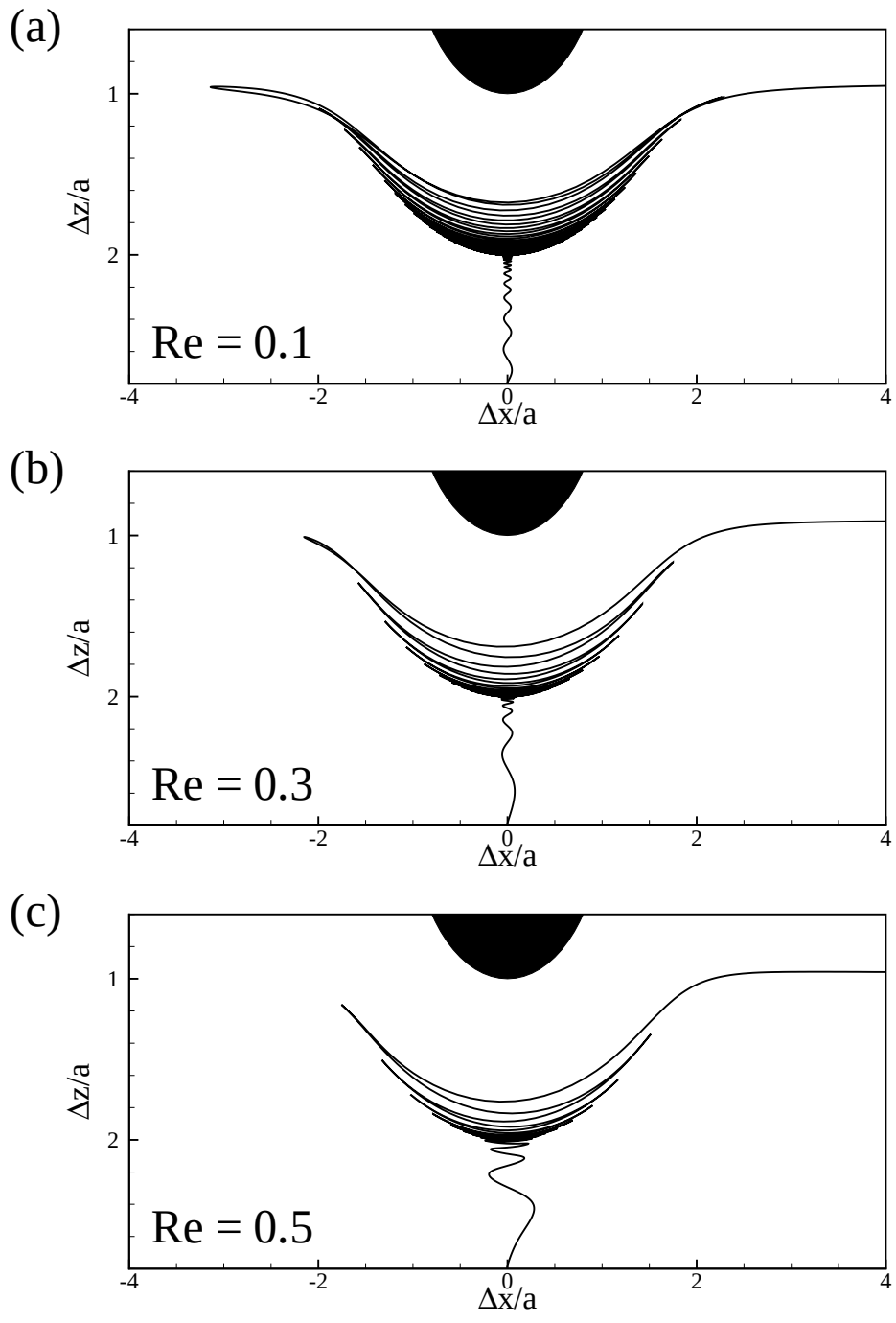

Figure 2.29: Relative trajectories in the $x-z$ plane for a particle pair in a linear shear flow at $Re_p = 0.1$ (a), 0.3 (b), and 0.5 (c).

iterative methods are described for solving for the particle stresslets and for lubrication effects in which the problems are written in terms of a symmetric positive definite system. The fully coupled lubrication and far-field interactions are then obtained efficiently through a suitably chosen preconditioned conjugate gradient method, in which the inverse of the ill-conditioned resistance matrix is calculated by a recursive formula. Solving the full system requires typically less than $7 \sim 8$ iterations while ensuring that the errors in the particle velocity are $O(10^{-3})$ or less.

The force-coupling method can be easily implemented with any existing numerical Stokes or Navier-Stokes solver. As such, the simulation of inhomogeneous and wall-bounded suspensions are possible with FCM. The no-slip boundary condition at a fixed rigid boundary is then naturally incorporated in the numerical simulation. Lubrication forces must be specified for the interaction of particles with a rigid wall following the same general procedures. There is a minor complication in that the force envelopes (2.4)-(2.5) are not compact and may extend outside of the flow domain even though the particles are full contained within the domain. The standard procedure has been to truncate the envelopes at the domain boundaries [135]. Here, a new FCM envelope near a wall is proposed.

To accelerate the convergence of the system for dynamic simulations, a fictitious inertia is added to the equation of motion of Stokes flows. Using the fictitious inertia, the computation time can be reduced to almost $1/2 \sim 2/3$, while an additional temporal error of $O(\delta t^2 \sim \delta t^3)$ is introduced. The solution procedure of FCM with the lubrication correction for Navier-Stokes flows is presented. Here, a first-order scheme for concentrated finite-inertia suspensions is provided and tested. A second order scheme is also proposed, which has not been implemented yet.

LC-FCM is tested for the various particle-pair interactions and in concentrated suspensions. For the computation of dynamically evolving, sheared suspensions of neutrally buoyant particles, numerical simulations with $O(1000)$ particles are performed. It is shown that the results are consistent with the previous theories and numerical simulations. It is also shown that the computational cost for homogeneous suspensions in a periodic cell, using a Fourier spectral method, is close to $O(N_p)$. The results also illustrate the importance of near-contact repulsion forces in non-Brownian suspensions and their contribution to the irreversible interaction of particles.

LC-FCM may be readily extended to bidisperse or polydisperse systems of particles.

For each combination of particles, the corresponding lubrication forces between the particles must be specified as in (2.134) and as given by [110]. Similarly, the FCM resistance functions for near-field interaction of each combination must be determined as in (2.135) and a table constructed similar to table 2.1. The basic procedures follow as before. The scale coefficient κ in the preconditioner (2.137) should be adjusted as in equation (2.124).

Chapter 3

Stokes flow: Concentrated suspensions in Couette flow

3.1 Introduction

Suspension of neutrally-buoyant non-colloidal particles in a linear shear flow is one of the most fundamental systems to study dynamics and rheology of suspension flows. Yet, hydrodynamic interaction between particles becomes so complex as the volume fraction increases that theoretical analysis of the system has been limited to the dilute to semi-dilute regimes (see [159, 203] for review). Most of our current understanding of non-colloidal suspensions comes from experimental and numerical observations. In providing detailed information about the micro-structure as well as the rheological properties, numerical simulations greatly contribute to our understanding on concentrated suspensions in ways not always available in experiments. The most widely used numerical method to study concentrated suspensions is the Stokesian Dynamics (SD) method [24, 23]. In the case of homogeneous sheared suspensions in which periodic boundary conditions are used for all three-directions, modeling an infinite domain, Stokesian Dynamics has been used for a wide range of volume fractions, for example, to investigate the rheology and micro-structure [197], shear-induced diffusion [141, 198], and chaotic behavior [59, 172].

Although the dynamics of concentrated suspensions in the unbounded domain is now well understood, much less is known about the behavior of suspensions in the wall-bounded domain, where the suspension field is highly inhomogeneous. There have been several ob-

servations on the distinctive mechanisms in the wall bounded suspensions, such as apparent wall-slip [99], particle structuring [113], and swapping of particle trajectories [244]. There have been a few numerical studies on the wall-bounded suspensions using the Stokesian Dynamics, where a wall is replaced with a chain of fixed spheres [164, 199]. Due to the high computational cost, dynamic simulations in the wall bounded flows have been limited to a monolayer simulation with $O(10)$ particles. Bossis *et al.* [22] and Swan & Brady [207] have extended Stokesian Dynamics for particle-wall interactions using the image method [18]. However, dynamic simulations of concentrated suspensions using these modification have not been reported yet.

There are only a few three-dimensional simulations of concentrated suspensions in Couette flow. Most of the simulations are performed using the lattice-Boltzmann (LB) method as developed by Nguyen & Ladd [162]. Kromkamp *et al.* [116] performed both two- and three-dimensional LB simulations of concentrated suspensions in a Couette flow. They showed that the wall structuring in two-dimensional simulation differs from the three-dimensional results. They observed dependency of some results on the computational resolution and ascribed the dependency to the ragged particle surface in the LB method. Kulkarni & Morris [119] performed three-dimensional LB simulations for the volume fraction up to 0.3 in a Couette flow to investigate the finite-Reynolds-number effects on the suspension rheology.

The main goal of this chapter is to investigate the effects of the confinement on the dynamics of suspension flows. The present simulations are among the first computational results on the dynamics of concentrated Stokes suspensions in a Couette flow with a full representation of no-slip conditions at a rigid wall. In section 3.2, the rheology and microstructure of Couette flow suspensions are investigated for wide ranges of volume fraction and channel height. The diffusive behavior and lengthscales of suspension flows are discussed in section 3.3. The effects of confinement and external torques on the disorder-order transitions of non-Brownian suspensions are shown in sections 3.4 and 3.5, respectively. The conclusions are given in section 3.6.

3.2 Wall effects on the rheology of concentrated suspensions

One of clear presentations about the wall effects on suspension rheology is given in Zarraga *et al.* [241], where they measured the effective viscosity and normal stress differences in various experimental devices. In a parallel plate geometry, they found that the rheological parameters are functions of the gap width when the gap width is smaller than $40a$, in which a is the particle radius. However, detailed mechanism responsible for the behavior is still not understood clearly. The main focus of this section is to investigate the changes of suspension dynamics near the wall. It is shown that particle layers are formed near the wall due to the strong particle-wall lubrication interactions. As a result of the particle layering, the rheological properties such as the relative viscosity and the normal stresses are found to be functions of H_y/a in which H_y is the channel height. At high volume fractions the suspension can be divided into three regions depending on the micro-structure; the wall region where particle layering is dominant, the core region in which suspension behaves similarly to homogeneous suspensions, and the buffer region in which the micro-structure shows the characteristics of both the shear structure and the particle layer.

3.2.1 Simulation parameters

FCM simulations are performed for three different volume fractions ($\phi = 0.2, 0.3, 0.4$). The computational domain in the horizontal directions is fixed ($H_x/a = 30, H_z/a = 20$), while the channel height is varied to investigate the effect of the wall ($H_y/a = 10,\ 20,\ 30$). The number of Fourier modes in $x-$ and $z-$directions are 96 and 64, respectively. The simulation parameters are shown in table 3.1. The radius of a sphere (a) and the shear rate ($\dot{\gamma}$) are fixed at reference values: $a = 1,\ \dot{\gamma} = 1$. The upper wall is moving with the velocity $\boldsymbol{V}_{wall} = (\dot{\gamma}H_y/2, 0, 0)^T$ and the lower wall is moving in the opposite direction with the same speed.

When the separation distance between two particles becomes very small (less than $10^{-2}a$), non-hydrodynamic effects, such as surface roughness, residual Brownian forces, and electrostatic forces, may play an important role. These effects will break the fore-after symmetry of particle interactions in Stokes flow. For example, Smart & Leighton [200] showed that the roughness of particles ranging from $43 - 6350\mu m$ in diameter is on the order of $10^{-2}a \sim 10^{-3}a$. Brady & Morris [25] showed the importance of these non-hydrodynamic

Table 3.1: Simulation parameters. N_y is the number of elements in the vertical direction. Every elements has the same length $E_L = 2.5$ and quadrature points $Q_y = 9$.

	ϕ	H_y	N_y	N_p	R_{ref}	F_{ref}	dt
C2S	0.2	10	4	285	2.01	100	2×10^{-3}
C3S	0.3	10	4	430	2.01	100	2×10^{-3}
C4S	0.4	10	4	567	2.01	100	2×10^{-3}
C2L	0.2	20	8	570	2.01	100	2×10^{-3}
C3L	0.3	20	8	860	2.01	100	2×10^{-3}
C4La	0.39	20	8	1122	2.01	100	2×10^{-3}
C4Lb	0.39	20	8	1122	2.004	100	2×10^{-3}
C4Lc	0.39	20	8	1122	2.001	1000	1×10^{-3}
C4H	0.4	30	12	1718	2.01	100	2×10^{-3}

forces on the non-Newtonian aspect of suspension flows. To model the non-hydrodynamic interactions, and specifically the effects of surface roughness of non-Brownian particles, a short-range contact force $\boldsymbol{F}_P^{ij}$ is used in the present simulations when the distance between particle i and j is less than a barrier cut-off distance R_{ref}. The form of the contact force is chosen to be similar to Dance *et al.* [49],

$$\boldsymbol{F}_P^{ij} = \begin{cases} -6\pi\mu\dot{\gamma}a^2 F_{ref} \left(\frac{R_{ref}^2 - |\boldsymbol{r}|^2}{R_{ref}^2 - 4a^2} \right)^6 \frac{\boldsymbol{r}}{|\boldsymbol{r}|} & \text{if } |\boldsymbol{r}| < R_{ref} \\ 0 & \text{otherwise,} \end{cases} \tag{3.1}$$

in which $\boldsymbol{r} = \boldsymbol{Y}^i - \boldsymbol{Y}^j$ and F_{ref} is a constant. It has been discussed that, as long as the contact force is sufficiently short ranged, the detailed expression of the contact force does not change the simulation results significantly [57, 141]. The effects of the roughness model or the contact force on the suspension rheology has been of interest and can be found in the literature [2, 25, 47, 97, 152].

Since the system is chaotic and ergodic, a time average is used to obtain statistics once the suspension flow reaches a statistically stationary state. The initial configurations are obtained by two different approaches; body-centered cubes with small random perturbations and a molecular dynamics simulation. It is observed that, once the suspension reaches a statistically stationary state, the statistics does not depend on the initial configuration. Simulations are performed for $\dot{\gamma}t \simeq 50$ to reach the stationary state. Then, the time average is performed over the period $T = 100\dot{\gamma}t$ except for C4Lc for which the simulation is performed until $T = 40\dot{\gamma}t$.

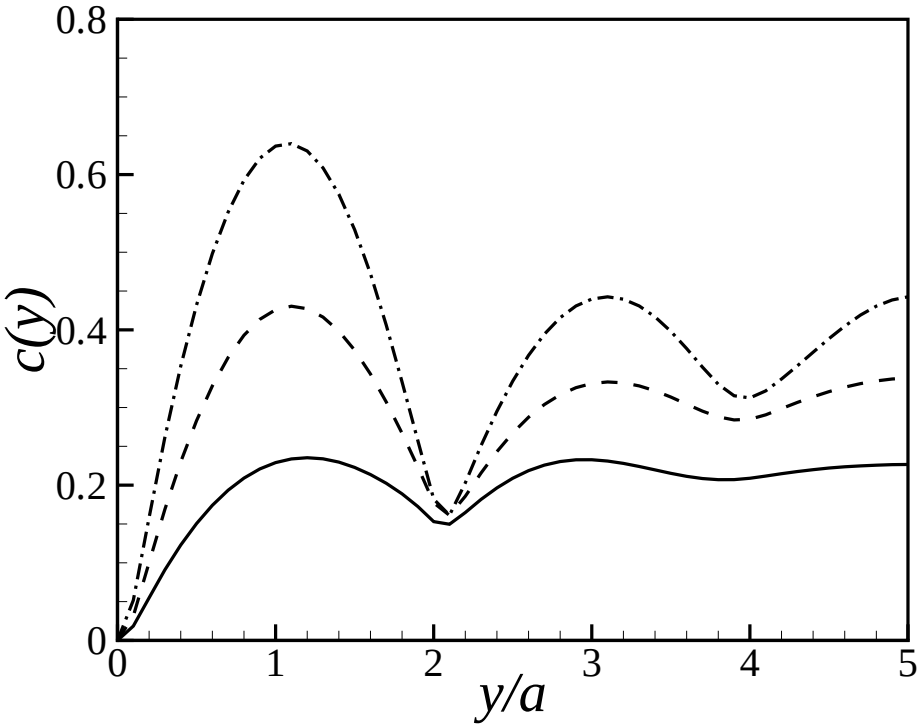

Figure 3.1: Concentration profiles for C2S (solid), C3S (dashed), and C4S (dash-dot).

3.2.2 Wall effects on particle concentration

In wall-bounded suspensions, once a particle moves close to a wall, the particle tends to stay near the wall for a long time due to the strong particle-wall lubrication force, which then results in the formation of stable particle layers near the wall. Using LB simulations, both Kromkamp *et al.* [116] and Kulkarni & Morris [119] observed a pronounced local concentration peak near the wall at high volume fractions, which was not reported in the earlier simulations of coplanar particles in Couette flow [199]. The concentration profiles and the two-dimensional pair-distribution functions are presented to characterize the particle layering and the near-wall effects on suspensions.

The local concentration is defined as

$$\langle c(x_2)\rangle = \frac{1}{H_x \times H_z}\langle \iint \chi(\boldsymbol{x}) dx dz\rangle, \tag{3.2}$$

in which $\chi(\boldsymbol{x})$ is an indicator function that is only non-zero if $\boldsymbol{x}$ is inside of a particle and $\langle\cdot\rangle$ denotes the ensemble (time) average.

Figure 3.1 shows the concentration profiles in the small domain ($H_y/a = 10$). Considering the symmetry, only half of the channel is drawn. The concentration profiles for C2S and C3S have a local peak in the wall region and become relatively flat away from the wall. On the other hand, the plateau is not observed in C4S, indicating that the wall effect is dominant across the whole channel. As the layering in the wall region becomes stronger, it is seen that the ratio of the first local peak concentration near the wall to the concentration in the center is an increasing function of ϕ. For C4S, the peak concentration in the particle layer is almost 1.5 times larger than that in the center region. Consistent with Kromkamp *et al.* [116], the location of the peak concentration moves toward the wall as ϕ increases. The local peaks are observed around 1.2, 1.1 and 1.08 for C2S, C3S, and C4S, respectively. Due to the finite size of the particles, there is a particle depletion layer around $y/a \simeq 2.1$ even for the lowest volume fraction in the present simulation (C2S).

Further insight about the relative position of particles comes from the particle pair-distribution. The pair-distribution functions projected onto the velocity/velocity-gradient plane, $g(\Delta x, \Delta y)$, and velocity-gradient/vorticity plane, $g(\Delta y, \Delta z)$, are shown in figure 3.2 for C4S. The pair-distribution functions are obtained for the reference particles centered in $4.5 \leq y/a \leq 5.5$. Two distinct streaks of high probability region are observed around $\Delta y/a \simeq \pm 2$ and ± 4, which correspond to the parallel particle layers at $y/a \simeq 1$ and 3. Due to the strong layering, there is a depletion layer between two particle layers ($\Delta y/a \simeq \pm 3 \sim 3.5$) in which the probability of finding another particle is low. In the core region $-2.5 < \Delta y/a < 2.5$ or $2.5 < y/a < 7.5$, $g(\Delta x, \Delta y)$ shows two shells of high probability near the compressional axis of the linear shear flow, similar to the results for sheared suspensions in an unbounded domain [197].

Figure 3.3 shows the concentration profiles in a large channel ($H_y/a = 20$). The concentration profiles for C2L and C3L are similar to those in the smaller channel ($H_y/a = 10$). For $\phi = 0.4$, the plateau of the concentration is observed when $y/a > 7$.

In addition, to show the effect of the contact force or particle roughness, the concentration profiles for C4La and C4Lc are compared in figure 3.3. In C4Lc, the contact force is activated when the distance between two particles is $a\epsilon < 0.001$. A very large F_{ref} is used to make the contact force behave similarly as the hard sphere potential. The minimum separation distances for C4La and C4Lc are $\epsilon_{min} \simeq 3 \times 10^{-3}$ and 5×10^{-4}, respectively. Comparison of the profiles for C4La and C4Lc shows that indeed the specific details of the

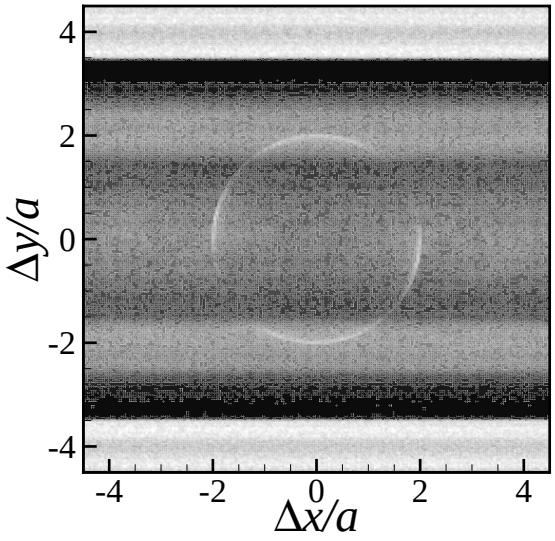

(a)

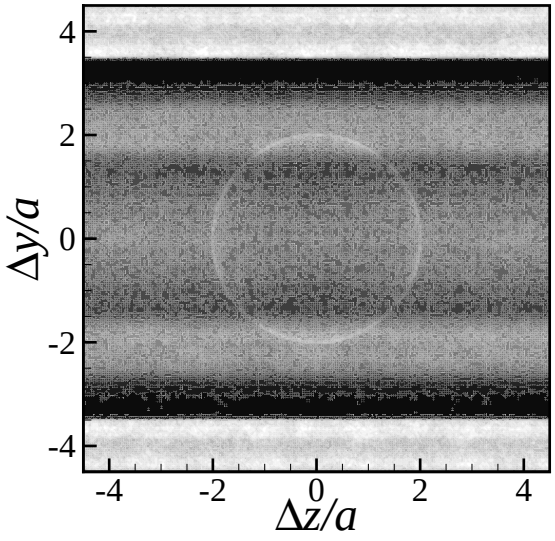

(b)

Figure 3.2: The pair-distribution function projected onto (a) $x-y$ and (b) $y-z$ planes for C4S. Light contours represent high probability.

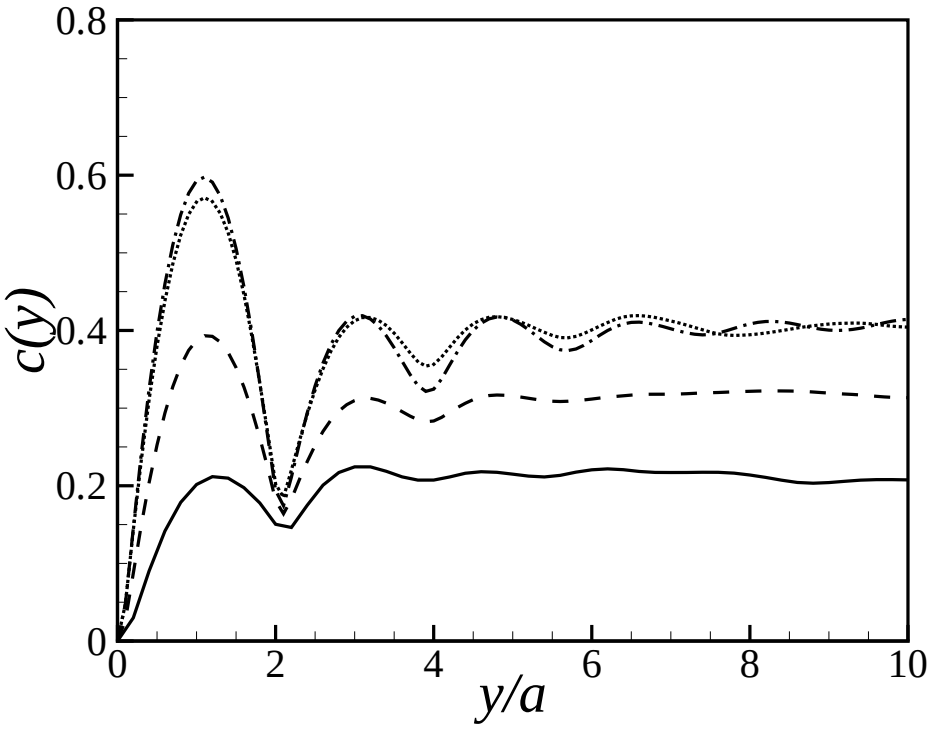

Figure 3.3: Concentration profiles for C2L (solid), C3L (dashed), C4La (dash-dot), and C4Lc (dotted).

contact force has only a slight effect on the concentration profile.

The pair-distribution function $g(\Delta x, \Delta y)$ for C4La is obtained for two different regions for the reference particles; $5.5 < y/a < 6.5$ (figure 3.4 a), a middle zone between the wall and the centerline, and $8 < y/a < 12$ (figure 3.4 b), close to the centerline. In figure 3.4 (a), three particle layers are observed in the lower half around $\Delta y/a \simeq -1.5$, -3, and -5, which correspond to the local concentration peaks near the wall. When $\Delta y > 0$, the particle layering is weak and the suspension is essentially homogeneous. Similar to suspensions in an unbounded domain, two shells of high probability region are observed oriented with the compressional axis of the mean rate of strain. Observation of the instantaneous suspension field reveals that the second and third particle layers are formed and then broken repeatedly with some period. In other words, unlike the first particle layer, the second and third particle layers exist on average not at each time instance. The pair-distribution function obtained in the core region (figure 3.4 b) is similar to the previous results for an unbounded domain [197, 233], implying the rheological properties in the core region may be explained by the results in the unbounded domain.

The concentration profiles for different H_y/a at $\phi = 0.4$ is compared in figure 3.5. It is shown that, as H_y/a increases, the peak concentration at the location of the first particle layer decreases. It is interesting to see that the concentration profiles for different H_y/a are almost similar except for the value of the first peak, indicating the width of particle layers is independent of H_y/a, if H_y/a is large enough. At $\phi = 0.4$, the suspension field is homogeneous if $y/a > 8$. This observation is consistent with the experimental result in Zarraga *et al.* [241] that the rheological properties are functions of the channel width when the channel is not wide enough. As H_y increases, the ratio of the homogeneous region to the particle layers becomes bigger, which makes the volume-averaged rheological properties independent of H_y/a in a wide channel.

Similar to the concentration, the average particle flux is defined as

$$c\boldsymbol{v}(x_2) = \frac{1}{H_x \times H_z} \sum_{i=1}^{N_p} \iint H(a - |\boldsymbol{x} - \boldsymbol{Y}^i|)\boldsymbol{V}^n dx dz, \tag{3.3}$$

where $H(x)$ is the Heaviside step function. Then, the averaged particle-phase velocity is

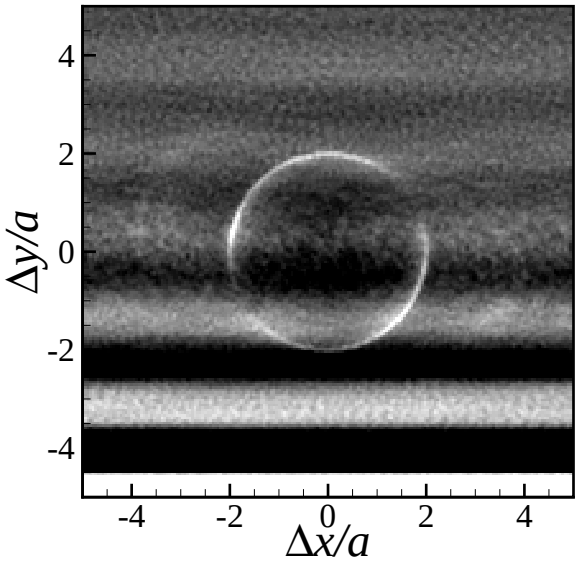

(a)

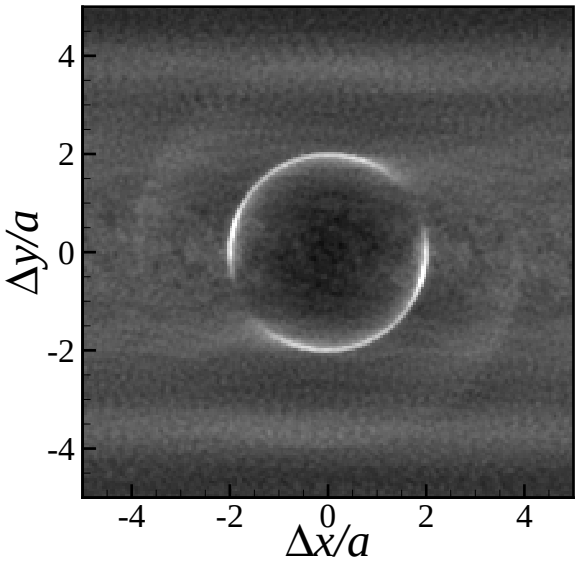

(b)

Figure 3.4: The pair-distribution functions for C4La projected onto $x-y$ plane for particles in (a) $5.5 < y/a < 6.5$ and (b) $8 < y/a < 12$. Light contours represent high probability.

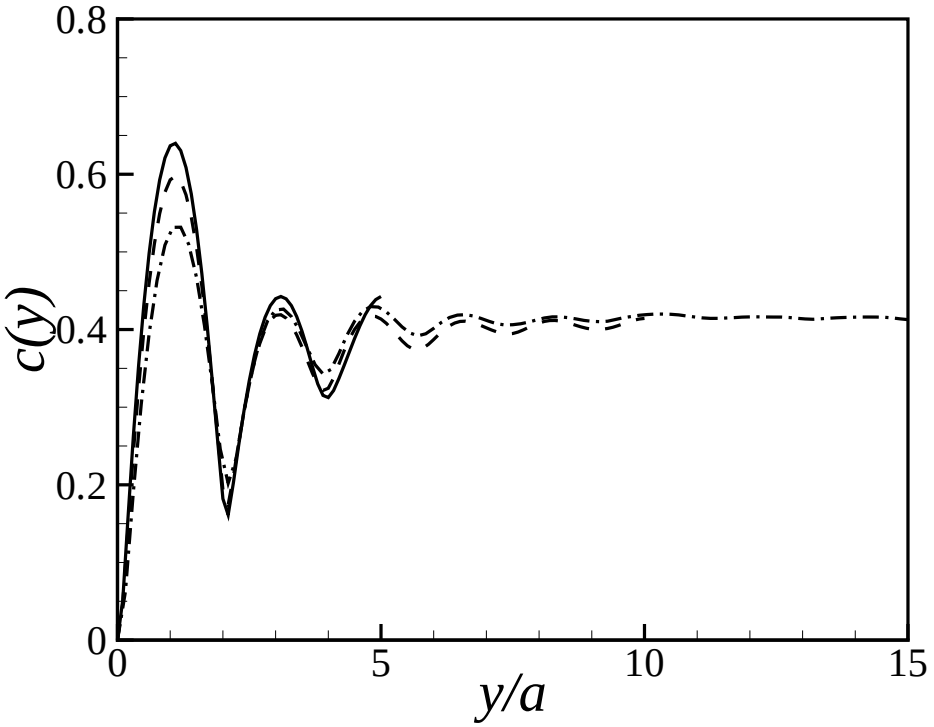

Figure 3.5: Concentration profiles for C4S (solid), C4La (dashed), and C4H (dash-dot).

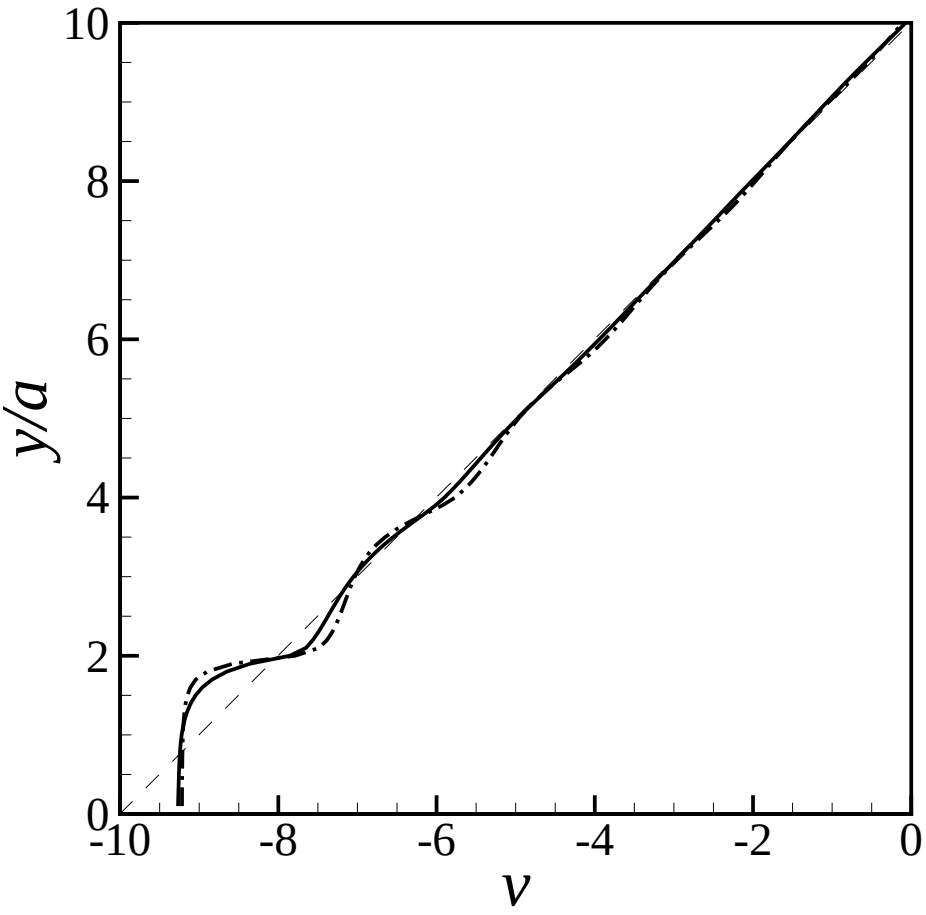

Figure 3.6: Average particle velocities for C3L (solid) and C4La (dash-dot). The dashed line is the linear velocity profile of Couette flow without suspensions.

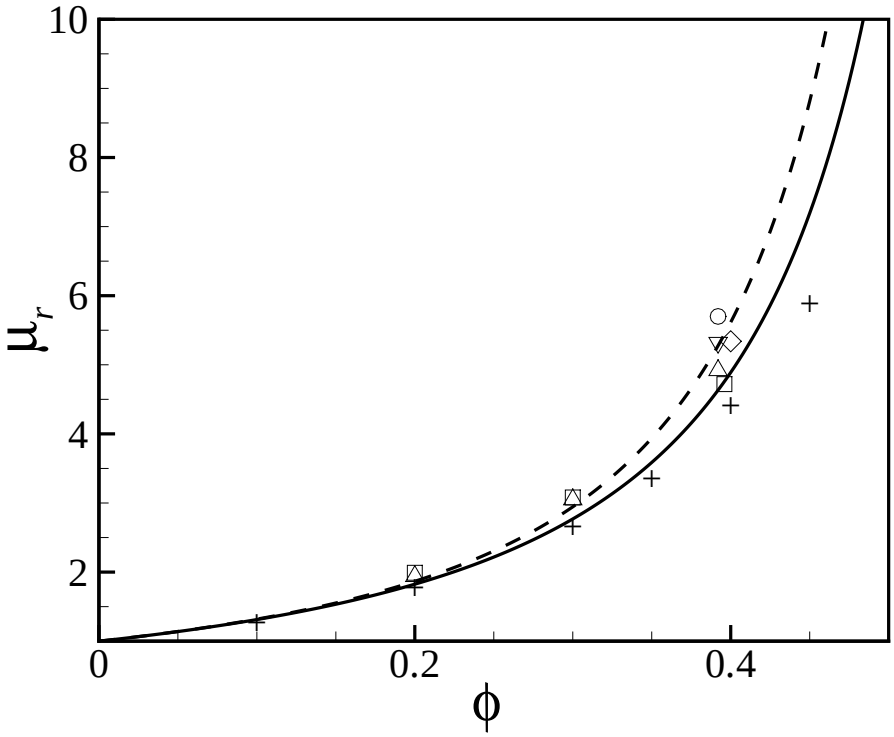

Figure 3.7: Relative viscosity μ_r: solid line, [115]; dashed line, Eilers fit; □, C2S, C3S, and C4S; △, C2L, C3L, and C4La; ▽, C4Lb; ○, C4Lc; ◇, C4H; +, [233].

obtained from

$$\langle \boldsymbol{v}(x_2) \rangle = \frac{\langle c\boldsymbol{v}(x_2) \rangle}{\langle c(x_2) \rangle}. \tag{3.4}$$

The particle-phase velocity profiles for C3L and C4La are shown in figure 3.6. Consistent with the previous results of Singh & Nott [199] and Kromkamp *et al.* [116], the particle-phase velocity profile is almost linear in the core region ($5 < y/a < 15$). Near the wall ($y/a < 0.7$), the particle-phase velocity is faster than the linear profile, which is responsible for the apparent wall slip observed experimentally in concentrated suspension flows [99].

3.2.3 Relative viscosity

The particle contribution to the bulk stresses is given by

$$\langle \sigma_{ij}^P \rangle = \frac{N_s}{Q^D} \left(\langle S_{ij} \rangle + \langle S_{ij}^e \rangle \right), \tag{3.5}$$

in which Q_D is the volume of the sampling domain over which the contribution is summed and N_s is the number of particles in the sampling domain. The hydrodynamic S_{ij} and contact-force contributions S^e_{ij} to the total stresses are calculated by

$$\langle S_{ij} \rangle = \frac{1}{N_s} \sum_{n=1}^{N_s} S^n_{ij}, \tag{3.6}$$

$$\langle S^e_{ij} \rangle = \frac{1}{N_s} \sum_{n=1}^{N_s} \sum_{k=n+1}^{N_s} -\frac{1}{2}(r^{nk}_i F^{nk}_{P,j} + r^{nk}_j F^{nk}_{P,i}). \tag{3.7}$$

The relative viscosity of the suspension μ_r in a linear shear flow is

$$\mu_r = 1 + \frac{1}{\mu\dot{\gamma}} \langle \sigma^P_{12} \rangle. \tag{3.8}$$

In figure 3.7, μ_r for $Q_D = |\Omega^D|$ is compared with two viscosity models,

1. [115],

$$\mu_r = \left(1 - \frac{\phi}{\phi_m}\right)^{-[\eta]\phi_m}, \tag{3.9}$$

2. Eilers fit [203],

$$\mu_r = \left(1 + \frac{\frac{1}{2}[\eta]\phi}{1 - \phi/\phi_m}\right)^2, \tag{3.10}$$

in which ϕ_m is the maximum packing fraction and $[\eta]$ is a fitting parameter. Stockel & Powell [203] showed that the relevant experimental data are well represented by Eilers' fit with $[\eta] = 2.5$ and $\phi_m = 0.65$. The high-frequency dynamic viscosity, μ_∞, in Yeo & Maxey [233] is obtained by the ensemble average of 1000 random configurations at each ϕ. It is shown that μ_r in the present simulation is in the range of previous empirical results. As micro-structures form in sheared suspensions, μ_r is typically larger than μ_∞. The difference between μ_r and μ_∞, called the excess viscosity $\Delta\mu = \mu_r - \mu_\infty$, is positive and an increasing function of ϕ [197].

Of particular note, Zarraga *et al.* [241] found in their parallel plate experiments for $\phi = 0.45$ that μ_r is an increasing function of H_y/a when $H_y/a < 40$ and then reaches a plateau if $H_y/a > 40$. It was suggested that the wall slip is a major mechanism responsible for the

Table 3.2: The deviatoric stress $\langle \sigma_{12}^P \rangle$ estimated in the core region Ω^C and the wall region Ω^W.

	Ω^C	Ω^W
C4La	4.18	3.65
C4H	4.58	3.86
[197]	4.49 ± 0.037	

decrease in the relative viscosity [5, 241]. It appears instead that the H_y/a dependency of μ_r is largely due to the organized micro-structure in the near-wall region (particle layering). In homogeneous concentrated suspensions, the dominant contribution to the relative viscosity comes from the normal lubrication interactions between particles, which is proportional to $\sim 1/\epsilon$ for a gap width $a\epsilon$ [73]. On the other hand, the lubrication interactions between two particle layers is mainly through tangential motions between particles in each layers for which the singularity is $\sim \log \epsilon$. Hence, if the particle layering is dominant, the viscosity may be smaller than that in a corresponding homogeneous suspension.

These observations may be compared with the simulation results for μ_r at different ϕ and H_y/a shown in figure 3.7. Since the particle layering is weak at low volume fractions, μ_r is less sensitive to H_y/a when $\phi \leq 0.3$. On the other hand, μ_r is a non-decreasing function of H_y/a at $\phi = 0.4$.

The comparison may be refined by dividing the channel into zones and evaluating the average particle stresses in each zone as opposed to the whole domain Ω^D of the channel. Table 3.2 shows the deviatoric particle stress estimated from the particles in the core region Ω^C and wall region Ω^W. Ω^C and Ω^W are chosen as

$$\Omega^W = (0, H_x) \times \{(0, H_w) \cup (H_y - H_w, H_y)\} \times (0, H_z), \tag{3.11}$$

$$\Omega^C = \Omega^D \setminus \Omega^W, \tag{3.12}$$

in which H_w is the width of the wall region. Here, $H_w = 5a$ is used at $\phi = 0.4$. For the comparison, the result for a homogeneous suspension from Sierou & Brady [197] is included. It may be seen that σ_{12}^P in Ω^C is close to the results obtained in an unbounded domain, and further that σ_{12}^P in Ω^C is consistently larger than that in Ω^W. The ratios of the deviatoric stress in Ω^C to that in Ω^W are about 1.15 and 1.19 for C4La and C4H, respectively.

Table 3.3: The relative viscosity for different R_{ref} at $\phi = 0.4$.

	R_{ref}	F_{ref}	ϵ_{min}	μ_r
C4La	2.01	100	3×10^{-3}	4.92
C4Lb	2.004	100	1×10^{-3}	5.31
C4Lc	2.001	1000	5×10^{-4}	5.70

Typically, μ_r obtained in the numerical simulations is somewhat lower than the experimental results. Sierou & Brady [197] argued that the discrepancy may come from the uncertainty in the contact force model. To show the effects of the contact force on rheological parameters, the relative viscosity μ_r at $\phi = 0.4$ is computed for three different values of R_{ref}; $R_{ref} = 2.01$ (C4La), 2.004 (C4Lb), and 2.001 (C4Lc). Together with the values of μ_r, the minimum separation distances ϵ_{min} in each case are shown in table 3.3. It is apparent that μ_r is dependent on the choice of the contact force. Since the major contribution to μ_r from the viscous lubrication interaction is proportional to $1/\epsilon$, μ_r increases as the minimum separation decreases. Comparing C4Lc and C4La, there is about 16% difference in μ_r.

3.2.4 Normal stresses

In sheared suspensions of non-colloidal particles, the irreversible effects originating from any non-hydrodynamic forces will result in an anisotropic micro-structure, which in turn lead to the development of the non-Newtonian stresses. Among these, the normal stresses in suspensions are of interest because of their importance in the prediction of the particle migration in inhomogeneous flows [160, 155, 164].

The first (N_1) and second (N_2) normal stress differences are defined as

$$N_1 = \sigma^P_{11} - \sigma^P_{22}, \tag{3.13}$$

$$N_2 = \sigma^P_{22} - \sigma^P_{33}. \tag{3.14}$$

Zarraga *et al.* [241] measured linear combinations of the normal stresses in suspensions of non-colloidal particles. They showed that, in Couette flow, both N_1 and N_2 are negative and $|N_2| > |N_1|$ for $\phi = 0.3 - 0.5$. Brady & Morris [25] showed theoretically that all three normal stress components should be compressive in a uniform shear flow. Using SD simulation, Sierou & Brady [197] calculated the normal stress differences for a wide range of ϕ ($0.1 \leq \phi \leq 0.5$) for a uniform shear flow. Their results show qualitatively consistent

behaviour with the experimental results in Zarraga *et al.* [241]. However, it was observed that $|N_2| \simeq |N_1|$ in contrast to the experimental fit $|N_2| \simeq 3.6|N_1|$ found by Zarraga *et al.* [241]. Origin of this difference between the numerical simulations and experiments is not clear. Possible influences include the effects of the particle-particle contact force or the shear-induced migration of particles in the circular Couette flow device, which introduces curvilinear flow effects, as opposed to the simple homogeneous shear of the SD simulations. Additionally, there is the influence of the walls and the layered structures in the experiments.

Figure 3.8 shows the normal stress differences from the present simulations normalized by the shear stress $\tau = \mu_r \mu \dot{\gamma}$. For comparison, the previous numerical results from SD simulations [197] are also presented. Since there is an appreciable wall effect even in the larger channels for the present simulations, a quantitative match with the previous SD simulations in an unbounded domain is not expected. Nevertheless, N_1 and N_2 in the larger domains ($H_y/a = 20,\ 30$) correspond well with the SD results. At $\phi = 0.4$, reducing R_{ref}, the differences in N_1 and N_2 between the present simulations and Sierou & Brady [197] decrease.

The second normal stress difference (N_2) calculated in the small channel ($H_y/a = 10$) shows a similar trend with the results in the larger domain but is larger in magnitude. On the other hand, there is a significant difference in N_1. Other SD simulations of unbounded sheared suspensions of non-colloidal particles have shown that the normal stresses are all negative and that $|\sigma^P_{11}| > |\sigma^P_{22}| > |\sigma^P_{33}|$ [240]. However, in the small channel (C4S), it is found that $|\sigma^P_{11}| \approx |\sigma^P_{22}| > |\sigma^P_{33}|$ with all negative values. It seems that the large N_2/N_1 in C4S is related with the particle layering, which spans the whole channel.

The ratio of the normal stress differences, N_2/N_1, estimated in the present simulations are shown in figure 3.9 along with the SD data of Sierou & Brady [197]. It is shown that $N_2/N_1 > 1$ for all the simulations while, from SD, $N_2/N_1 < 1$. Since the normal stress is sensitive to the micro-structure, the particle layers may be responsible for the difference. For example, in C4S where the wall effect is the strongest, $N_1 \simeq 0$. To identify the effects of the walls, N_2/N_1 in the core Ω^C and the wall Ω^W regions are shown in figure 3.9 (b), where $H_w = 2a$ and $3a$ are used for $\phi = 0.2$ and 0.3, respectively, in (3.11). N_2/N_1 in Ω^C quantitatively agrees well with Sierou & Brady [197]. On the other hand, N_2/N_1 estimated in Ω^W is larger than 3. In C2L, C3L, and C4La, $1 < N_2^{\Omega^W}/N_2^{\Omega^C} < 1.6$ while $0.2 < N_1^{\Omega^W}/N_1^{\Omega^C} < 0.3$. This results suggest that the normal stresses measured in the

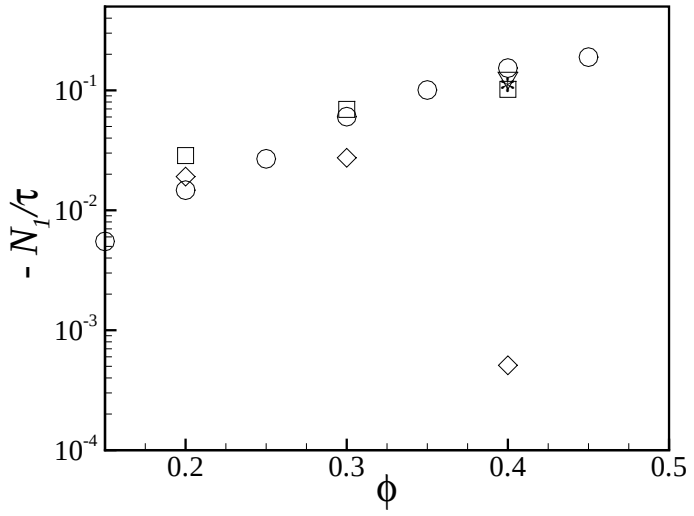

(a)

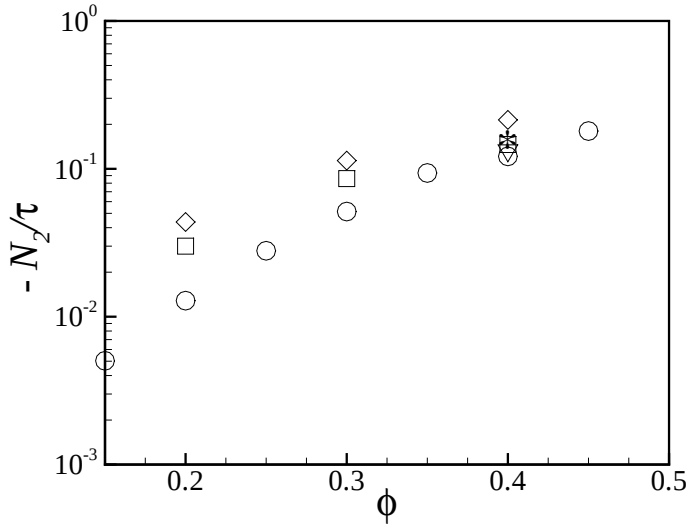

(b)

Figure 3.8: Normalized normal stress differences (a) $-N_1/\tau$ and (b) $-N_2/\tau$. ◊, C2S, C3S and C4S; □, C2L, C3L and C4La; ▽, C4Lc; ∗, C4H; ○, [197].

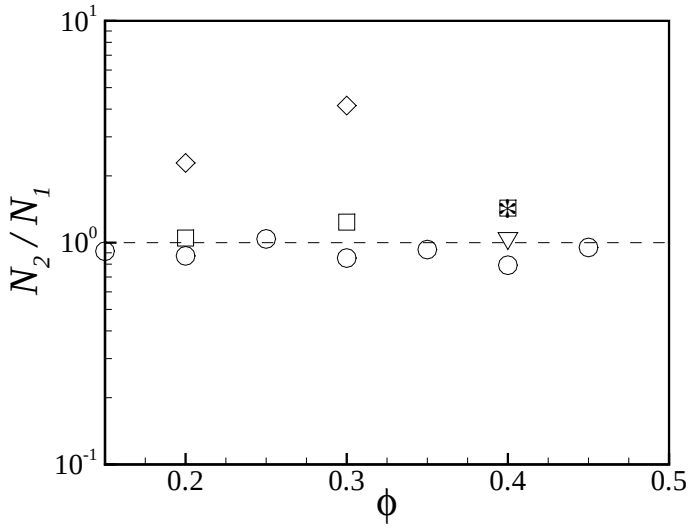

(a)

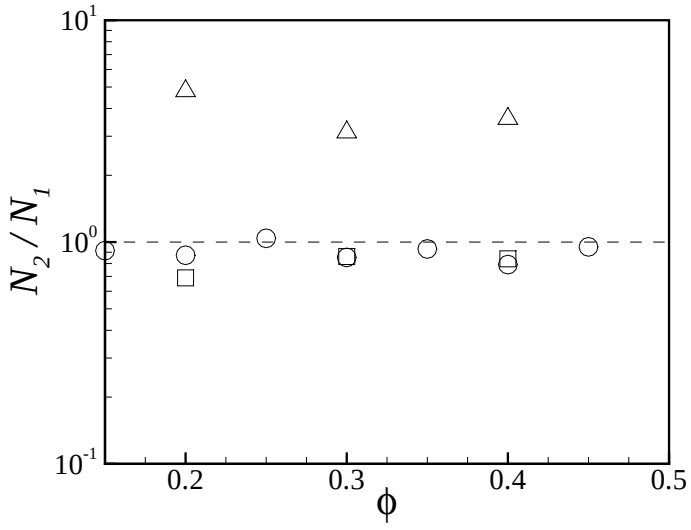

(b)

Figure 3.9: (a) Ratio of N_2 to N_1 in Ω^D; ◊, C2S, C3S and C4S; □, C2L, C3L and C4La; ▽, C4Lc; ∗, C4H. (b) Ratio of N_2 to N_1 in Ω^C (□) and Ω^W (△) for C2L, C3L and C4La. ◦ denotes [197].

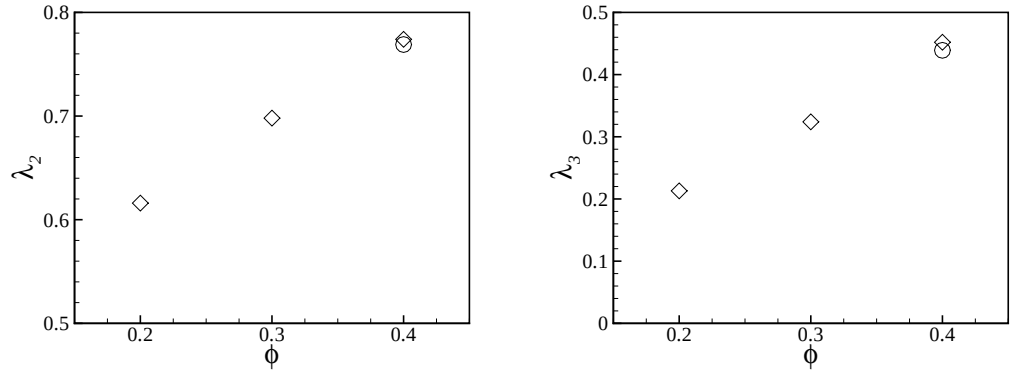

(a) (b)

Figure 3.10: Anisotropy parameters (a) λ_2 and (b) λ_3. $\Diamond$, C2L, C3L and C4La; $\circ$, C4H.

wall bounded domain will be different from those obtained the numerical simulation in the unbounded flows. If H_y/a is large enough such that $|\Omega^C|/|\Omega^W| >> 1$, it is expected that the rheological properties would be similar to those observed in an unbounded domain. However, in figure 3.9 (a), it is observed that the difference between C4La and C4H is negligible, in which $|\Omega^C|/|\Omega^W| = 1$ and 2 for C4La and C4H, respectively. It seems that, in the largest channel used in the present simulation ($H_y/a = 30$), the presence of the wall has a significant effect on the suspension rheologies. As a result, it is not straightforward how to extrapolate the rheological properties for large $|\Omega^C|/|\Omega^W|$ from the present simulation results.

3.2.5 Normal stresses and continuum models

While numerical simulations based on the individual particle motion provide invaluable insight into the detailed dynamics, most of the simulation techniques are computationally too intensive to apply for engineering problems with complex geometries. To predict the behaviour of the suspensions in such a flow condition, there have been several attempts to develop a continuum model [126, 160, 155, 164, 227]. One of the successful approaches is proposed by Morris & Boulay [160], in which the constitutive law for the particle stress for shear flows is given by

$$\boldsymbol{\sigma}^P = -\mu\mu_n(\phi)\dot{\gamma}\boldsymbol{Q} + 2\mu\mu_r(\phi)\boldsymbol{e}. \tag{3.15}$$

In this formulation, μ_n is the normal stress viscosity defined as

$$\mu_n(\phi) = K_n \left(\frac{\phi/\phi_m}{1 - \phi/\phi_m} \right)^2, \tag{3.16}$$

where K_n is a rheological fitting parameter. The material property tensor $\boldsymbol{Q}$ is

$$\boldsymbol{Q} = \begin{bmatrix} 1 & 0 & 0 \\ 0 & \lambda_2 & 0 \\ 0 & 0 & \lambda_3 \end{bmatrix}, \tag{3.17}$$

in which the anisotropy parameters are $\lambda_2 = \sigma^P_{22}/\sigma^P_{11}$ and $\lambda_3 = \sigma^P_{33}/\sigma^P_{11}$.

Morris & Boulay [160] suggested that $\lambda_2 \approx 0.8$ and $\lambda_3 \approx 0.5$ provide a good approximation to the suspension rheology and migration. Figure 3.10 shows the anisotropy parameters λ_2 and λ_3 as a function of ϕ. It is shown that both λ_2 and λ_3 approach the suggested value at high ϕ. In the experiments by Zarraga *et al.* [241], a measure of the anisotropy $(N_2 - N_1)/\sigma_{33}$ is an increasing function of ϕ for $\phi < 0.4$ and then reaches a plateau. Hence, there is a possibility that both λ_2 and λ_3 become constants at higher ϕ.

The values of μ_n calculated from FCM and equation (3.16) are shown in figure 3.11. $K_n = 0.75$ and the maximum packing $\phi_m = 0.63$ are used. The qualitative agreement of the model equation with the FCM results are satisfactory.

3.2.6 Micro-structure

Here, we investigate further the details of the micro-structure using the pair distribution function $g(r, \theta, \psi)$ for C4La. Here, θ denotes the azimuthal angle measured from the flow direction (positive x) and ψ is the polar angle about the x-axis, measured from the vorticity direction (positive z). Since most contributions to the rheological properties come from the particles near contact, the pair distribution function is shown only for $2 < r/a < 2.1$.

Figure 3.12 shows the pair-distribution function $g(\theta)$ in the $x - y$ plane, the plane of shear, obtained by averaging over $\pi/2 - \delta < \psi < \pi/2 + \delta$, in which $\delta = \pi/60$, and over the reference particles whose centers are located in the core region. Considering the mirror symmetry, only $0 < \theta < \pi$ is shown. It is shown that the probability to encounter another particle around the compressive axis is much higher than that in the extensive axis, which is consistent with $g(\Delta x, \Delta y)$ (figure 3.4 b). The asymmetry, which is responsible for the

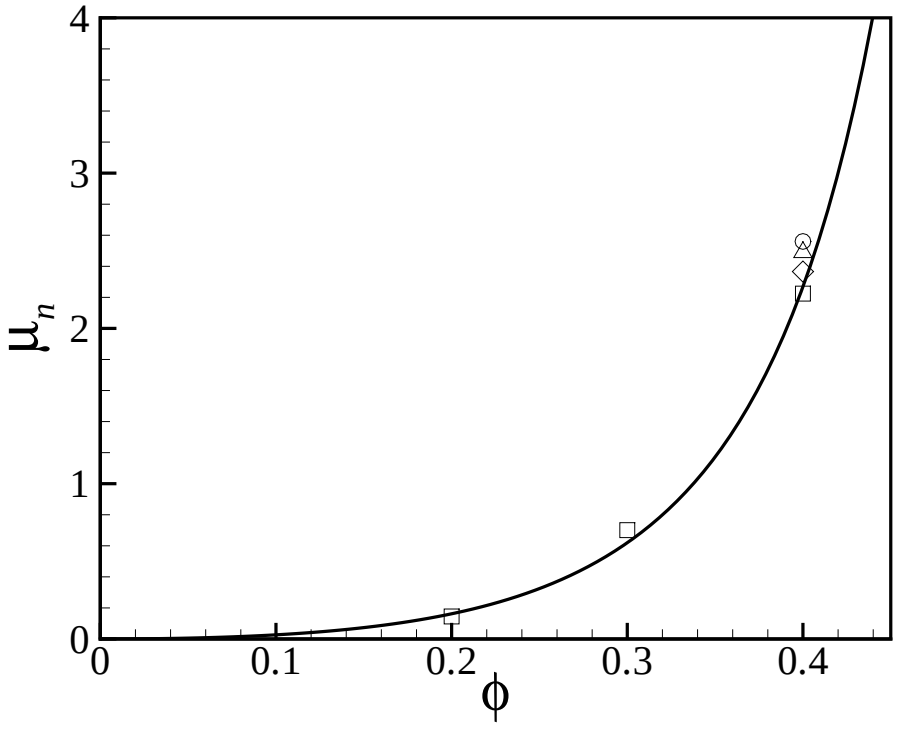

Figure 3.11: The normal stress viscosity in terms of ϕ. □, C2L, C3L and C4La; ◊, C4Lb; △, C4Lc; ○, C4H; —— [160].

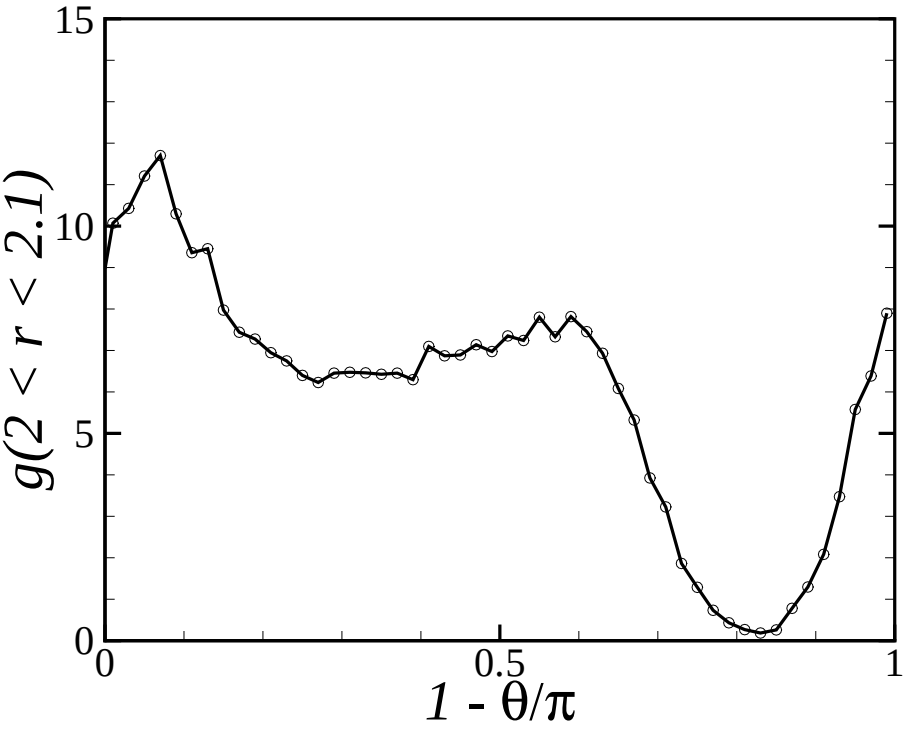

Figure 3.12: The pair distribution function for particles of which center is located in $5 \leq y/a \leq 15$.

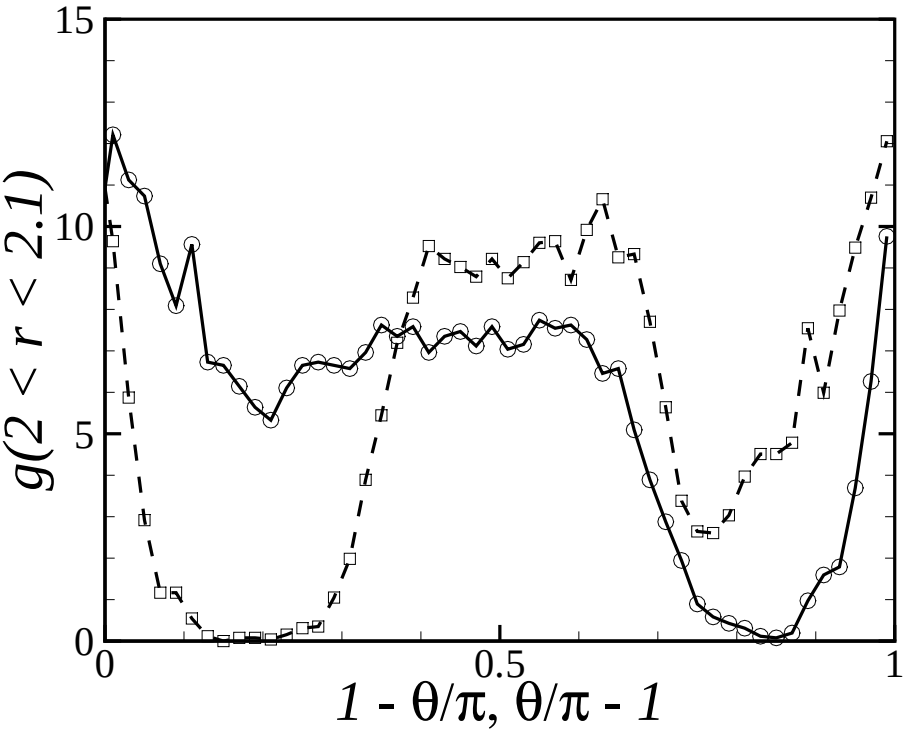

Figure 3.13: The pair distribution function for particles of which center is located in $2 \leq y/a \leq 5$. Solid line, $1 - \theta/\pi$; dashed line, $\theta/\pi - 1$.

non-Newtonian behaviour, has been observed both in experiments [169] and in numerical simulations [119, 197].

The corresponding pair-distribution function $g(\theta)$ for the reference particles centered in $2 < y/a < 5$ is shown in figure 3.13. Because the particles are in a buffer region between the strongly structured particle layer around $y/a \simeq 1$ and the free shear region (core region), the pair-distribution function is no longer mirror-symmetric. In other words, $g(\theta)$ in the upper hemisphere $0 < \theta/\pi < 1$ is different from the lower hemisphere $1 < \theta/\pi < 2$. It is observed that $g(\theta)$ in the upper hemisphere resembles that in the core region qualitatively. However, $g(\theta)$ in the lower hemisphere is distinguished by the increased probability near $\theta/\pi \simeq 3/2$, which comes from the interaction with the particle layer below.

Figure 3.14 shows $g(\theta)$ for the reference particles close to the wall, $1 \leq y/a \leq 2$. Distinctive peaks are observed near $\theta/\pi \simeq 0$ and 1, indicating that it is much more probable for a particle near the wall to experience the lubrication interaction with another particle in the same particle layer than particles in another region. A plateau is observed near

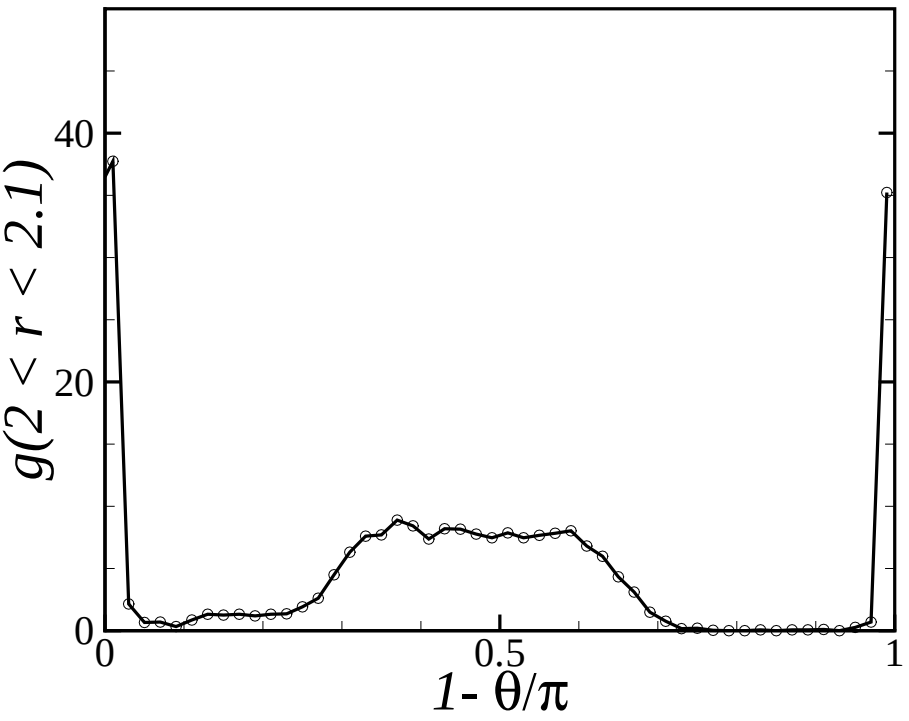

Figure 3.14: The pair distribution function for particles of which center is located in $1 \leq y/a \leq 2$.

$\theta/\pi = 0.5$ due to the interaction with the second particle layer. The location of this plateau is consistent with $g(\theta)$ for the lower hemisphere shown in figure 3.13 for particles centered further away from the wall. Although $g(\theta)$ is not symmetric, the asymmetry is much weaker compared to the core region (figure 3.12), which is responsible for the small $|N_1|$ in the wall region (figure 3.8, 3.9).

3.3 Effects of confinement on the mobility of the particles

The interaction between three or more particles in Stokes flow is chaotic [100] and, thus, even small non-hydrodynamic effects, which come from, for example, surface roughness or short-range interparticle forces, make the system unpredictable and irreversible [58, 172]. As a result, non-colloidal particles in sheared suspensions, where the dynamics is determined mainly by hydrodynamic interactions, exhibit a diffusive behavior similar to colloidal suspensions, where Brownian motion is the driving mechanism [64, 126, 26]. Due to a substantial number of studies over the past decade (see [203, 159] for review), now our knowledge on the shear-induced diffusion process of concentrated non-colloidal suspensions in an open domain, *i.e.* far from a solid boundary, is much more advanced. However, much less is known about the diffusion process in wall-bounded suspensions.

Most studies of the diffusion processes in confined suspensions have been focused on hard-sphere fluids or colloidal suspensions in thermodynamic equilibrium, *i.e.* in the absence of flow. Mittal *et al.* [156] calculated the position-dependent diffusivity of confined hard-sphere fluids using discontinuous molecular dynamics simulations. Michailidou *et al.* [153] have studied the short-time self-diffusion of colloidal suspensions near the wall from both experimental and numerical results. Nugent *et al.* [165] and Sarangapani & Zhu [188] studied the diffusion of colloidal suspensions bounded by two parallel walls for a wide range of the gap width between two walls to investigate the dynamic lengthscale of structural reorganization. Eral *et al.* [66] investigated the effects of smooth and rough walls on the diffusion of concentrated colloidal suspensions. They showed that even in the center of the channel, the particles exhibit subdiffusive behavior. In flowing suspensions, Zurita-Gotor *et al.* [244] estimated the local self-diffusivity in the dilute limit from binary particle interactions. Asmolov [7] has computed the diffusion of non-colloidal particles in dilute wall-bounded suspensions (volume fraction $\phi \leq 0.02$) under a steady shear using a constant

dipole model. Still, there is only a limited number of studies on the shear-induced diffusion in wall-bounded concentrated suspensions.

In this section, we study the confinement effects on suspension dynamics focusing on the crossflow diffusion of the particles as a function of the distance from the wall on the intermediate timescale $t^* \sim O(100)$, in which t^* is the time normalized by the shear rate $\dot{\gamma}$, $t^* = \dot{\gamma}t$. The main results are presented for concentrated suspensions in a wall-bounded Couette flow, where the bulk volume fraction is $\phi = 0.40$. The channel is divided into four zones, considering the suspension microstructure [230], and the behavior of particles in each zone is investigated. Particularly, we are interested in the variance of particle displacement, which is a measure of the spreading of the suspended particles relative to the mean position. It is found that the variance of the wall-normal displacement shows anomalous diffusive behavior, $\sigma_y^2 \sim t^\nu$, in which $\nu \neq 1$. Depending on the initial location, particles exhibit super- ($\nu > 1$) or subdiffusion ($\nu < 1$) in the velocity-gradient (wall-normal) direction. Anomalous diffusion has been observed in transport processes in porous media [60] or passive tracer dispersion in flows with coherent structures [167, 201, 239]. In this study, we report on anomalous diffusion induced not by a coherent structure in flow but by complex multibody hydrodynamic interactions. The anomalous diffusion near the wall is linked to strong intermittency of particle motion. Unexpectedly, even particles in the core of the channel show a subdiffusive behavior, which may be related with the restriction on the available lengthscale by the confinement. The diffusive behaviors of particles in the core of the channel for four different volume fractions ($\phi = 0.25$, 0.30, 0.35, and 0.40) are compared.

The computational domain size is $H_x \times H_y \times H_z = 30a \times 30a \times 20a$, in which a is the particle radius and x, y, and z denote the velocity (streamwise), velocity-gradient (wall-normal), and vorticity (spanwise) directions, respectively. The periodic boundary conditions are used in the horizontal ($x - z$) directions. The no-slip boundary condition is used on the wall. Unless otherwise stated, all results are obtained at the volume fraction $\phi = 0.4$ with 1718 neutrally-buoyant spheres. The smooth repulsive potential is applied for particle pairs whose center-to-center distance is smaller than $2.01a$. The magnitude of the near-contact force is determined to keep the minimum separation distance between particle surfaces $a\epsilon_{min} \simeq 0.002$.

Figure 3.15 (a) shows the area fraction ϕ_A as a function of the distance from the wall.

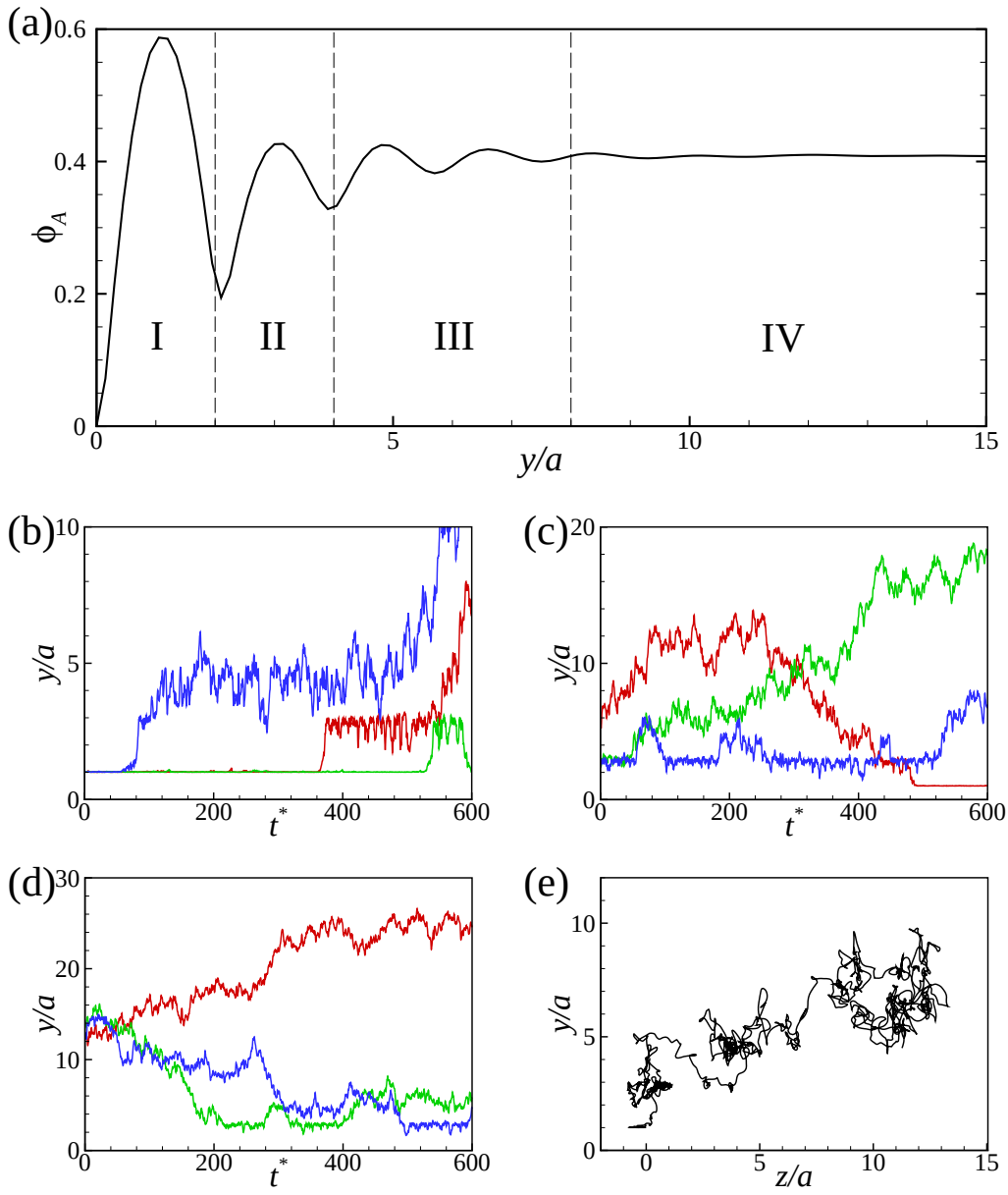

Figure 3.15: (a) Area fraction profile for the bulk volume fraction $\phi = 0.4$. Considering the symmetry, ϕ_A is shown only for the lower half of the channel. The wall-normal displacements as a function of time are shown for particles which are initially in (b) Zone I, (c) Zone II + III, and (d) Zone IV. (e) shows a representative trajectory in $y - z$ plane for a particle whose initial location is in Zone I.

$\phi_A(y)$ is defined by $\phi_A(y) = \iint \chi(\boldsymbol{x})dxdz/(H_x \times H_z)$, where $\chi(\boldsymbol{x})$ is a particle-phase indicator function. A significant fluctuation of ϕ_A is observed near the wall. Due to the strong particle-wall lubrication interaction, a well structured particle layer develops near the wall (Zone I). Above the particle layer, there is a region in which the behavior of the suspension flow is still strongly affected by the wall (Zone II). In the core region (Zone IV), the rheology of suspension flow behaves similarly to a homogeneous shear flow. There is a buffer region (Zone III) between the discrete (Zone I + II) and the continuous (Zone IV) regimes. Detailed analysis of the rheology and suspension microstructure in each zone is given in 3.2.

Figure 3.15 (b–d) illustrate the trajectories of particles whose initial locations are in (b) Zone I, (c) Zone II + III, and (d) Zone IV. Most particles in Zone I stay in the first particle layer for a long period of time $t^* \simeq O(100)$ before moving to Zone II. In Zone II, the particles are again trapped in the second particle layer ($y/a \simeq 3$). The existence of another particle layer is observed around $y/a \simeq 5$, in which the wall-normal displacement is largely restricted to $4 < y/a < 6$ for a long period of time. In figure 3.15 (c), it is shown that some particles in Zone II move toward the core of the channel while some particles are trapped in the second or third particle layers exhibiting oscillatory motions around $y/a \simeq 3$ or 5. In contrast, the particles in Zone IV exhibit more standard diffusive behavior (figure 3.15 d). However, some of the particles in Zone IV migrate towards the wall relatively quickly ($t^* \simeq 200$) and they are trapped in the particle layers. Figure 3.15 (e) shows a representative trajectory of a particle initially located in Zone I plotted in $y-z$ plane. The wall-normal displacement of the particles in the particle layers ($y/a < 7$) is strongly suppressed by cages formed by the surrounding particles, while the particles are more mobile in the horizontal direction (z). A similar behavior has been observed for confined hard sphere fluids in equilibrium, where the diffusivity in the horizontal direction is larger than that in the wall-normal direction [156]. Near the wall, the travel time of a particle between each particle layers is much shorter than the residence time inside of the particle layers. The particle trajectories suggest that there is a strong spatial coherence induced by the wall in concentrated suspensions. Moving from the first particle layer (Zone I) to the second (Zone II) and the third particle layers (Zone III), the residence time of a particle in each particle layer decreases and, at the same time, the wall-normal fluctuation around the center of a particle layer becomes stronger.

The variance of each component of the particle displacement is defined as $\sigma_i^2(t) =$

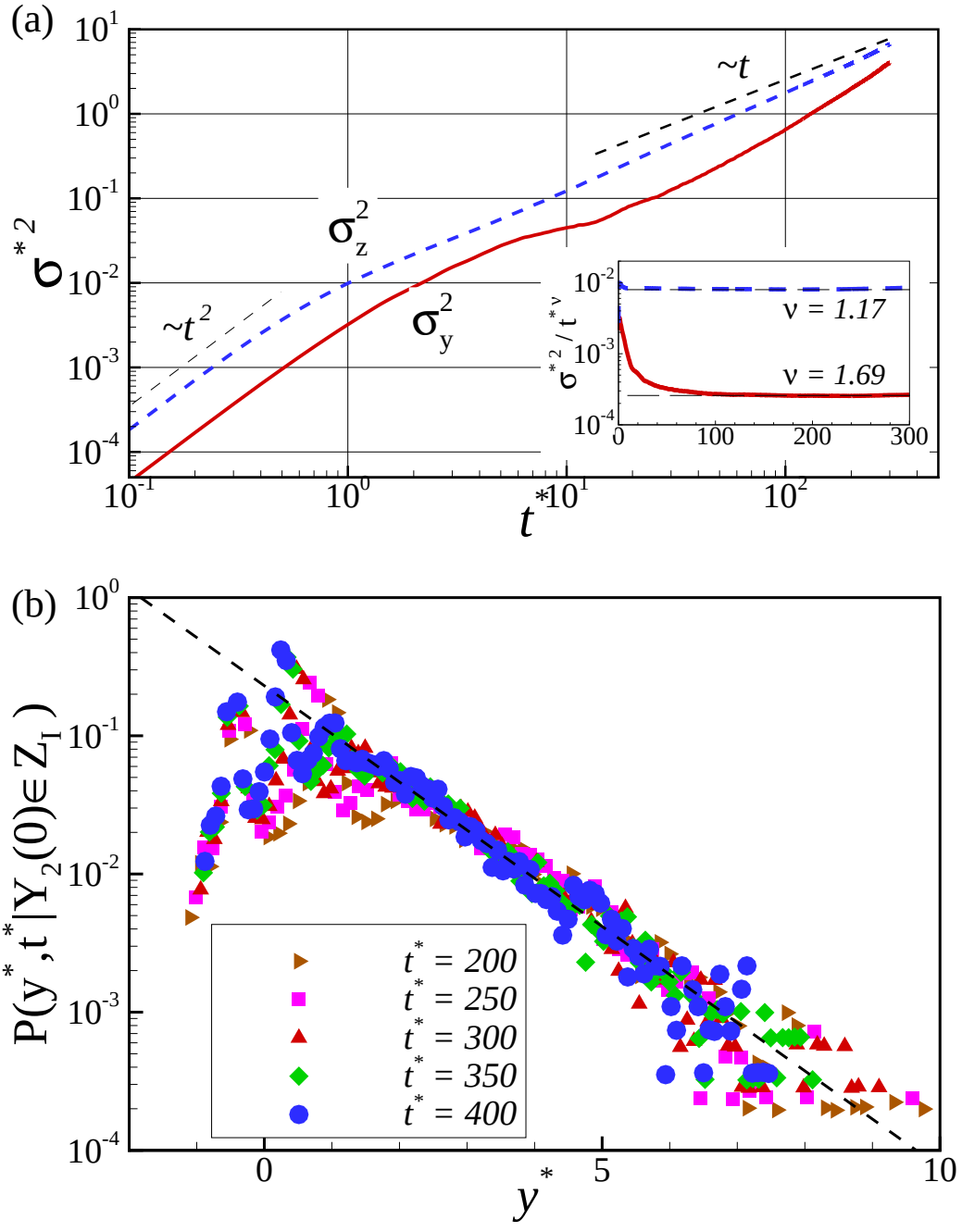

Figure 3.16: (a) Variances of the wall-normal and spanwise displacements of the particles in Zone I at $t^* = 0$. The inset shows the variances divided by t^{ν}. (b) The probability density functions (PDF) of the standardized wall-normal displacements at different time instances. The dashed line is $\sim \exp(-0.8y^*)$.

$\langle \tilde{Y}_i^2(t) \rangle - \langle \tilde{Y}_i(t) \rangle^2$, in which $\boldsymbol{Y}(t)$ is the location of a particle at time t and $\tilde{\boldsymbol{Y}}(t) = \boldsymbol{Y}(t) - \boldsymbol{Y}(0)$. Figure 3.16 (a) shows the normalized variance ($\sigma^{*2} = \sigma^2/a^2$) for the particles in Zone I at $t^* = 0$. σ^2 in both y and z directions show a ballistic behavior $\sim t^2$ for short time intervals while the particle velocity remains strongly correlated. For $t^* \sim O(100)$, both σ_y^2 and σ_z^2 grow faster than $\sim t$, indicating superdiffusion. In the inset of figure 3.16 (a), it is clearly seen that $\sigma_y^2 \sim t^{1.69}$ and $\sigma_z^2 \sim t^{1.17}$. In homogeneous suspensions, the variances are highly anisotropic and $\sigma_y^2(t)/\sigma_z^2(t) > 1$ [58]. However, in Zone I, σ_y^2 is much smaller than σ_z^2.

Figure 3.16 (b) shows the probability density functions (PDF) for the normalized wall-normal displacement. The PDFs are computed for the particles in Zone I at $t^* = 0$. Here, the normalized wall-normal displacement is defined as $y^* = (\tilde{Y}_2(t) - \langle \tilde{Y}_2(t) \rangle)/\sigma_y(t)$. The normalized PDFs show a remarkable self-similarity. The positive tails of the PDFs almost collapse onto one curve after the superdiffusion is observed ($t^* > 200$). The tail of the PDF shows an exponential decay $\sim \exp(-\alpha y^*)$ with $\alpha = 0.8$ (inset of figure 3.16 b). As a measure of the intermittency, we computed the flatness factor, which is the fourth moment of the normalized PDF. The flatness factor of the PDF is about 18, compared to 3 of a Gaussian distribution, indicating that there is a large fraction of the particles, which travel in a much faster rate compared to the mean spreading rate. The intermittent events, jumps to Zone II and III shown in figure 3.15 (b, e), seem to be responsible for the slow decay of the PDF.

Figure 3.17 shows the changes of the PDF of the wall-normal particle velocity (V_2) in time for the particles initially located in Zone I. The particle velocity is normalized as $V_2^* = (V_2(t) - \langle V_2(t) \rangle)/\sigma_V(t)$, in which σ_V is the standard deviation of V_2. The third moments of the normalized PDFs in figure 3.17 (a) are about 0.1, suggesting that the wall-normal velocity PDFs $P(V_2^*)$ are nearly symmetric. Similar to the wall-normal displacement PDF, $P(V_2^*)$ has a much wider tail compared to the Gaussian distribution. The flatness factor of $P(V_2^*)$ is a decreasing function of time. The flatness factors are 18, 13, and 10 at $t^* = 200$, 300, and 400, respectively. This decrease of the flatness factor in time is related with the reduced frequency of the intermittent events, as the particles migrate into Zone III and IV.

To investigate the changes of $P(V_2^*)$ in time in more detail, the positive tail of $P(V_2^*)$ is shown in a log-log plot in figure 3.17 (b). Interestingly, $P(V_2^*)$ consists of three distinctive

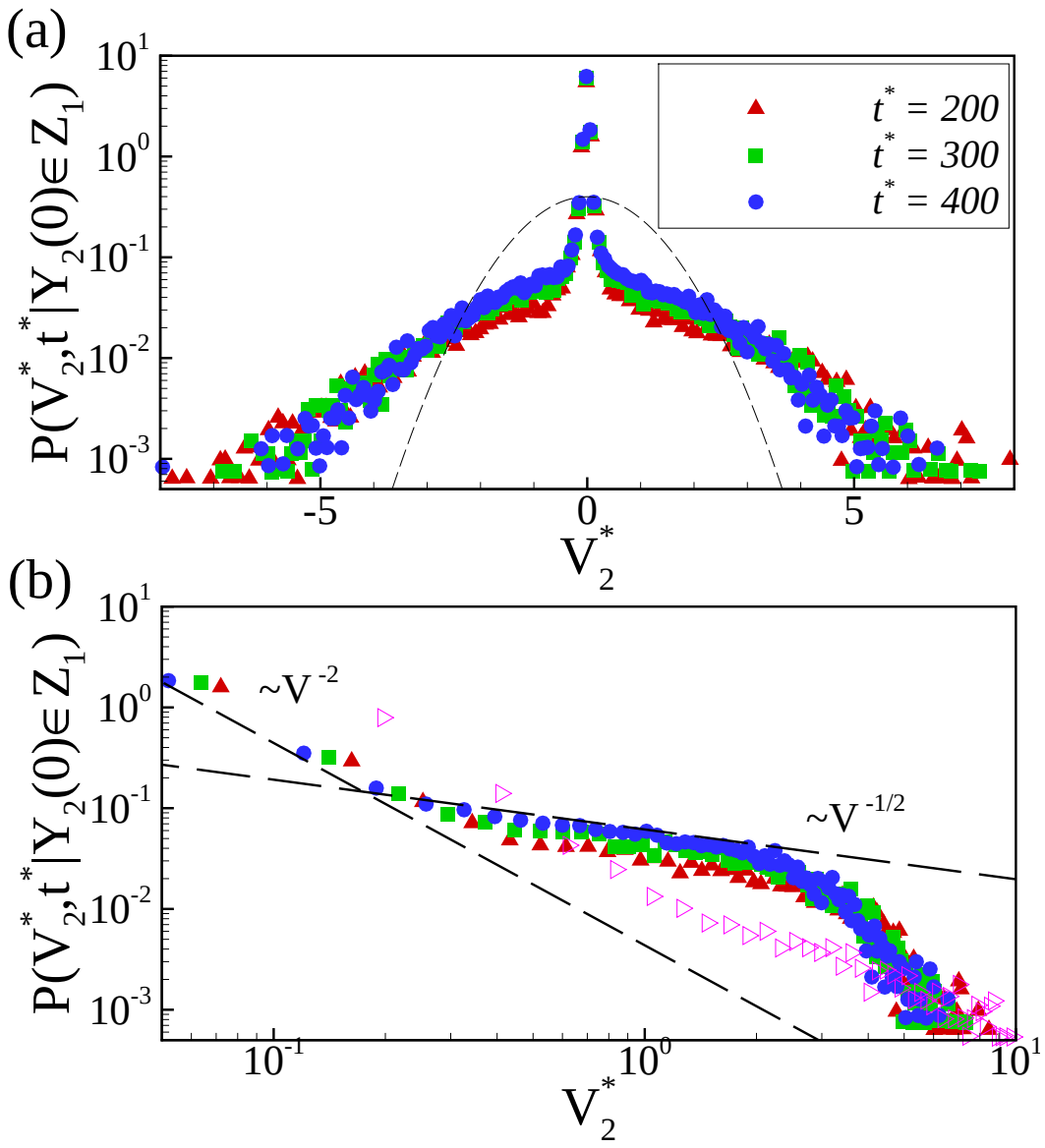

Figure 3.17: (a, b) PDFs of the wall-normal velocity V_2 of the particles initially located in Zone I. The velocity PDFs are shown for $t^* = 200$, 300, and 400. The dashed line in (a) is the Gaussian distribution. In (b), $\triangleright$ is the velocity PDF for $t^* = 10$.

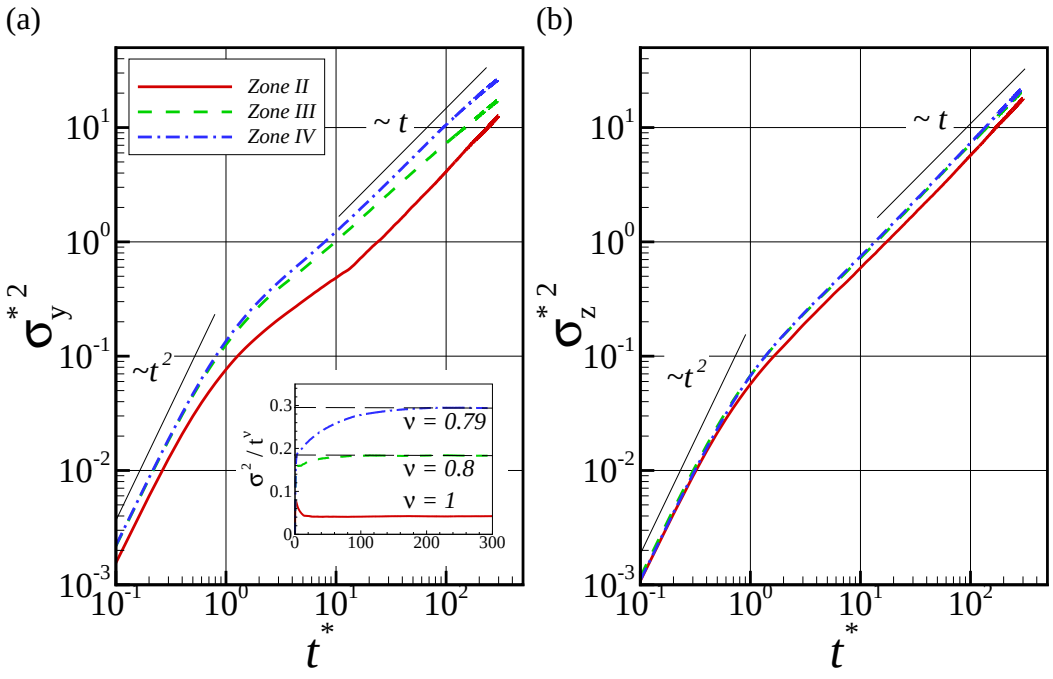

Figure 3.18: Variances of the (a) wall-normal and (b) spanwise displacements of particles in Zones II – IV.

ranges. In the central range of small V^*, the velocity PDF shows an algebraic decay $\sim V_2^{*\beta}$ with $\beta \simeq -2$. The V^{*-2} behavior in this core seems to be due to the particles remaining in Zone I. For comparison, $P(V_2^*)$ at $t^* = 10$, when most of the particles are still in Zone I, is drawn in the same plot. It is shown that $P(V_2^*)$ at $t^* = 10$ is well approximated by V^{*-2}. Around $V_2^* \simeq 0.3 \sim 0.4$, the exponent β changes from -2 in the core to $-1/2$ in an intermediate range. The crossover point gradually moves towards the origin as the particles leave Zone I and migrate to the channel center. A mechanism responsible for the slow decay $\sim V^{*-1/2}$ is not clear. The behavior seems to be related with the particles in Zone II or III. However, the $V^{*-1/2}$ behavior is somewhat surprising, because the velocity PDF for the particles in other Zones, even that calculated in Zone II, is essentially Gaussian. For large V_2^*, $P(V_2^*)$ shows an exponential decay.

σ_y^2 for Zones II – IV are shown in figure 3.18 (a). As the diffusive behavior changes from superdiffusion in Zone I to subdiffusion in Zones III, Zone II shows normal diffusion ($\sigma^2 \sim t$) with $D_y^* = 2.1 \times 10^{-2}$, in which D^* is the diffusivity normalized by $\dot{\gamma} a^2$. In figure 3.15 (a), it is shown that ϕ_A reaches a plateau in Zone IV, implying that the suspension may behave similarly to a homogeneous suspension. Indeed, in 3.2, it is shown that rheology and

suspension microstructure in Zone IV are comparable to those in homogeneous suspensions. Therefore, it is natural to assume that σ^2 would show normal diffusion as in homogeneous suspensions. Unexpectedly, the particles in Zone IV exhibit subdiffusion for $t^* > 150$. The inset shows the variances divided by t^ν. It is shown that $\sigma_y^2 \sim t^{0.8}$ for the particles in Zones III and $\sigma_y^2 \sim t^{0.79}$ for Zone IV.

Figure 3.18 (b) shows σ_z^2 for Zones II – IV. Unlike σ_y^2, normal diffusion is observed in the vorticity direction. In the wall-normal displacement, the variance for Zone IV is significantly larger than that for Zone III; ${\sigma^*}_y^2 = 17.5$ and 26.6 at $t^* = 300$ for Zone III and IV, respectively. However, ${\sigma^*}_z^2$ for Zone III and IV are almost the same; 21.4 and 22.3 for Zone III and IV at $t^* = 300$. In figure 3.15 (e), it is observed the wall-normal movement is strongly suppressed near the wall while the spanwise displacement is less restricted. As a result, σ_z is larger than σ_y for Zones I – III. In Zone IV, σ_y becomes larger than σ_z similar to the results in homogeneous suspensions. The diffusivities in the vorticity direction computed from σ_z^2 are $D_z^* = 3.1 \times 10^{-2}$, 3.6×10^{-2}, and 3.7×10^{-2} for Zone II, III, and IV, respectively. D_z^* in Zone III and IV are similar to that in homogeneous shear flow.

The changes of area fraction profiles in time for different initial groups of particles are shown in figure 3.19. As the outward flux from Zone I should be equal to the inward flux from Zone II to Zone I, the particles in Zone II have much higher probability of migrating towards the core (Zone III + IV). In figure 3.19 (a), it is shown that only a small fraction of particles move into Zone I while most of them migrate towards the outer region, which may explain the apparent normal diffusion in Zone II (figure 3.18 a). On the other hand, for the particles in Zone III, a large fraction of particles move to Zone I+II, in which they are trapped in particle layers (figure 3.19 b). For $y/a > 6$, the spreading of ϕ_A to Zone IV is almost Gaussian. However, for $y/a < 6$, ϕ_A shows a complex behavior as particles migrate into Zone II and subsequently into Zone I. ϕ_A in Zone I is an increasing function of t^*, while ϕ_A in the second particle layer ($y/a \simeq 3$) stays almost constant for $t^* = 100 \sim 400$. Subdiffusion may occur if there are stagnation or recirculating regions in the fluid flow, in which particles are arrested [239]. The subdiffusion in Zone III can be understood in the same context. Some particles in Zone III quickly move to the near wall region and they are trapped in the particle layers hovering around the same wall-normal position for a long time, while others migrate to the channel core. However, for Zone IV, only a small fraction of the particles reach Zones I and II and most of the particles remain in Zones III and IV

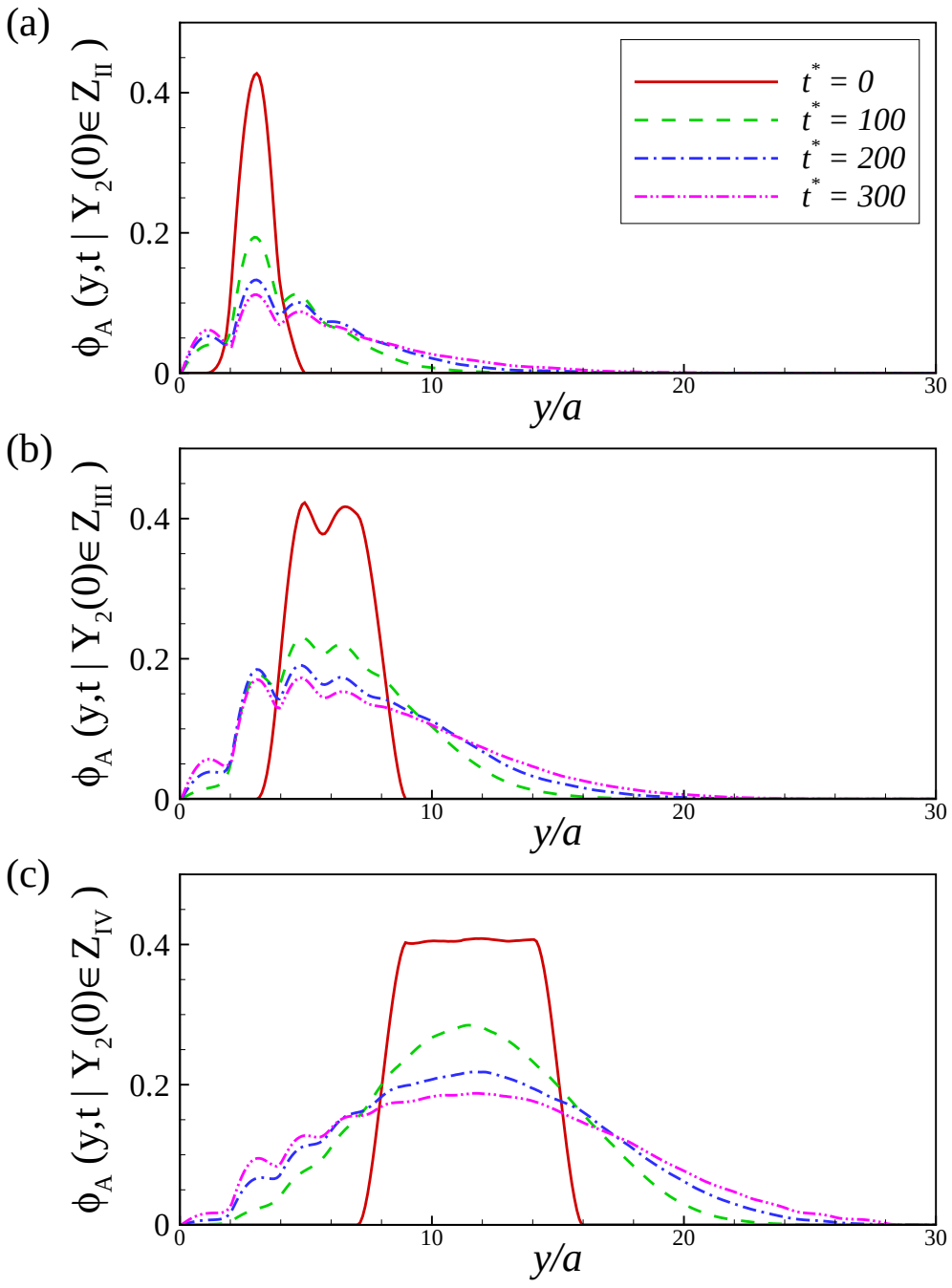

Figure 3.19: The area fraction profiles at different time instances for the particles whose initial locations are in (a) Zone II, (b) Zone III, and (c) Zone IV.

in the time interval considered (figure 3.19 c). The subdiffusion in Zone IV can not be explained solely by the particle entrapment in the near-wall region.

To investigate the diffusive behavior of the particles in the core of the channel more clearly, σ_y^2 is computed for the particles only near the center of the channel, $12 \leq y/a \leq 18$, for $0.25 \leq \phi \leq 0.40$ (figure 3.20 a). At $t^* = 200$, $\sigma_y^* = 2.87$, 3.58, 4.18, and 4.54 for $\phi = 0.25$, 0.30, 0.35, and 0.40, respectively, indicating that most of the particles have not reached the near-wall region (Zone I+II) yet.

The variances in the wall-normal direction divided by t^* are shown in figure 3.20 (b). For $\phi = 0.25$, normal diffusion is observed for $t^* > 50$ with $D_y^* = 2.1 \times 10^{-2}$. However, for $\phi \geq 0.30$, subdiffusive behaviors are observed for $t^* > 100$. Considering that σ_y^* at $t^* = 100$ are 2.59, 3.02, and 3.32 for $\phi = 0.30$, 0.35, and 0.40, respectively, the origin of the subdiffusivity is not the particle entrapment as in the case of Zone III. For $\phi = 0.25$, it is interesting to observe that the linear region ($\sim t$) is developed for $t^* > 50$, while such a linear behavior has been observed at smaller t^* in homogeneous suspensions ($t^* > 20$) [58].

One possible explanation of this subdiffusive behavior is the restriction on the length-scale of suspension flows by the size of confinement. In previous studies of confinement effects on the dynamics of equilibrium colloidal suspensions, it has been shown that, as the lengthscale of structural reorganization is limited by H_y/a, the mobility of particles and relaxation processes are significantly slowed [165, 188, 66]. In sheared suspensions, the dynamics is closely related to the formation of hydroclusters, which have a long correlation length [151]. However, in a confined suspensions, the lengthscale available for the formation of hydroclusters is limited by the confinement size and the emergence of a wall-induced microstructure, namely, a particle layer. For example, for $\phi = 0.40$ and $H_y/a = 30$, the suspension field is uniform only in $10 < y/a < 20$, indicating that the available lengthscale for a shear-induced suspension structure to develop is only $L \sim 10a$. This restriction on lengthscale may disable some of large-scale dynamic modes. The disturbance of these large-scale collective motions leads to the subdiffusion on the intermediate timescale $t^* \sim O(100)$, over which normal diffusion has been observed in homogeneous suspensions.

To support the argument, σ_y^2 for $\phi = 0.40$ and $H_y/a = 40$ is shown in figure 3.20 (b), where σ_y^2 is computed from the particles in the core of the channel $17 \leq y/a \leq 23$. Normal diffusion is observed from $t^* > 50$ with $D_y^* = 5.7 \times 10^{-2}$, which is comparable to the result in homogeneous suspensions [198], suggesting that $H_y/a = 40$ channel is large enough to

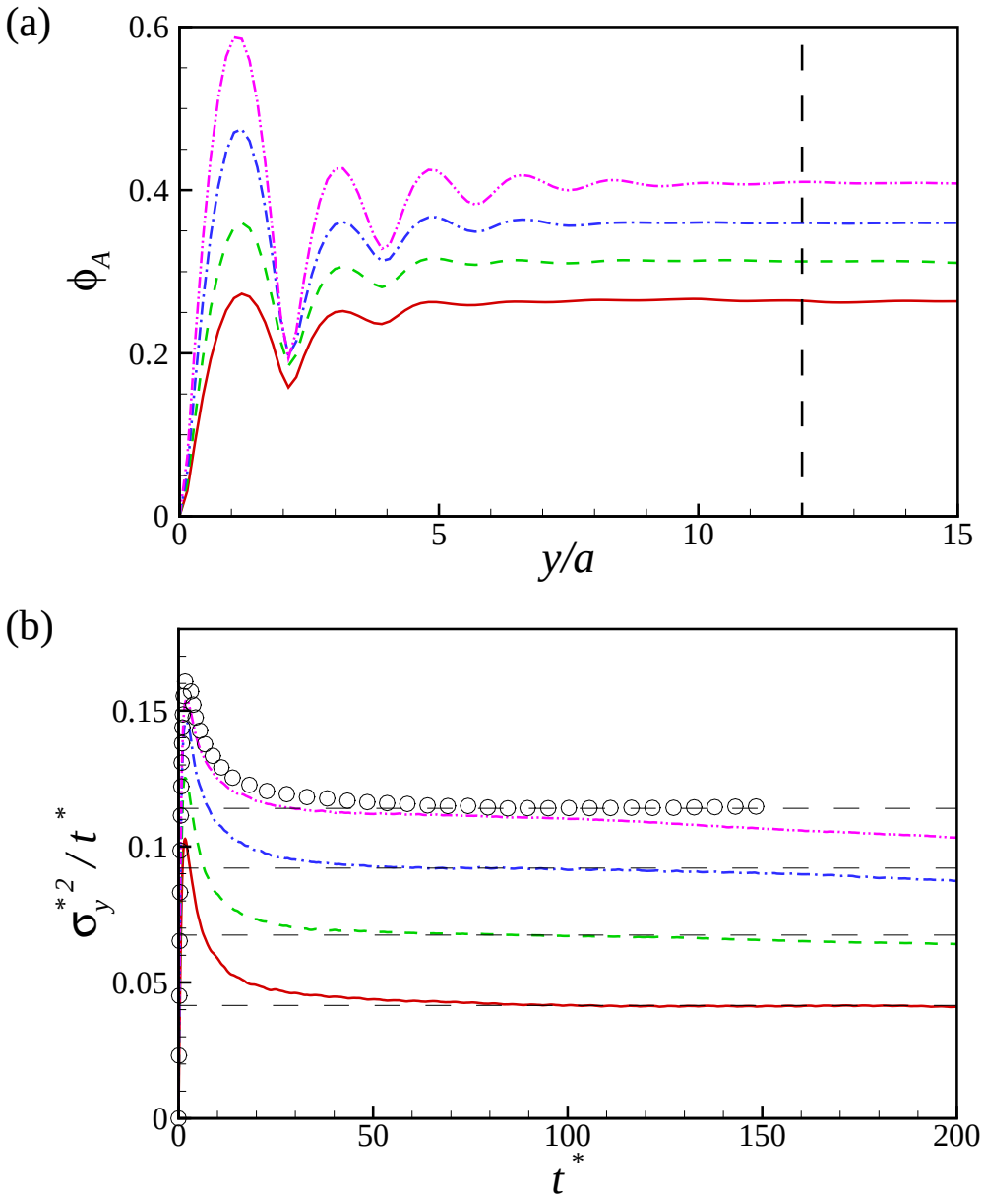

Figure 3.20: The area fraction profiles (a) and variances of the wall-normal displacement (b) for $\phi = 0.25$ (solid), 0.3 (dashed), 0.35 (dash-dot), and 0.40 (dash-dot-dot), $H_y/a = 30$. In (b), the circles are for $\phi = 0.40$ and $H_y/a = 40$.

accommodate a large-scale suspension structure. This observation is consistent with the experiments of [241], where they found that the suspension rheology is independent of H_y, when $H_y/a > 40$. Comparing $\phi = 0.25$ to 0.30, the diffusive behavior changes from normal diffusion at $\phi = 0.25$ to subdiffusion at $\phi = 0.30$, though the available lengthscales estimated from the ϕ_A profiles are similar, suggesting that the lengthscale of the hydroclusters increases with the volume fraction. However, to confirm the changes of the lengthscale with ϕ, extensive studies for a wide range of ϕ_A and H_y/a are still required.

We have shown that concentrated non-colloidal suspensions in a wall-bounded Couette flow exhibit anomalous diffusion on the intermediate timescale, on which normal diffusion is observed for homogeneous suspensions. The channel is divided into four zones and the behavior of particles in each zone is investigated. For the diffusion perpendicular to the wall, particles exhibit anomalous diffusion due to a strong spatial coherency induced by the wall effects. Particularly, the particles in a well-structured particle layer located next to the wall (Zone I) show superdiffusive behavior. The probability density functions both for the displacement and the wall-normal velocity show wider tails compared to the Gaussian distribution, indicating the stochastic processes involved in the motion of the particles are highly intermittent. Subdiffusion is observed for the particles in Zone III and IV. As a buffer zone between superdiffusion in Zone I and subdiffusion in Zone III, normal diffusion is observed in Zone II. The subdiffusion in Zone III is related with the trapping of the particles in the particles layers near the wall, Zone I + II. In confined suspensions, the available lengthscale for the suspension dynamics is restricted by the size of the confinement, which will disable some of the large-scale dynamic modes [66]. The subdiffusion in Zone IV seems to be related with a disturbance in large-scale collective motions, such as the formation of hydroclusters, by the size of the confinement. As the volume fraction increases from $\phi = 0.25$ to 0.40, the diffusive behavior of the particles in the channel center changes from normal to subdiffusion, implying the largest lengthscale related with suspension dynamics increases with the volume fraction. It is worthwhile to note that, while most modeling approaches to suspension flows are based on the results in homogeneous suspensions, the present study indicates that the models may fail to predict the diffusive behavior not only near the wall (Zone I+II) but also in the core (Zone IV).

3.4 Ordering transitions

Colloidal suspensions undergo an intriguing phase behavior when subjected to a shear flow. In the absence of flow, a colloidal suspension develops a crystalline structure above a freezing volume fraction, $\phi_f = 0.494$ for hard-sphere colloids [179, 184], which can be melted by applying a strong shear to the system [54]. On the other hand, if a shear is applied to disordered colloidal suspensions for the volume fraction $\phi > \phi_f$, crystallization takes place rapidly at low shear rate yet it melts into a fluid at higher shear rate [222]. The shear melting is observed when the Péclet number $Pe = 6\pi\mu\dot{\gamma}a^3/k_BT$ is of $O(1)$. Here, μ is the viscosity of the solvent, $\dot{\gamma}$ is the shear rate, a is the particle radius, and k_BT is the thermal energy. Interestingly, another disorder-order transition has been observed at much higher shear rate $Pe \gg 1$ [4]. Sierou & Brady [197] have demonstrated the existence of shear-induced ordering in homogeneous non-Brownian suspensions ($Pe \to \infty$) using the accelerated Stokesian Dynamics simulations. Subsequently, Kulkarni & Morris [120] performed numerical simulations for a wide range of Pe, $1 \leq Pe \leq 10^4$, and showed the similar phase behavior for $Pe \geq 10^3$. Non-equilibrium phase transitions, in general, are of interest both in theoretical studies [43, 44] and in engineering applications [71]. As the dynamics are determined by a balance between driving forces, the process can be controlled by altering external fields. For example, in colloidal suspensions under an oscillatory shear, different types of crystalline structure can be obtained by changing the frequency and magnitude of the oscillation [150].

When a concentrated suspension is confined by solid boundaries, the dynamics of the suspension becomes dramatically different from the bulk properties [66, 153, 165, 230]. In the absence of flow ($Pe = 0$), phase behaviors of confined molecular or colloidal systems have been extensively studied over the last two decades (see [182] for review). Courtemanche & Swol [45] showed that crystallization of hard-sphere (HS) fluid occurs at a smooth boundary earlier than in the bulk fluid, *i.e.* below liquid-crystal coexistence, which is later known as 'wall-induced ordering'. Schmidt & Löwen [191, 192] calculated the phase diagram of HS fluids confined by two parallel walls for $2 < H/a < 4$, where H is the separation distance between walls and a denotes the particle radius. Varying H/a for a fixed volume fraction ϕ, they observed strong discontinuous phase transitions between different crystal structures, *e.g.* layered, buckled, and rhombic crystals. Recently, Fortini & Dijkstra [72] performed

extensive Monte Carlo simulations and calculated the equilibrium phase diagram of HS fluids for $2 < H/a < 10$. However, considering the relevance of highly confined suspensions to many industrial processes such as surface coating, lubricants, and microfluidic devices [80, 178, 195], surprisingly little is known for the effects of confinement on the dynamics of concentrated suspensions under shear flow. Sheared suspensions are different from the aforementioned equilibrium HS fluids in that the dynamics are determined by both long-range multi-body hydrodynamic interactions and short-range lubrication and interparticle forces. In colloidal suspensions under oscillatory shear flows, Haw *et. al.* [88] observed that crystal structures near a wall are more ordered than those in the center. However, they did not show any quantitative results. Cohen *et al.* [40] found that a new crystalline structure emerges in a strongly confined system in colloidal suspensions for $\phi = 0.61 \pm 0.02$ under large oscillatory shear.

In this section, we study the ordering transition of concentrated suspensions confined by two parallel walls under steady shear in the limit of infinite Pe, where dynamics are solely determined by hydrodynamic interactions and short-range interparticle forces. It is found that the particles near the walls start forming hexagonally organized strings in the plane normal to the flow at a volume fraction as low as $\phi \simeq 0.48$, while the center of the channel remains disordered. The ordered state depends not only on the volume fraction but also on the ratio of the channel height to the particle radius H_y/a. The effect of the channel height on the order structure is investigated for $8 \leq H_y/a \leq 21$ at $\phi = 0.52$.

3.4.1 Simulation parameters

The computational domain in x- and z-directions are fixed, $H_x/a = 30$ and $H_z/a = 20$, and H_y is varied; $8 \leq H_y/a \leq 30$. Periodic boundary conditions are used in $x-$ and $z-$directions. The number of particles ranges from 688 for $\phi = 0.48$ and $H_y/a = 10$ to 2235 for $\phi = 0.52$ and $H_y/a = 30$.

To model non-hydrodynamic effects, we employ a contact force model. The contact force on particle i from particle j is given by

$$\boldsymbol{F}_C^{ij} = \begin{cases} -6\pi\mu\dot{\gamma}a^2 F_{ref} \left(\frac{R_{ref}^2 - |\boldsymbol{r}|^2}{R_{ref}^2 - 4a^2}\right)^6 \frac{\boldsymbol{r}}{|\boldsymbol{r}|} & \text{if } |\boldsymbol{r}| < R_{ref} \\ 0 & \text{otherwise,} \end{cases} \tag{3.18}$$

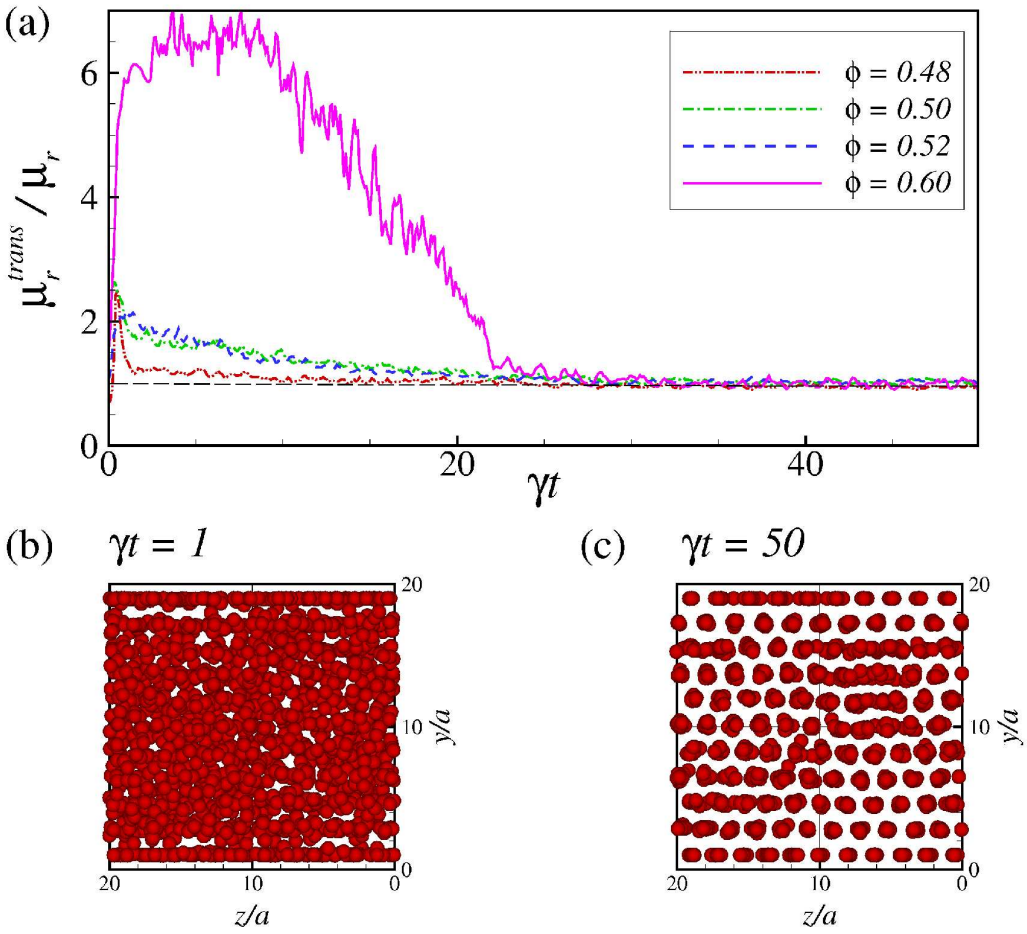

Figure 3.21: (a) Transient behavior of the relative viscosity normalized by the relative viscosity in the stationary state. The channel height is fixed; $H_y/a = 20$. Snapshots (end view) for $\phi = 0.52$ and $H_y/a = 20$ at $\dot{\gamma}t = 1$ (b) and 50 (c). For visualization, the particle radius is reduced to 1/2 of the actual size.

in which $\boldsymbol{r} = \boldsymbol{Y}^i - \boldsymbol{Y}^j$, F_{ref} is a constant, and R_{ref} is a cut-off distance. In the present study, the contact force is activated if the shortest distance between two particle surfaces (ϵ) is less than $0.01a$, *i.e.* $R_{ref}/a = 2.01$. F_{ref} is chosen to keep the minimum separation distance $\epsilon_{min} \simeq 0.002a$. In this study, $F_{ref} = 200$ is used for $\phi = 0.46 \sim 0.54$ and $F_{ref} = 600$ for $\phi = 0.60$. Once $\boldsymbol{F}_C$ is computed for all the neighboring particles, it is added to $\boldsymbol{F}^P$.

To generate initial configurations, small particles are seeded randomly in the computational domain. Then, a molecular dynamics simulation with a repulsive potential is performed, while slowly increasing the particle radius until the desired volume fraction is reached. Figure 3.21 shows the development of the relative viscosity μ_r in time for $H_y/a = 20$. Once shear is applied, the suspension exhibits a disordered fluid state at first

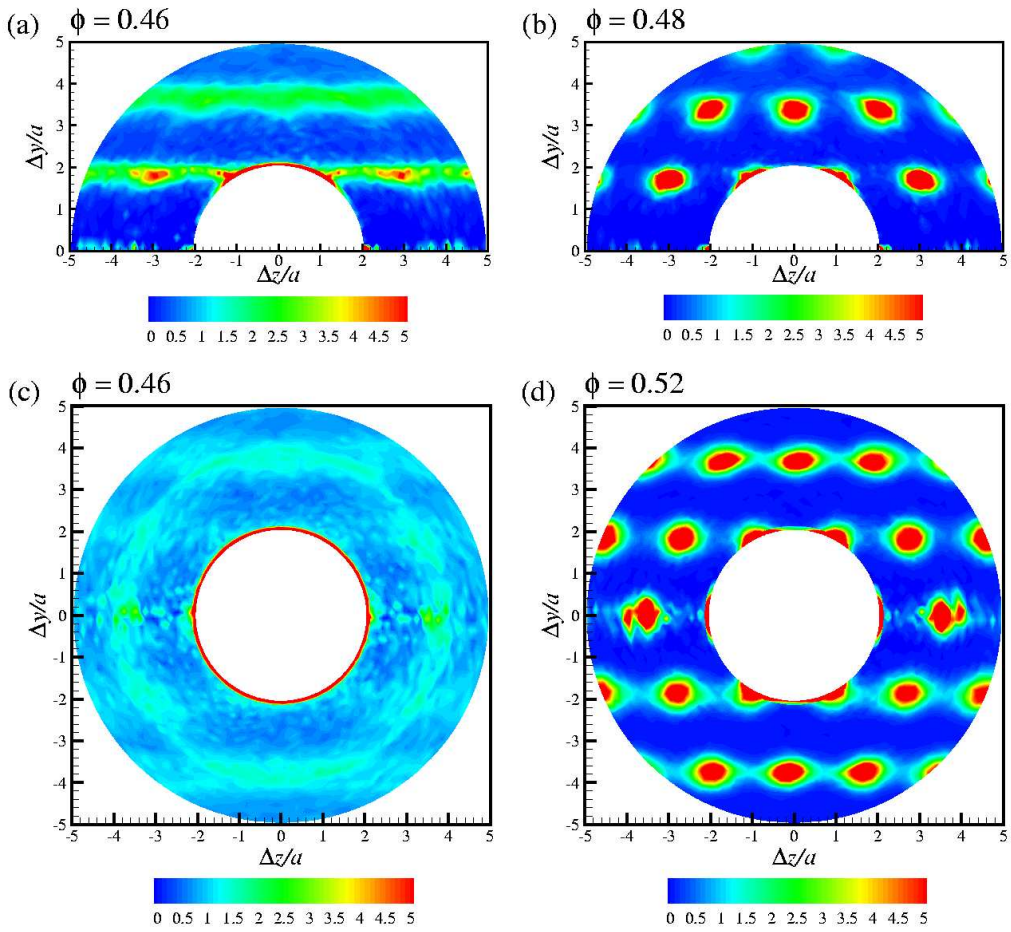

Figure 3.22: 2-dimensional pair distributions in the velocity-gradient–vorticity $(y-z)$ plane for $H_y/a = 20$ obtained in (a,b) Ω^W and (c,d) Ω^C.

(figure 3.21 b), which accompanies a sharp increase of μ_r. The peak μ_r is observed to be in between the high-frequency shear viscosity and the dynamic shear viscosity. For $\phi = 0.60$, the peak μ_r is around 70. As order develops (figure 3.21 c), μ_r drops slowly. In most cases, a stationary state is reached after $\dot{\gamma}t \simeq 40 \sim 50$, which is much faster than for the homogeneous shear results in Kulkarni & Morris [120] ($\dot{\gamma}t \simeq 150$).

3.4.2 Wall-induced ordering

In wall-bounded suspensions, the behavior of suspensions near the wall is radically different from the center of the channel. Depending on the micro-structures, Yeo & Maxey [230] showed that the wall-bounded suspensions of non-Brownian particles can be divided into three regions, the wall, buffer, and core regions. The wall region is distinguished by a strong particle layering. In the core region, the suspension is similar to that in a homogeneous shear

flow. In the buffer region, the suspension micro-structure is no longer reflexional symmetric due to the interactions with particle layers below (wall region) and the shear structure above (core region). To show the different levels of ordering near the wall and in the channel center, we investigate the micro-structures in the wall Ω^W and the core Ω^C regions; $\Omega^W = (0, H_x) \times \{(0, 1.5a) \cup (H_y - 1.5a, H_y)\} \times (0, H_z)$ and $\Omega^C = (0, H_x) \times (5a, H_y - 5a) \times (0, H_z)$. For $H_y/a = 10$, Ω^C is defined as $\Omega^C = (0, H_x) \times (4a, 6a) \times (0, H_z)$.

First, the ordering transition is investigated by varying ϕ for $H_y/a = 20$. The pair distribution function in spherical polar coordinates $g(r, \theta, \psi)$ is calculated for particles in Ω^W and Ω^C, in which r is the radial distance, θ is the azimuthal angle measured from the velocity direction, and ψ denotes the polar angle measured from the vorticity direction. Figure 3.22 shows $g(r, \theta, \psi)$ in the velocity-gradient–vorticity $(y - z)$ plane, *i.e.* $\theta = \pi/2$. At $\phi = 0.46$, the dominant structure in Ω^W is the particle layering and a weak hexagonal order is observed, while $g(r, \psi)$ in Ω^C shows an isotropic ring-like structure indicating the suspension is homogeneous. At $\phi = 0.48$, a hexagonal order begins to be developed in Ω^W, while the suspension in Ω^C is still in disordered state. At $\phi = 0.52$, the whole channel is almost completely ordered (figure 3.22 c). As the suspension in Ω^C is in the disorder-order coexistence state, $g(r, \psi)$ for $\phi = 0.50$ shows a mixture of the hexagonal structure (figure 3.22 d) and the ring-like structure (figure 3.22 c).

Figure 3.23 shows the area fraction ϕ_A as a function of y for $H_y/a = 20$. ϕ_A is calculated by $\phi_A = \iint \chi(\boldsymbol{x}) dx dz/(H_x \times H_z)$. Here, $\chi(\boldsymbol{x})$ is an indicator function which is non-zero if $\boldsymbol{x}$ is inside of particles. For $\phi \leq 0.46$, ϕ_A is higher near the wall. The values of the first peaks near the walls are insensitive to ϕ. It seems that the high volume fraction near the wall leads to the earlier transition in Ω^W than in Ω^C. At $\phi = 0.46$, the value of the local peaks is a decreasing function of distance from the wall. Similar to $\phi = 0.40$, if H_y/a is large enough, ϕ_A may become uniform around the core of the channel. However, once the ordered structure is present across the entire channel ($\phi = 0.52$), ϕ_A is no longer a decreasing function of distance from the wall. The peaks of ϕ_A are almost constant across the channel. The area fraction profiles suggest that the particles form a layered structure at high volume fractions in confined suspensions, in which the suspension dynamics are dependent on the interaction between discrete particle layers, and, thus, the previous continuum model approaches, which rely on the rheological functions based on well-mixed suspensions, may not be suitable to apply for suspensions near the ordering transitions.

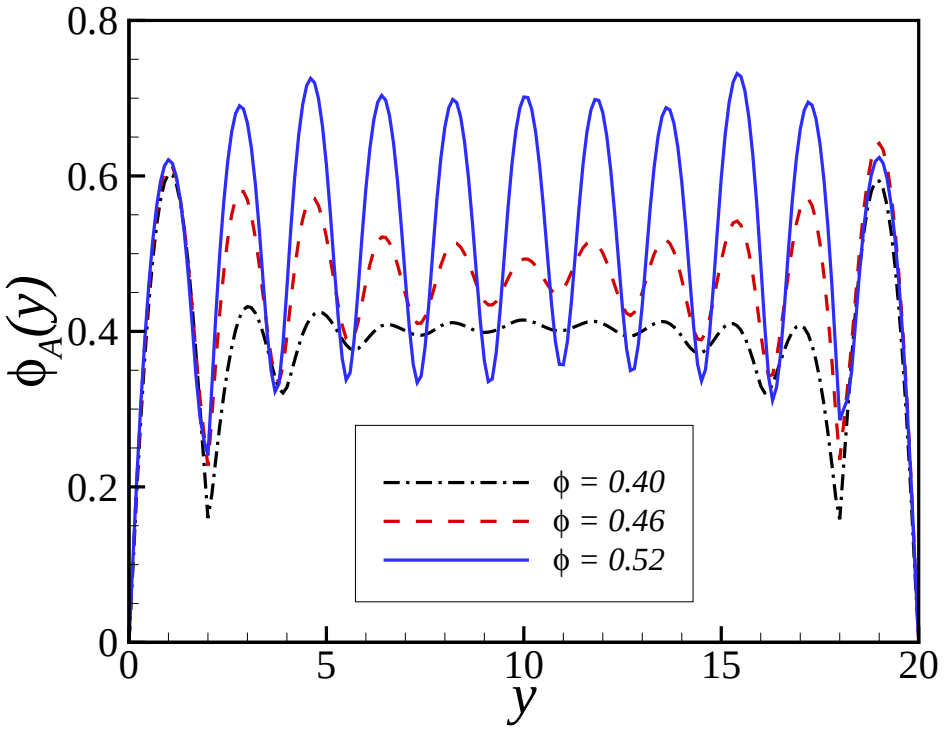

Figure 3.23: Area fraction profiles for $H_y/a = 20$.

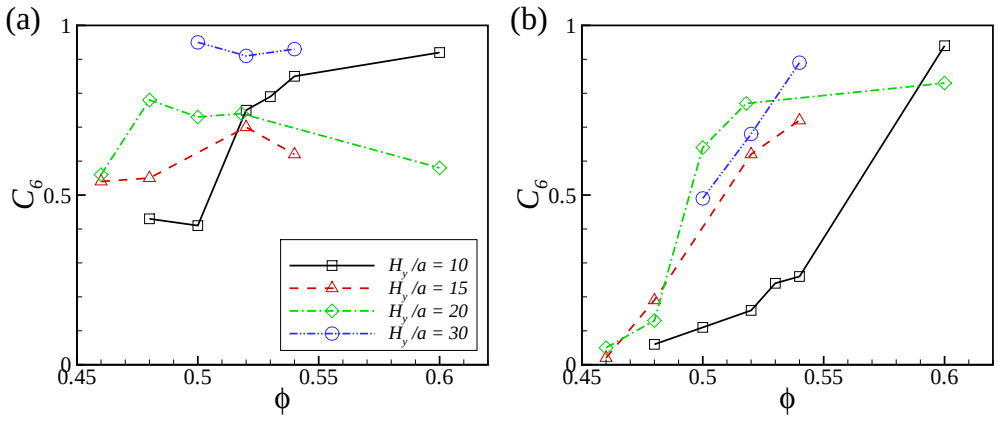

Figure 3.24: Order parameter C_6 in (a) Ω^W and (b) Ω^C.

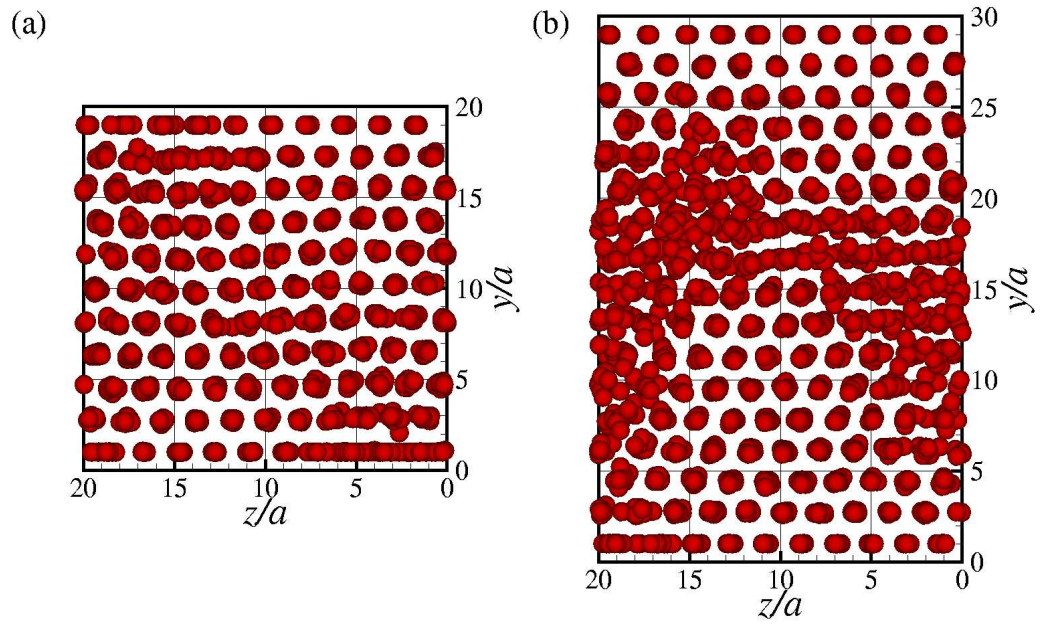

Figure 3.25: Snapshots (end view) for $\phi = 0.52$; (a) $H_y/a = 20$ and (b) $H_y/a = 30$. For visualization, the particle radius is reduced to 1/2 of the actual size.

Figure 3.24 shows the hexagonal order parameter C_6 estimated in Ω^W and Ω^C. Similar to the bond-orientational order parameter, C_6 is defined as [120]

$$C_6 = \frac{\int_0^{2\pi} g(\psi)\cos(6\psi)d\psi}{\int_0^{2\pi} g(\psi)d\psi}, \tag{3.19}$$

in which $g(\psi)$ is the pair-distribution function in the $y-z$ plane averaged over $2a < r < 2.1a$. The values of C_6 lie in the range $0 \leq C_6 \leq 1$, *i.e.* $C_6 = 1$ for a perfect hexagonal structure and $C_6 = 0$ for an isotropic micro-structure. In general, C_6 in Ω^W is larger than that in Ω^C consistent with the wall-induced ordering. For $H_y/a = 15$, the hexagonal ordering in Ω^W is not evident when $\phi \leq 0.48$. On the other hand, for $H_y/a = 20$, $C_6 \simeq 0.8$ at $\phi = 0.48$, indicating that the particles in Ω^W begin to be ordered into hexagonal strings at $\phi = 0.48$. When $\phi \geq 0.52$ and $H_y/a = 20$, C_6 in Ω^C and Ω^W are almost the same, implying the presence of the hexagonal order in the whole channel. The decrease of C_6 in Ω^W at high volume fraction is mainly due to the small sampling volume. Since the sampling volume of C_6 for Ω^W is small, even if there are only a few defects in the sampling volume, C_6 can be significantly reduced by these defects. If C_6 is computed for the whole domain, it is a non-decreasing function of ϕ for a given H_y/a.

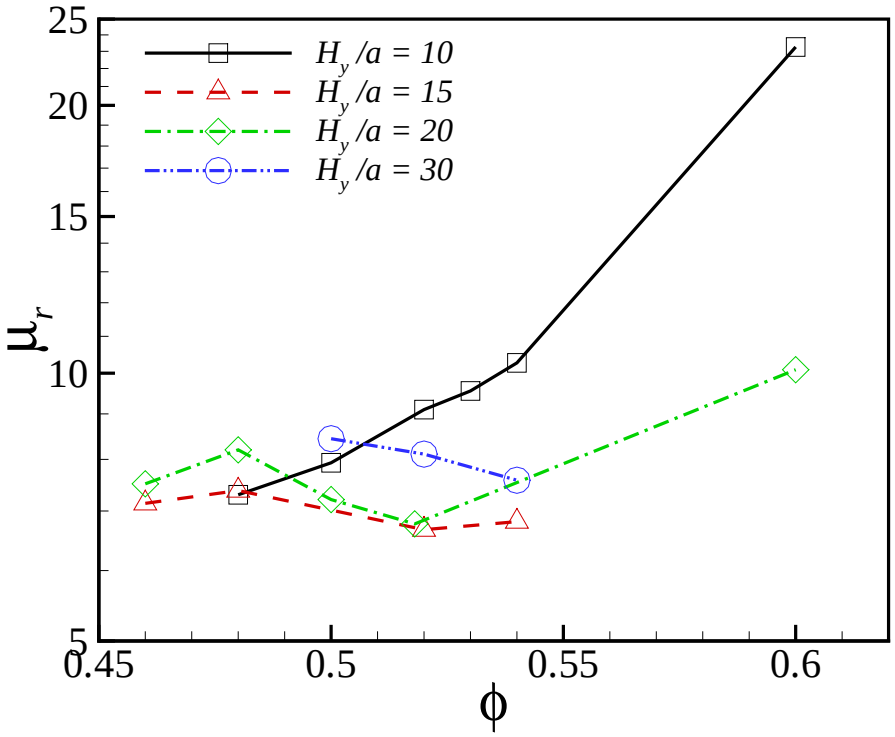

Figure 3.26: The relative viscosity for various ϕ and H_y/a.

In a larger channel ($H_y/a = 30$), the wall effects become weaker in the channel center, which in turn weakens the ordered structure in Ω^C. At $\phi = 0.50$, C_6 in Ω^C are 0.65 and 0.5 for $H_y/a = 20$ and 30, respectively. On the other hand, a better order is observed near a wall. Figure 3.25 shows snapshots for different H_y at $\phi = 0.52$. For $H_y/a = 20$, most particles are assembled into nearly linear strings which are organized as a hexagonal array with a few defects. However, for $H_y/a = 30$, a disordered fluid region emerges in the channel core. Typically, most experiments of non-colloidal suspensions are performed in a wide channel, for example $H_y/a > 40$ [241]. Therefore, it is likely that the suspension is in the disorder-order coexistence state, for which the bulk behavior resembles that of the homogeneous suspension. This may be one reason that ordering transitions in the non-colloidal suspension has not been investigated so far in experiments.

The relative viscosity μ_r is shown in figure 3.26. For $H_y/a = 15$ and 20, μ_r begins to decrease at $\phi = 0.48$ as the hexagonal order develops. Once the hexagonal order is dominant across the entire channel, μ_r increases again ($\phi > 0.52$). The value of μ_r for $H_y/a = 30$ is larger than those in the smaller channels due to the emergence of disordered region in Ω^C,

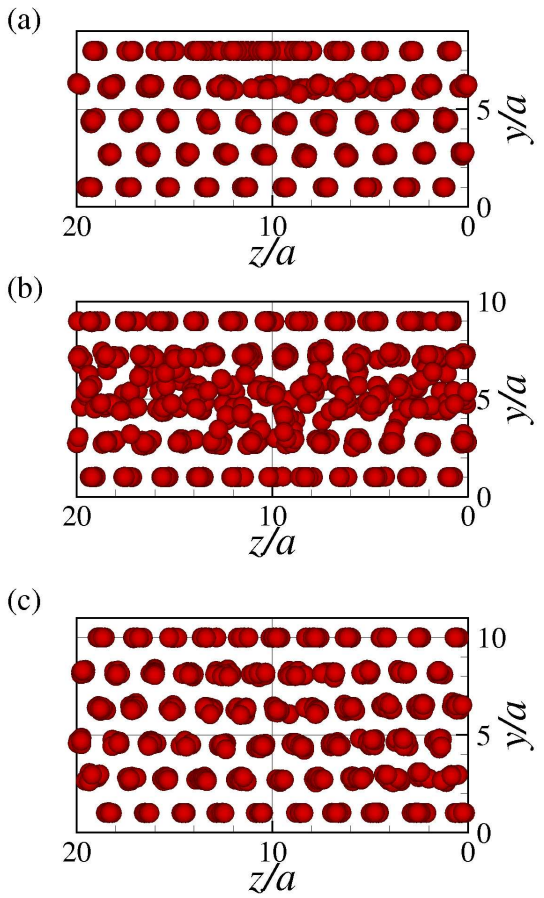

Figure 3.27: Snapshots (end view) for $\phi = 0.52$; (a) $H_y/a = 9$, (b) $H_y/a = 10$, (c) $H_y/a = 11$. For visualization, the particle radius is reduced to 1/2 of the actual size.

in which μ_r is higher. It is expected that, in a large channel $H_y/a > 40$, the disordered region is much larger than the ordered region so that the bulk properties would resemble those without the ordered structures. Unlike the results in the three wider channels, μ_r for $H_y/a = 10$ is an increasing function of ϕ.

3.4.3 Effects of the channel height on the order structures

In the equilibrium phase transition ($Pe = 0$) of strongly confined colloidal suspensions, a sequence of crystal layers is observed depending on the commensurability of the crystal structures with the channel height; $n\square \rightarrow n\triangle \rightarrow (n+1)\square \rightarrow \cdots$. Here, $n\square$ and $n\triangle$, respectively, denote n crystal layers of square and hexagonal lattice symmetries in the horizontal ($x - z$) plane. Depending on the commensurability, first-order melting and freezing transitions are observed between different crystal structures [192]. At higher volume frac-

Table 3.4: Channel height H_y/a, characteristic gap width η, number of particle layers N, and order parameter C_6 for $\phi = 0.52$.

H_y/a	8	9	10	11	12.5	15	17.5	19	19.5	20	21
η	4.46	5.04	5.62	6.20	7.06	8.51	9.95	10.82	11.10	11.39	11.97
N	-	5	-	6	7	8	10	11	11	11	12
C_6	0.59	0.88	0.50	0.82	0.88	0.67	0.89	0.94	0.86	0.78	0.86

tions, the alternating sequence of square and hexagonal crystal layers is disturbed by the emergence of other crystal structures, such as rhombic, buckling, or prism phases [72]. In flowing suspensions, the particle layers slide over each other and ordered structures must accommodate this. Hence, it is not expected that the ordered structures and the commensurability will exactly follow what has been observed in the thermodynamic phase transitions of HS fluids or colloidal suspensions.

To investigate the effects of H_y/a on the ordering transition in flowing suspensions, the numerical simulations are performed for varying H_y/a from 8 to 20 for $\phi = 0.52$ and 0.54. Figure 3.27 shows snapshots for $\phi = 0.5$ at different channel heights H_y/a. Increasing H_y/a from 9 to 11, it is shown that the suspension exhibits phase transitions from the hexagonal order (figure 3.27 a) to a mixed state (figure 3.27 b) and, then, again to the ordered state (figure 3.27 c).

Figure 3.28 shows the order parameter C_6 as a function of H_y/a for $\phi = 0.52$ and 0.54. It is shown that the order structure is very sensitive to H_y when $H_y/a \leq 11$. For $\phi = 0.52$, the suspensions are in an ordered state for $H_y/a = 9$ and 11 and in a disordered state for $H_y/a = 8$ and 10. The similar behavior is observed for $\phi = 0.54$. The oscillation in C_6 becomes smaller for larger H_y. When H_y/a is changed from 10 to 11, C_6 decreases from 0.88 to 0.50, while, increasing $H_y/a = 19$ to 20, it changes from 0.94 to 0.78.

The change in the order state is due to the commensurability of the order structures with the available space between two walls. As the most distinguishable structure is the simple hexagonal lattice in the $y - z$ plane, a characteristic gap width can be defined as

$$\eta = \frac{H_y - 2a}{\sqrt{3}a} + 1. \tag{3.20}$$

The characteristics gap width are shown in table 3.4 together with the number of particle layers N and the order parameter C_6. The number of particle layer is well approximated

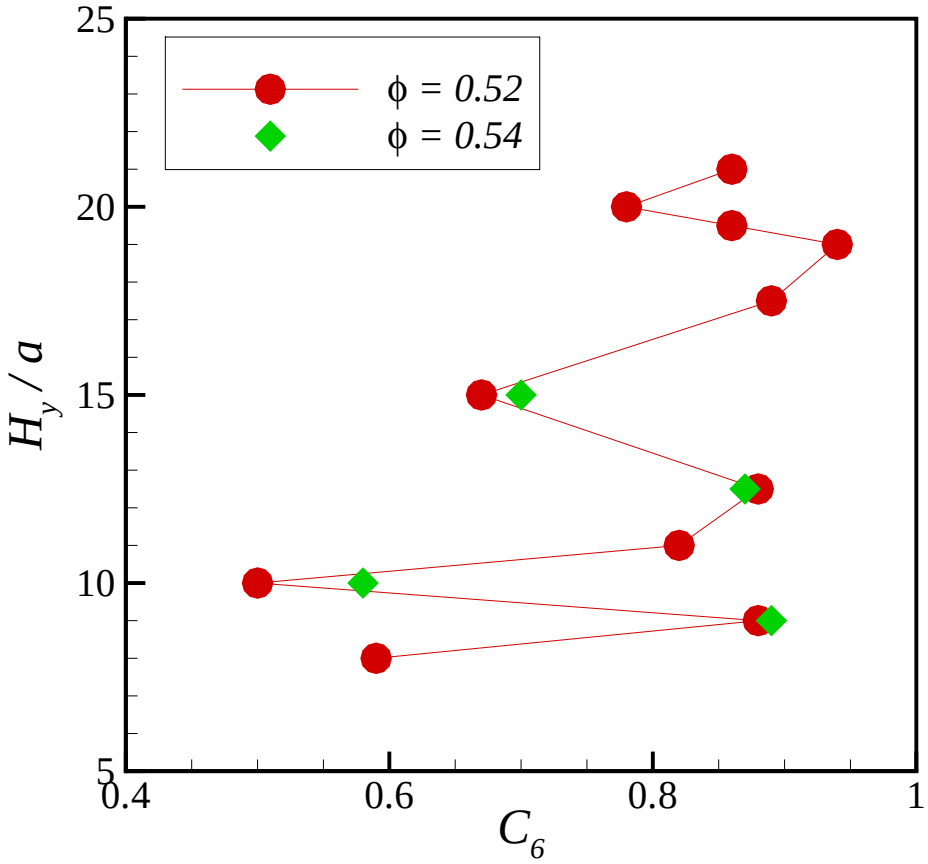

Figure 3.28: The order parameter as a function of H_y/a for $\phi = 0.52$ and 0.54.

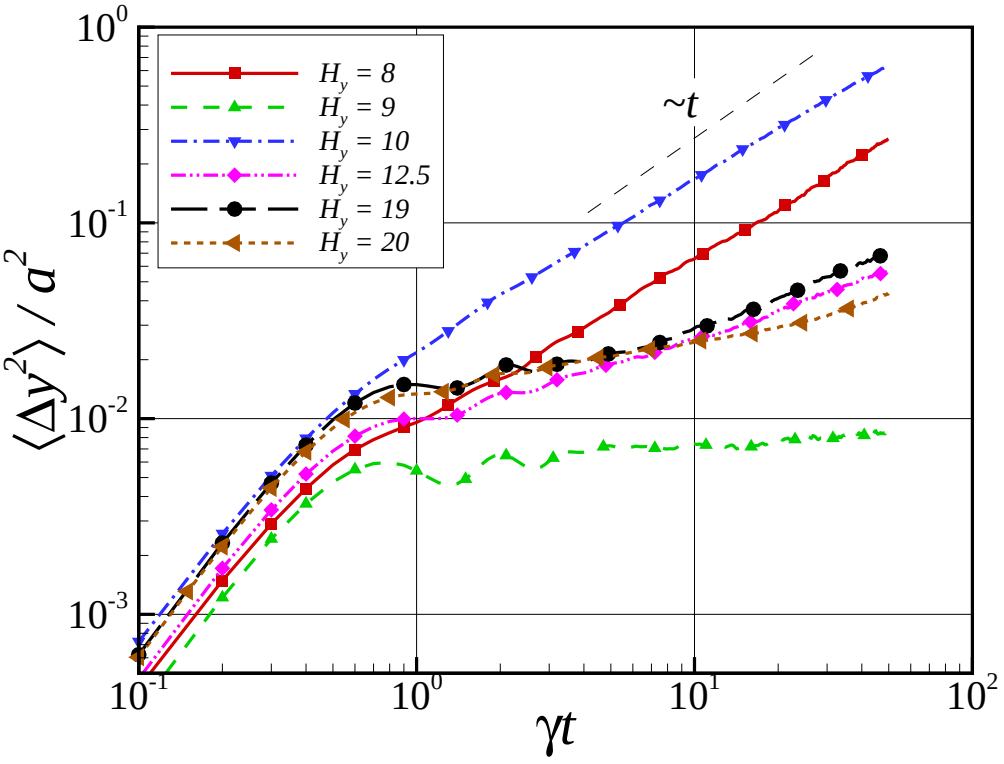

Figure 3.29: The normalized mean-square vertical displacements $\langle [Y_2(t) - Y_2(0)]^2 \rangle / a^2$ for $\phi = 0.52$.

by η. As expected, the suspension is in more ordered state (large C_6) when η is close to an integer, or small $|N - \eta|$. When η is increased or decreased from an integer, the distance between particle layers increases making particles more mobile. As a result, the order structure becomes unstable and the suspension becomes disordered.

The mean-square displacement (MSD) in the vertical direction $\langle [Y_2(t) - Y_2(0)]^2 \rangle$ normalized by a^2 is shown in figure 3.29. After a short ballistic regime ($\dot{\gamma} t \sim O(10^{-1})$), MSDs for $H_y/a = 8$ and 10 show a sub-diffusive behavior, $\langle [Y_2(t) - Y_2(0)]^2 \rangle \sim t^{\nu}$ with the exponent $\nu = 0.86$ on the intermediate time scale of the present simulation. Previously, Yeo & Maxey [229] showed that confined non-Brownian suspensions for $\phi = 0.40$ exhibit sub-diffusion on the time scale of $\dot{\gamma} t \sim O(100)$. In the long term, the vertical particle displacement is confined by the size of the channel height. When an ordered structure is developed, the vertical displacement of particles is restricted by the cage formed by neighboring particles. For $H_y/a = 19$ and 20 , in which the suspensions are in a mixed state, the particles in the core of the channel behaves similarly to the disordered state, while mobility of the parti-

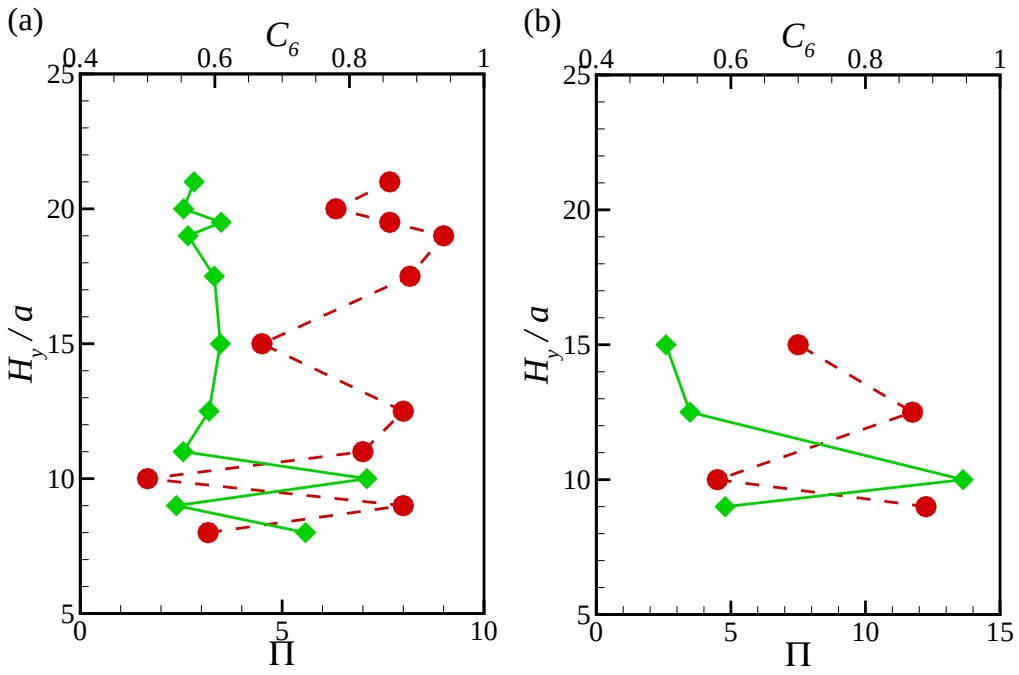

Figure 3.30: The particle pressure Π (♦) and the order parameter C_6 (•) as a function of H_y/a for (a) $\phi = 0.52$ and (b) 0.54.

cles near the walls is significantly reduced due to the ordered structure. Hence, MSDs for $H_y/a = 19$ and 20 are significantly lower than those in a disordered state ($H_y/a = 8$ and 10). For $H_y/a = 9$, the entire channel is in an ordered state and the vertical displacement of particles is observed only near defects. Hence, there is a large increase in MSDs between ordered ($H_y/a = 9$) and mixed states ($H_y/a = 12.5$, 19, and 20).

The bulk particle pressure Π normalized by $\mu\dot{\gamma}$ is shown in figure 3.30. The definition of Π is

$$\Pi = -\frac{1}{3}(\sigma_{11} + \sigma_{22} + \sigma_{33}). \tag{3.21}$$

Here, σ_{ij} denotes the particle stress computed from the stresslet and the interparticle potential. In a strongly confined system ($H_y/a < 12$), the oscillation of Π is almost exactly opposite to C_6. However, in larger channels, the correlation between Π and C_6 becomes less clear. Because the wall effect is strong across the entire channel in small channels, the order structure and, thus, the rheological parameters are mainly determined by the commensurability. On the other hand, in a larger channel, there is a competition between the

confinement effect and the shear around the core of the channel. Therefore, rheology does not exactly follow the commensurability of the channel.

Figure 3.31 (a) shows the order structure in the horizontal ($x-z$) plane for $\phi = 0.52$ and $H_y/a = 9$. A rhombic phase is observed for the horizontal structure. A stable rhombic phase is also observed in the equilibrium phase transitions of confined HS fluids as an interpolating structure between square and hexagonal symmetric structures [192]. Fortini & Dijkstra [72] found that the rhombic phase is stable between $n\square$ and $n\triangle$ for $n \leq 5$, *i.e.* $H_y/a < 10$. However, in flowing suspensions, a rhombic phase is observed for a wide range of H_y/a. When $\phi \leq 0.54$, only rhombic phases are observed for the range of parameters in the present study of non-Brownian (infinite Pe) suspensions. In flowing suspensions, the disturbance flow induced by a particle decays slowly, which leads to a long-range correlation. The long-range hydrodynamic interactions result in the earlier order transition in sheared non-Brownian suspensions than that seen in HS fluids. However, near the lower boundary of order transitions, the volume fraction is still too low to develop a fully three-dimensional crystal structure. As the hydrodynamic force induced by the shear flow is anisotropic, an ordered structure is formed in the $y-z$ plane first. It seems that the rhombic phase in the $x-z$ plane in figure 3.31 (a) is a transitional structure that supports a hexagonal structure in the $y-z$ plane at the given volume fraction. In contrast, suspensions at higher volume fractions may show a phase behavior similar to HS fluids. At $\phi = 0.60$, 5 layers of the hexagonal symmetric structure are observed for $H_y/a = 9$ (figure 3.31 b), which is followed by 6 layers of nearly rectangular structure for $H_y/a = 10$ (figure 3.31 c).

3.5 Effects of external torques on rheology and ordering transitions

Manipulating rheological properties of suspension flows by imposing electric or magnetic fields is of current interest due to its relevance to a wide range of technological applications [71, 86, 111]. In electrorheological (ER) or magnetorheological (MR) fluids, a dramatic increase of the apparent viscosity is observed, when particles are assembled into well-organized large-scale structures, such as chains or stripes, by applied fields [46, 170]. It is also known that the apparent viscosity can be reduced by applying an external torque on the particles in ferrofluids [10]. In ER fluids, such a decrease of apparent viscosity can be achieved by a

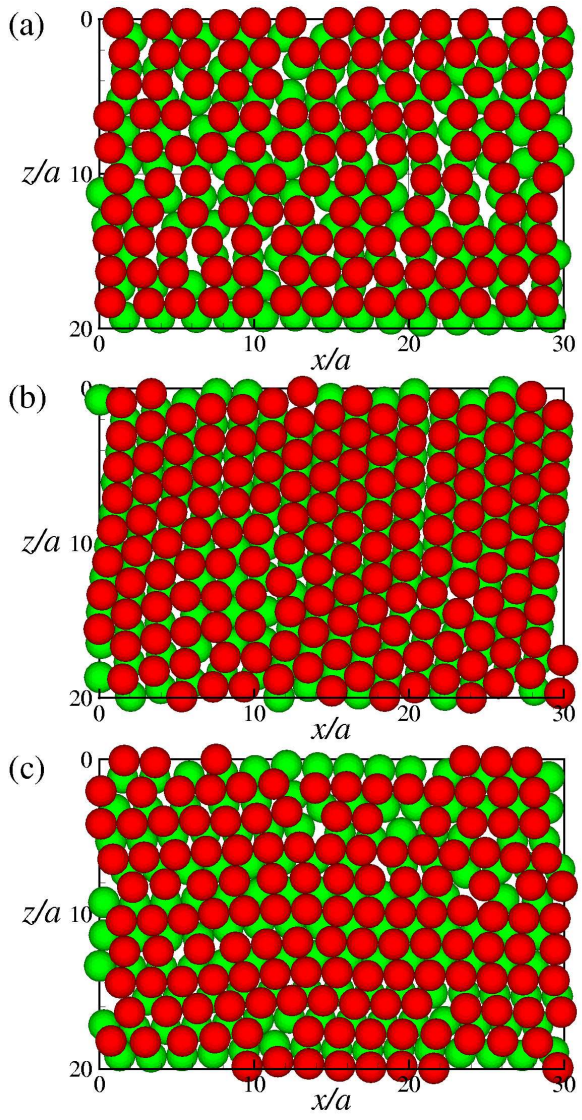

Figure 3.31: Order structures in the horizontal plane for (a) $\phi = 0.52$ and $H_y/a = 9$, (b) $\phi = 0.60$ and $H_y/a = 9$, and (c) $\phi = 0.60$ and $H_y/a = 10$. Green (lighter) particles are in the lower layer and red (darker) particles are in the upper layer.

DC electro-rotation of suspended particles (Quincke rotation) [102]. If a DC electric field is applied in the velocity-gradient direction on suspensions under a steady shear, the particles experience an electric torque in the vorticity direction, which makes the particles act as a colloidal motor [127, 134]. Lemaire *et al.* [127] have suggested a simple model to predict the apparent viscosity of sheared suspensions under Quincke rotation. However, the detailed micro-structure and rheological behavior of sheared suspensions under an external torque are not fully understood.

Rheological properties of suspension flows, such as the apparent viscosity and the normal stress differences, are closely related to the micro-structure of the suspension. For example, in suspensions of non-Brownian particles under a steady shear, irreversible effects introduced by small roughness elements on the particle surface, residual Brownian force, and/or surface charge result in an anisotropic micro-structure, which is responsible for the non-Newtonian rheology [25]. In recent studies of the colloidal [120] and non-Brownian suspensions [197, 231] under a steady shear, an ordering transition is observed at high volume fractions ($\phi \simeq 0.50$). This non-equilibrium phase transition of non-Brownian particles is different from the thermodynamic phase transition of colloidal particles in that the process is driven mostly by the shear-induced hydrodynamic interactions between particles. As the suspension undergoes the ordering transition, the apparent viscosity decreases significantly. Particularly, Yeo & Maxey [231] showed that the ordering transition and, hence, the changes in the apparent viscosity are complex functions of the ratio of the channel height to the particle radius and the volume fraction.

In this section, we show a possibility of manipulating the ordering transition of non-Brownian suspensions in a Couette flow by applying external torques in the vorticity direction to the particles. At high volume fractions $\phi \geq 0.48$, where the ordering transition occurs, the suspension can be more ordered or disordered depending on the sign of the external torque. Applying negative torque can hinder the ordering transition, which is then accompanied by an increase in the shear viscosity. As a consequence, contrary to previous results at low volume fractions ($\phi \leq 0.20$) [127], the shear stress of the suspension is not reduced dramatically by negative torques. On the other hand, a positive torque has a favorable effect on the hexagonal order. However, above a certain threshold, the order begins to be weakened by the positive torque. At moderate volume fractions $\phi \leq 0.4$, the shear and vortex viscosities are neither sensitive to the sign nor the magnitude of torque.

3.5.1 Simulation parameters

We focus on the volume fractions around which an ordering transition of non-Brownian suspensions occurs, $\phi = 0.48 \sim 0.52$ [231]. The computational domain is $H_x \times H_y \times H_z = 30a \times 20a \times 20a$, in which a is the particle radius and H_x, H_y, and H_z denote the lengths of the domain in the velocity (x), velocity-gradient (y), and vorticity (z) directions, respectively. Periodic boundary conditions are used in the horizontal directions (x and z). The computational domain is bounded by two parallel walls located at $y = 0$ and H_y. The lower wall is fixed and the upper wall is moving in the x-direction with velocity $V_{upp} = \dot{\gamma} H_y$, where $\dot{\gamma}$ is the nominal shear rate. The external torque is varied between $-3 \leq T^* \leq 3$, in which T^* is the torque normalized by the fluid viscosity μ_0 and $\dot{\gamma}$, $T^* = T/8\pi\mu_0\dot{\gamma}a^3$. In Couette flow, the suspended particles rotate in the clockwise (negative) direction. When a negative torque is applied, the particles rotate faster and a positive torque retards the rotation. To model irreversible forces, an elastic contact force is used when the shortest distance between two particle surfaces ($a\epsilon$) is smaller than $0.01a$ [230]. The magnitude of the contact force is set to keep the minimum separation distance $a\epsilon_{min} \simeq 0.002$ in all simulations.

Initial random configurations for the simulations are generated by a molecular dynamics procedure. First, the simulations with zero torque are allowed to evolve until the suspension reaches a stationary state. Then, an external torque is applied to the suspension. It usually takes about $t\dot{\gamma} \simeq 100$ to reach a new stationary state after a torque is applied.

3.5.2 Results and discussions

Figure 3.32 shows illustrative examples of the effects of an external torque on ordering transitions. For $H_y/a = 20$, an ordering transition begins around $\phi = 0.48$ [231]. At $\phi = 0.48$, the suspension is in a mixed disordered-ordered state whereby a hexagonal order exists near the wall with a disordered state in the core of the channel (figure 3.32 a). The suspension has a fully hexagonal order across the whole channel when $\phi \geq 0.52$ (figure 3.32 c). When the positive torque $T^* = 2$ is applied to the suspension in a mixed state ($\phi = 0.48$), the hexagonal order near the wall is more pronounced (figure 3.32 b). On the other hand, at $\phi = 0.52$, the hexagonal order in the core of the channel is disturbed after the particles are subjected to the negative torque $T^* = -2$ (figure 3.32 d).

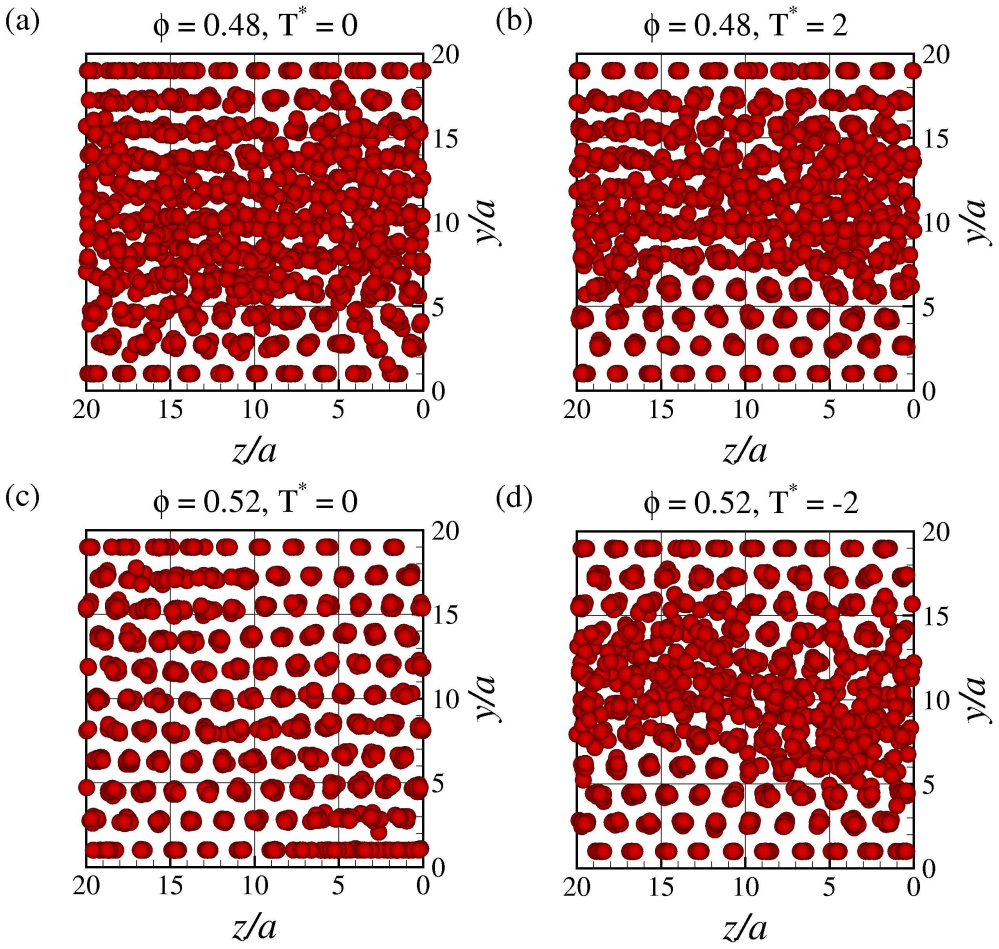

Figure 3.32: Snapshots (end view) for $\phi = 0.48$ (a,b) and $\phi = 0.52$) (c,d). For visualization, the particle radius is reduced to 1/2 of the actual size.

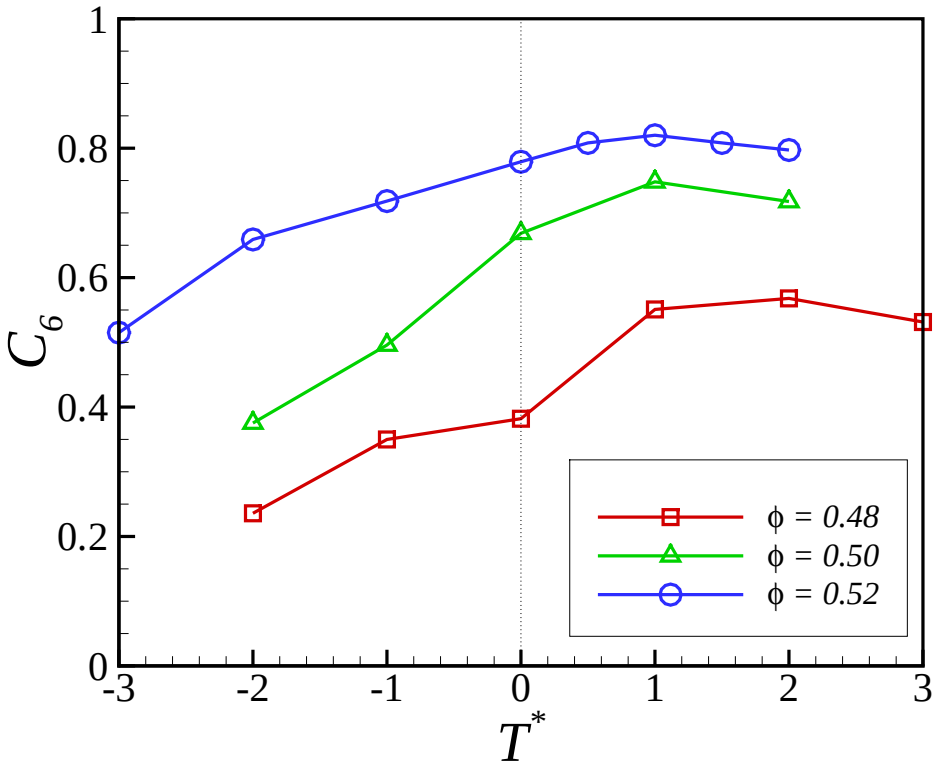

Figure 3.33: The order parameter C_6 as a function of the non-dimensional torque T^*.

To investigate the hexagonal order quantitatively, Kulkarni & Morris [120] suggested a hexagonal order parameter C_6,

$$C_6 = \frac{\int_0^{2\pi} g(\psi)\cos(6\psi)d\psi}{\int_0^{2\pi} g(\psi)d\psi}, \tag{3.22}$$

in which ψ denotes the azimuthal angle measured from the positive vorticity (z) direction and $g(\psi)$ is the pair-distribution function in $y-z$ plane averaged over the radial interval $2a < r < 2.1a$. $C_6 = 1$ for a perfect hexagonal order in $y-z$ plane and $C_6 = 0$ if the suspension micro-structure is isotropic. C_6 for different ϕ is shown in figure 3.33 as a function of T^*. It is clearly seen that the hexagonal order is always weakened by the negative torque. On the other hand, the effect of positive torque on the suspension is not straightforward. When a positive torque is applied, C_6 increases at first and then starts decreasing slowly after a threshold T^*_{crit}. T^*_{crit} seems to depend on the order state at $T^* = 0$. Both for $\phi = 0.50$ and 0.52, T^*_{crit} is observed around $T^* \simeq 1$, while T^*_{crit} for $\phi = 0.48$ is found at larger T^*, $T^* \simeq 2$.

The shear stress of suspension flows at low Reynolds number in the presence of particle torques is [13, 230]

$$\tau^* = 1 + \langle\sigma^*_{xy}\rangle + 3\phi T^*, \tag{3.23}$$

in which $\langle\cdot\rangle$ denotes an average over the whole suspension, and τ^* and σ^*_{xy} are, respectively, the shear stress and $x-y$ component of the symmetric part of the particle stress tensor normalized by $\mu_0\dot{\gamma}$. The sum of the first two terms on the right hand side of (3.23) corresponds to the effective shear viscosity; $\mu_s/\mu_0 = 1+\langle\sigma^*_{xy}\rangle$. In suspensions under steady shear, normal relative motions between particles, which may occur during tumbling of a particle doublet by the shear flow, generate stresslets proportional to the inverse of the gap between particles ($\sim 1/\epsilon$), which is a major contributor to μ_s [73]. However, once the hexagonal order is developed, most particle interactions are tangential relative motions between particle strings, whose contribution to μ_s ($\sim \log\epsilon$) is much smaller than that from the normal motion. As a consequence, in the previous studies on suspensions under a steady shear, the decrease of μ_s is observed if a hexagonal order is present in suspensions [120, 197, 231].

The shear viscosity is shown in figure 3.34 (a). In general, μ_s is a decreasing function

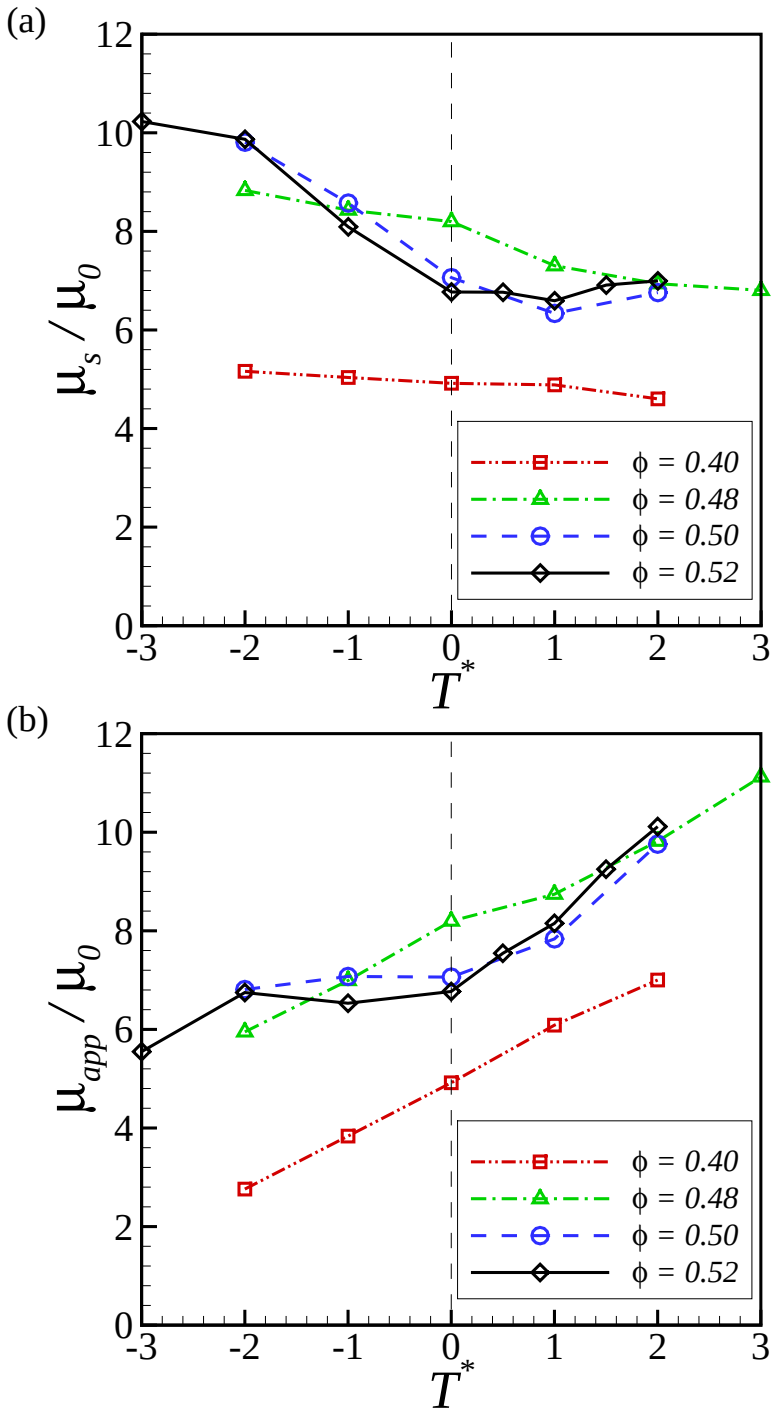

Figure 3.34: The shear (a) and apparent viscosities (b) as functions of the non-dimensional torque.

of T^*. At $\phi = 0.40$, where the suspension is in a disordered state, μ_s is much less sensitive to the external torque. There is only less than 10% difference between μ_s for $T^* = -2$ and 2. At $\phi = 0.48$, in which the ordered region is confined near the wall, the changes in μ_s by negative T^* is not significant similar to $\phi = 0.40$. A dramatic increase of μ_s is observed at $\phi \geq 0.50$ when negative T^* is applied. As the hexagonal order is disturbed by negative T^*, a disordered region emerges in the channel core, which in turn results in the increase of μ_s. On contrary, the decrease of μ_s by positive T^* is most pronounced for $\phi = 0.48$; μ_s is decreased about 15% by changing T^* from 0 to 2. However, when a positive torque is applied on the already ordered suspensions ($\phi \geq 0.52$), the changes in μ_s are not noticeable. Local minima of μ_s are observed for $\phi = 0.50$ and 0.52, which correspond to the maxima of C_6 in figure 3.33.

Although the shear viscosity is an important parameter in studying suspension rheology, it is not easy to obtain μ_s directly in the experiments of sheared suspensions under an external torque. Here, we show the apparent viscosity, which can be obtained by measuring the shear stress on the top wall. The apparent viscosity of suspension μ_{app} is defined by a simple constitutive equation, $\tau = \mu_{app}\dot{\gamma}$, or $\mu_{app} = \mu_s + 3\mu_0\phi T^*$. The definition of μ_{app} implies that, if suspension micro-structure, or μ_s, is not altered by an external torque, μ_{app} can be increased or decreased by changing T^* and it may be possible to observe even a "negative viscosity" [127]. The theoretical prediction of the "negative ER effect" by [127] assumes that μ_s is a function of ϕ only, *i.e.* the micro-structural change is negligible. The result for $\phi = 0.40$ indicates that the assumption in [127] is indeed valid at lower volume fractions ($\phi \leq 0.40$). However, once a ordering transition occurs, μ_s becomes a function of both ϕ and T^* and the previous analysis is no longer applicable in this regime. If suspensions are in a ordered state, the magnitude of negative T^* needed to observe the "negative ER effect" would be much higher than that predicted by the analytical model [127].

The apparent viscosity is shown in figure 3.34 (b). As μ_s is only weakly dependent on T^* at $\phi = 0.40$, μ_{app} is seen to be a linear function of T^*. A notable change in μ_{app} is observed when $\phi \geq 0.50$. For $\phi \geq 0.50$, the contribution from negative T^* to μ_{app} is somehow balanced by the increase of μ_s. As a result, μ_{app} remains almost unchanged regardless of the magnitude of negative T^* in the range of the present study. For $\phi = 0.52$, it is observed that, after a threshold $T^* \simeq -2$, μ_{app} begins to decrease.

One of the important rheological parameters in ER or MR fluids is the vortex viscosity

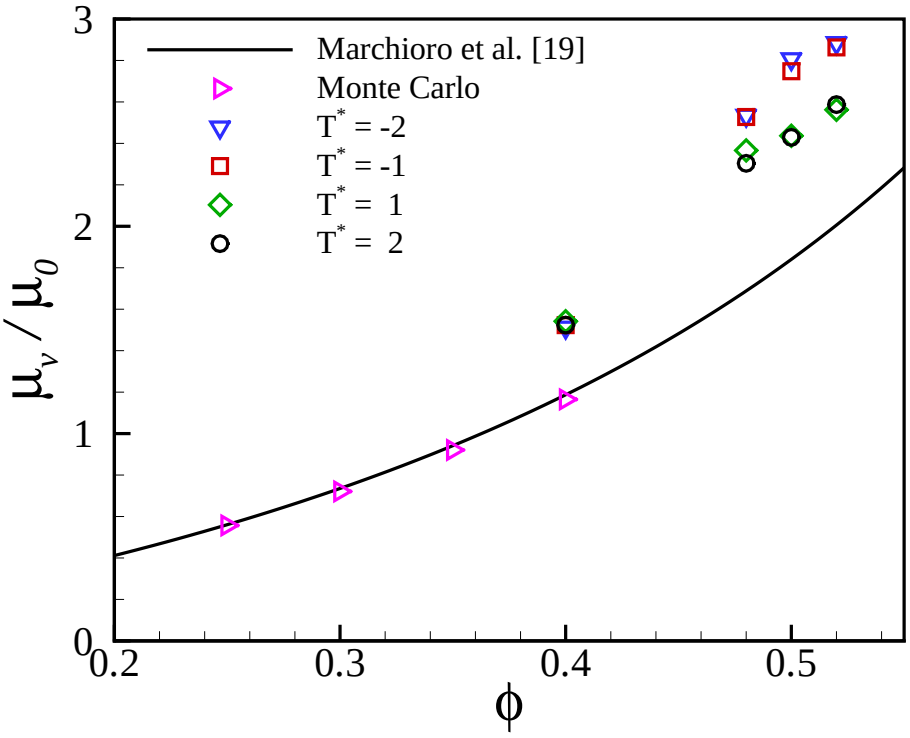

Figure 3.35: Variations in the vortex viscosity μ_v as a function of volume fraction for different values of the non-dimensional torque in a confined shear flow. Also shown are results of Monte Carlo simulations for randomly seeded suspensions in a homogeneous uniform shear flow, compared to prior results [143].

μ_v, which is a measure of the hydrodynamic resistance to an applied external torque. The vortex viscosity μ_v is defined as [27, 68]

$$\frac{\mu_v}{\mu_0} = \frac{3\phi T^*}{2\langle\Omega_z\rangle/\dot{\gamma} + 1}, \tag{3.24}$$

in which $\langle\Omega_z\rangle$ is the averaged angular velocity of the particles in the vorticity direction. In an infinite domain, Marchioro *et al.* [143] have calculated μ_v by a Monte Carlo procedure for a wide range of ϕ. For a comparison, μ_v computed by FCM in a tri-periodic domain is shown in figure 3.35 together with the numerical fitting curve by Marchioro *et al.* [143]. μ_v in the present simulation is estimated from an ensemble average of 100 random configurations for each ϕ. The agreement with [143] is excellent. Due to the absence of any microstructure, μ_v obtained by the Monte Carlo approach does not depend on the sign or magnitude of T^*.

In figure 3.35, the vortex viscosity estimated by dynamic simulations of the confined

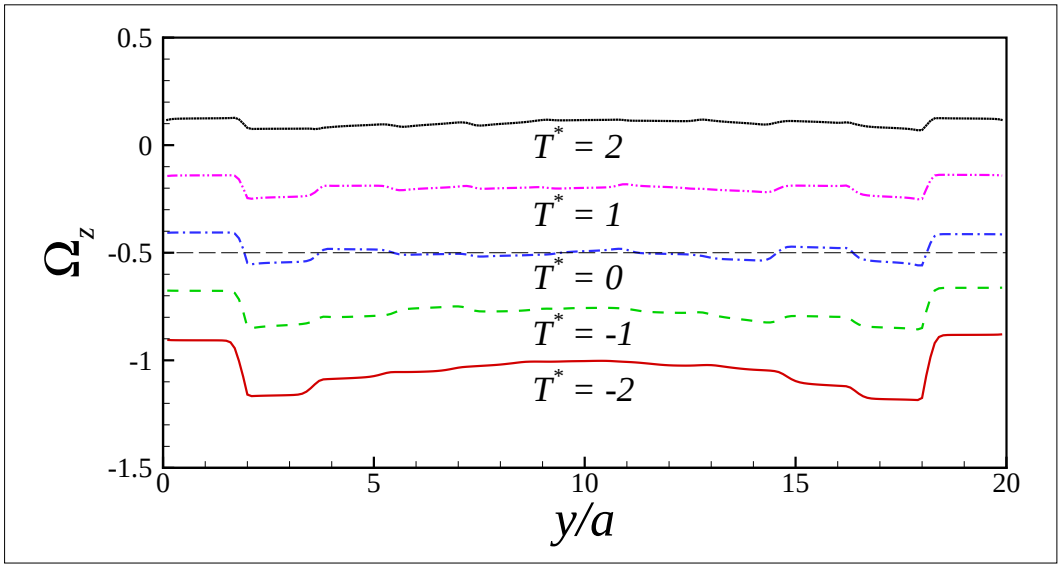

Figure 3.36: Effects of the torque on the angular velocity in the vorticity direction for $\phi = 0.52$ and $H_y/a = 20$.

steady shear flow is presented. At $\phi = 0.4$, it is observed that μ_v obtained in the dynamic simulations is larger than that by the Monte Carlo approach in an infinite domain. In the previous boundary element computation of confined sheared suspensions, the vortex viscosity of confined suspensions was slightly lower than that of the infinite domain [68]. Hence, the increase of the vortex viscosity seen in the present dynamic simulations may be due to the formation of hydroclusters [151]. At $\phi = 0.40$, μ_v is not sensitive to the signs and magnitudes of T^*. On the other hand, a bifurcation of μ_v is observed when $\phi \geq 0.48$, where the hexagonal order is present in the suspension. In general, μ_v for negative T^* is always larger than that for positive T^*. At $\phi = 0.48$, μ_v for positive T^* is a decreasing function of T^* for $T^* \leq 2$, as the suspension becomes more ordered, while the effect of the negative torque, disturbing the order structure, is not noticeable. It seems that, because the suspension is already in a disordered state except near the wall, μ_v is less sensitive to the magnitude of torque for negative T^*. On the contrary, $\phi \geq 0.50$, μ_v does not change significantly when $T^* > 0$.

The changes in the ordered state correspond to the changes in the angular velocities of the suspended particles. In a homogeneous suspension, the additional hydrodynamic force from neighboring particles due to the external torques tend to be canceled out. In a wall-bounded sheared suspensions, however, the symmetry in the suspension microstructure is

broken and the response of the suspension to an external torque now depends on the sign of the torque. Figure 3.36 shows the mean angular velocity in the vorticity direction for $\phi = 0.52$ and $H_y/a = 20$. Similar to the mean particle velocity (3.4), the mean angular velocity is defined as

$$\phi_A \Omega_z(y) = \frac{1}{H_x \times H_z} \sum_{i=1}^{N_p} \iint H(a - |\boldsymbol{x} - \boldsymbol{Y}^i|) \Omega_z^n dx dz, \tag{3.25}$$

$$\langle \Omega_z(y) \rangle = \frac{\langle (\phi_A \Omega_z)(y) \rangle}{\langle \phi_A(y) \rangle}. \tag{3.26}$$

The particle-wall resistance relation for the hydrodynamic torque in a shear flow is given by [22, 230],

$$Y^C \Omega_z^D / \dot{\gamma} = T^* + 3Y^A (V_x - V_x^\infty)/4a\dot{\gamma} - Y^H = T^* + T_G^*, \tag{3.27}$$

where Ω_z^D is the retarded angular velocity $\Omega_z^D = \Omega_z + 0.5\dot{\gamma}$, Y^C, Y^A, and Y^H are the resistance functions, which depend on the distance from the wall, V_x is the translational velocity in the velocity direction, and V_x^∞ is the background velocity by the imposed shear rate. When a particle is close to the wall, both Y^C and T_G^* are positive, which indicates that the suspended particles near the wall rotate more slowly than the bulk when $T^* = 0$. Similarly, for negative T^*, $|T^* + T_G^*| < |T^*|$ and the particles near the wall rotates slower than those in the core of the channel. On the other hand, if a positive torque is applied, $|T^* + T_G^*| > |T^*|$, indicating $|\Omega^D|$ for the particles near the wall becomes larger than that in the core. The asymmetric response to the sign of T^* may be explained by these wall-induced hydrodynamic interactions. As the dynamics of the wall layer is decoupled from that in the core before an ordering transition occurs, the wall effects are localized near the wall and the bulk dynamics does not change noticeably. However, near the ordering transition, a long-range correlation develops and the wall-induced hydrodynamic interactions may alter the overall suspension dynamics.

Here, we have not specified a way to impose an external torque on the particles. The external torque may be achieved by applying magnetic or electric fields as seen in ferro- or ER fluids. However, in concentrated suspensions, electric or magnetic coupling between particles may be important, which is not considered in the present study. The effect of electric or magnetic coupling between particles is a subject of further investigation.

3.6 Conclusions

In this chapter, we have reported on the fully three-dimensional numerical simulations of concentrated suspensions of non-colloidal particles in Couette flow using the force coupling method. To investigate the wall effects on the suspension dynamics, wide ranges of volume fraction and channel height are considered; $\phi = 0.20 \sim 0.60$ and $H_y/a = 10 \sim 40$, in which ϕ is volume fraction and H_y and a denote the channel height and the particle radius. In the Couette flow suspensions, there is a critical volume fraction around which the suspension dynamics are completely changed. In an analogy to hard-sphere liquids, the suspension can be categorized by disordered fluid and ordered crystal regimes below and above the critical point, respectively. It is found that the critical volume fraction depends on the channel height. We have investigated the dynamics in the disordered fluid regime in the first two sections (3.2 and 3.3) and in the ordered crystal regime in the last two sections (3.4 and 3.5).

In concentrated suspensions, the strong particle-wall lubrication inhibits particles near the wall from being resuspended into the core region. As a result, one or more particle layers are formed near the wall depending on the volume fraction. Although the present simulations are performed only for the plane Couette flow, it seems that the particle layering at high volume fraction is common in most wall-bounded flows. Even in the Poiseuille flows where most particles migrate toward the center of the channel, there is evidence of the particle layering [84]. In the disordered fluid regime, since the micro-structure inside of the particle layer is significantly different from that in homogeneous suspensions, it is not straightforward to predict the rheological properties in wall-bounded flows from the results obtained in unbounded domain. It is found that the width of the particle layer is not sensitive to H_y/a once the channel is wide enough. At $\phi = 0.4$, it is observed that the layering of particles is dominant for $0 \leq y/a \leq 7$ and beyond this the suspension is quasi-homogeneous similar to unbounded suspensions. Based on the observation, the rheological properties are calculated separately in the core and wall regions.

The rheological properties, such as the relative viscosity and normal stress differences, in the core region agree well with the results in an unbounded domain. In the wall region, the formation of particle layers leads to rheology of the suspension distinct from unbounded suspensions. As H_y/a increases, the ratio of the core region to wall region grows larger so

that the bulk rheological properties should resemble more those in unbounded suspensions. Interestingly, there is no difference in the normal stress differences between $H_y/a = 20$ and $H_y/a = 30$ at $\phi = 0.4$ in the present simulations, even though the ratio of the core to wall region increases from 1 to 2. It should be noted that even at $H_y/a = 30$ it seems that suspensions are still in a discrete regime. Hence, a simple extrapolation to higher H_y/a from the present results may not be appropriate.

The micro-structure clearly shows the different dynamics depending on the distance from the wall. At $\phi = 0.4$, the micro-structure in the core region resembles that in the homogeneous suspensions. The shear structure (higher probability near the compressive axis) is missing in the pair-distribution function $g(\theta)$ for particles in the particle layer ($y/a < 2$). In the particle layer, most particle-particle interactions arise from the normal motion between the particles in the same particle layer ($\theta = 0$ or π) or from the tangential interaction with particles above ($\theta = \pi/2$). In the buffer layer ($2 < y/a < 5$), the pair-distribution function $g(\theta)$ shows the characteristics of both the homogeneous suspension and the particle layer.

It is shown that concentrated Couette flow suspensions exhibit anomalous diffusion on the intermediate timescale, on which normal diffusion is observed for homogeneous suspensions. Based on the results in section 3.2, the channel is divided into four zones and the behavior of particles in each zone is investigated. For the diffusion perpendicular to the wall, particles exhibit anomalous diffusion due to a strong spatial coherency induced by the wall effects. Particularly, the particles in a well-structured particle layer located next to the wall (Zone I) show superdiffusive behavior. The probability density functions both for the position and the wall-normal velocity show wider tails compared to the Gaussian distribution, indicating the stochastic processes involved in the motion of the particles are highly intermittent, which may be related with the superdiffusivity of the particles. Subdiffusion is observed for the particles in Zone III and IV. As the diffusive behavior changes from superdiffusion in Zone I to subdiffusion in Zone III, normal diffusion is observed in Zone II. The subdiffusion in Zone III is related with the trapping of the particles in the particles layers near the wall, Zone I + II. In confined suspensions, the available lengthscale for the suspension dynamics is restricted by the size of the confinement, which will disable some of the large-scale dynamic modes [66]. It seems that subdiffusion in Zone IV is related with a disturbance in large-scale collective motions, such as the formation of hydroclusters, by

the size of the confinement. As the volume fraction increases from $\phi = 0.25$ to 0.40, the diffusive behavior of the particles in the channel center changes from normal to subdiffusion, implying the largest lengthscale related with suspension dynamics increases with the volume fraction. It is worthwhile to note that, while most modeling approaches to suspension flows are based on the results in homogeneous suspensions, the present study indicates that the models may fail to predict the diffusive behavior not only near the wall (Zone I+II) but also in the core (Zone IV).

As the bulk volume fraction approaches $\phi \simeq 0.50$, non-colloidal Couette flow suspensions undergo a phase transition. This non-equilibrium phase transition is of interest in that the suspension will cease to flow due to the divergence of the effective viscosity as the volume fraction approaches the random close packing limit if the ordering transition does not occur. When a Couette flow suspension is in an ordered state, the effective viscosity is significantly lower than that in the high frequency limit. One of the first observations of the shear-induced ordering of non-colloidal suspensions is done by Abbott *et al.* in 1991 [3] in the experiments of concentrated suspensions of bimodal particles in the circular Couette flow. However, the ordering transitions of non-colloidal suspensions had been virtually unexplored until the first numerical observation by Sierou & Brady in 2002 [197] in an infinite domain.

Here, it is shown that the shear-induced crystallization of non-Brownian suspensions under a strong confinement is dramatically different from the previous results in homogeneous suspensions [120, 197]. As the volume fraction is higher near the wall than the bulk, an ordering transition occurs earlier in the wall region. At $\phi = 0.48$ and $H_y/a \geq 15$, a hexagonal structure ($y - z$ plane) of particle strings (x-direction) is observed near the wall, while the suspension in the core of the channel is still in disordered state. For a strongly confined system $H_y/a \leq 11$, the order state and rheology depend on the commensurability. However, due to the competition between the wall effects and shear-induced hydrodynamic forces, the relation is not so clear for larger channels $H_y/a \geq 20$. At $\phi = 0.60$, it is observed that the order structure in horizontal plane exhibits a transition from triangular to rectangular structures, similar to the equilibrium phase transitions in hard-sphere fluids. It is shown that due to the complex phase behavior, the rheological parameters, such as the relative viscosity and the particle pressure, are nonlinear functions of both the channel height and the volume fraction.

We have shown a possibility of manipulating the ordering transition of non-Brownian

suspensions in a Couette flow by applying external torques in the vorticity direction to the particles. At high volume fractions $\phi \geq 0.48$, where the ordering transition occurs, the suspension can be more ordered or disordered depending on the sign of the external torque. Applying negative torque can hinder the ordering transition, which is then accompanied by an increase in the shear viscosity. As a consequence, contrary to previous results at low volume fractions ($\phi \leq 0.20$) [127], the shear stress of the suspension is not reduced dramatically by negative torques. On the other hand, a positive torque has a favorable effect on the hexagonal order. However, above a certain threshold, the order begins to be weakened by the positive torque. At moderate volume fractions $\phi \leq 0.4$, the shear and vortex viscosities are neither sensitive to the sign nor the magnitude of torque.

Chapter 4

Stokes flow: Concentrated suspensions in Poiseuille flow

4.1 Introduction

The study on suspensions of solid particles in Poiseuille flows is essential in understanding many biological and engineering flows [178, 203]. Since the pioneering works by Batchelor [13, 14, 15], homogeneous suspensions, *e.g.* suspensions in a linear shear flow far from a solid boundary, have been extensively studied and, at least, the bulk rheological behaviour of a homogeneous suspension is well understood [159, 197]. In Poiseuille flow, however, the shear rate varies in the wall-normal direction and, as a consequence, a migration of the suspended particles towards the core region of the channel has been observed, which in turn makes the suspension field inhomogeneous. One of the first observations of the inhomogeneities in the suspension field dates back to Karnis *et al.* [105]. Nevertheless, the theoretical development on Poiseuille-flow suspensions has been slow due to the complex hydrodynamic interactions and lack of detailed experimental as well as numerical data about the suspension dynamics.

Karnis *et al.* [105] found, in the experiments in a pressure-driven tube flow, that a plug flow is developed at high volume fractions in the core region of the channel, in which the translational particle velocity is almost uniform. Since then, several experimental studies on concentrated Poiseuille-flow suspensions have been performed both in a channel [98, 98, 112, 139, 194] or in a tube flow [84]. The experimental studies reveal that the suspended particles migrate towards the core region of the channel, resulting in a gradient in the local

volume fraction, which is highest in the core of the channel and decreases closer to the wall, and a blunting of the velocity profile in the core region. Leighton & Acrivos [126] proposed a phenomenological model based on the gradient of volume fraction and the local shear rate to predict the shear-induced migration. Nott & Brady [164] suggested a suspension balance model, which relates the shear-induced migration to the particle stresses, based on the phase-averaged mass and momentum conservation equations [61]. Morris & Boulay [160] and, subsequently, Miller & Morris [155] proposed modifications of the suspension balance model, which has now become a standard predictive model. A more systematic theoretical analysis of slightly inhomogeneous suspensions has been performed by [143, 242]. Through the theoretical studies, it is now generally understood that the imbalance of the normal stresses in the wall-normal direction induces the particle migration. However, still there is no direct measurement of the local suspension properties across the channel, supporting the theoretical studies.

Measuring suspension properties, such as particle stresses, is a challenging task. For example, it is only recently that the particle pressure of Couette-flow suspensions has been successfully measured [52]. Numerical simulations, based on Stokesian dynamics, have provided invaluable information in understanding suspension dynamics [23]. However, due to a lack of suitable numerical techniques, numerical simulations of concentrated suspensions have largely been limited to homogeneous suspensions [197] or, for inhomogeneous suspensions, to two-dimensional simulations [164, 199]. Since Nguyen & Ladd [162] developed a numerical method to incorporate lubrication interactions into the lattice-Boltzmann method (LBM), LBM becomes a popular tool to investigate the three-dimensional wall-bounded suspensions [116, 119, 215]. More recently, Yeo & Maxey [233] modified the force-coupling method to account for the near-field interactions and for the fast three-dimensional simulations of concentrated suspensions. This scheme, which incorporates low-order force multipole representations and viscous lubrication corrections, has been successfully employed to study wall-bounded Couette flows of concentrated suspensions [230, 231, 232].

Here, we report on three-dimensional numerical simulations of concentrated suspensions of $O(1000)$ monodisperse non-colloidal particles in plane Poiseuille flows using the force-coupling method. The main goals of this study are to investigate the dynamics of Poiseuille-flow suspensions via phase-averaged suspension quantities, examining these as functions of the distance from the wall and both the bulk and local volume fractions, and to provide

statistics essential in developing and verifying the suspension models. The remainder of this chapter is organized as follows: the simulation parameters are shown in section 4.2; the volume fraction profiles are compared with the previous experiments in section 4.3.1; section 4.3.2 describes the velocity statistics, such as mean and fluctuating particle velocities. In section 4.4, the particle stresses are investigated as functions of the distance from the wall and compared with the suspension model by Morris & Boulay [160].

4.2 Simulation parameters

We use the force-coupling method (FCM) developed in Chapter 2 to compute the particle-particle and particle-wall hydrodynamic interactions for Poiseuille flow in a channel. Here, the interparticle potential force is computed as

$$\boldsymbol{F}_{ij}^{P} = \begin{cases} -6\pi\mu a V_{ref} \left(\frac{R_{ref}^2 - |\boldsymbol{r}|^2}{R_{ref}^2 - 4a^2} \right)^6 \frac{\boldsymbol{r}}{|\boldsymbol{r}|} & \text{if } |\boldsymbol{r}| < R_{ref} \\ 0 & \text{otherwise,} \end{cases} \tag{4.1}$$

in which V_{ref} is a constant, $\boldsymbol{r}$ is a relative position vector $\boldsymbol{Y}^j - \boldsymbol{Y}^i$, and R_{ref} is a cut-off distance. To minimize the effects of the contact force on the suspension dynamics, the contact force is activated only when the separation distance between particles $\epsilon < 0.002a$, *i.e.* $R_{ref}/a = 2.002$. V_{ref} is chosen to keep the minimum separation distance $\epsilon_{min} \simeq 0.001a$.

To verify the numerical method, we compare the translational velocity of a single particle parallel to the wall calculated by FCM to the numerical result by Ganatos *et al.* [76] (GWP82). In GWP82, a boundary collocation technique was used to compute the translational velocity of a sphere, which is almost exact for $Y/a \geq 1.1$. Lomholt & Maxey [135] have shown that FCM results agree well with GWP82 for $Y_2/a \geq 1.1$. Here, we compare FCM simulations with GWP82 for $Y_2/a < 1.1$, where the lubrication interaction becomes important. The FCM simulations are performed for the computational domain $H_x \times H_y \times H_z = 30 \times 20 \times 20$ and the particle radius $a = 1$.

Table 4.1 shows the translational velocity normalized by the centerline velocity V/u_c for a particle near the bottom wall. The agreement with GWP82 is very good. The difference in the velocity is at most $O(10^{-3})$. For the particle very close to the wall, $Y/a \leq 1.01$, there is about 7% difference between FCM and GWP82. There is some uncertainty in the simulation

Table 4.1: The translational velocity of a particle at different vertical locations Y. The channel height is $H_y/a = 20$. The particle velocity is normalized by the centerline velocity u_c.

Y/a	FCM	GWP82
1.1	0.156	0.155
1.04	0.128	0.128
1.01	0.102	0.097
1.001	0.078	0.073

Table 4.2: Simulation parameters. Φ is the bulk volume fraction and N_p is the number of particles. N_x and N_z are the number of Fourier modes in the streamwise and spanwise directions, respectively. N_y is the number of spectral elements in the wall-normal direction. The length of each spectral elements are the same, $l_E = H_y/N_y$. The same numbers of quadrature points Q_E and the spectral modes P_E are used for every elements; $Q_E = 10$ and $P_E = 8$.

	Φ	H_x/a	H_y/a	H_z/a	N_x	N_y	N_z	N_p
P3S	0.3	30	18	20	96	9	64	773
P4S	0.4	30	24	20	96	12	64	1,376
P2L	0.2	40	40	30	128	20	96	2,292
P3L	0.3	40	40	30	128	20	96	3,438
P4L	0.4	40	40	30	128	20	96	4,584

results by GWP82 at these small separation distances. Due to the computational limitations at that time, they were able to compute a fully converged solution only for $Y/a \geq 1.1$ and, for locations below $Y/a = 1.1$, some functions were estimated by an extrapolation from the value at $Y/a = 1.1$. Still, the difference between the FCM results and GWP82 in the absolute value is small $\sim O(10^{-3})$. In order to resolve the hydrodynamic forces exactly for the parabolic velocity profile of a Poiseuille flow, it would be necessary to include the force quadrupole and degenerate sextupole. If a channel is much larger than the particle radius, however, the quadratic variation of the fluid velocity at the location of a particle can be effectively approximated by a linear function, which is resolved by the stresslet. It is worth noting that, using lower order, regularized force multipoles, FCM approximately resolves higher-order multipoles such as the degenerate force quadrupole and octapole, which come from the Faxén corrections.

A numerical simulation of Poiseuille flow can be performed either fixing the driving force (mean pressure gradient) or keeping the mass flux constant. In the previous Stokesian Dynamics simulations, constant mass flux simulations were performed and the pressure

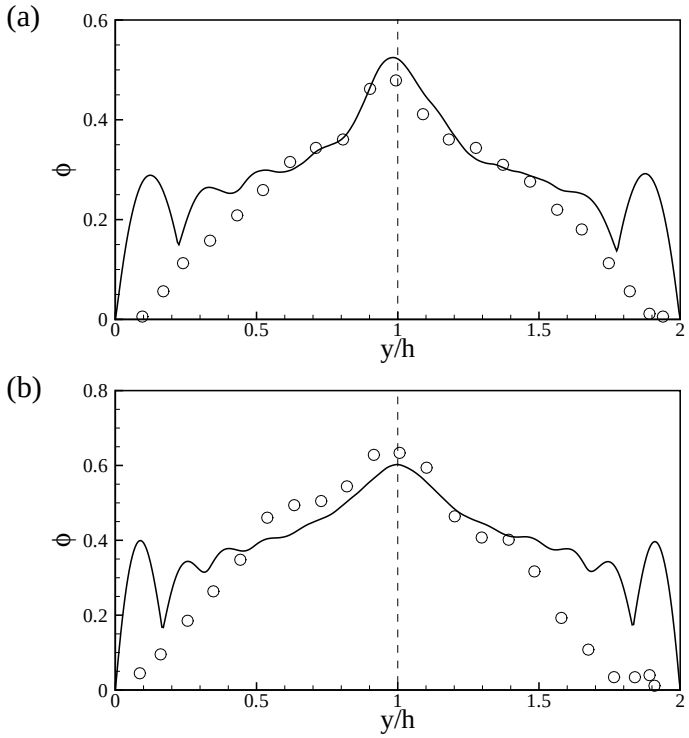

Figure 4.1: The area fraction profiles for (a) P3S and (b) P4S. The solid lines are the present simulation results and the circles are from Lyon & Leal [139].

gradient was estimated a posteriori, which is a natural choice for a resistance formulation [158, 164]. On the other hand, in the force-coupling method, which is written as a mobility problem, it is easier to control the pressure gradient. Hence, we use a constant pressure gradient condition for the present simulations and the mass flux is estimated in a post-processing stage. The simulation parameters are shown in table 4.2.

4.3 Volume fraction and velocity statistics

4.3.1 Volume fraction profile

In Poiseuille flows, the shear rate varies across the channel, which results in an inhomogeneous stress field. As a result, the suspended particles tend to migrate into the center region of the channel. It is well known that, due to the migration, the local volume fraction becomes an increasing function of the distance from the wall.

Here, we define the averaged area fraction, $\phi(y)$, as

$$\phi(y) = \frac{1}{H_x \times H_z} \left\langle \iint \chi_p(\boldsymbol{x}) dx dz \right\rangle, \tag{4.2}$$

in which $\chi_p(\boldsymbol{x})$ is an indicator function for the particle phase and $\langle \cdot \rangle$ is an ensemble average. The bulk volume fraction is given by the average of $\phi(y)$ across the channel, i.e. $\Phi = \int \phi(y) dy / H_y$.

In figure 4.1, the area fraction profiles obtained by the present simulations are compared with the experiments 562 ($\Phi \simeq 0.3$) and 482 ($\Phi \simeq 0.4$) in Lyon & Leal [139]. Both the simulation and the experimental results show a local peak at the core of the channel. The ϕ profiles of the present simulations agree well with [139] near the core of the channel. However, near the wall, the volume fraction profiles of the experiments quickly drop to zero, while the FCM simulation predicts the existence of a particle layer and that ϕ decreases more slowly in the intermediate region, $y/h < 0.5$. Here, h is the half channel gap $h = H_y/2$

The existence of a wall layer has been reported in several numerical simulations of wall-bounded Couette-flow suspensions [116, 119, 215, 230]. As there is no net hydrodynamic lift force acting on a particle in Stokes flows, the upward (or downward) vertical displacement of a particle in a shear flow is usually understood by the interaction with another particle below (or above) the center of the reference particle. However, once a particle is located next to the wall, the particle interacts only with particles above and, moreover, a strong particle-wall lubrication interaction makes it harder for the particle to move away from the wall. In experiments, however, usually there are some uncertainties in the experimental conditions, such as size and shape variations, roughness elements on the surface of the particle or the wall, and interaction forces due to electrostatic charge or polymer coating. There is a possibility that such imperfections may disrupt the particle layer observed in the numerical simulations. It is also important to note that, in concentrated suspensions, it is challenging to measure the volume fraction accurately, particularly, near the wall. For example, in figure 4.1, the local volume fractions in [139] are much smaller than the simulation results near the wall, while similar in the core. As a result, if the bulk volume fraction is estimated by an average of the data over the channel height, it will be lower than the actual volume fraction. Roughly, the bulk volume fractions estimated from the experimental data are $\Phi^e \simeq 0.23$ and 0.32 for $\Phi = 0.3$ and 0.4, respectively.

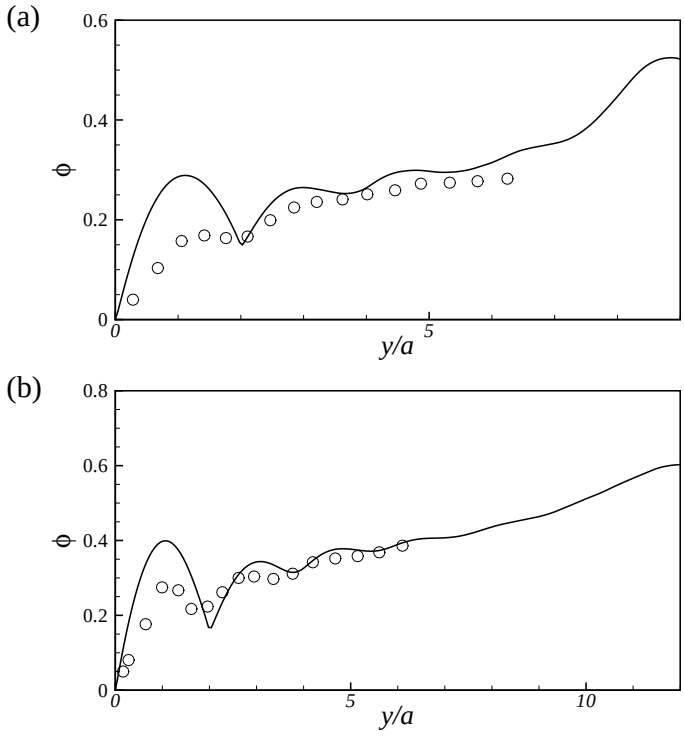

Figure 4.2: The area fraction profiles near the wall for (a) P3S and (b) P4S. The solid lines are the present simulation results and the circles are from Hampton *et al.* [84].

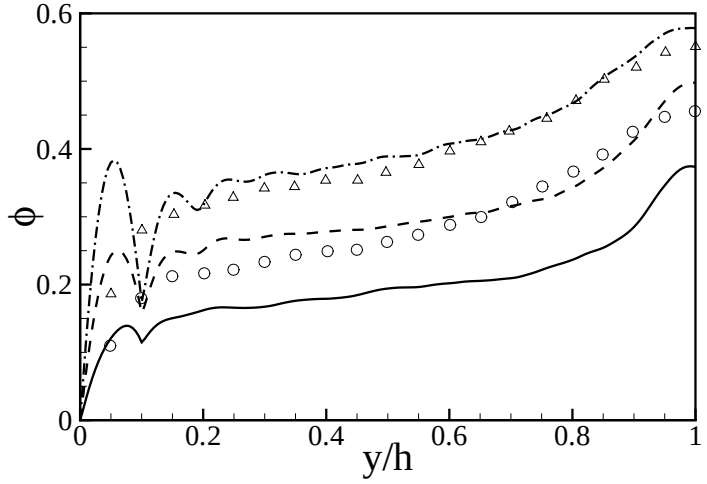

Figure 4.3: The area fraction profiles for P2L (solid), P3L (dashed), and P4L (dash-dot). The symbols are the experiments by Gilchrist [79]: $\circ$, $\Phi = 0.298$; $\triangle$, $\Phi = 0.411$.

Hampton *et al.* [84] have measured the volume fraction profiles of concentrated suspensions in a pressure-driven tube flow using nuclear magnetic resonance imaging. In their experiments of non-colloidal particles of diameter $2a = 3175\mu m$, they observed the particle layering at high volume fractions $\Phi \geq 0.30$. Figure 4.2 shows the volume fraction profiles near the wall. Because of the difference in the geometry, straight channel in the simulations versus circular tube in the experiment, it is not straightforward to compare the volume fraction profiles over the whole flow. Still, there is a good agreement in the volume fraction profiles near the wall. Unlike the results in [139], which showed a rapid decrease of ϕ profile, the volume fraction profiles of [84] agree well above the one particle diameter $y/a > 2$ both for $\Phi = 0.30$ and 0.40. At $\Phi = 0.30$, the volume fraction profile of [84] shows a weak local peak near $y/a \simeq 1$, suggesting the existence of the particle layer. However, the local volume fraction is somewhat lower than the simulation results. For $\Phi = 0.40$, the quantitative agreement is quite satisfactory even in the particle layer. It is worthwhile to note that the volume fraction in [84] is obtained by an average over a small bin, while ϕ in the simulation is computed by a direct integration of the indicator function. Further discussions about the volume fraction profiles are provided in section 4.5.

One of the most recent measurements of concentrated suspensions in Poiseuille flows were performed by Gilchrist's group [78, 77] in a wide channel, $H_y/a = 80$. In figure 4.3,

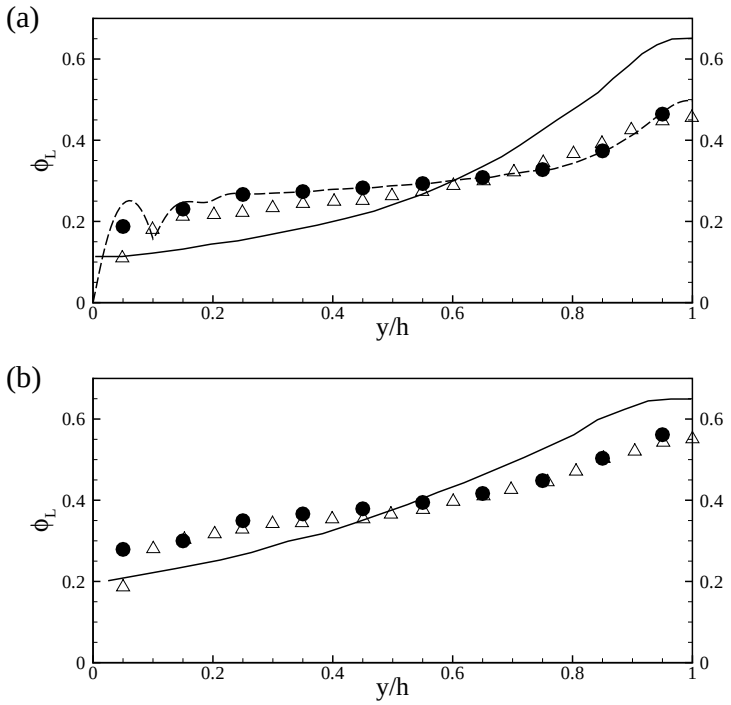

Figure 4.4: The local volume fraction profiles for (a) $\Phi = 0.3$ and (b) $\Phi = 0.4$; •, P3L and P4L; △, Gilchrist [79]; ——, Yapici *et al.* [227]. The dashed line in (a) is the area fraction (ϕ) profile of P3L.

the volume fraction profiles for $H_y/a = 40$ are compared with the experimental data [79]. The wall-normal distance is normalized by the channel half gap h. The particle radius in the experiments is about $0.5\mu m$, suggesting that there may be some limited effects from Brownian motion. Nevertheless, it is shown that the simulation and experimental data are consistent. Again, it is observed that the bulk volume fractions estimated by an average over the channel height in the experiments are lower than the actual volume fractions. Near the wall, the local volume fractions in the experiments are lower than the simulations. The first data points of the experiments are at $y/a \simeq 2a$, where the ϕ profiles show local minima. For $\Phi = 0.20$, the particle layering from the simulations is less pronounced, consistent with the results of [84].

A local volume fraction can be computed from ϕ as

$$\phi_L(y) = \frac{1}{2w} \int_{y-w}^{y+w} \phi(s) ds, \tag{4.3}$$

in which $2w$ is the width of the averaging interval. The definition is similar to the procedure

used in the experimental measurements and we set $w = a$. In contrast to the ϕ profiles, the near-wall layer and the particle depletion layer near $y/a \simeq 2$ are smoothed out in the ϕ_L profiles, as shown in figure 4.4. Elsewhere ϕ_L and ϕ are nearly indistinguishable. For comparison, we also show the volume fraction profiles from the continuum model of Yapici *et al.* [227]. While the volume fraction profiles computed by the continuum model are qualitatively similar with the experiments and the present simulations, it is shown that the continuum model predicts higher volume fraction around the core of the channel and the volume fraction decreases more rapidly with the distance from the center.

4.3.2 Velocity statistics

As the suspension field is homogeneous in a plane parallel to the wall, we define a phasic average of a variable $\boldsymbol{g}$ as Drew [61],

$$\langle \boldsymbol{g}\chi_p \rangle(y) = \frac{1}{H_x \times H_z} \left\langle \sum_{i=1}^{N_p} \iint \boldsymbol{g}^i \chi_p^i(\boldsymbol{x}) dx dz \right\rangle, \tag{4.4}$$

in which $\boldsymbol{g}^i$ and χ_p^i are the value of $\boldsymbol{g}$ and the indicator function of the i-th particle. Then, an average of $\boldsymbol{g}$ for the particle phase can be defined as,

$$\langle \boldsymbol{g} \rangle(y) = \frac{\langle \boldsymbol{g}\chi_p \rangle(y)}{\phi(y)}. \tag{4.5}$$

The particle-phase velocities normalized by the centerline velocity u_c for P3S and P4S are compared with the experiments by Lyon & Leal [139] in figure 4.5. Following [139], the centerline velocity is estimated from a parabolic velocity profile, which has the same bulk velocity as that of the particle phase Q_p;

$$Q_p = \frac{1}{H_y} \int \langle V_x \rangle dy. \tag{4.6}$$

Here, V_x is the particle velocity in the streamwise (x) direction. The velocity profiles show an excellent agreement except very near the wall $y/h < 0.2$. In the FCM simulations, due to the particle-wall lubrication interaction, there is an almost step-function increase in the particle velocity around $y/h \simeq 0.2$.

Figure 4.6 shows the average particle-phase velocity profiles for different Φ in a larger

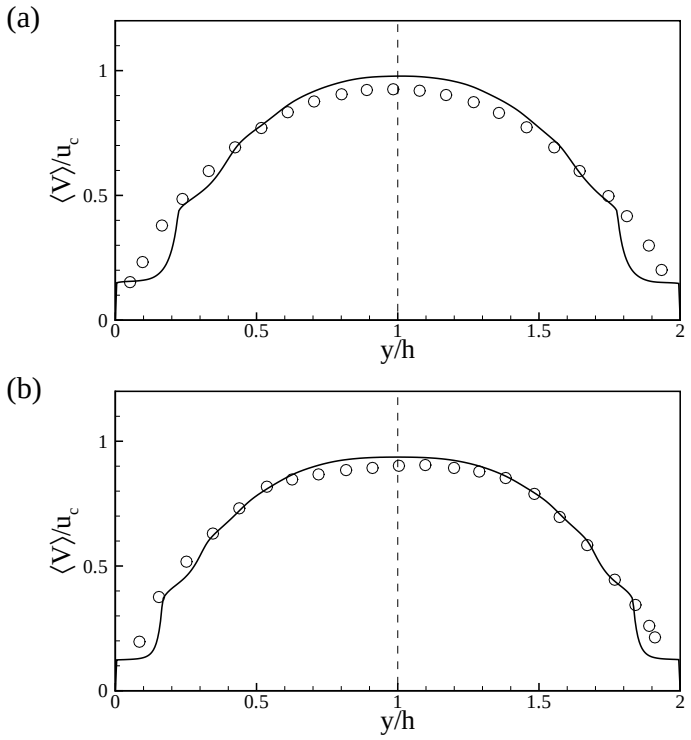

Figure 4.5: The averaged particle velocity for (a) P3S and (b) P4S. The solid lines are the present simulation results and the symbols are from [139].

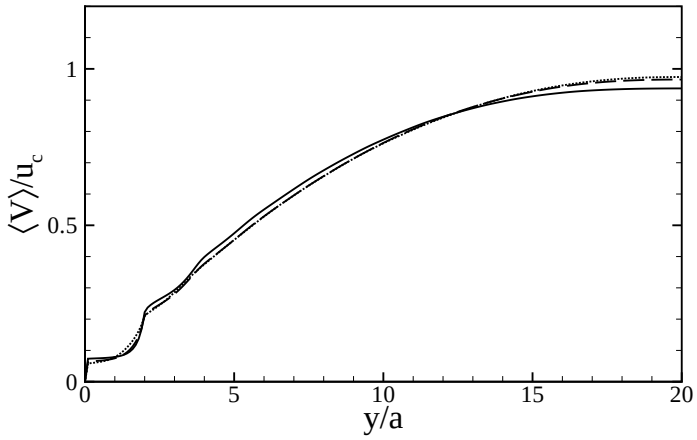

Figure 4.6: The average particle-phase velocity profiles for $H_y/a = 40$. Dotted line, P2L; dashed line, P3L; solid line, P4L.

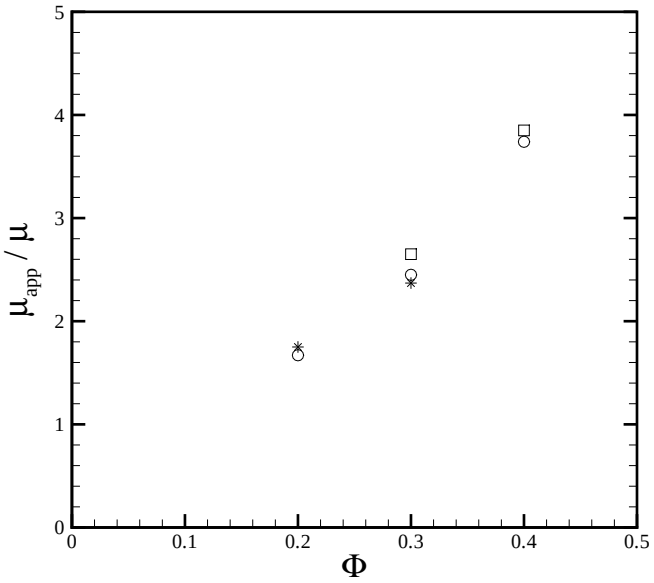

Figure 4.7: Apparent viscosity estimated from the mean flux: □ P3S and P4S; ∘ P2L, P3L, and P4L; ∗ Nott & Brady [164].

channel ($H_y/a = 40$). It is shown that the velocity profile becomes more blunted as Φ increases. The blunting of the velocity profile is more pronounced as Φ increases from 0.3 to 0.4. The maximum ϕ at the center of the channel for P4L is $\phi(h) \simeq 0.58$, while that for P3L is about 0.50. It has been observed that a sheared suspension may undergo a phase transition around $\Phi \simeq 0.52$ in wall-bounded suspensions [231] and $\Phi \simeq 0.54$ in homogeneous suspensions [120, 197]. In the experiments of concentrated suspensions in a pressure-driven channel flows for $\Phi = 0.41$, Gao *et al.* [77] found a crystal structure in the core region of the channel and noted that the suspension in the core of a pressure-driven channel flow behaves similarly to a confined fluid. The drop in the maximum velocity at the center of the channel at $\Phi = 0.40$ may be related to the high local volume fraction.

In a standard Poiseuille flow in a straight channel, the relation between the bulk velocity Q^∞, mean pressure gradient, and fluid viscosity is

$$Q^\infty = \frac{H^2}{12\mu} f^D. \tag{4.7}$$

Similarly, the apparent viscosity of Poiseuille-flow suspensions is defined by Cokelet [41] as

$$\mu_{app} = \frac{H^2}{12Q^p} f^D. \tag{4.8}$$

Hence, the apparent viscosity in the present simulation is simply

$$\frac{\mu_{app}}{\mu} = \frac{Q^\infty}{Q^p}. \tag{4.9}$$

Figure 4.7 shows the apparent viscosity estimated in the present simulations. Also shown are results from the Stokesian Dynamics simulations (SD) of Nott & Brady [164]. These SD simulations were performed for a constant suspension velocity, so μ_{app} is estimated from their mean pressure gradient data. The SD data are for ($\Phi = 0.20,\ H_y = 40.40a$) and ($\Phi = 0.30,\ H_y = 18.32a$). As the SD results of [164] are from the two-dimensional simulations of co-planar particles, the bulk volume fraction is estimated from the bulk area fraction as $\Phi = \frac{2}{3}\phi_A^b$. For $\Phi = 0.20$, the agreement between P2L and SD is good, while μ_{app} for P3S is about 10% larger than that of SD obtained in the same H_y. However, considering the differences in the simulation conditions, the overall agreement is reasonable. It has been observed, in Couette-flow suspensions, that the apparent viscosity is an increasing function of the channel height H_y/a for $H_y/a < 40$ [230, 241]. By contrast, in Poiseuille-flow suspensions, we observe that μ_{app} decreases in a larger channel. A similar behaviour has been observed by [164] for $\phi_A^b = 0.4$. However, their simulations for $\phi_A^b = 0.30$ predicted the opposite; an increase of μ_{app} in wider channels.

The particle-phase velocity fluctuation is computed as

$$v_i = \left[\frac{\langle V_i^2 \chi_p \rangle}{\phi} - \left(\frac{\langle V_i \chi_p \rangle}{\phi} \right)^2 \right]^{1/2}. \tag{4.10}$$

Figure 4.8 shows the velocity fluctuations normalized by the mean velocity Q^p in a larger channel $H_y/a = 40$. For all three components, the maxima of the velocity fluctuations are observed at $y/a \simeq 2$, where ϕ becomes minimum. Due to the wall slip, v_x and v_z have a finite value at $y \simeq \epsilon_{wall}$, in which ϵ_{wall} is the minimum separation distance between the particle and the wall. In the present study, $\epsilon_{wall} \simeq 0.001a$. The vertical velocity fluctuation is a smooth function of y near the wall, which is a natural consequence of the impermeability of the wall. It is shown that the normalized velocity fluctuations increase with Φ. Near the

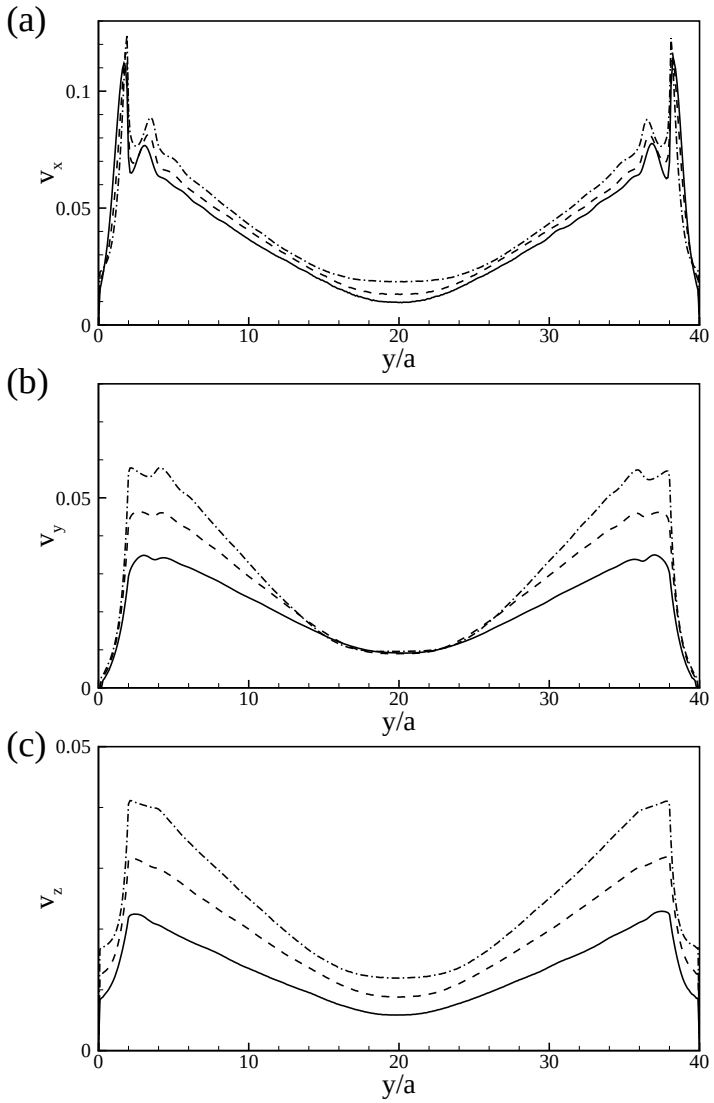

Figure 4.8: The particle-phase velocity fluctuations normalized by the mean particle-phase velocity Q^p for (a) streamwise, (b) wall-normal, and (c) spanwise components: Solid line, P2L; dashed line, P3L; dash-dot line P4L.

Table 4.3: The coefficients of the fitting curves for velocity fluctuations.

	v_x			v_y		v_z	
	C_0	C_1	C_2	C_0	C_1	C_0	C_1
P2L	0.0863	-0.117	0.0359	0.0439	-0.0402	0.0243	- 0.0212
P3L	0.0928	-0.126	0.0411	0.0598	-0.0607	0.0363	- 0.0326
P4L	0.103	-0.146	0.0516	0.0756	-0.0850	0.0476	- 0.0449

core of the channel ($16 \leq y/a \leq 24$), v_y is not sensitive to the changes in Φ unlike the other two components, v_x and v_z. As a consequence, in the core of the channel, $v_x > v_y > v_z$ at $\Phi = 0.20$, which becomes $v_x > v_z > v_y$ at $\Phi = 0.40$. The streamwise and spanwise velocity profiles become more blunted near the core as the volume fraction increases. At $\Phi = 0.40$, v_x and v_z are almost constant over $16 \leq y/a \leq 24$.

Near the wall and the core of a channel, the finite size of the suspended particles plays an important role in the suspension dynamics and, hence, it is not expected that a continuum analysis would apply. If a channel is wide enough, there exists an intermediate region, in which the spatial variation of the ensemble averaged suspension field is quasi-homogeneous on a particle scale. The suspension dynamics may be well approximated by a continuum theory in this intermediate region. Studying ensemble averaged suspension quantities in such a "well-mixed" region is important in developing a continuum model to predict the behaviour of suspension flows [61, 160, 164].

Here, we find fitting expressions for each velocity fluctuations normalized by Q^p. The fitting curves are defined as

$$P(v_i) = \sum_{p=0}^{M_P} C_p \left(\frac{y}{h}\right)^p, \tag{4.11}$$

in which M_P is the maximum order of the polynomial and C_p's are fitting coefficients. The coefficients C_p are shown in table 4.3. Different M_P are tested and it is found that v_x is well represented by a quadratic polynomial of y/h, while v_y and v_z are linear in y/h. For v_y and v_z, the slopes of the curves are linearly proportional to Φ. That is, $v_y \sim 2\kappa(y/h)\Phi$ and $v_z \sim \kappa(y/h)\Phi$ in the intermediate region, in which κ is a constant, $\kappa \simeq 0.1$.

Figure 4.9 shows the velocity fluctuations normalized by the fitting curves. The velocity fluctuations are well represented by the fitting expressions above $y/h \simeq 0.3$ for $0.2 \leq \Phi \leq 0.4$. On the other hand, near the core of the channel, the velocity fluctuations start to

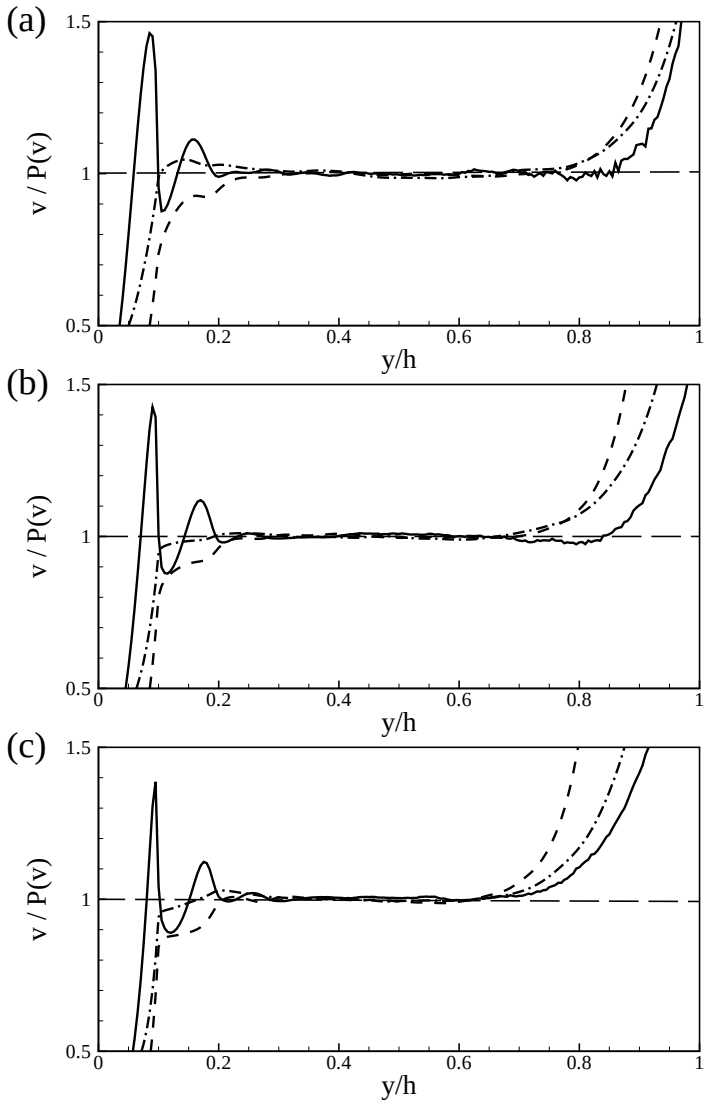

Figure 4.9: The particle-phase velocity fluctuations normalized by the fitting curves for (a) P2L, (b) P3L, and (c) P4L: solid line, v_x; dashed line, v_y; dash-dot line, v_z.

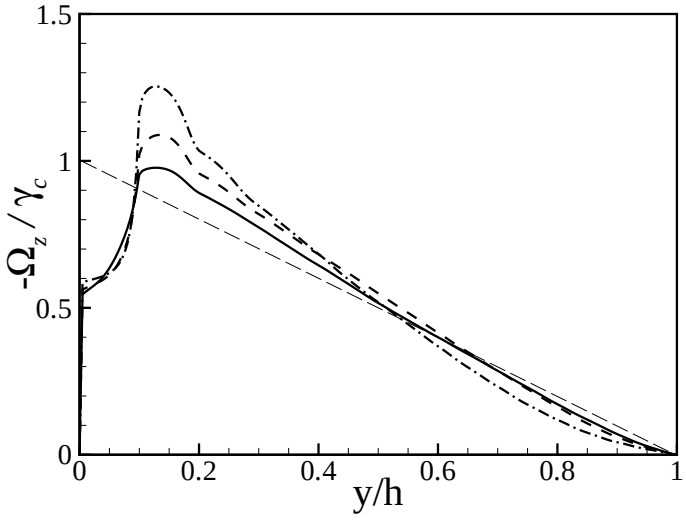

Figure 4.10: The average angular velocity normalized by $\dot{\gamma}_c = u_c/h$. Solid line, P2L; dashed line, P3L; dash-dot line, P4L. Long-dash line is the rate-of-rotational of clear flow.

deviate from the fitting expressions around $y/h \simeq 0.75, 0.7$, and 0.65 for $\Phi = 0.2$, 0.3, and 0.4, respectively. These changes in the functional form of the velocity fluctuations indicate that the width of the core region is an increasing function of Φ, while that of the wall layer is not so sensitive to the bulk volume fraction.

Next, we consider the mean angular velocity of the particles. The anti-symmetric part of the velocity gradient tensor (rate-of-rotation) of the clear flow, i.e. without suspended particles, is

$$A_{12} = -\frac{1}{2}\frac{du/dy}{\dot{\gamma}_c} = -1 + \frac{y}{h}, \tag{4.12}$$

in which $\dot{\gamma}_c$ is the shear-rate based on u_c, $\dot{\gamma}_c = u_c/h$. Using this scaling, we show the average angular velocity in the spanwise (vorticity) direction $\langle \Omega_z \rangle$ of the particle phase normalized by $\dot{\gamma}_c$ in figure 4.10. Similar to v_x and v_z, the angular velocity has a finite value very near the wall $y \simeq \epsilon_{wall}$. Note that, in the present study, the suspended particles never touch the wall due to the lubrication and potential forces. There is a thin liquid film, whose thickness ϵ_{wall} is determined mainly by the potential force and the effects of the wall on the angular velocity of the suspended particles are through the particle-wall lubrication interaction. In experiments, ϵ_{wall} may be determined by the surface asperities and, hence, the angular velocity of the particles may be affected not only by the particle-wall lubrication but also by

a friction force between the particles and the wall. Due to the lack of any experimental data, it is difficult to quantify the effects of the friction at present. However, it is not expected that the effect of the particle-wall contact is significant in the suspension dynamics outside of the first particle layer.

As observed in the velocity fluctuations, the angular velocity profile can be divided into three regions. Near the wall, the rotation of the particles in the particle layer is significantly hindered due to the particle-wall lubrication interaction, which is followed by a sudden increase of Ω_z above the first particle layer. In an intermediate region, the angular velocity decreases faster than that of the clear flow and the slope of Ω_z is an increasing function of the volume fraction. Consistent with the blunting of $\langle V \rangle$, the slope of Ω_z near the core of the channel decreases at larger Φ.

In figure 4.11, the angular velocity is compared with the wall-normal gradient of the particle-phase velocity. The velocity gradient is multiplied by $1/2$ analogous to the rate-of-rotation. Near $y/a \simeq 2$, the velocity gradient diverges because the particle-phase velocity profile is not smooth at the depletion layer just above the particle layer (figure 4.6). In an intermediate region, both the angular velocity and the particle velocity gradient can be approximated by linear functions, indicating that in the intermediate region the particle velocity is still a quadratic function of y.

4.4 Particle stresses

4.4.1 Normal stresses

Following Drew [61], the ensemble averaged momentum conservation equations for the particle phase in Stokes flows are

$$\boldsymbol{\nabla} \cdot \langle \chi_p \sigma \rangle - \langle \sigma \cdot \boldsymbol{\nabla} \chi_p \rangle = 0, \tag{4.13}$$

in which σ is the stress tensor and χ_p is the particle-phase indicator function. The ensemble averaged equations are exact for every $\boldsymbol{x} \in \Omega^D$, where Ω^D is a domain of interest. However, due to the difficulties in dealing with the singular term, $\boldsymbol{\nabla}\chi_p$, a volume average of (4.13) on a scale much smaller than the spatial variation of the suspension field is sometimes more useful. After integrating over a small volume Ω^S and applying the mean value theorem to

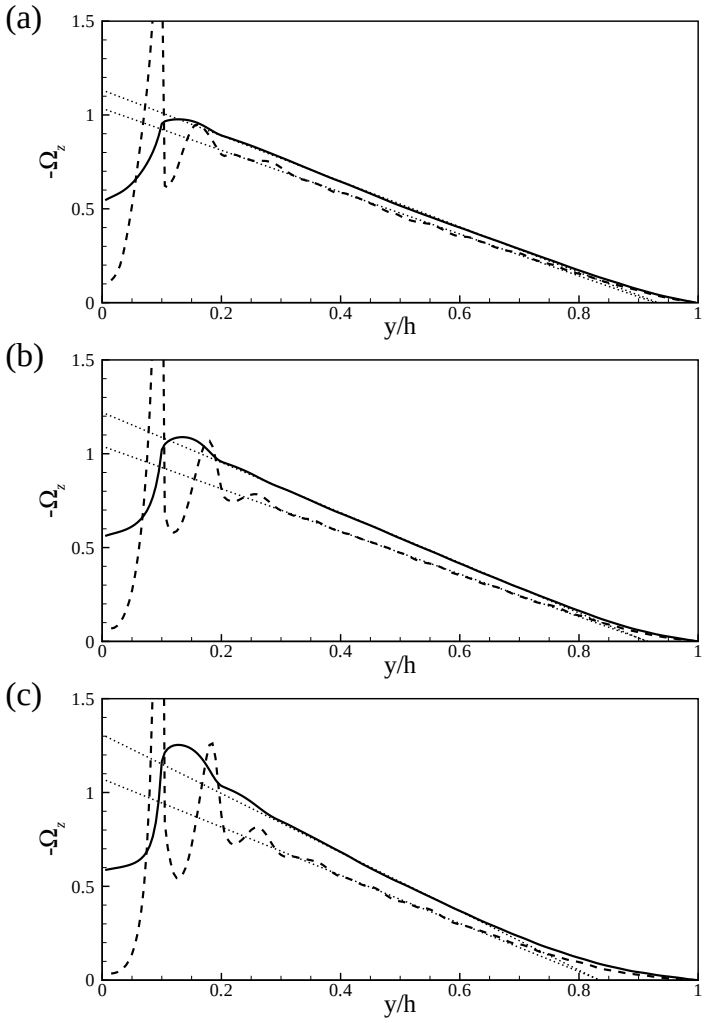

Figure 4.11: The angular velocity (solid line) and $\frac{1}{2}\frac{d\langle V\rangle}{dy}$ (dashed line) normalized by $\dot{\gamma}_c = u_c/h$ with fitting curves (dotted line) for (a) P2L, (b) P3L, and (c) P4L.

the first term, the averaged momentum conservation equations become

$$\frac{\partial}{\partial x_j}\langle\chi_p\sigma_{ij}\rangle + \frac{1}{|\Omega^S|}\left\langle\int_{\partial S_p\cap\Omega^S}\sigma_{ij}n_j dS\right\rangle = 0, \tag{4.14}$$

in which ∂S_p is the surface of the particles in a realization and n_j is a unit outward normal vector on the particle surface. The surface integral is performed over the particle surfaces inside of Ω^S. The ensemble average and the surface integral do not commute because ∂S_p changes for each realization. Equation (4.14) is accurate to $O(a/L)$, where L is a macroscopic lengthscale.

The second term of (4.14) represents the interphase force [142] and is usually modeled as the average hydrodynamic drag force on the particles [160, 164]. A proper treatment of the interphase force in an inhomogeneous suspension is still not clear [128]. In a suspension where the lengthscale of the spatial variation of suspension quantities is much larger than the particle size, the phasic-averaged stress may be approximated as $\langle\chi_p\sigma_{ij}\rangle \simeq \phi_L\langle\sigma_{ij}^p\rangle$, in which $\langle\sigma_{ij}^p\rangle$ is the volume averaged particle stresses in a small volume Ω^s;

$$\phi_L = \frac{1}{|\Omega^s|}\int_{\Omega^s}\langle\chi_p\rangle d^3\boldsymbol{x}, \tag{4.15}$$

$$\langle\sigma_{ij}^p\rangle = \frac{1}{|\Omega^s|}\int_{\Omega^s}\frac{\langle\chi_p\sigma_{ij}\rangle}{\langle\chi_p\rangle}d^3\boldsymbol{x}. \tag{4.16}$$

The volume average may be taken in $|\Omega^s| \sim O(a^3)$. In microfluidic devices, however, usually the spatial variation of suspension fields is non-negligible even at the particle scale and the volume averaging process has to be performed very carefully. Thus, in the present study, we study the behaviours of the phasic-averaged stresses $\langle\chi_p\sigma\rangle$, avoiding the issues with the volume average. To compute the ensemble average, the stress inside of a particle is assumed to be uniform in a statistical sense and evaluated from the sum of the particle stresslet (2.132) and the interparticle force (3.18) contributions,

$$\sigma = \frac{1}{|\Omega_p|}\left(\mathbf{S} - \sum^{N_b}\frac{1}{2}\boldsymbol{r}\boldsymbol{F^p}\right), \tag{4.17}$$

in which $|\Omega_p|$ is the volume of a particle, N_b is the number of the particles within the cut-off distance, $R_{ref} = 2.002a$.

The normal particle stresses are shown in figure 4.12 as functions of the distance from

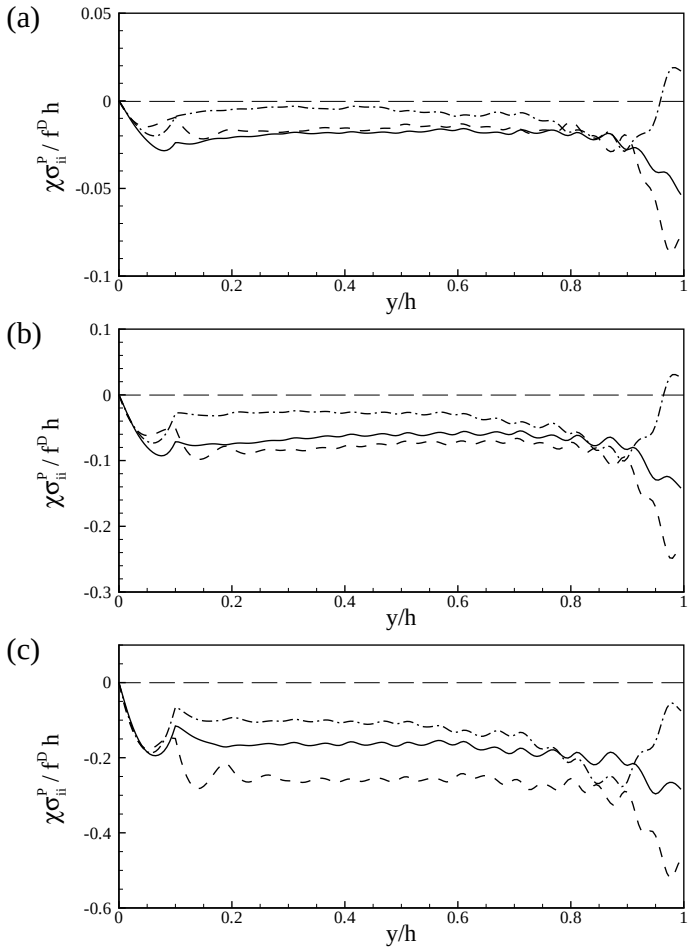

Figure 4.12: The phasic-average of the particle stresses normalized by $f^D h$ for (a) P2L, (b) P3L, and (c) P4L. Solid line, $\langle \chi_p \sigma^p_{11} \rangle$; dashed line, $\langle \chi_p \sigma^p_{22} \rangle$; dash-dot line, $\langle \chi_p \sigma^p_{33} \rangle$.

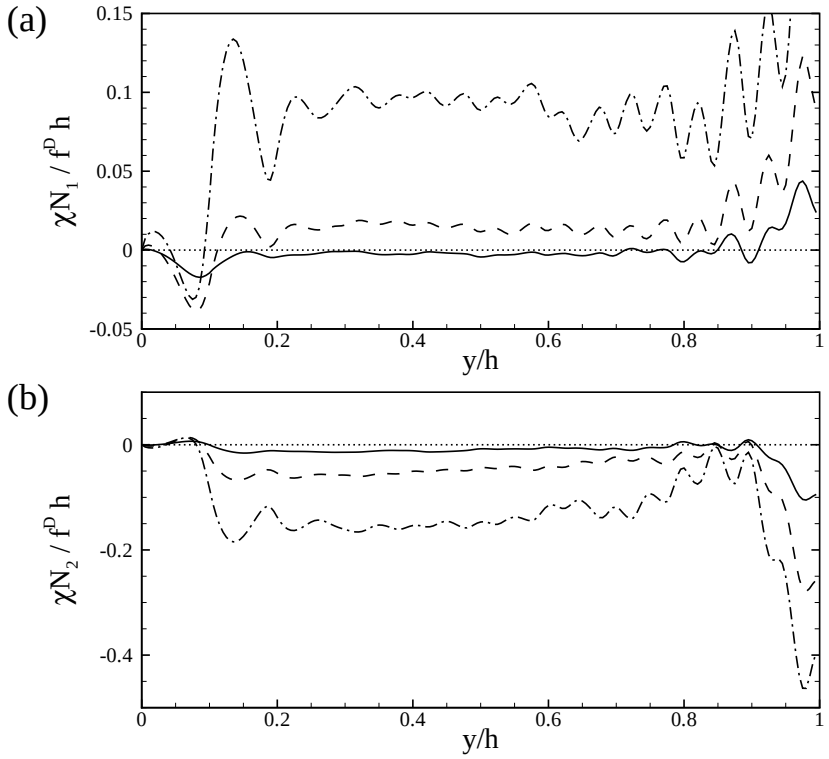

Figure 4.13: The (a) first and (b) second normal stress differences normalized by $f^D h$. Solid line, P2L; dashed line, P3L; dash-dot line, P4L.

the wall. The particle stresses are normalized by $f^D h$. These show that the normal stresses are relatively uniform in the intermediate region. Now, it is generally accepted that the migration of the suspended particles in Poiseuille flows is induced by the gradient of the particle normal stresses, $\boldsymbol{\nabla} \cdot (\phi_L \langle \sigma^{\mathbf{P}} \rangle)$ [159]. The uniform particle normal stresses $\langle \chi_p \sigma_{ii} \rangle$ in the intermediate region indicates that indeed the suspension in the region has reached an equilibrium state in an average sense. Consistent with the velocity statistics, the particle stresses show anomalous behaviour near the wall and in the core of the channel.

One of the important rheological parameters in suspension flows are the first and second normal stress differences, which are defined as

$$N_1 = \sigma^p_{11} - \sigma^p_{22}, \tag{4.18}$$

$$N_2 = \sigma^p_{22} - \sigma^p_{33}. \tag{4.19}$$

Figure 4.13 shows the normal stress differences normalized by $f^D h$. For suspensions in a homogeneous linear shear flow, it was shown that all of the normal stress components

are negative and $|\sigma_{11}| \geq |\sigma_{22}| \geq |\sigma_{33}|$ [240]. Both in experiments [241] and in numerical simulations [197, 230], it has been observed that both N_1 and N_2 for the suspensions of non-colloidal particles are negative. However, in figure 4.12, it is found that, in the intermediate region, N_1 is negative only for $\Phi = 0.20$ and becomes positive for $\Phi \geq 0.30$. A similar feature of the normal stress differences has been observed in the dissipative particle dynamics simulations of colloidal suspensions in a parabolic flow by Pan *et al.* [168]. They showed that the first normal stress difference normalized by the local shear rate is positive for some range of y. However, their simulations are for Brownian suspensions in a reverse Poiseuille flow in a periodic domain [9], i.e. without no-slip wall boundaries, and data are presented in terms of a local Péclet number, so it is difficult to make a direct comparison. It is important to note that the normal stress difference is relatively sensitive to the details of the near-contact force model, in contrast to the effective viscosity or particle pressure. For example, in the experiments of Zarraga *et al.* [241], the ratio of the normal stress differences is shown to be $|N_2|/|N_1| \simeq 3.6$, while $|N_1| \simeq |N_2|$ in the numerical simulations [197, 230]. Sierou & Brady [197] have shown that introducing a frictional contact force between the suspended particles increases $|N_2|$. Still, it is not clear how to incorporate these non-hydrodynamic effects into numerical simulations. These issues remain to be explored further.

The particle pressure of suspension flows can be defined as

$$\Pi = -\frac{1}{3}(\sigma_{11}^P + \sigma_{22}^P + \sigma_{33}^P). \tag{4.20}$$

In the modeling of suspension flows, it is assumed that the particle-phase contribution to the total pressure, $\phi_L \Pi \sim \mu f(\phi_L)\dot{\gamma}_L$. Here, ϕ_L is the local volume fraction, $f(\phi_L)$ is an empirical relation and $\dot{\gamma}_L$ is the local shear rate. In other words, $\phi_L \Pi$ normalized by the local shear stress $\mu\dot{\gamma}_L$ is a function of the local volume fraction only. In figure 4.14 (a), the particle-phase contribution to the total stress normalized by the local shear stress is shown as a function of ϕ. As shown in figure 4.4, ϕ_L is almost the same as ϕ except near the wall. Hence, hereafter we do not distinguish ϕ from ϕ_L. The local shear rate is estimated by

$$\dot{\gamma}_L = 2\left(1 - \frac{y}{h}\right)\frac{u_c}{h}. \tag{4.21}$$

We find that there is a remarkable similarity in the normalized particle pressure profiles. Except for the data near the core of the channel, which diverges as $\dot{\gamma}_L \to 0$, the normalized

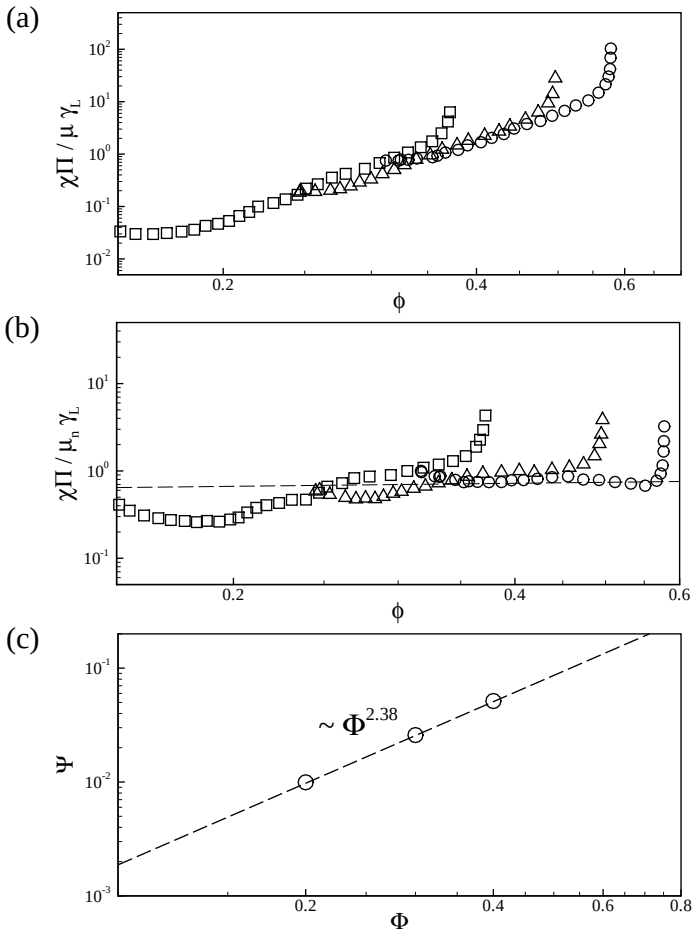

Figure 4.14: The average particle pressure normalized by the local shear rate $\dot{\gamma}_L$ (a) and the normal viscosity model by Morris & Boulay [160] (b): □, P2L; △, P3L; ∘, P4L. (c) The volume average of the particle pressure scaled by the apparent viscosity as a function of the bulk volume fraction. The dashed line is $\Psi = e^{-0.8}\Phi^{2.38}$.

pressure profiles in the intermediate region almost collapse onto one curve, suggesting that the particle pressure is indeed a function of the local volume fraction and $\dot{\gamma}_L$ only.

Morris & Boulay [160] proposed an empirical relation for the particle pressure as

$$\phi\Pi = \mu_n(\phi)\left(\frac{1+\lambda_2+\lambda_3}{3}\right)\dot{\gamma}_L, \tag{4.22}$$

$$\mu_n(\phi) = \mu K_n\left(\frac{\phi}{\phi_m}\right)^2\left(1-\frac{\phi}{\phi_m}\right)^{-2}. \tag{4.23}$$

Here, K_n is an empirical coefficient, ϕ_m is the maximum random packing fraction, $\lambda_2 = \sigma^p_{22}/\sigma^p_{11}$, and $\lambda_2 = \sigma^p_{33}/\sigma^p_{11}$. In Miller & Morris [155], they suggested that $\lambda_2 \simeq 0.8$, $\lambda_3 \simeq 0.5$, $K_n = 0.75$ and $\phi_m = 0.68$ would give a good agreement with suspension rheology. In figure 4.14 (b), the particle pressure scaled by the empirical relation of [160] is shown in terms of ϕ;

$$\frac{\langle\chi_p\Pi\rangle}{\mu_n\dot{\gamma}_L} = \frac{\langle\chi_p\Pi\rangle}{\mu\left(\frac{\phi}{\phi_m}\right)^2\left(1-\frac{\phi}{\phi_m}\right)^{-2}\dot{\gamma}_L}. \tag{4.24}$$

Since the parameters λ_2 and λ_3 suggested by [155] are different from the simulation results (figure 4.14 a), here we use a rheological fitting parameter $K_p = (1+\lambda_2+\lambda_3)K_n/3$, instead of dealing with each normal stress component separately. It is shown that the functional form of their normal stress viscosity model μ_n shows an excellent agreement with the present simulation results. The model parameter $K_p = 0.63$ gives a good approximation for the range of $0.25 \leq \phi \leq 0.55$.

The volume average of particle pressure over $\Omega^D = H_x \times H_y \times H_z$ scaled by the apparent viscosity is shown in figure 4.14 (c) as a function of the bulk volume fraction. The scaled particle pressure is defined as

$$\Psi = \frac{\mu}{\mu_{app}}\frac{\langle\overline{\Pi}\rangle}{f^D h}. \tag{4.25}$$

Here, the volume averaged particle pressure is

$$\langle\overline{\Pi}\rangle = \frac{1}{|\Omega^D|}\int_{\Omega^D}\langle\chi_p\Pi\rangle\, d^3\boldsymbol{x} = \Phi\left\langle\frac{1}{N_p}\sum_{i=1}^{N_p}\Pi^i\right\rangle, \tag{4.26}$$

in which Φ is the bulk volume fraction. The scaled particle pressure is shown in figure 4.14

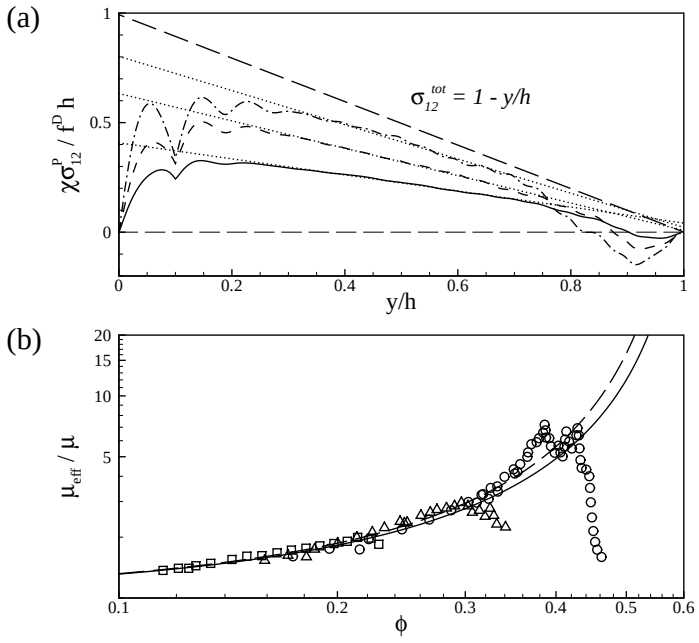

Figure 4.15: (a) The particle shear stress, $\chi_p\sigma_{12}$, normalized by $f^D h$ and shown with corresponding fitting curves. The long-dashed line represents the total shear stress normalized by $f^D h$. From top to bottom, the lines indicate P4L, P3L, and P2L. (b) The effective viscosity as a function of the local volume fraction: □, P2L; △, P3L; ∘, P4L. Solid line is an empirical relation by Krieger & Dogherty [115] and dashed line is Eilers' fit.

Table 4.4: The fitting coefficients for the particle-phase contribution to the total stress $\langle\chi_p\sigma_{12}\rangle$.

	P2L	P3L	P4L
C_0	0.41	0.63	0.80
C_1	-0.37	-0.63	-0.78

(c). This shows that, with the limited data available, the particle pressure scaled by the apparent viscosity is well approximated by $\Psi = e^{-0.8}\Phi^{2.38}$.

4.4.2 Shear stresses

The shear component of the particle stress tensor $\langle\chi_p\sigma_{12}\rangle$ normalized by $f^D h$ is shown in figure 4.15 (a). As with the velocity statistics, there is an intermediate region in which $\chi_p\sigma_{12}$ is a linear function of y/h. The fitting coefficients are given in table 4.4. As σ_{12} is proportional to $\dot\gamma$ ($\sigma_{12} \sim \dot\gamma$), in a linear shear flow, it is somewhat surprising to observe that σ_{12}^p becomes negative in the core of the channel, where $\dot\gamma_L$ is positive. Recently, Guasto *et*

al. [83] performed experiments of concentrated suspensions under an oscillating pressure gradient for the bulk volume fraction $\Phi = 0.40$. They found that there is a long-range correlated motion for the particles near the core of the channel. A similar long-range correlation has been seen in the present simulations. The magnitude of the negative values of σ_{12}^p increase with the volume fraction, indicating that such negative values of σ_{12}^p are a distinguishing feature of concentrated suspensions.

In a Poiseuille flow, the total shear stress normalized by $f^D h$ is linear in y/h,

$$\langle \sigma_{12} \rangle = \langle \chi_p \sigma_{12} \rangle + \langle \chi_f \sigma_{12} \rangle = \left(1 - \frac{y}{h}\right) f^D h, \tag{4.27}$$

in which χ_f is the fluid-phase indicator function. Analogous to Couette-flow suspensions, we define an effective viscosity as,

$$\frac{\mu_{eff}}{\mu_0} = \frac{\langle \sigma_{12} \rangle}{\langle \chi_f \sigma_{12} \rangle} = 1 + \frac{\langle \chi_p \sigma_{12} \rangle}{(1 - y/h) f^D h - \langle \chi_p \sigma_{12} \rangle}. \tag{4.28}$$

The effective viscosity is compared with empirical viscosity relations in figure 4.15 (b). The empirical viscosity relations are:

1. Krieger & Dogherty [115],

$$\frac{\mu_{eff}}{\mu_0} = \left(1 - \frac{\phi}{\phi_m}\right)^{-[\eta]\phi_m}, \tag{4.29}$$

2. Eilers' fit [203],

$$\frac{\mu_{eff}}{\mu_0} = \left(1 + \frac{\frac{1}{2}[\eta]\phi}{1 - \phi/\phi_m}\right)^2, \tag{4.30}$$

in which ϕ_m is the maximum packing fraction and $[\eta]$ is a fitting parameter. Following Stickel & Powell [203], $\phi_m = 0.63$ and $\eta = 2.5$ are used. It is shown that the effective viscosity evaluated in the intermediate region agrees well with these empirical relations.

As a first step to investigate the origin of the negative σ_{12}^p in the core, the particle stress is decomposed into the hydrodynamic stresslet and the interparticle force contributions. As the stresslet is also related with the interparticle force, it is not possible to exactly decouple the interparticle force contribution from the hydrodynamic contribution. Still,

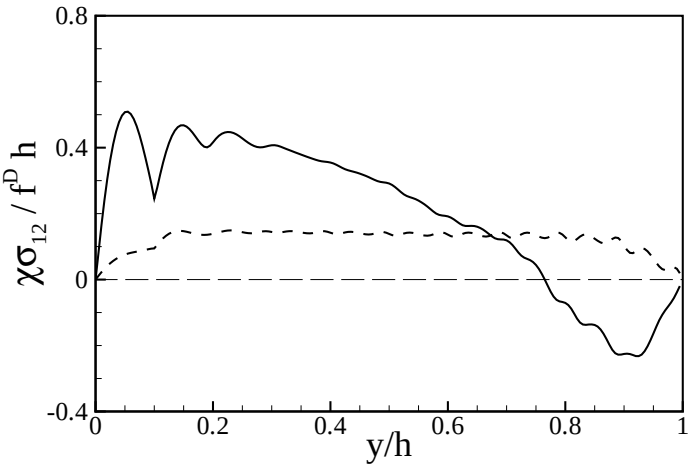

Figure 4.16: Decomposition of $\langle \chi_p \sigma_{12} \rangle$ into the contributions from the hydrodynamic stresslet (solid line) and the interparticle force (dashed line) for P4L. All the variables are normalized by $f^D h$.

the simple decomposition is helpful to investigate the behaviour qualitatively. Figure 4.16 shows the stresslet and interparticle force contributions for P4L. Here, the interparticle force contribution is uniform except near the wall and in the core of the channel. The interparticle force contribution is always positive. The negative σ_{12}^p is due to the hydrodynamic stresslet.

4.4.3 Pair-distribution function

The pair-distribution functions $g(x, y)$ projected onto the velocity-velocity-gradient $(x - y)$ plane are shown in figure 4.17. The pair-distribution functions are obtained at $\Phi = 0.40$ (P4L). The pair-distribution function obtained for $7 \leq y/a \leq 13$ is very similar to that in a homogeneous linear shear flow [221, 230]. There are two shells of high probability region around the compressional axis of the shear flow at $r/a \simeq 2$, which is followed by the second high probability region around $r/a \simeq 3.5$. The second high probability shell shows the similar behaviour with the first shell, higher probability around the compressional axis and lower probability near the extensional axis. Since the volume fraction is an increasing function of y in this region, the contour plot shows a background gradation in color in the wall normal direction, indicating the higher probability of a particle encounter at the higher y/a.

The pair distribution function near the core of the channel shows a very different behaviour from that in a linear shear flow. In the upper hemisphere, there are three shells

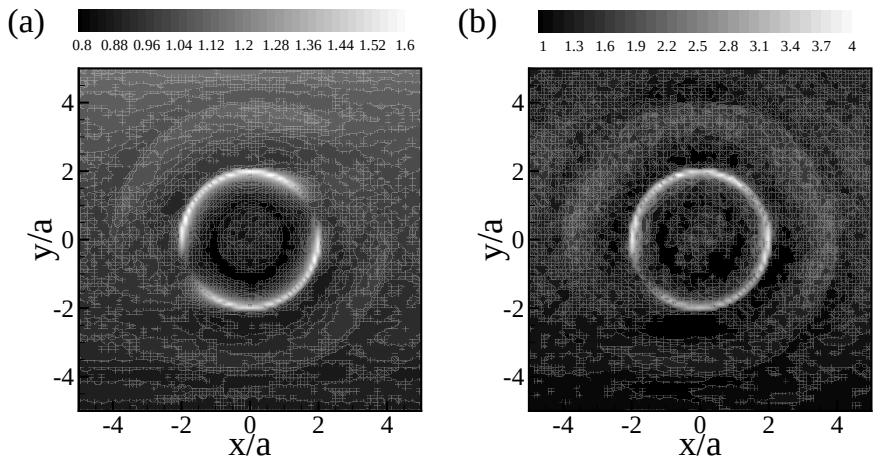

Figure 4.17: The pair-distribution functions for the reference particles in (a) $7 \leq y/a \leq 13$ and(b) $18 \leq y/a \leq 19$. The lighter the contour, the higher the probability.

of the high probability regions and the probability of a particle encounter in each shells is relatively isotropic. Near $\theta = 5/4\pi$, in which θ is the azimuthal angle measured from the positive $x-$axis, the probability in the first shell becomes relatively low, suggesting that, in the lower hemisphere, the micro-structure still resembles that in a linear shear flow. However, such a low probability region is not observed in the first high probability shell in the upper hemisphere. Unlike the pair-distribution in $7 \leq y/a \leq 13$, the highest probabilities at $r/a \simeq 2$ are observed around $\theta \simeq 0,\ \pi/2$, and $3\pi/2$. A similar behaviour has been observed by Gao *et al.* [77] in their experiments of colloidal suspensions in a pressure-driven flow. It is interesting that the pair-distribution function qualitatively agrees well, even though Brownian motion is not considered in the present simulations.

4.5 Discussions

In the preceding sections, we have summarized the results obtained from the numerical simulations of concentrated suspensions in a plane Poiseuille flow. In this study, we focus on suspensions in narrow channels ($H_y/a \leq 40$). These include results for the nonuniform distribution of particles across the channel, the particle velocity statistics and particle stresses.

The volume fraction profiles calculated from the force-coupling simulation at the bulk volume fractions $\Phi = 0.3$ and 0.4 show a quantitatively good agreement with the experi-

ments by [139] near the core of the channel under experimental conditions similar to the simulation parameters in the present study. However, near the wall, the volume fraction profiles in [139] show a much faster decrease than the present simulations. On the other hand, the numerically simulated volume fraction profiles near the wall match the experiments by Hampton *et al.* [84] in pressure-driven tube flows. This discrepancy may come from the differences in the experimental setup and measurement techniques. In the laser Doppler velocimetry measurements of Lyon & Leal [139], they first measured the particle velocity and the local volume fraction is then estimated indirectly from the velocity measurement data based on the time interval between particles arriving in the measuring volume. The simulated velocity profiles show a good agreement with [139] across the whole channel, suggesting that there might be some measurement error or statistical bias involved in estimating the local volume fraction. The authors also noted the limitations of the measurement technique near the wall. Using nuclear magnetic resonance imaging, Hampton *et al.* [84] were able to measure directly the local volume fraction. In their experiments with large monodisperse particles ($2a \simeq 3000\mu m$), they also observed the formation of a coherent particle layer near the wall similar to that seen in the present simulations.

The results for the velocity fluctuations indicate that the channel can be divided into three regions; near-wall, intermediate and core region. In the near-wall region, the particle-wall lubrication interaction and the finite size effects become important and the behaviour in the region is very different from what is expected from the homogeneous suspensions. In the intermediate region, it is found that the streamwise velocity fluctuation is well approximated by a quadratic function of y/h, while the wall-normal and spanwise velocity fluctuations show nearly linear dependencies on y/h. It is shown that both the spanwise angular velocity and the wall-normal velocity gradient are linear functions of y/h in the intermediate region, which suggest that the wall-normal and spanwise velocity fluctuations are associated with the local shear rate. In homogeneous suspensions, the squared wall-normal and spanwise velocity fluctuations, which are linked to "suspension temperature", are shown to be $\sim \dot{\gamma}\Phi$ and $\langle v_y^2 \rangle / \langle v_z^2 \rangle \simeq 4$ for a wide range of Φ [59]. Similarly, the ratio of the vertical to the spanwise velocity fluctuations in Poiseuille flow suspensions are $v_y'/v_z' \simeq 1.8$ for the range of volume fraction $\Phi = 0.2 \sim 0.4$ in the intermediate region. However, the linear behaviours of wall-normal and spanwise velocity fluctuations (see table 4.3) scale well with the local shear gradient and the bulk volume fraction Φ, not the local volume fraction. As the

volume fraction increases, the intermediate region, where the velocity statistics can be approximated by a linear or quadratic function, decreases and the core region becomes wider. In the core region, the velocity fluctuations become almost uniform. While the streamwise and spanwise velocity fluctuations are shown to be increasing functions of the volume fraction, the wall-normal velocity fluctuations remain almost constant in the range of volume fraction considered in the present study. Although the local shear rate is zero at the center of the channel, the velocity fluctuations remain finite, suggesting a non-local structure contributes to the dynamics in the region.

The behaviour of the normal particle stresses is very different from what is expected based on the results for homogeneous suspensions in a linear shear flow. The normal stress differences are not only functions of the distance from the wall, but also functions of the bulk volume fraction. At the bulk volume fraction $\Phi = 0.20$, both the first and second normal stresses differences are negative, as in a homogeneous suspensions. However, at higher volume fractions $\Phi \geq 0.30$, the first normal stress difference becomes positive while the second normal stress difference remains negative. A similar behaviour has been observed in the dissipative particle dynamics simulations by Pan *et al.* [168]. The contribution of the particle pressure to the total pressure scaled by the local shear rate of the suspension flow is shown to be a function of the local volume fraction, as suggested in some suspension modeling approaches. The particle pressure contribution is well represented by the functional form of the normal stress model given by Morris & Boulay [160].

The effective viscosity is estimated by the ratio of the total shear stress to the fluid-phase shear stress. It is shown that the effective viscosity, at least in the intermediate region, shows a good agreement with empirical relations commonly used in Couette-flow suspensions. Unexpectedly, the particle shear stress becomes negative in the core region of the channel, in which the local strain rate is small but still positive. It is shown that the negative shear stress arises from hydrodynamic stresslet. The origin of this anomalous behaviour is a subject of a further investigation.

Chapter 5

Finite-Reynolds-number flow: Hydrodynamic interaction between spinning particles

5.1 Introduction

Dynamic self-assembly of discrete particles, which occurs by the subtle balance between a driving force and dissipation, has been attracted a great attention due to its potential application for a smart material [71]. This study is motivated by the experiments of dynamic self-assembly of magnetic particles reported by Grzybowski *et al.* [81, 82]. In their experiment, millimeter-size disks with a permanent dipole moment coplanar with the disk are placed just beneath the liquid-air interface. As a bar magnet rotates at a constant angular frequency in the plane parallel to the liquid surface, a magnetic torque is applied to the disks, which makes the disks rotate about their centers at the same angular frequency with the bar magnet, and, at the same time, a gradient of the magnetic force results in a centripetal force toward the axis of the rotation of the bar magnet. The balance between the body force/torque on the disks induced by the rotating magnetic field and hydrodynamic interactions due to the vortex-like flow generated by the spinning of the disks drives the formulation of supraparticle aggregates.

The goal of this chapter is to investigate the hydrodynamic interactions in a system analogous to the experiments of Grzybowski *et al.* [81, 82]. In the present study, instead

of the disks beneath the liquid-air interface, hydrodynamic interaction between spheres completely immersed in a liquid and initially seeded in a coplanar configuration is studied. The similarity in the hydrodynamic interactions between two different situations will be briefly discussed in 5.2. The external body force and torque on the spheres by the rotating magnetic field are, respectively, modeled as a constant body force towards the center of the computational domain and a constant torque in the axis perpendicular to the plane of the spheres (vertical direction). Here, we focus particularly on the hydrodynamic interaction between spinning particles under finite fluid inertia. The force-coupling method for the Navier-Stokes equations described in 2.4 is employed for the numerical simulations. A cubic tri-periodic domain is used and the Navier-Stokes equations are solved by using a Fourier spectral method. The length of the each directions of the computational domain is chosen as $2L = 24a$ or $48a$, in which a is the particle radius. We found that the computational domain is big enough that the effect of the periodicity on hydrodynamics is negligible.

5.2 Results

First, we study the flow field induced by the rotation of a sphere at finite Reynolds number. The Reynolds number is based on the particle radius (a) and angular velocity (ω), $Re_\omega = \omega a^2/\nu$, in which ν is the kinematic viscosity of the fluid. Figure 5.1 shows the azimuthal velocity u_ϕ as a function of the radial distance (r) in the equatorial plane ($\theta = \pi/2$) specified in terms of the spherical polar coordinate (r, θ, ϕ). Comparing the analytical solution and FCM solution in Stokes flow, it is shown that FCM reproduces the analytical solution exactly in the far field $r/a > 1.3$. Near the particle surface $1 \leq r/a < 1.3$, FCM slightly underestimates u_ϕ, which is a result of the regularized multipole. It is shown that the azimuthal velocity at $Re_\omega = 8$ is very similar to that in Stokes flow.

In this study, the rotating magnetic field is represented by a body torque applied on the suspended particles. From the estimate in the Stokes limit, the body torque is initially set to $T^{ext} = 8\pi\mu a^3\omega_0$ and μ is gradually adjusted to achieve the desired Re_ω. Here, ω_0 is an arbitrary reference value. The relation between T^{ext} and ω has been studied thoroughly in the literature. Let us define a non-dimensional torque coefficient as $M = 2T^{ext}/\rho a^5\omega^2$. In the Stokes limit, Lamb has shown that $M = 16\pi/Re_\omega$ [122]. Sawatzki [189] showed in his experiment that the Stokes-limit theory by Lamb is valid for $Re_\omega < 3$. Dennis *et al.*

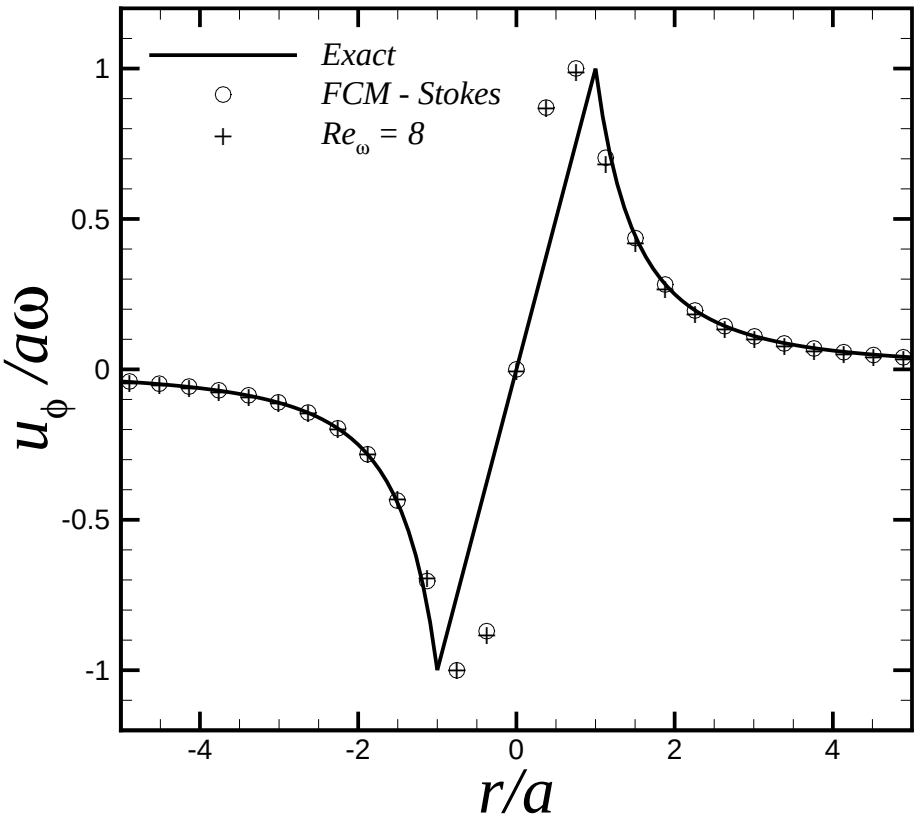

Figure 5.1: The azimuthal velocity in the equatorial plane normalized by the particle radius a and the angular velocity ω. The solid line is the analytical solution at zero Reynolds number.

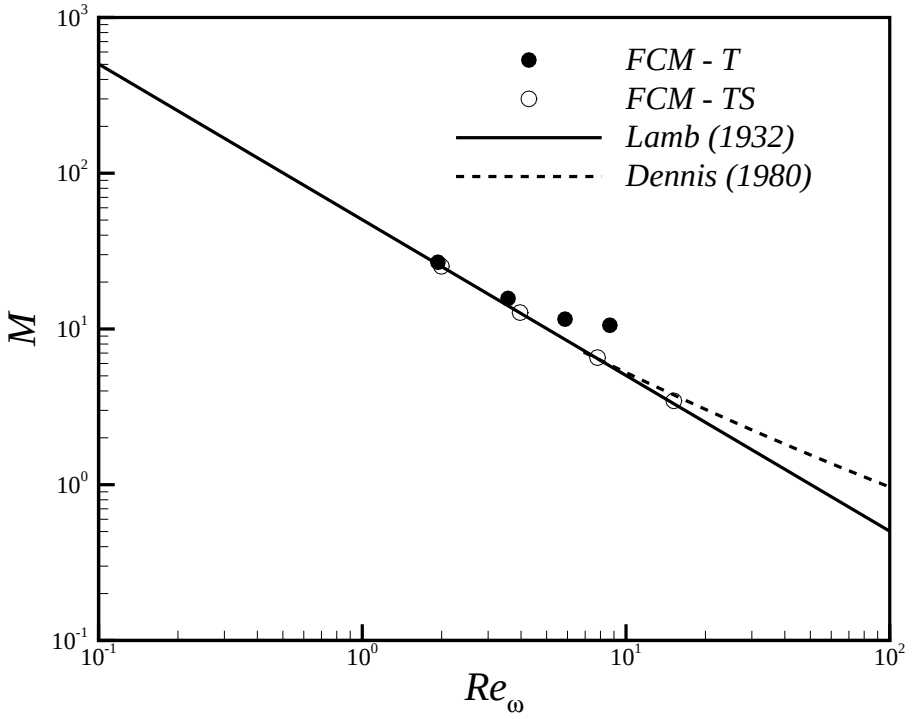

Figure 5.2: The non-dimensional torque coefficient M as a function of the Reynolds number Re_ω. The solid and hollow symbols are, respectively, FCM simulations without and with the stresslet.

[53] investigated the same system numerically and confirmed the experiments of Sawatzki. At finite Re_ω, the $M - Re_\omega$ relation is given by $M = 16\pi(1 + f(Re_\omega))/Re_\omega$, in which $f(Re_\omega)$ is an empirical correlation. In figure 5.2, the FCM results are shown together with the Lamb's Stokes-limit theory [122] and the empirical correlation of Dennis *et al.* [53]. First, the FCM simulations are performed without considering the stresslet (FCM-T), *i.e.* without the rigidity constraint $\int E_{ij}\Delta_D dx = 0$. In Stokes flow, the flow field induced by the rotation of a sphere is purely due to the couplet and the stresslet is zero. Hence, at the smallest Reynolds number $Re_\omega = 2$, M obtained by FCM-T agrees well with the Lamb's theory. However, for larger Re_ω, FCM-T overestimates the torque coefficient. Once the stresslet is added (FCM-TS), the torque coefficient obtained by FCM-TS shows a very good agreement for $Re_\omega < 10$. At $Re_\omega = 16$, FCM-TS somehow underestimates M compared to the empirical correlation [53].

Rotation of a sphere in an otherwise quiescent flow induces a secondary meridional circulation with an inflow at the poles and outflow on the equator. Figure 5.3 shows the secondary flow induced by the rotation of a sphere at $Re_\omega = 2$. The flow inside of the sphere is shown to illustrate the internal circulation and the location of the stagnation points. At low Re_ω, the flow velocity around a sphere can be estimated analytically by using a regular perturbation method. Bickley [17] has found the solution to $O(Re_\omega)$,

$$\begin{aligned} u_r &= -\frac{\omega a^3}{8r^2}(3\cos^2\theta - 1)\left(1 - \frac{a}{r}\right)^2 Re_\omega, \\ u_\theta &= \frac{\omega a^4}{4r^3}\left(1 - \frac{a}{r}\right)\sin\theta\cos\theta Re_\omega, \\ u_\phi &= \frac{\omega a^3}{r^2}\sin\theta + O(Re_\omega^2). \end{aligned} \tag{5.1}$$

The analytical solution illustrates that the radial-direction component of the stresslet is non-zero, which explains the error in the prediction of $M - Re_\omega$ relation by FCM-T simulations (figure 5.2).

Figure 5.4 shows the flow field induced by two co-rotating coplanar spheres. The spheres are subject to a fixed attraction force which keeps them at a constant separation distance. Here, the center-to-center distance is kept $2R/a = 6$. In Stokes flows, a pair of co-rotating coplanar spheres will follow a circular path moving in response to the flow generated by the other particle and there is no net hydrodynamic force in the direction connecting the centers of the spheres. However, at finite Reynolds number, there is a net repulsive hydrodynamic

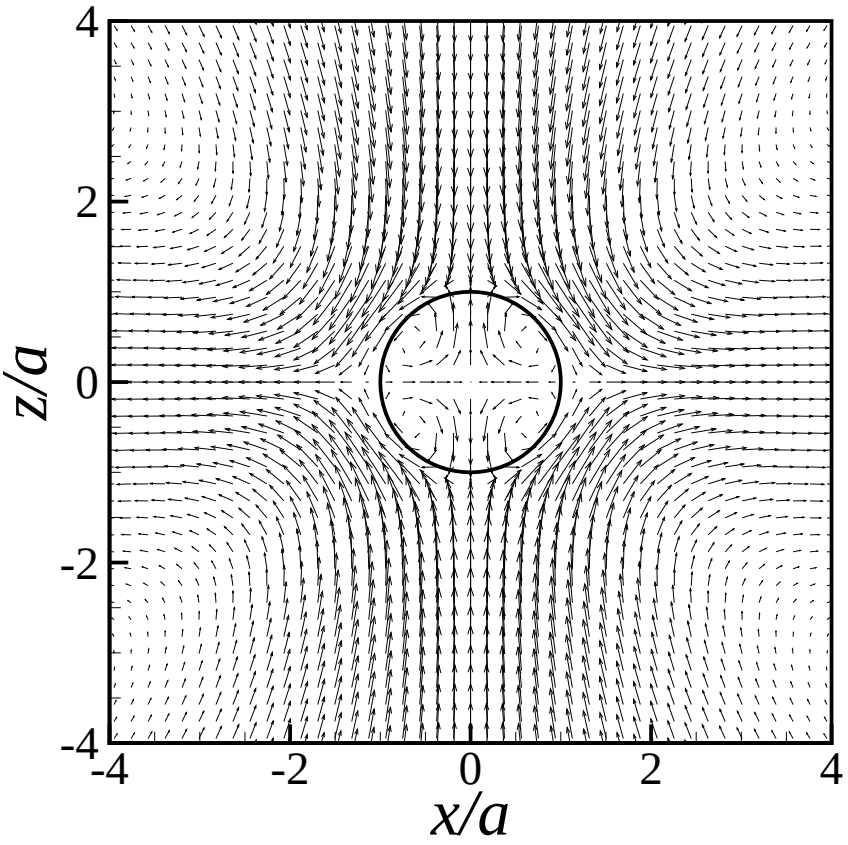

Figure 5.3: Secondary flow in the $x - z$ plane for a sphere spinning about the z axis at $Re_\omega = 2$.

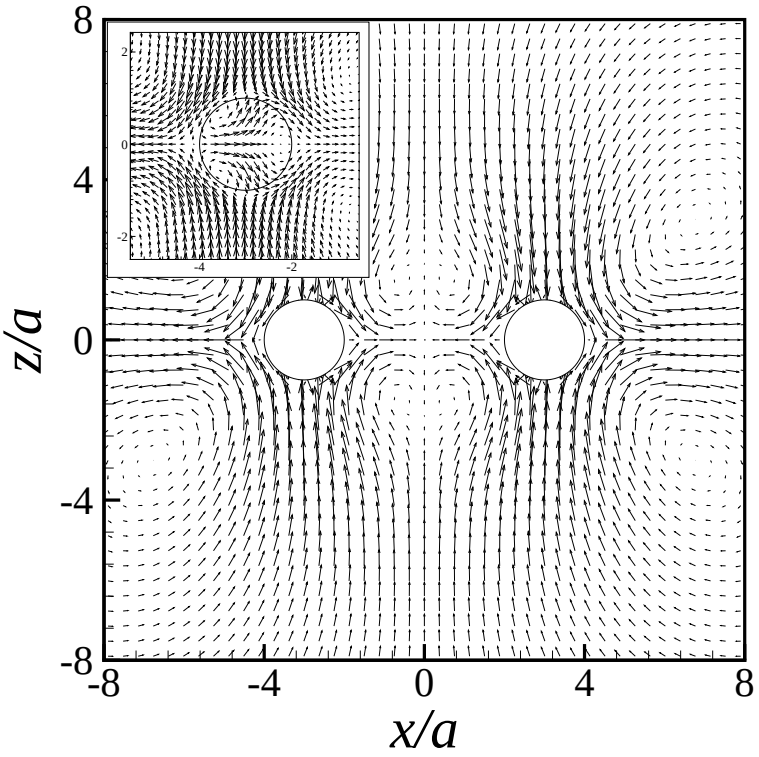

Figure 5.4: Flow field in the $x - z$ plane for a pair of co-rotating spheres at $Re_\omega = 2$. The spheres are rotating about the z axis. Inset shows the detailed velocity field for the sphere located at $x/a = -3$.

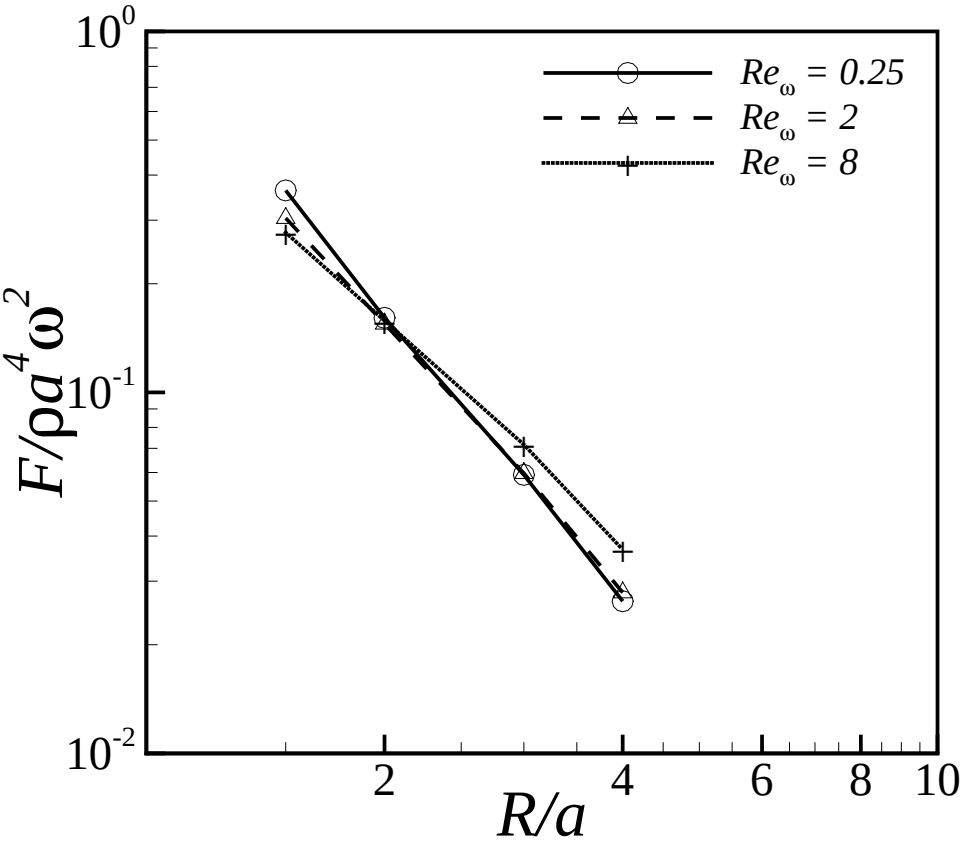

Figure 5.5: Hydrodynamic repulsion force between two co-rotating spheres as a function of the distance between the particles $2R$.

force between the spheres due to the outflow near the equator. It is worth noting that, even in the case of counter-rotating spheres, the hydrodynamic interaction between coplanar spheres will be repulsive.

The experiments of Grzybowski *et al.* [81, 82] used the disks with a permanent dipole, not spheres in the present simulations. It is well known that, when a disk rotates under finite fluid inertia, a secondary flow is generated by the nonlinear interaction, which is the celebrated "von Kármán viscous pump" problem. Similar to the rotating sphere, an inflow towards the rotating disk in the direction perpendicular to the disk is generated and, near the disk surface, there is an outflow (positive u_r) parallel to the disk surface. Hence, the hydrodynamic repulsion they observed in the experiments also comes from the secondary flow. Although we use spheres instead of disks, the hydrodynamics involved is very similar in essence.

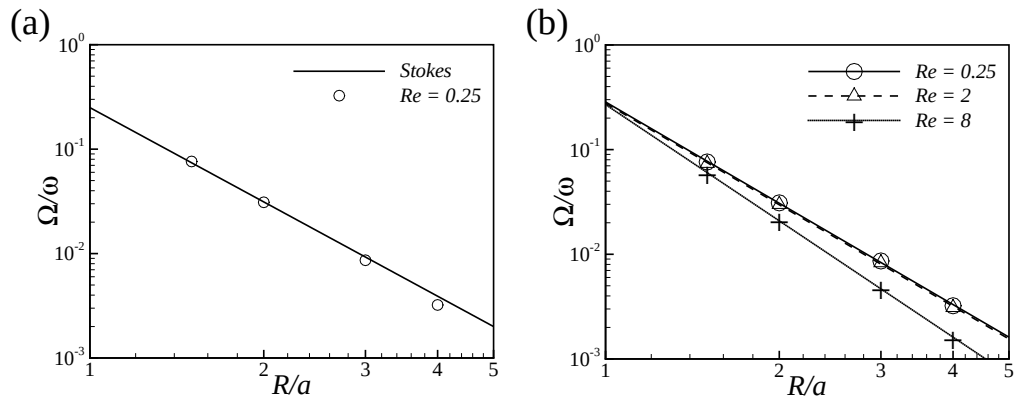

Figure 5.6: Precession angular velocity Ω for a pair of co-rotating spheres in terms of the separation distance R: (a) comparison of the FCM results at $Re_\omega = 0.25$ with the Stokes-limit estimate and (b) FCM results for $Re_\omega = 0.25$, 2, and 8. The lines in (b) are the fitting curves.

The hydrodynamic repulsion force F between the spheres is estimated from the force required to keep R constant. The two spheres are initially seeded at the desired separation distance and the attraction force ($G = -F$) is adjusted by using a penalty method;

$$\frac{dG}{dt} = -\lambda(R - R_{ref}), \tag{5.2}$$

in which λ is a penalty coefficient and R_{ref} is the target separation distance. The hydrodynamic repulsion force is shown in figure 5.5. The repulsion force shows a power-law decay $\sim (R/a)^{-\kappa}$. It is shown that the exponent is a decreasing function of Re_ω; $\kappa = 2.64$, 2.42, and 2.05 for $Re_\omega = 0.25$, 2, and 8, respectively.

In Stokes flow, the precession angular velocity Ω of the co-rotating particle pair can be predicted analytically by a superposition of the velocity perturbations of each particle. The azimuthal velocity of a particle induced by the rotation of a second particle is $u'_\phi = \omega a^3/(2R)^2$. Then, the angular velocity of the two particle system is

$$\Omega = \frac{u_\phi}{R} = \frac{\omega}{4}\left(\frac{a}{R}\right)^3. \tag{5.3}$$

In figure 5.6 (a), Ω for $Re_\omega = 0.25$ are shown together with the theoretical prediction in Stokes flow. It is shown that the simulation results agree well with the theoretical prediction. The precession angular velocity as a function of both R and Re_ω is shown in figure 5.6 (b). Similarly to F, the precession angular velocity shows a $\sim (R/a)^{-\xi}$ behavior

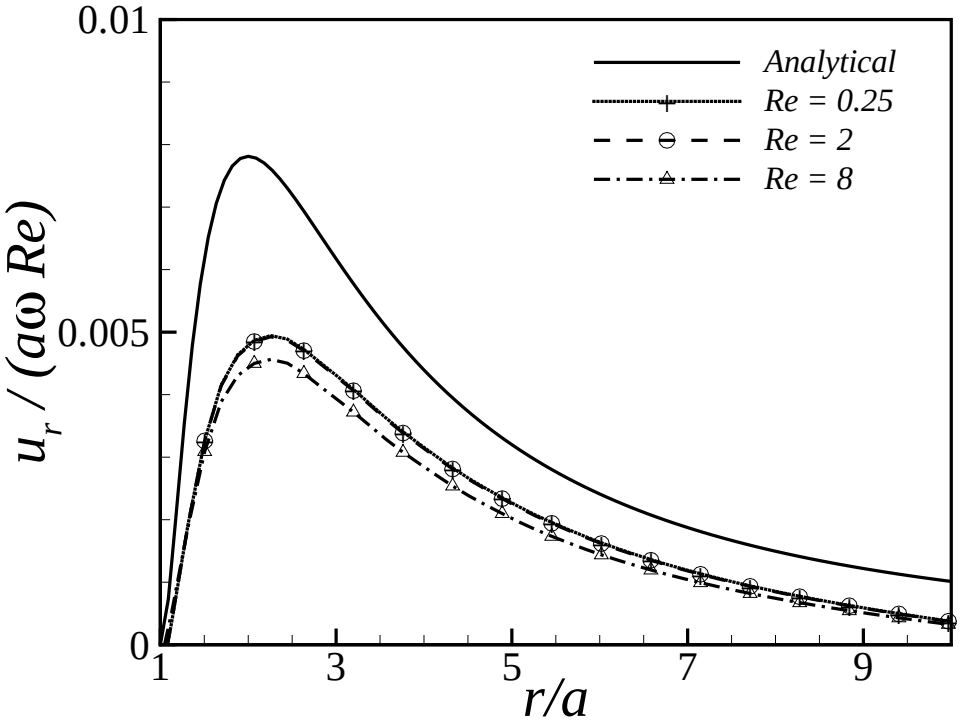

Figure 5.7: Comparison of the radial velocity u_r obtained from FCM-TS with the analytical solution by Bickley [17].

with the exponent different from that for F (κ). Here, the exponents are ξ = 3.21, 3.22, and 3.69 for Re_ω = 0.25, 2, and 8, respectively.

We now consider the quantitative difference between the analytical and FCM solutions. Figure 5.7 shows the radial velocity obtained by FCM and the analytical prediction of Bickley [17]. The FCM solutions for Re_ω = 0.25 and 2 collapse onto one curve while that of Re_ω = 8 is somehow smaller. It is shown that the FCM solutions show qualitatively similar behavior with Bickley [17]. However, the magnitude of u_r is much smaller than the analytical result.

The flow field generated by the rotation of a sphere in Stokes flow is given by

$$\boldsymbol{u} = (\boldsymbol{\omega} \times \boldsymbol{x}) f(r). \tag{5.4}$$

The nonlinear term for the perturbation solution of order Re_ω is obtained from the Stokes

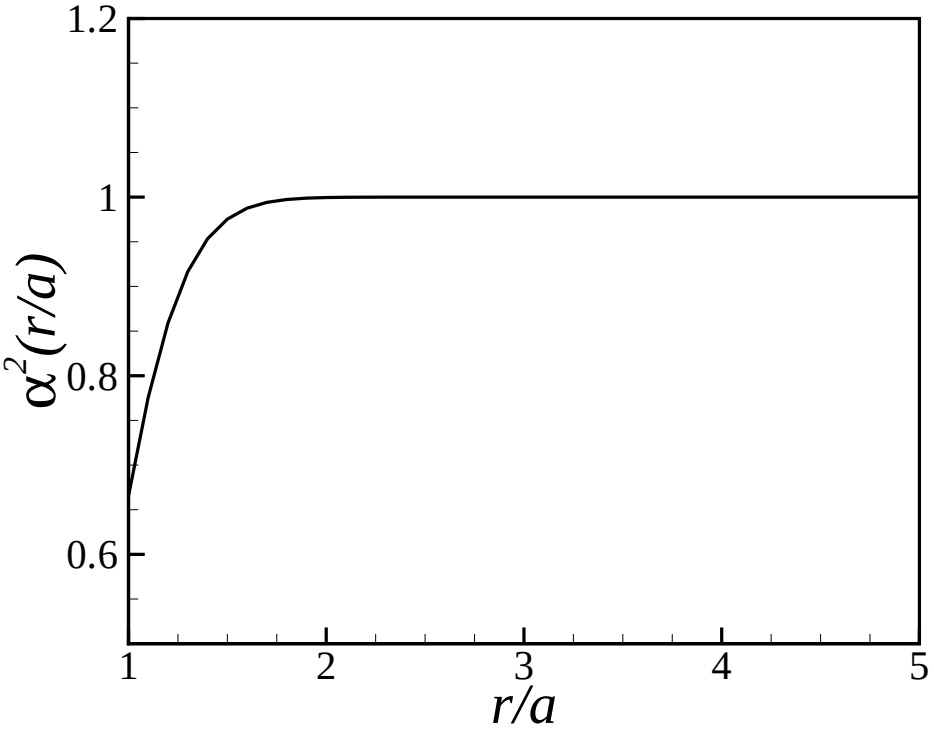

Figure 5.8: Ratio of the magnitude of the non-linear interaction of FCM-TS to that of the analytical Stokes solution.

solution as

$$\begin{aligned}(\boldsymbol{u}\cdot\boldsymbol{\nabla})u_i &= \epsilon_{ijk}\epsilon_{lpq}\omega_j\omega_p x_q f(r)\left(\delta_{kl}f(r)+\frac{x_k x_l}{r}\frac{df}{dr}\right)\\ &= -(|\boldsymbol{\omega}|^2\delta_{ij}-\omega_i\omega_j)x_j f^2(r). \end{aligned} \tag{5.5}$$

The scalar function $f(r)$ for Stokes flow is $f^S(r)=(a/r)^3$ and that of FCM f^{FCM} is

$$f^{FCM}(r)=f^S(r)\left[\mathrm{Erf}\left(\frac{r}{\sigma_D\sqrt{2}}\right)-\frac{2}{\sigma_D}\left(\frac{2}{\pi}\right)^{1/2}\exp\left(-\frac{r^2}{2\sigma_D^2}\right)\right]=f^S(r)\alpha(r). \tag{5.6}$$

The ratio of the nonlinear term in the first-order perturbation solution of FCM to Stokes solution is simply $\alpha^2(r)$. The behavior of α^2 is shown in figure 5.8. As FCM resolves the far-field solution almost exactly, α for $r/a>2$ becomes almost 1. On the other hand, near the particle surface, FCM underestimates the nonlinear term as low as 65% of the exact solution.

To show the effect of the difference in the nonlinear term more clearly, FCM for Stokes flow is solved using the nonlinear term from the analytical solution as an external force. That is

$$[-(\boldsymbol{u}\cdot\boldsymbol{\nabla})\boldsymbol{u}]_{Stokes}=-\boldsymbol{\nabla}p+\frac{1}{Re}\nabla^2\boldsymbol{u}+(\boldsymbol{G}\cdot\boldsymbol{\nabla})\Delta_D. \tag{5.7}$$

To minimize the effects of the periodicity, we use a larger computation domain; $L/a=48$. The radial velocity obtained by solving (5.7) is shown in figure 5.9. It is shown that the agreement between the FCM solution with a nonlinear-correction and the analytical solution is very good. It should be noted that this system is one of the worst cases for FCM to simulate. The secondary flow is very sensitive to the no-slip surface representation. While, due to the use of a regularized multipole, the no-slip particle surface is approximated by a smooth profile, which results in the underestimation of the gradient of the flow velocity near the particle surface. This numerical test suggests that the nonlinear interaction can be computed correctly by adding a correction force.

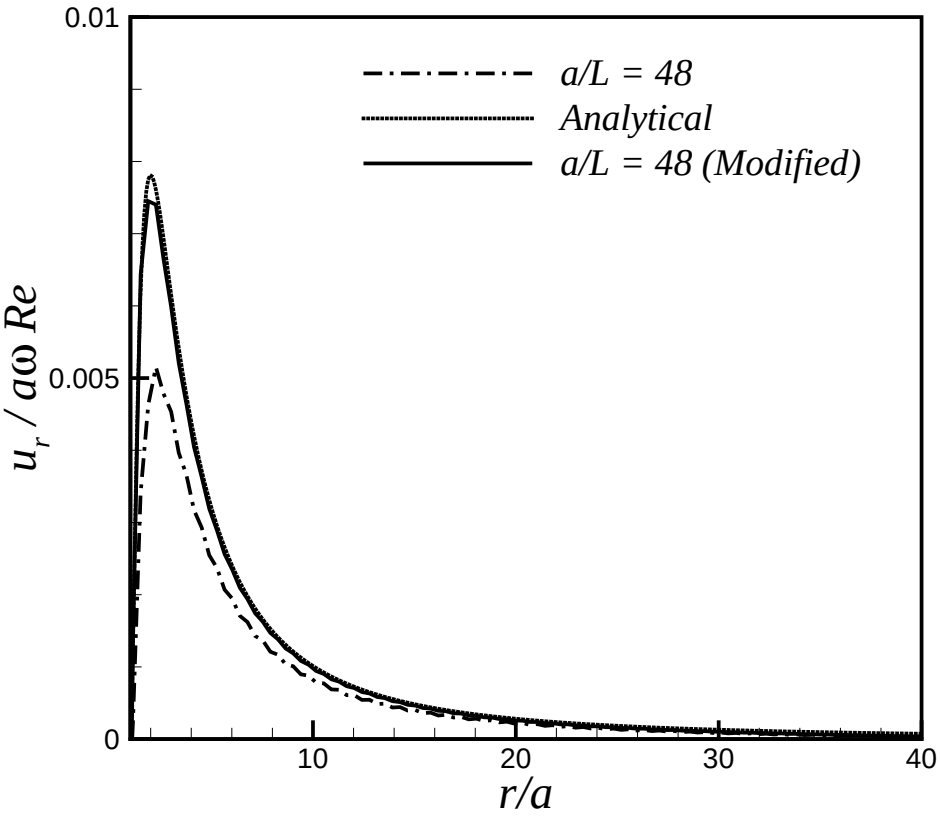

Figure 5.9: Comparison of the radial velocity u_r obtained from FCM-TS with a nonlinear-interaction-correction with the analytical solution by Bickley [17].

5.3 Summary

In this chapter, the hydrodynamic interaction between spheres rotating under an external body torque at small but finite Reynolds number. It is shown that a secondary meridional circulation develops around a rotating particle by the nonlinear interaction and, due to the secondary flow, there is a net repulsive hydrodynamic force between a pair of rotating, coplanar sphere. This result suggests that the dynamic self-assembly observed in the experiments [81, 82] is a result of the balance between the magnetic attraction force and the hydrodynamic repulsion force. It is found that FCM underestimates the magnitude of the secondary flow, which is related with the smooth particle surface representation. It is shown that, by adding a simple correction force, the secondary flow can be reproduced correctly in FCM. A more general and robust correction scheme is a subject of further investigation.

Chapter 6

Finite-Reynolds-number flow: Concentrated suspensions in a linear shear flow

6.1 Introduction

Most studies on the suspension flows, particularly for moderate to high volume fractions, have been focused on the Stokes limit, *i.e.* at zero Reynolds number. However, even under very small fluid inertia, *e.g.* Reynolds number of $O(10^{-2}) \sim O(10^{-1})$, it has been shown that suspension dynamics becomes very different from that in the Stokes limit [33, 39, 85, 118, 193]. The effects of the fluid inertia on suspension dynamics and rheology is important in many biological and engineering flows. For example, while the bulk Reynolds number of blood flow in arteries is $O(10^2)$, the particle-scale Reynolds number remains $O(0.1) \sim O(1)$. However, still it is not clearly understood how mechanical properties of the bulk fluid are affected by inertia.

Since the pioneering studies by Schowalter [130] and Acrivos [114, 173], the dynamics of a single sphere in a shear flow under finite fluid inertia has been studied extensively [11, 19, 154, 171, 204]. Compared to the suspension dynamics in the dilute limit, *i.e.* without considering hydrodynamic interaction between the suspended particles, there are only a limited number of studies about the Reynolds-number effects on semi-dilute to concentrated suspensions in a linear shear flow. One of the main reasons behind the slow progress is

that numerical simulation of suspension flows is computationally challenging because the numerical method should be able to resolve the small gap between suspended particles, which is in many cases as small as $O(10^{-3}) \sim O(10^{-2})$ of the particle radius, as well as long-range multibody hydrodynamic interactions on the lengthscale of $O(1) \sim O(10)$ of the particle radius. Nguyen & Ladd [162] developed a lattice-Boltzmann method (LBM) supplemented with a near-field correction scheme, which facilitated the study of finite-inertia suspensions. Yan *et al.* [226] and, subsequently, Kulkarni & Morris [118] have studied hydrodynamic interactions between two spherical particles in a wall-bounded linear shear flow from LB simulations. In particular, Kulkarni & Morris [118] have shown that the topology of the relative trajectory changes from an open or closed trajectory in Stokes flow to an open, reversing, or spiralling trajectory under finite fluid inertia. In their two-dimensional LB simulations of cylinders suspended in a wall-bounded linear shear flow, Kromkamp *et al.* [117] investigated the Reynolds number effects, particularly, focused on the self-diffusion of the cylinders. Verberg & Koch [215] performed three-dimensional LB simulations of suspensions of inertial particles in a wall-bounded linear shear flow to study the effects of both fluid and particle inertia on suspension rheology. In the LB simulations of suspensions of neutrally buoyant particles in a wall-bounded linear shear flow, Kulkarni & Morris [119] have reported the changes in the particle stresses and microstructures under finite fluid inertia. As shown above, most of the studies using LBM have been performed in a wall-bounded linear shear flow. However, Yeo & Maxey [230, 229] have shown that the dynamics of wall-bounded suspensions becomes very complicated due to the coherent structures induced by the wall. To identify the finite-Reynolds-number effect on suspension dynamics clearly, it is necessary to investigate suspensions in a homogeneous linear shear flow.

In the present study, we report the changes in rheology and diffusion of concentrated suspensions of neutrally buoyant spheres in a homogeneous linear shear flow under finite fluid inertia. The force-coupling method with a lubrication correction scheme is employed for the numerical simulations of concentrated suspensions in a homogeneous linear shear flow. The details of the simulation parameters are given in 6.2. In 6.3, the effects of fluid inertia on the velocity statistics and diffusivity are reported. The changes in suspension rheology under finite fluid inertia are shown in 6.4 and the microstructures are analyzed in 6.5.

6.2 Simulation parameters

The force-coupling simulations for mono-disperse suspensions at finite Reynolds numbers are performed in a tri-periodic cubic domain. A Fourier spectral method is used to solve the Navier-Stokes equations. The computational mesh is deformed with the shear flow to satisfy the periodic boundary condition. Details of the numerical method are given in 2.4 and 2.5.1.

The size of the computational domain is fixed, $(H_x \times H_y \times H_z) = (2\pi \times 2\pi \times 2\pi)$, and the number of Fourier modes used in the simulations is $(N_x \times N_y \times N_z) = (64 \times 64 \times 64)$. Here (x, y, z), or (x_1, x_2, x_3), denotes the flow, velocity gradient, and vorticity directions. The radius of the suspended particles is $a = 0.3$. The numbers of the suspended particles for each volume fractions (ϕ, N_p) are $(0.2, 438)$, $(0.3, 657)$, and $(0.4, 876)$. The time step size is changed from $\dot{\gamma}\delta t = 1 \times 10^{-3}$ for $Re_{\dot{\gamma}} = 0.005$ to $\dot{\gamma}\delta t = 5 \times 10^{-5}$ for $Re_{\dot{\gamma}} = 2$, in which $\dot{\gamma}$ is the shear rate and $Re_{\dot{\gamma}} = \frac{\rho \dot{\gamma} a^2}{\mu_0}$ is the particle Reynolds number. The initial particle configurations are obtained from molecular dynamics simulations. The systems are sheared for $50 \sim 100\ \dot{\gamma}t$ to reach a stationary state. Then, the simulations are performed for $T^* = 500 \sim 1000\dot{\gamma}t$ after the system reaches a stationary state to gather the statistics. Since the system is ergodic, the time average is used instead of an ensemble average.

As a model for non-hydrodynamic interaction between particles, an inter-particle potential force is used. The potential force to particle β from particle α is given as

$$\boldsymbol{F}_P^{\alpha\beta} = \begin{cases} -6\pi\mu_0\dot{\gamma}a^2 F_{ref} \left(\frac{R_{ref}^2 - |\boldsymbol{r}|^2}{R_{ref}^2 - 4a^2} \right)^6 \frac{\boldsymbol{r}}{|\boldsymbol{r}|} & \text{if } |\boldsymbol{r}| < R_{ref} \\ 0 & \text{otherwise,} \end{cases} \tag{6.1}$$

in which $\boldsymbol{r} = \boldsymbol{Y}^\alpha - \boldsymbol{Y}^\beta$, R_{ref} is the cut-off distance, and F_{ref} is a constant. To minimize the effects of the potential force on the suspension dynamics, the force parameters are chosen to make the potential force behave close to the hard-sphere potential; $R_{ref} = 2.004a$ and $F_{ref} = 5 \times 10^4$. The effects of the potential force on the suspension rheology are briefly discussed in 6.4.

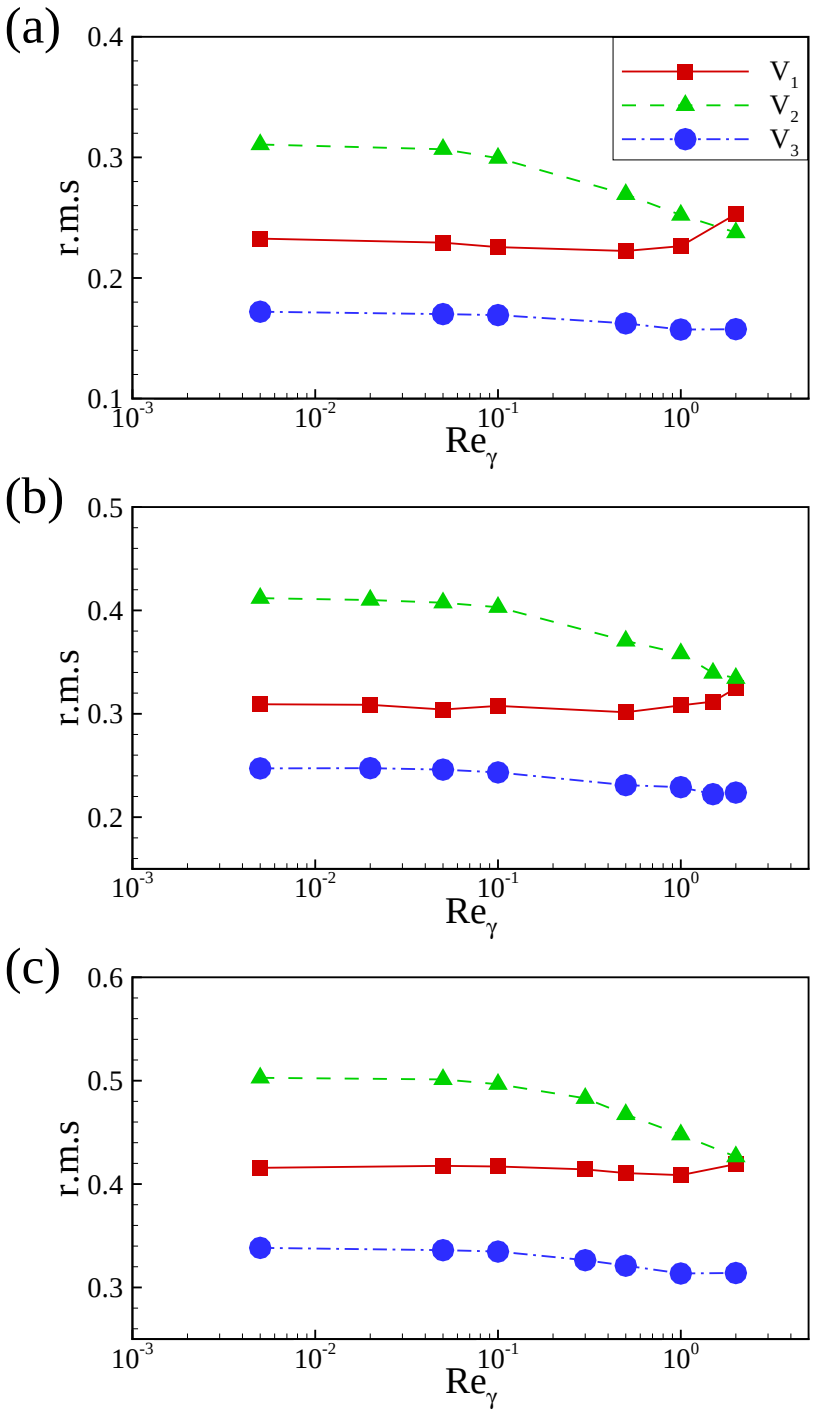

Figure 6.1: Root-mean-square velocity fluctuation normalized by $a\dot{\gamma}$; (a) $\phi = 0.20$, (b) $\phi = 0.30$, and (c) $\phi = 0.40$.

6.3 Velocity statistics

Figure 6.1 shows root-mean-square (r.m.s) velocity fluctuations normalized by the shear rate and the particle radius ($\dot{\gamma}a$). Root-mean-square velocity fluctuation is computed by

$$v_i' = \left[\frac{1}{T} \int_0^T \overline{(V_i(s) - \dot{\gamma} Y_2(s) \delta_{i1})^2} ds \right]^{1/2}, \tag{6.2}$$

in which $\boldsymbol{V}$ is the particle velocity, $\boldsymbol{Y}$ is the position of the particle, and the overline indicates the average over the suspended particles. It is shown that $\boldsymbol{v}'$ does not change significantly when $Re_{\dot{\gamma}} < 0.1$. Consistent with the Stokesian Dynamics simulations of Drazer *et al.* [59] at zero Reynolds number, v_2' is the largest and $v_2' > v_1' > v_3'$ for small $Re_{\dot{\gamma}}$. For $Re_{\dot{\gamma}} > 0.1$, v_2' and v_3' are decreasing functions of the Reynolds number, while v_1' slightly increases when $Re_{\dot{\gamma}} > 0.5$. As the volume fraction ϕ increases, the increase of v_1' with $Re_{\dot{\gamma}}$ becomes less pronounced. The ratio of $v_1'(Re_{\dot{\gamma}} = 2)$ to $v_1'(Re_{\dot{\gamma}} = 0.005)$ changes from 0.087 to 0.051 and, then, to 0.009 for $\phi = 0.20$, 0.30, and 0.40, respectively. Hence, the overall "suspension temperature" $T^{sus} = ({v_1'}^2 + {v_2'}^2 + {v_3'}^2)/3$ normalized by $\dot{\gamma}a$ becomes a decreasing function of $Re_{\dot{\gamma}}$. Similar decrease of T^{sus} with increasing $Re_{\dot{\gamma}}$ has been observed by Verberg & Koch [215]. However, since they considered the wall-bounded suspensions at high Stokes numbers (high particle inertia), a quantitative comparison is not feasible.

The auto-correlation function for the particle velocity is defined as

$$\rho_i^V(\tau) = \frac{\langle V_i(0) V_i(\tau) \rangle}{{v_i'}^2}, \tag{6.3}$$

in which τ is a time-lag. Figure 6.2 shows the auto-correlation functions for $\phi = 0.30$. The auto-correlation function shows three distinctive regions. Near the origin $\dot{\gamma}\tau < 0.2$, the auto-correlation functions for larger $Re_{\dot{\gamma}}$ decays faster. The effects of the finite inertia is more pronounced in the intermediate timescale, $0.5 < \dot{\gamma}\tau < 4$. In contrast to the early-time dynamics, the decay rate of the auto-correlation functions in the intermediate timescale is smaller at larger $Re_{\dot{\gamma}}$ and, hence, the negative loop of ρ^V becomes smaller. Finally, the auto-correlation functions for $\dot{\gamma}\tau > 4$ collapse onto one curve.

A Lagrangian integral timescale can be defined by

$$T_i^L = \int_0^\infty \rho_i^V(s) ds. \tag{6.4}$$

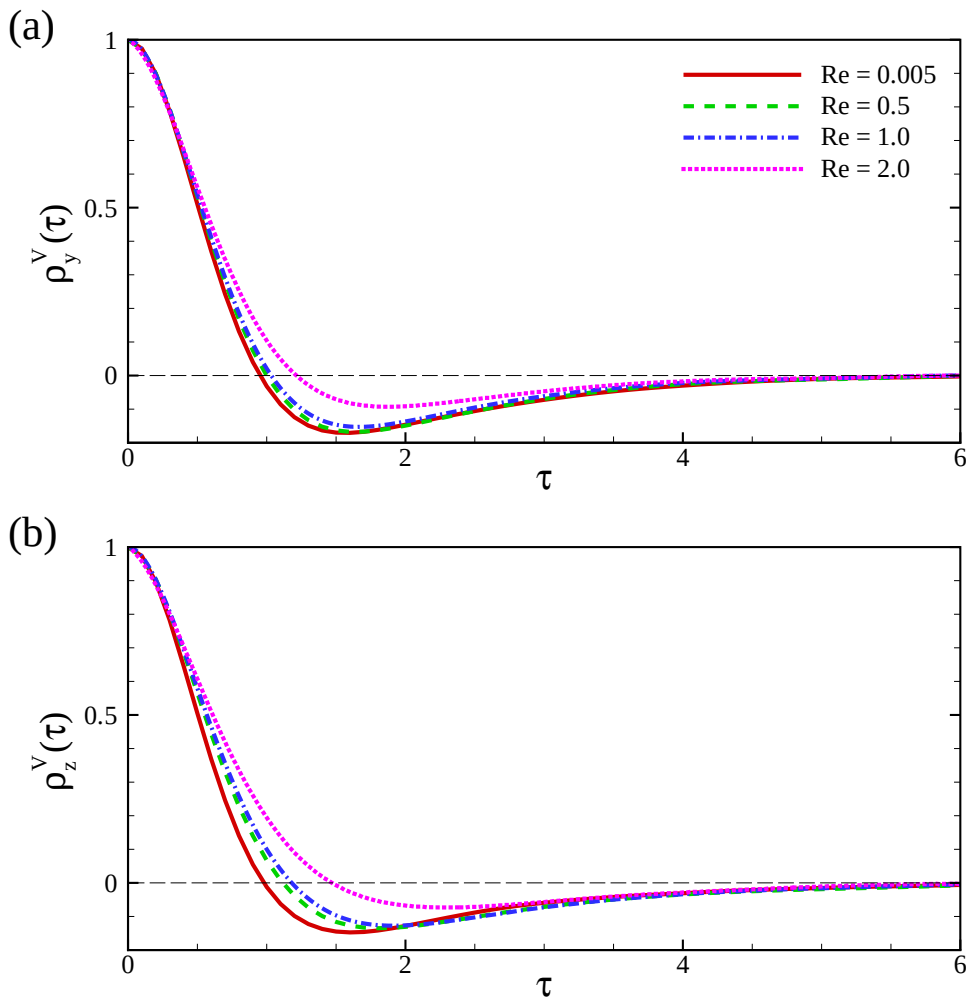

Figure 6.2: Auto-correlation functions for the (a) velocity-gradient- and (b) vorticity-direction velocities for $\phi = 0.30$. The time-lag τ is normalized by the shear rate $\dot{\gamma}$.

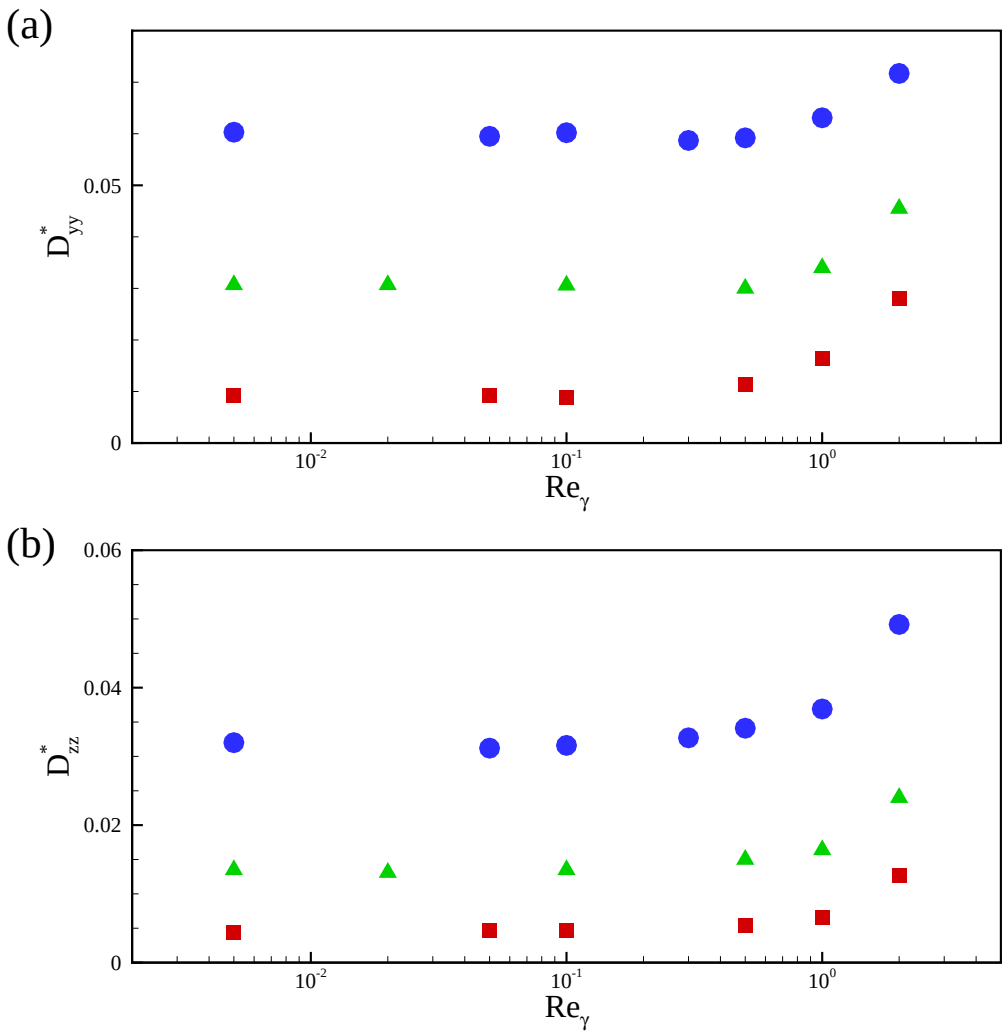

Figure 6.3: The self-diffusivities normalized by $\dot{\gamma}a^2$ in the (a) velocity-gradient and (b) vorticity directions as functions of $Re_{\dot{\gamma}}$: ■, $\phi = 0.20$; ▲, $\phi = 0.30$; ●, $\phi = 0.40$.

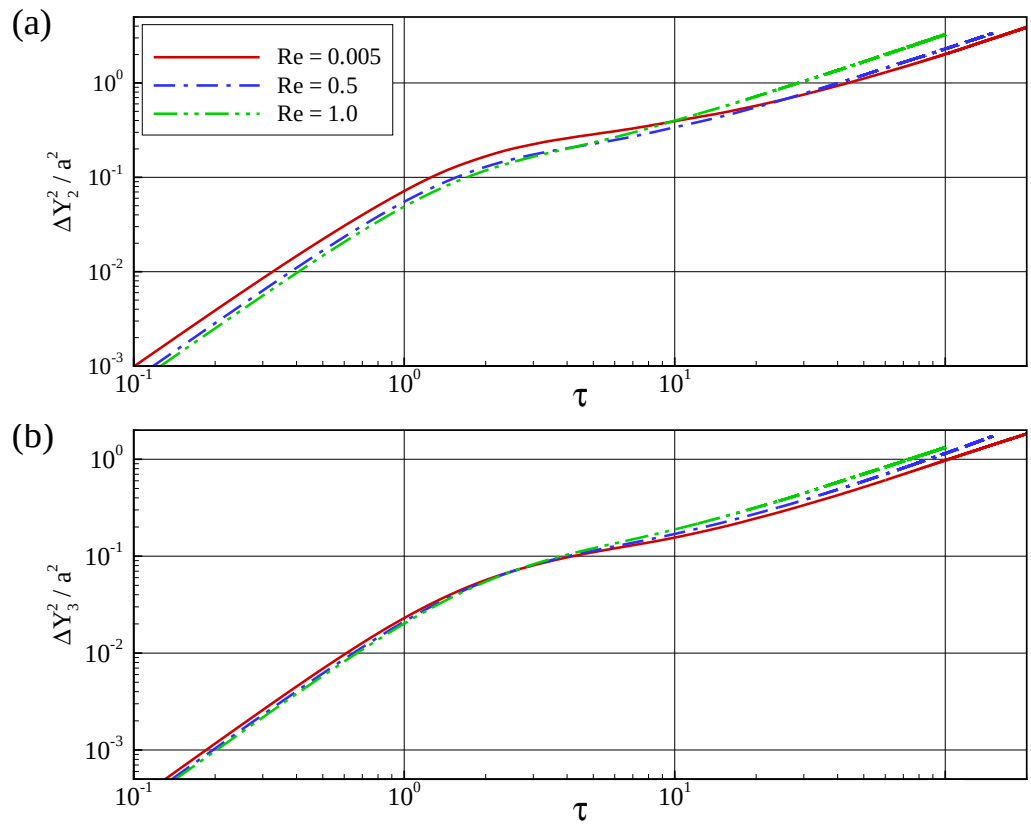

Figure 6.4: Mean-square displacements normalized by the particle radius a^2 for $\phi = 0.20$ in the (a) velocity-gradient and (b) vorticity directions.

The integral timescale is related to the self-diffusivity of the suspended particles as

$$D_{ii} = v_i'^2 T_i^L. \tag{6.5}$$

The self-diffusivity normalized by the shear-rate and the particle radius (D_{ii}^*) is shown in figure 6.3. For $0.2 \leq \phi \leq 0.4$, the diffusivity remains almost a constant for $Re_{\dot{\gamma}} < 0.1$. The diffusivity for $Re_{\dot{\gamma}} < 0.1$ is quantitatively consistent with the Stokesian Dynamics simulations of Sierou & Brady [198] at zero Reynolds number. Although the velocity fluctuation v' is attenuated at larger $Re_{\dot{\gamma}}$, the diffusivity is shown to be an increasing function of $Re_{\dot{\gamma}}$ for $Re_{\dot{\gamma}} > 0.1$. As shown in figure 6.2, the particle motion in finite-$Re_{\dot{\gamma}}$ flows has longer correlation than in Stokes flows, which contributes to the increase in the integral timescale and, consequently, increase in the diffusivity.

Figure 6.4 shows the mean-square displacements (MSD) for $\phi = 0.20$. The central limit theorem dictates that the mean-square displacement of the particles exhibiting stochas-

tic motion should be proportional to the travel time τ in the long-time limit ($\tau \gg T^L$); $\langle \Delta Y_i^2(\tau) \rangle \sim \tau$, in which $\Delta Y_i(\tau) = Y_i(\tau) - Y_i(0)$. The diffusivity can be obtained from this relation as,

$$D_{ii} = \frac{1}{2} \frac{d}{d\tau} \langle \Delta Y_i^2(\tau) \rangle \Big|_{\tau = T^D} \quad \text{for } T^D \gg T^L. \tag{6.6}$$

The diffusivities computed from (6.5) and (6.6) should be the same. We estimated the diffusivities from those two relations and the differences between them were always less than 10%, which is due to the statistical noise.

In the short-time limit $\tau \ll T^L$, the particle motion is still strongly correlated to the initial velocity and, hence, MSD is proportional to τ^2. In the τ^2 regime, MSD is smaller at larger $Re_{\dot{\gamma}}$, which is consistent with the decrease of v' with increasing $Re_{\dot{\gamma}}$. In the intermediate timescale $\dot{\gamma}\tau \sim O(1)$, the growth-rate of MSD for $Re_{\dot{\gamma}} = 0.005$ becomes smaller than 1; MSD $\sim \tau^\nu$ and $\nu \simeq 0.5$, which is related with the negative loop in the velocity auto-correlation. In figure 6.2, it is shown that the velocity auto-correlation functions decay more slowly at larger $Re_{\dot{\gamma}}$. In agreement with the velocity auto-correlations, the range of the intermediate region decreases and the growth-rate ν in the region increases as $Re_{\dot{\gamma}}$ increases. Hence, although the initial MSD in the τ^2 regime for larger $Re_{\dot{\gamma}}$ is smaller, in the diffusive regime, MSD becomes an increasing function of $Re_{\dot{\gamma}}$.

The probability density functions (PDF) of the particle velocity $P(V_i)$ are shown in figure 6.5. The probability density functions are normalized by the corresponding standard deviations (v_i'). Drazer *et al.* [58] have shown that $P(V_y)$ at zero Reynolds number changes from an exponential distribution $P(V) \sim \exp(-\alpha|V|)$ at low ϕ to a Gaussian distribution $P(V) \sim \exp(-\alpha V^2)$, in which α is a fitting coefficient. In figure 6.5 (a, c), $P(V_y)$ for $\phi = 0.20$ shows a slower decay for $|V_y/v_y'| > 3$ compared to the Gaussian distribution, while $P(V_y)$ for $\phi = 0.40$ is nearly Gaussian. The flatness factor of $P(V_y)$ for $Re_{\dot{\gamma}} = 0.005$ changes from 3.17 at ϕ0.20 to 3.02 at $\phi = 0.40$. For the particle velocity in the vorticity direction, the core of $P(V_z)$ ($|V_z/v_z'| < 3$) is well represented by the Gaussian distribution whereas large magnitude events ($|V_z/v_z'| > 3$) show a $\sim \exp(-\alpha|V|)$ behavior. Both in $P(V_y)$ and $P(V_z)$, the velocity PDFs becomes wider at larger $Re_{\dot{\gamma}}$, indicating that the system becomes more intermittent at larger $Re_{\dot{\gamma}}$. Using the lattice-Boltzmann simulations, Kulkarni & Morris [119] showed that the velocity PDF becomes narrower at larger $Re_{\dot{\gamma}}$.

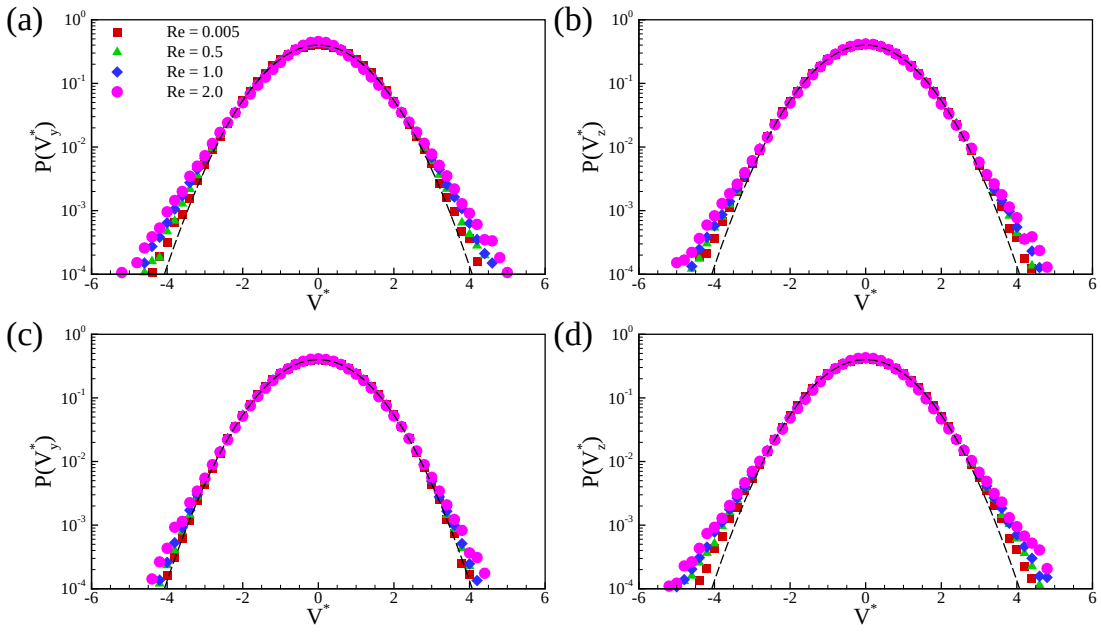

Figure 6.5: The probability density functions (PDF) of particle velocity for (a, b) $\phi = 0.20$ and (c, d) $\phi = 0.40$; (a,c) are PDFs of the particle velocity in the velocity-gradient direction and (b, d) are PDFs for the vorticity direction. The dashed line is the Normal distribution. Each pdf is normalized by its standard deviation.

This contradictory result between the present simulations and [119] may come from the difference in normalization. In the present study, the particle velocity is normalized by the standard deviation to investigate the changes in the intermittency, while Kulkarni & Morris [119] showed PDFs for the particle velocity normalized by $\dot{\gamma}a$.

6.4 Particle stresses

6.4.1 Shear stress

Following Batchelor [13], the bulk stress of homogeneous suspension flows is given by

$$\langle \sigma_{ij} \rangle = -\delta_{ij} \left\langle \int_{\Omega^D \setminus \Omega^p} p dV \right\rangle + 2\mu_0 E^B_{ij} + \left\langle \sigma^p_{ij} \right\rangle - \rho \langle u'_i u'_j \rangle, \tag{6.7}$$

in which Ω^D is the control volume, Ω^P is the volume occupied by the particles, ρ is the density of the fluid, E^B is the ensemble averaged strain-rate tensor of the bulk fluid, $\boldsymbol{u}'$ is the fluctuating velocity of the bulk fluid, and σ^p is the particle stress. In homogeneous suspensions, the bulk strain rate is $E^B_{ij} = \dot{\gamma}/2(\delta_{i1}\delta_{j2} + \delta_{i2}\delta_{j1})$. The last term of (6.7) is

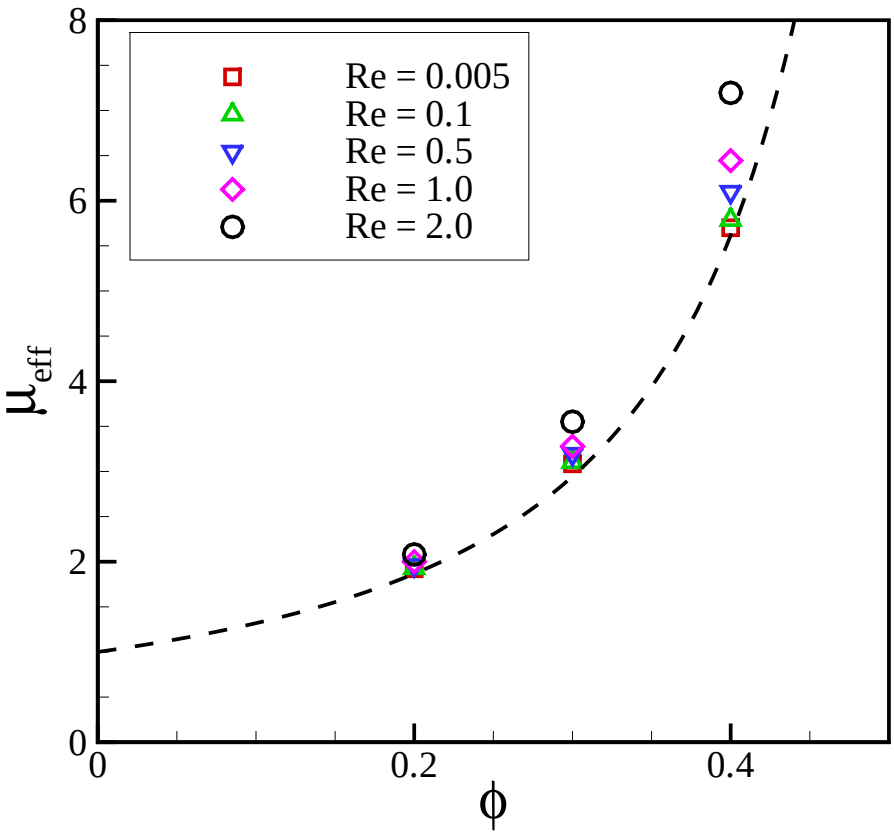

Figure 6.6: The changes in the effective viscosity with ϕ and $Re_{\dot{\gamma}}$. The dashed line is the Eilers' fit [203].

the Reynolds stress. Since we consider only small $Re_{\dot{\gamma}}$, the Reynolds stress is not expected to contribute significantly to the total stress. Kulkarni & Morris [119] suggested that the Reynolds stress is negligibly small compared to the particle stress term when $Re_{\dot{\gamma}}$ is $O(1)$ or smaller. The particle stress tensor is computed from

$$\langle \boldsymbol{\sigma}^p \rangle = n \left(\langle \boldsymbol{S} \rangle - \langle \boldsymbol{r} \otimes \boldsymbol{F}_p \rangle \right). \tag{6.8}$$

Here, n is the number density, S_{ij} is the stresslet, and $\boldsymbol{F}_p$ is the interparticle potential force.

Here, the effective viscosity is computed from the bulk viscosity of the suspension flow,

$$\frac{\mu_{eff}}{\mu_0} = 1 + \frac{\langle \sigma_{12}^P \rangle}{\mu_0 \dot{\gamma}}. \tag{6.9}$$

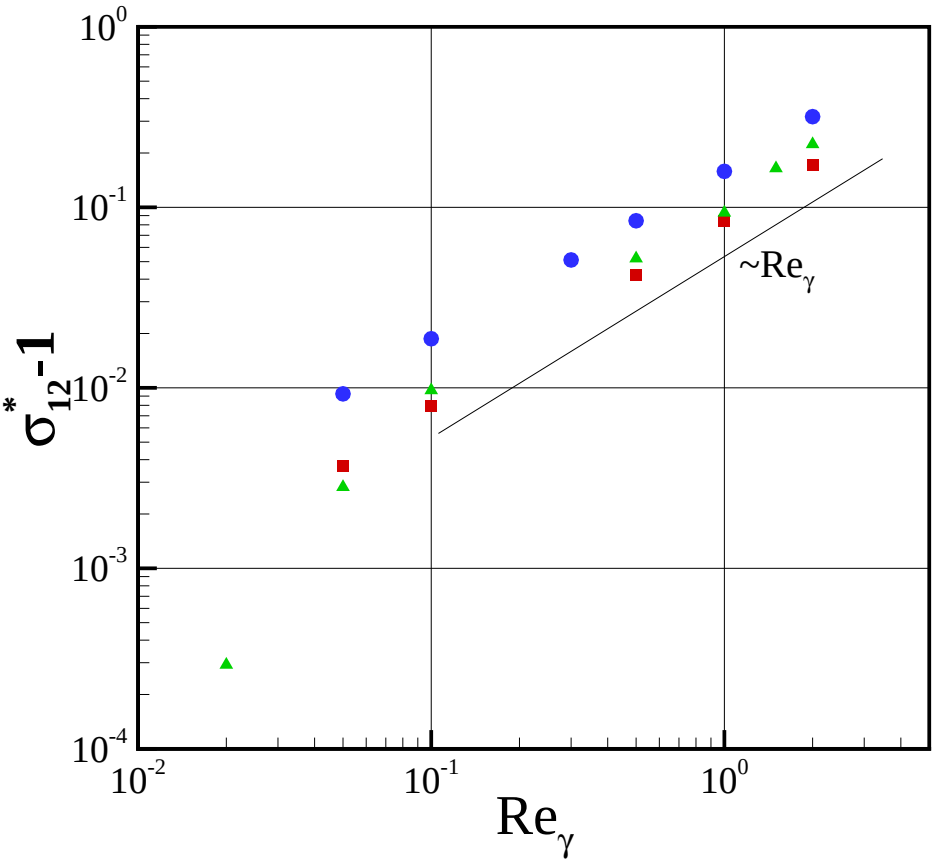

Figure 6.7: The normalized particle shear stress as a function of $Re_{\dot{\gamma}}$. The particle stress is normalized by its value at $Re_{\dot{\gamma}} = 0.005$. ■, $\phi = 0.20$; ▲, $\phi = 0.30$; •, $\phi = 0.40$.

The Reynolds stress term is not considered in the present study. The effective viscosity is shown in figure 6.6 together with the Eilers' fit [203],

$$\frac{\mu_{eff}}{\mu_0} = \left(1 + \frac{\frac{1}{2}[\eta]\phi}{1 - \phi/\phi_m}\right)^2. \tag{6.10}$$

Here, the fitting parameters are chosen as $\eta = 2.5$ and $\phi_m = 0.63$. It is shown that μ_{eff} estimated for $Re_{\dot{\gamma}} = 0.005$ agrees well with the empirical relation. In agreement with Kulkarni & Morris [119], μ_{eff} increases with the increase in $Re_{\dot{\gamma}}$.

To investigate the changes of σ^P_{12} with $Re_{\dot{\gamma}}$ further, the particle shear stress is normalized its value at $Re_{\dot{\gamma}} = 0.005$ and one is subtracted from the normalized particle shear stress: $\Delta\sigma^*_{12} = \sigma^P_{12}(\phi, Re_{\dot{\gamma}})/\sigma^P_{12}(\phi, 0.005) - 1$. In the dilute limit, Lin *et al.* [130] have shown analytically that the particle shear stress is proportional to $Re^{3/2}_{\dot{\gamma}}$. Mikulencak & Morris [154]

showed, in their finite element simulations of a single neutrally buoyant particle in finite-Reynolds-number shear flow, that the particle shear stress does follow the $Re_{\dot{\gamma}}^{3/2}$ scaling at low Reynolds numbers ($Re_{\dot{\gamma}} < 10^{-1}$) with a coefficient different from that suggested by Lin *et al.* [130]. In their simulations, it is shown that the increase of the particle shear stress with $Re_{\dot{\gamma}}$ changes from $Re_{\dot{\gamma}}^{3/2}$ to $Re_{\dot{\gamma}}$ around $Re_{\dot{\gamma}} \simeq 10^{-1}$. Using the lattice-Boltzmann simulations, Verberg & Koch [215] have shown that the stresslet for $\phi = 0.30$ grows proportional to $Re_{\dot{\gamma}}$ for $10^{-2} < Re_{\dot{\gamma}} < 1$ and then it shows $\sim Re_{\dot{\gamma}}^{0.6}$ behavior. Similar to their results, in figure 6.7, it is shown that $\Delta\sigma_{12}^*$ is proportional to $Re_{\dot{\gamma}}$ in $0.1 < Re_{\dot{\gamma}} < 2$. In the present study, the $Re_{\dot{\gamma}}^{0.6}$ scaling is not observed. Again, it should be noted that the numerical simulations of [215] are high-Stokes-number suspensions while, in the present study, we consider neutrally buoyant particles.

The probability density functions for the shear component of the particle stresslet $P(S_{12}^*)$ is shown in figure 6.8. Here, the particle stresslet is estimated from the sum of hydrodynamic stresslet and interparticle potential contributions;

$$\boldsymbol{S}_{12}^* = S_{12} - \frac{1}{2}\sum_{nb} \boldsymbol{r} \otimes \boldsymbol{F}_P, \tag{6.11}$$

in which nb is the number of particles in the cut-off distance; $R_{ref} < 2.004a$. The pdf is standardized by its mean and standard deviation s_{12}' so that $P(S_{12}^*)$ has zero mean and standard deviation of 1. For $Re_{\dot{\gamma}} = 0.005$, $P(S_{12}^*)$ is strongly skewed to the right. The skewness factors at $Re_{\dot{\gamma}} = 0.005$ are 1.25, 1.31, and 1.63 for $\phi = 0.2$, 0.3, and 0.4, respectively. As $Re_{\dot{\gamma}}$ increases, S_{12}^* becomes highly intermittent. The probability of the positive intermediate magnitude events $0 < S_{12}^*/s_{12}' < 5$ decreases at larger $Re_{\dot{\gamma}}$, while the probability of intermittent events, more than 5 times larger than s_{12}', rapidly increases with the increase in $Re_{\dot{\gamma}}$. In the inset of figure 6.8, it is shown that the positive tail of $P(S_{12}^*)$ changes from an exponential decay $\sim \exp(-\alpha|S_{12}^*|)$ at $Re_{\dot{\gamma}} = 0.005$ to an algebraic decay $\sim {S_{12}^*}^{-\beta}$ at $Re_{\dot{\gamma}} = 2$. The fitting parameters (α, β) are (1.2, 2.9) for $\phi = 0.2$ and (1.1, 2.0) for $\phi = 0.4$. In all cases, the tail of pdfs drops quickly to zero after $S_{12}^*/s_{12}' > 20$. It is not clear whether this exponential decay at large S_{12}^* is because of the insufficient sample size to resolve such an intermittent event or of a physical mechanism. It is worthwhile to noted that if the pdf exhibits a $\sim {S_{12}^*}^{-2}$ behavior for all $S_{12}^* \in (L, \infty)$, in which L is a constant, even the first moment is divergent, which is not physical.

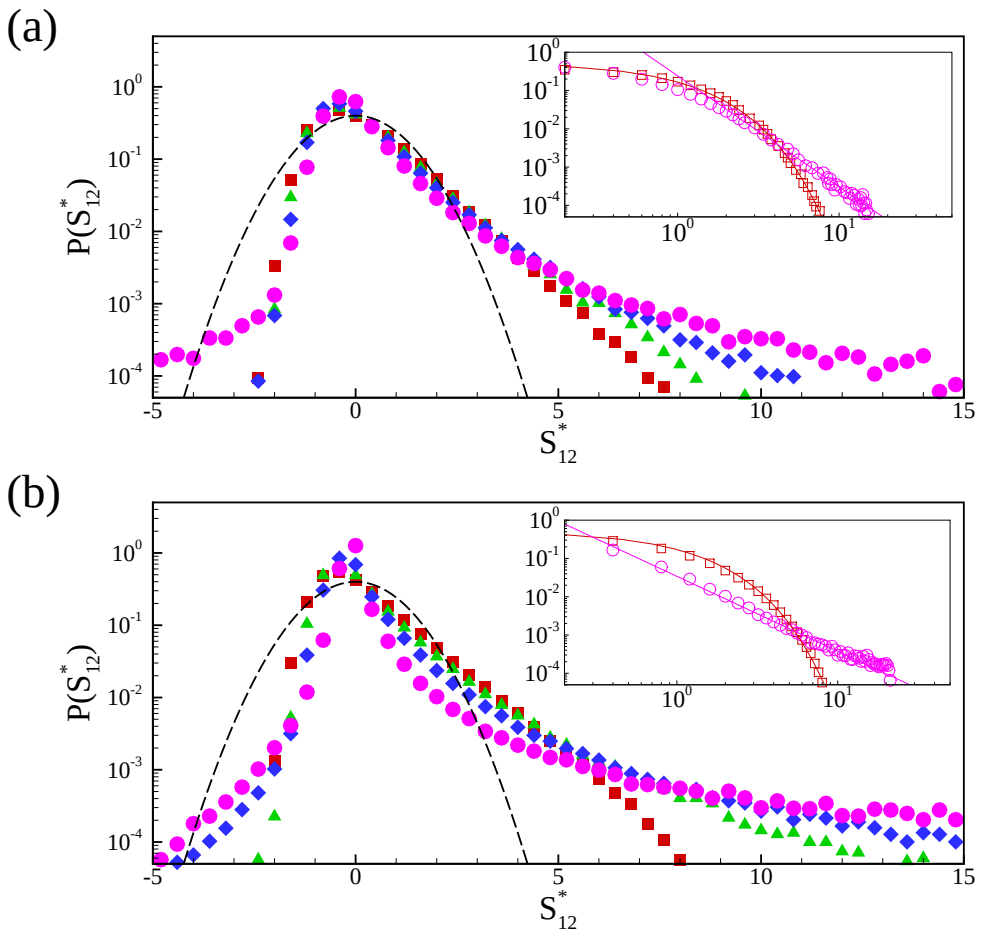

Figure 6.8: The standardized probability density functions of the shear component of the particle stresslet for (a) $\phi = 0.20$ and (b) $\phi = 0.40$: ■, $Re_{\dot{\gamma}} = 0.005$; ▲, $Re_{\dot{\gamma}} = 0.5$; ♦, $Re_{\dot{\gamma}} = 1.0$; •, $Re_{\dot{\gamma}} = 2.0$. The dashed line is the Normal distribution. The inset shows the positive tails of the pdfs for $Re_{\dot{\gamma}} = 0.005$ and $Re_{\dot{\gamma}} = 2.0$.

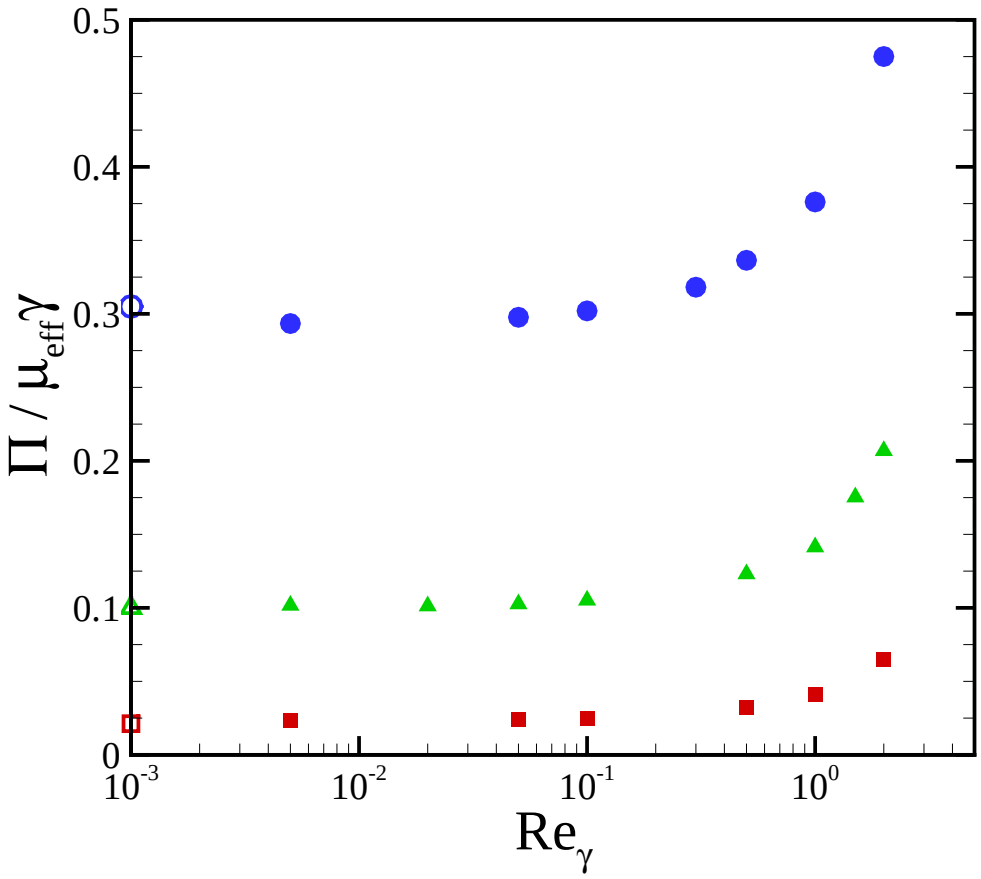

Figure 6.9: The particle pressure normalized by the effective viscosity: ■, $\phi = 0.20$; ▲, $\phi = 0.30$; •, $\phi = 0.40$. The hollow symbols are the numerical results of Sierou & Brady [197] at zero Reynolds number.

6.4.2 Normal stresses

Figure 6.9 shows the particle pressure normalized by the effective viscosity and the shear rate. The particle stress is defined as

$$\Pi = -\frac{1}{3}\langle \sigma_{11}^P + \sigma_{22}^P + \sigma_{33}^P \rangle. \tag{6.12}$$

The normalized particle pressure is almost uniform for $Re_{\dot{\gamma}} < 0.1$ and then begins to increase with the increase in $Re_{\dot{\gamma}}$, indicating that the particle pressure increases faster than the shear stress. The hollow symbols are the Accelerated Stokes Dynamics simulations of Sierou & Brady [197]. It is shown that the present simulation results at low $Re_{\dot{\gamma}}$ agree well with the results of [197] at zero Reynolds number.

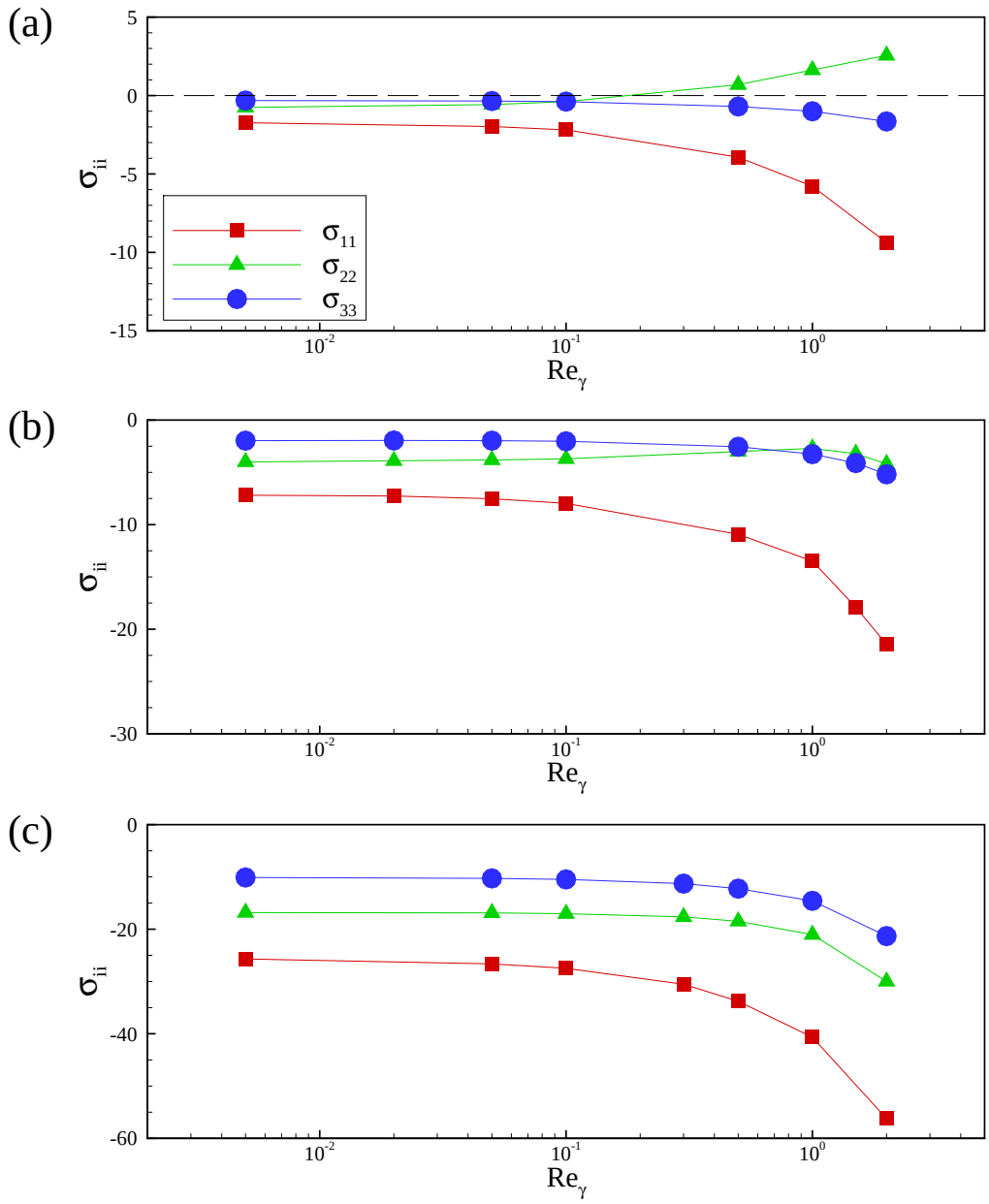

Figure 6.10: Normal stresses normalized by $\mu_0\dot{\gamma}$ as functions of $Re_{\dot{\gamma}}$ for (a) $\phi = 0.2$, (b) $\phi = 0.3$, and (c) $\phi = 0.4$.

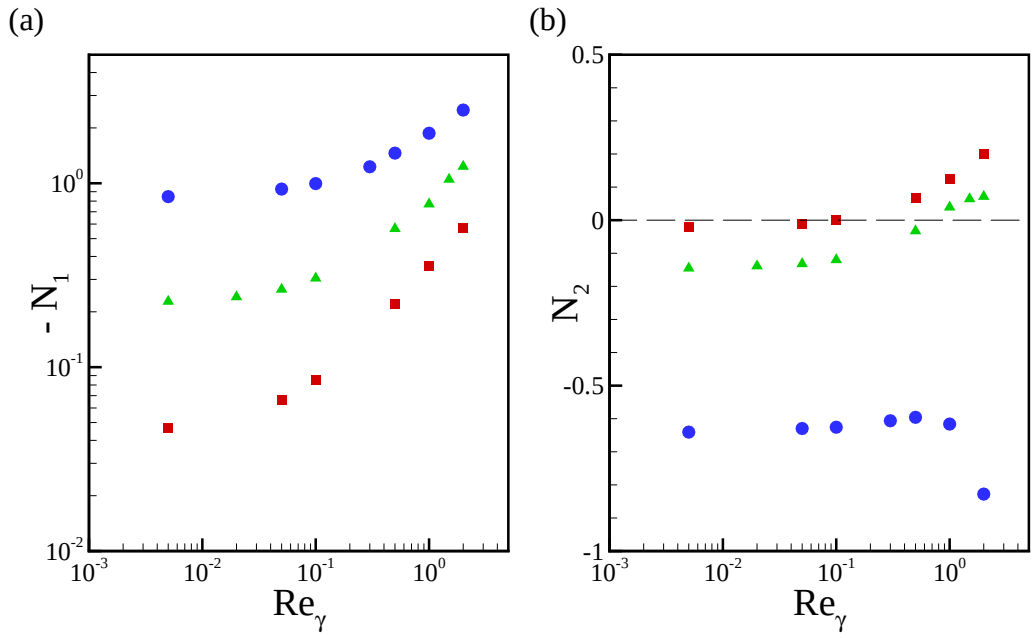

Figure 6.11: First (a) and second (b) normal stress differences normalized by $\mu_0\dot{\gamma}$ as functions of $Re_{\dot{\gamma}}$: ■, $\phi = 0.20$; ▲, $\phi = 0.30$; ●, $\phi = 0.40$.

Each components of the particle normal stresses are shown in figure 6.10. In Stokes-flow suspensions, all three normal stress components are negative [240]. It is shown that the normal stresses at $Re_{\dot{\gamma}} = 0.005$ are all negative. In the range of ϕ in the present study, σ_{11}^P and σ_{33}^P are always negative and the magnitude ($|\sigma_{11}^P|$ and $|\sigma_{33}^P|$) increases with $Re_{\dot{\gamma}}$. On the other hand, σ_{22}^P for $\phi = 0.2$ is negative at $Re_{\dot{\gamma}} = 0.005$ and σ_{22}^P increases with $Re_{\dot{\gamma}}$, which eventually becomes positive for $Re_{\dot{\gamma}} > 10^{-1}$. Similarly, for $\phi = 0.3$, σ_{22}^P increases with $Re_{\dot{\gamma}}$ at first and, then, starts decreasing for $Re_{\dot{\gamma}} > 1$. For $\phi = 0.4$, the behavior of σ_{22}^P becomes a monotonic function of $Re_{\dot{\gamma}}$ similar to σ_{11}^P and σ_{33}^P. These changes in the normal stresses will be discussed further in 6.5.

The first (N_1) and second (N_2) normal stress differences normalized by $\mu_0\dot{\gamma}$ are shown in figure 6.11. The normal stress differences are defined as

$$N_1 = \sigma_{11}^P - \sigma_{22}^P, \tag{6.13}$$

$$N_2 = \sigma_{22}^P - \sigma_{33}^P. \tag{6.14}$$

Consistent with the Stokes-flow suspensions, both N_1 and N_2 are negative at $Re_{\dot{\gamma}} = 0.005$. In the range of $Re_{\dot{\gamma}}$ of the present study, N_1 is always negative. For $Re_{\dot{\gamma}} < 0.1$, N_1 looks

to converge to an asymptotic value. For $Re_{\dot{\gamma}} > 0.1$, N_1 grows proportional to $Re_{\dot{\gamma}}^{\beta}$, in which β is a growth factor. For comparison, the theory in the dilute limit ($\phi \to 0$) given in Lin *et al.* [130] predicts $\sim Re_{\dot{\gamma}}^{1/3}$ growth for large $Re_{\dot{\gamma}}$. The growth factor in concentrated suspensions is shown to be a decreasing function of ϕ; $\beta = 0.63$, 0.56, and 0.37 for $\phi = 0.2$, 0.3, and 0.4, respectively. Unlike N_1, it is shown that N_2's for $\phi = 0.2$ and 0.3 become positive for $Re_{\dot{\gamma}} > 0.1$ and $Re_{\dot{\gamma}} > 0.5$, respectively. This behavior of N_2 is qualitatively similar with Kulkarni & Morris [118]. However, in their lattice-Boltzmann simulations of a wall-bounded Couette-flow suspensions, N_2 becomes positive at larger ϕ for $\phi \leq 0.2$ and N_2 stays negative for $\phi = 0.3$, whereas, in the present simulation, the positive N_2 is observed for the volume fraction up to 0.3. The quantitative difference between the present study and [118] may come from the effects of the confinement. The channel height of [118] is $20a$. Yeo & Maxey [230] have shown in Stokes-flow suspensions that the near-wall structure has a significant effects on suspension rheology in concentrated suspensions $\phi \geq 0.3$. It is also important to note that the normal stress differences are sensitive to the choice of the interparticle potential force.

6.5 Microstructure

Here, the changes in the suspension microstructure is investigated by analyzing the pair-distribution functions, $g(r, \theta, \psi)$, in which r is the radial distance, θ and ψ are, respectively, the azimuthal angle measured from the flow direction and the polar angle measured from the positive z-direction. In essence, the pair-distribution function is related with the probability to find a particle with respect to the reference particle at the origin.

Figure 6.12 shows the pair distribution in the shear plane, *i.e.* for $\psi = \pi/2$. Both for $\phi = 0.2$ and 0.4, the thickness of the boundary layer near the compressive principal axis of shear flow, $\theta = 3/4\pi$, is reduced at $Re_{\dot{\gamma}} = 1.0$ compared to that of $Re_{\dot{\gamma}} = 0.005$. At the same time, the wake in the expansive principal axis direction, $\theta = 1/4\pi$, is thickened at larger $Re_{\dot{\gamma}}$.

The near-contact pair-distribution in the plane of shear $g_{nb}(\theta)$ is estimated by averaging $g(r, \theta)$ over $2 < r < 2.1$. As shown in figure 6.12, $g_{nb}(\theta)$ rapidly decreases near the expansive principal axis $\theta = 1/4\pi$. Consistent with Kulkarni & Morris [118], the width of this wake region increases with $Re_{\dot{\gamma}}$. It is shown that the separation point, where g_{nb} starts decreasing

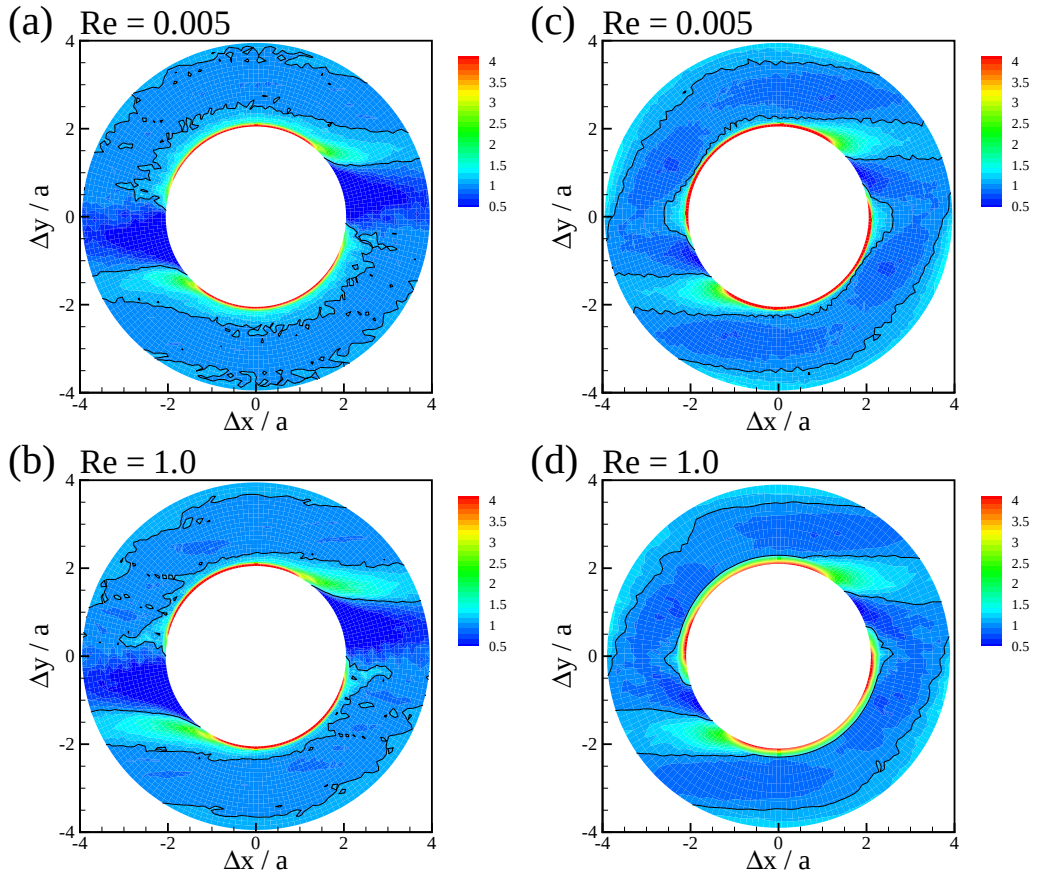

Figure 6.12: The pair-distribution function in the plane of shear for (a, b) $\phi = 0.2$ and (c, d) $\phi = 0.4$. The line denotes $g(r, \theta) = 1$.

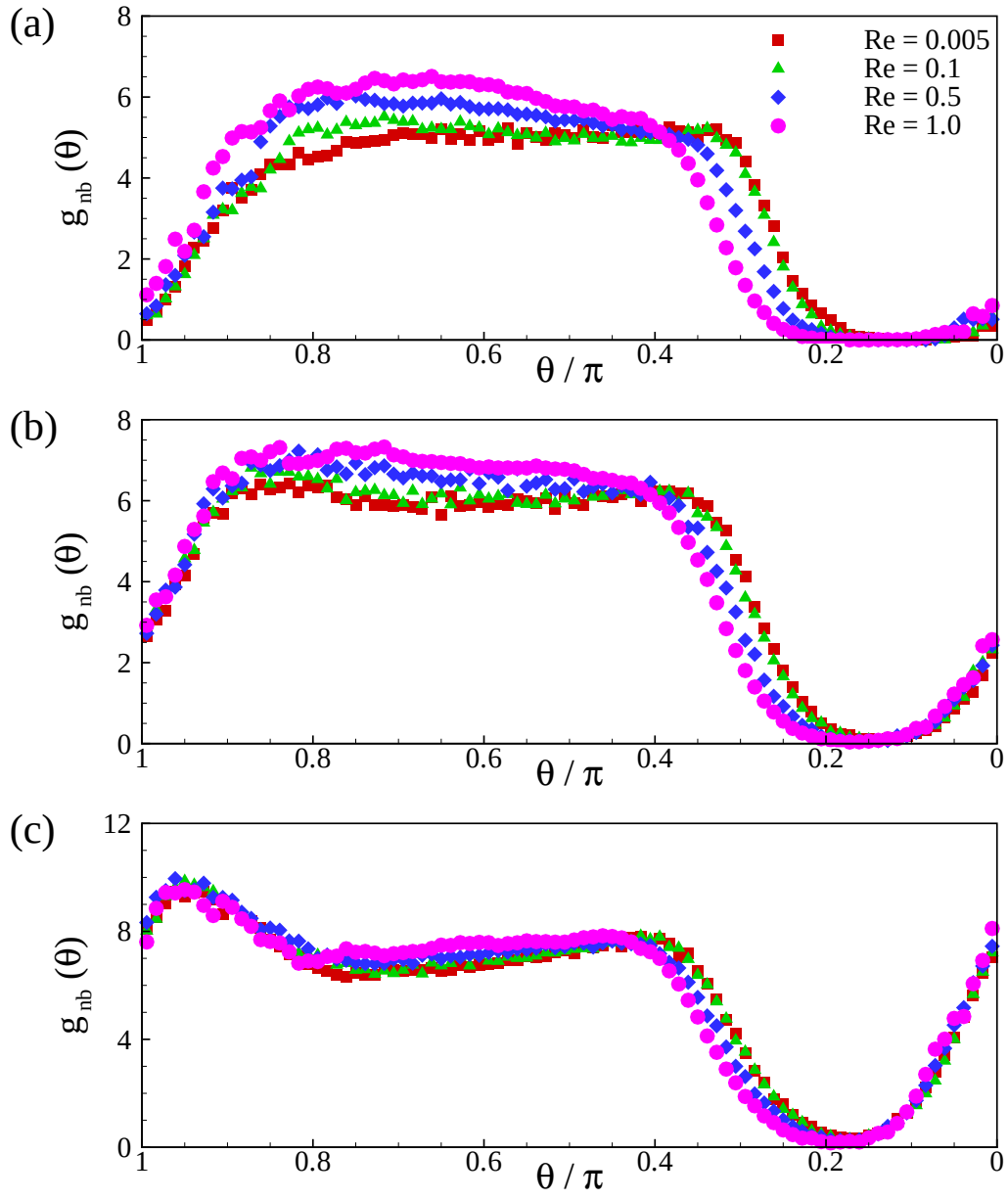

Figure 6.13: The near-contact pair-distribution function in the plane of shear for (a) $\phi = 0.2$, (b) $\phi = 0.3$, and (c) $\phi = 0.4$.

rapidly, moves towards the upstream (larger θ). Around the compressive principal axis, g_{nb} is found to be an increasing function of $Re_{\dot{\gamma}}$. The increase of g_{nb} depends also on ϕ and, at $\phi = 0.4$, the changes of g_{nb} is not so conspicuous as in $\phi = 0.2$. In Kulkarni & Morris [118], they found a local peak of g_{nb} near $\theta = 0$, or π, which grows rapidly with $Re_{\dot{\gamma}}$. However, in the present study, we could not find such a local peak near $\theta = 0$. Considering that Yeo & Maxey [230] have been shown that g_{nb} of the particles in the near-wall particle layer has a distinctive peak at $\theta = 0$, it is possible that the local peak in [118] is due to the contribution from the near-wall particle layer.

To investigate the relation between the microstructural changes and the rheology further, we define a pair-distribution weighted by the particle stress tensor as

$$S^*_{ij} g(\boldsymbol{r}) = \left\langle \frac{\sum_{p=1}^{N_s} S^*_{ij} \mathbf{1}_{\Omega_{\boldsymbol{r}}}(\Delta \boldsymbol{Y}^p)}{n N_s |\Omega_{\boldsymbol{r}}|} \right\rangle, \tag{6.15}$$

in which $\Omega_{\boldsymbol{r}}$ is a small volume centered at $\boldsymbol{r}$, $\mathbf{1}_{\Omega_{\boldsymbol{r}}}(\boldsymbol{x})$ is an indicator function of $\Omega_{\boldsymbol{r}}$, N_s is the number of particles in the domain of interest centered at the reference particle, $\Delta \boldsymbol{Y}^p$ is the separation vector, and S^*_{ij} is the particle stresslet of the reference particle. If S^*_{ij} is 1, the pair-distribution function is recovered from (6.15).

Figure 6.14 shows g_{nb} weighted by the shear component S^*_{12} and normalized by the mean of S^*_{12}. For $Re_{\dot{\gamma}} = 0.005$, g_{ng} shows a plateau in $0.4 < \theta/\pi < 0.8$, while the weighted g_{nb} shows two local peaks near $\theta \simeq 0.75$ and the separation point, around which the $\sim 1/\epsilon$ normal lubrication interaction is important. There is a local minimum of $S^*_{12} g_{nb}$ near $\theta = \pi/2$, where the lubrication interaction between two particles becomes $\sim \log \epsilon$ of the sliding motion. The near-contact pair-distribution functions show a nearly uniform growth in $0.4 < \theta/\pi < 0.8$ with $Re_{\dot{\gamma}}$. However, the weighted pair-distribution clearly indicates the increased contribution to the total S^*_{12} from the events around the compressive direction ($\theta/\pi = 0.75$). On the other hand, the contribution in $\theta/\pi < 0.6$ to the separation point does not change noticeably with $Re_{\dot{\gamma}}$.

The near-contact pair-distribution weighted by S^*_{11} is shown in figure 6.15. Similar to that of S^*_{12}, two local minima are observed around $\theta/\pi \simeq 0.85$ and 0.45. The absolute values of the two local minima increase with $Re_{\dot{\gamma}}$. The second peak becomes more pronounced at larger $Re_{\dot{\gamma}}$ and the location of the second peak is shifted towards the upstream as $Re_{\dot{\gamma}}$

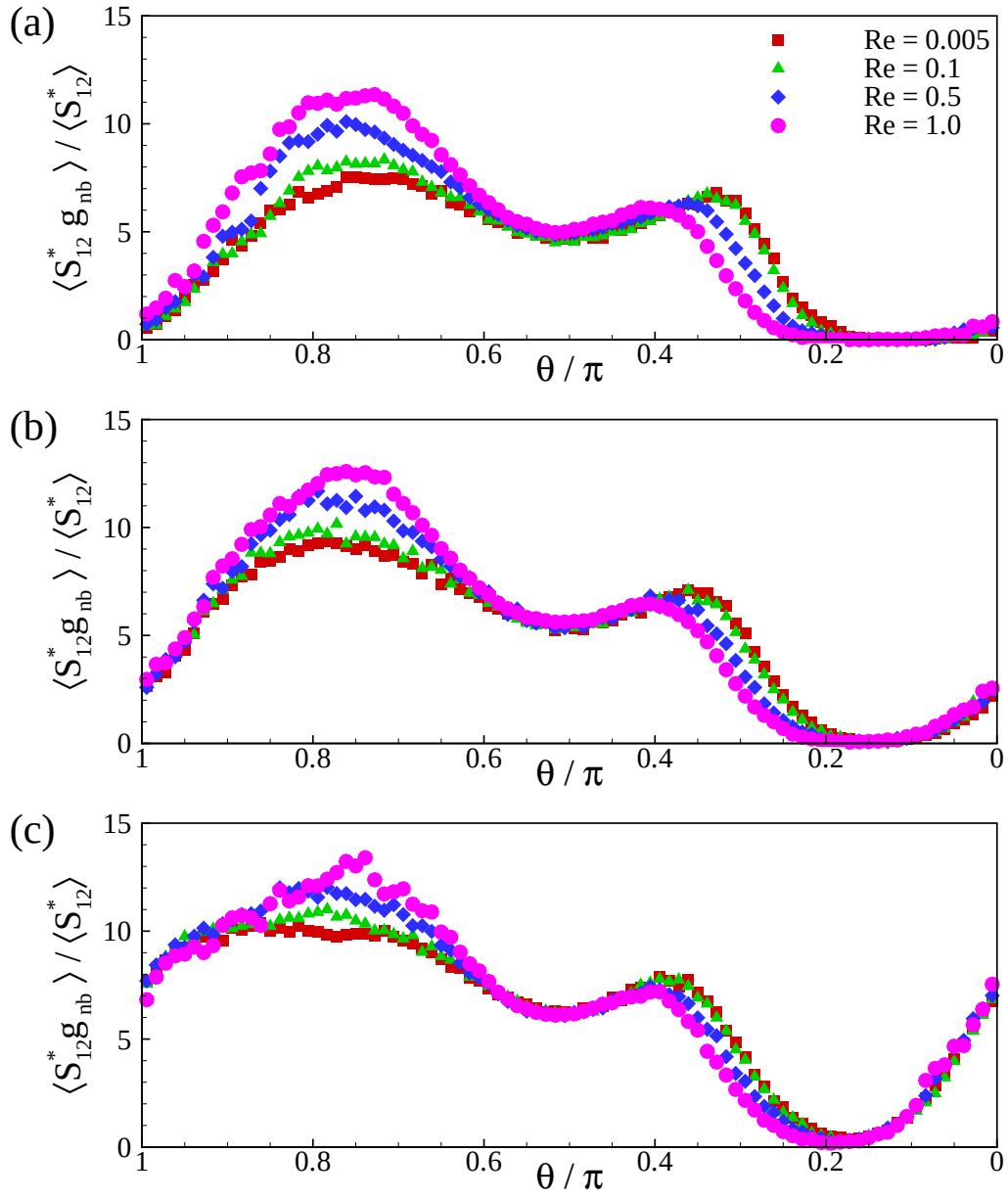

Figure 6.14: The near-contact pair-distribution function weighted by S_{12}^* for (a) $\phi = 0.2$, (b) $\phi = 0.3$, and (c) $\phi = 0.4$. The weighted g_{nb} is normalized by $\langle S_{12}^* \rangle$.

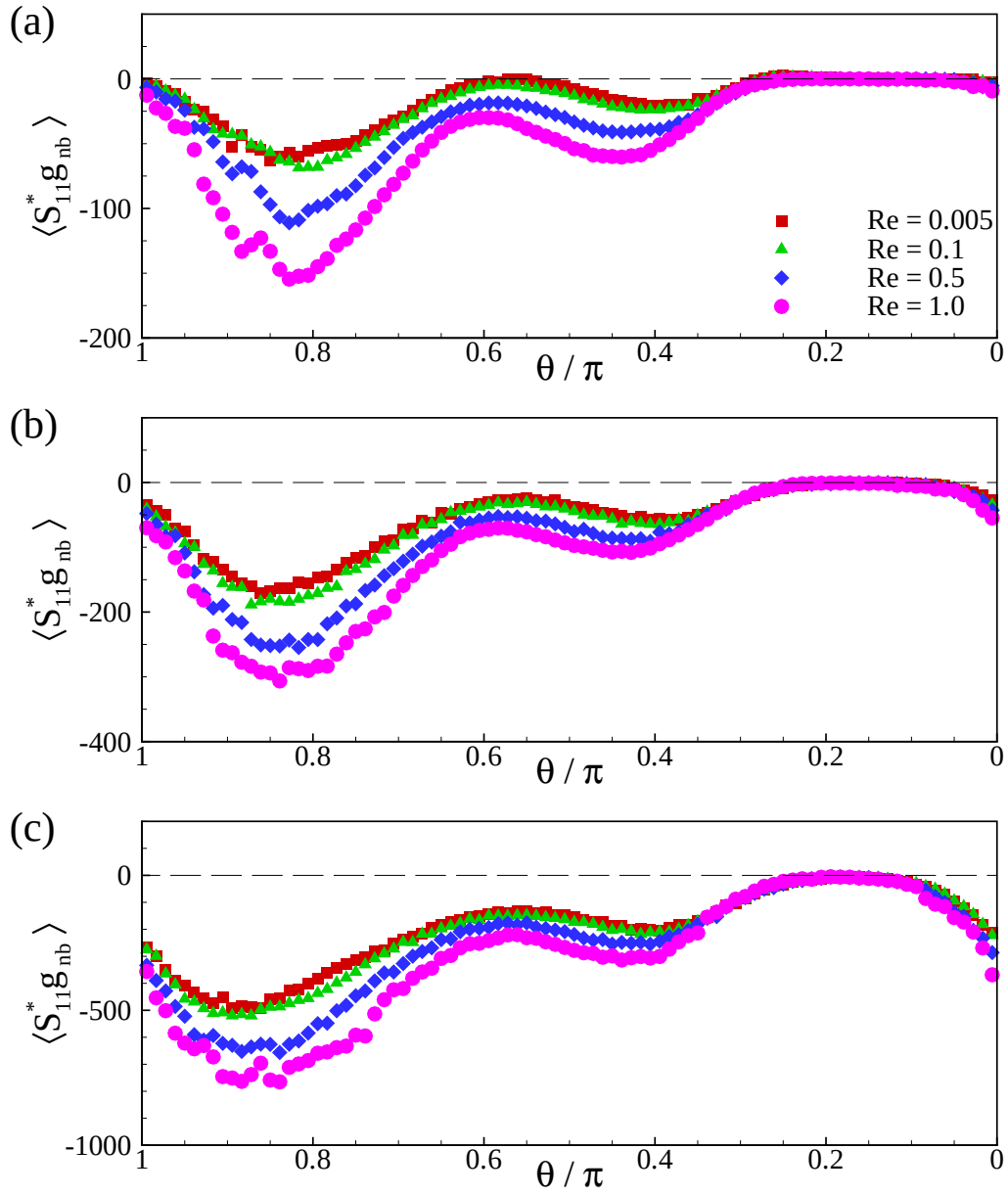

Figure 6.15: The near-contact pair-distribution function weighted by S_{11}^* for (a) $\phi = 0.2$, (b) $\phi = 0.3$, and (c) $\phi = 0.4$. The weighted g_{nb} is normalized by $\mu_0 \dot{\gamma} a^3$.

increases.

Figure 6.16 shows the S^*_{22}-weighted g_{nb}. In S^*_{22} at $Re_{\dot\gamma} = 0.005$, a positive peak is observed around $\theta/\pi \simeq 0.35$ for $\phi = 0.2$, $\theta/\pi \simeq 0.38$ for $\phi = 0.3$, and $\theta/\pi \simeq 0.40$ for $\phi = 0.4$. As $Re_{\dot\gamma}$ increases, the magnitude of the positive peak is augmented and the width of the positive $S^*_{22}g_{nb}$ becomes larger. This changes in the microstructure explain the positive σ^P_{22} at larger $Re_{\dot\gamma}$ observed for $\phi = 0.2$ and 0.3. At $\theta = 0$, S^*_{22} is very close to zero for $\phi = 0.2$ and becomes negative at larger ϕ. Since S^*_{22} at $\theta = 0$ should be zero when only a particle-pair hydrodynamic interaction is considered, this negative S^*_{22} at $\theta = 0$ comes from the mean field. The effects of the fluid inertia is pronounced only around the local minimum and maximum and $S^*_{22}g_{nb}$ is not sensitive to $Re_{\dot\gamma}$ near the equator ($0 < \theta/\pi < 0.3$ and $0.9 < \theta/\pi < 1$).

In the normal stress in the vorticity direction $S^*_{33}g_{nb}$ for $\phi = 0.2$ at $Re_{\dot\gamma} = 0.005$ (figure 6.17 a), a positive peak is observed near the compressive principal axis whereas there is a local minimum around the separation point near the expansive principal axis. The magnitude of the positive peak decrease with ϕ and eventually becomes negative at $\phi = 0.4$. For $\phi = 0.2$, with the increase in the Reynolds number, the magnitude of the negative peak becomes larger and moves towards the upstream, while $S^*_{33}g_{nb}$ near the peak ($0.75 < \theta/\pi < 15$) remains almost unchanged. On the contrary, for $\phi = 0.4$, $S^*_{33}g_{nb}$ decreases with $Re_{\dot\gamma}$ almost uniformly in $0.4 < \theta/\pi < 1$.

The three-dimensional structure of the weighted g_{nb} for $\phi = 0.3$ and $Re_{\dot\gamma} = 0.005$ is shown in figure 6.18. For S^*_{11}, S^*_{22}, and S^*_{12}, the major contribution to the mean stresses comes from the events near the shear-plane ($\psi = \pi/2$). On the other hand, S^*_{33} has a more complex three-dimensional structure. Around $\psi = \pi/4$ and $3\pi/4$, there are two negative S^*_{33} regions in the upper hemisphere and at the same ψ positive S^*_{33} regions also observed in the lower hemisphere. The magnitude of the negative S^*_{33} in the upper hemisphere is almost a order of magnitude larger than that of the positive S^*_{33} in the lower hemisphere.

6.6 Concluding remarks

In this chapter, the rheology and dynamics of concentrated suspensions under finite fluid inertia have been studied by using the force-coupling method described in 2.4. The force-coupling simulations are performed for suspensions in a homogeneous linear shear flow for

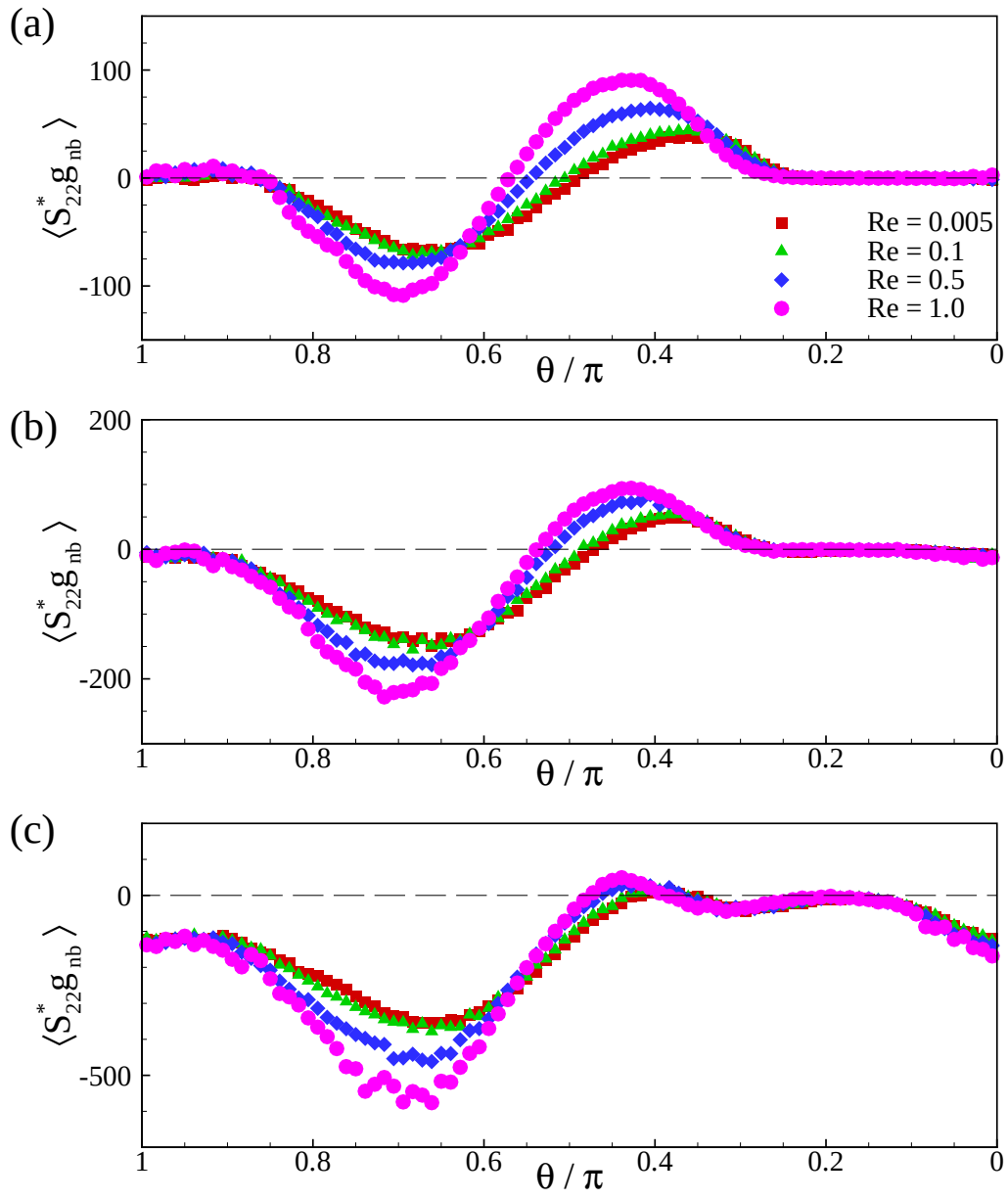

Figure 6.16: The near-contact pair-distribution function weighted by S^*_{22} for (a) $\phi = 0.2$, (b) $\phi = 0.3$, and (c) $\phi = 0.4$. The weighted g_{nb} is normalized by $\mu_0\dot{\gamma}a^3$.

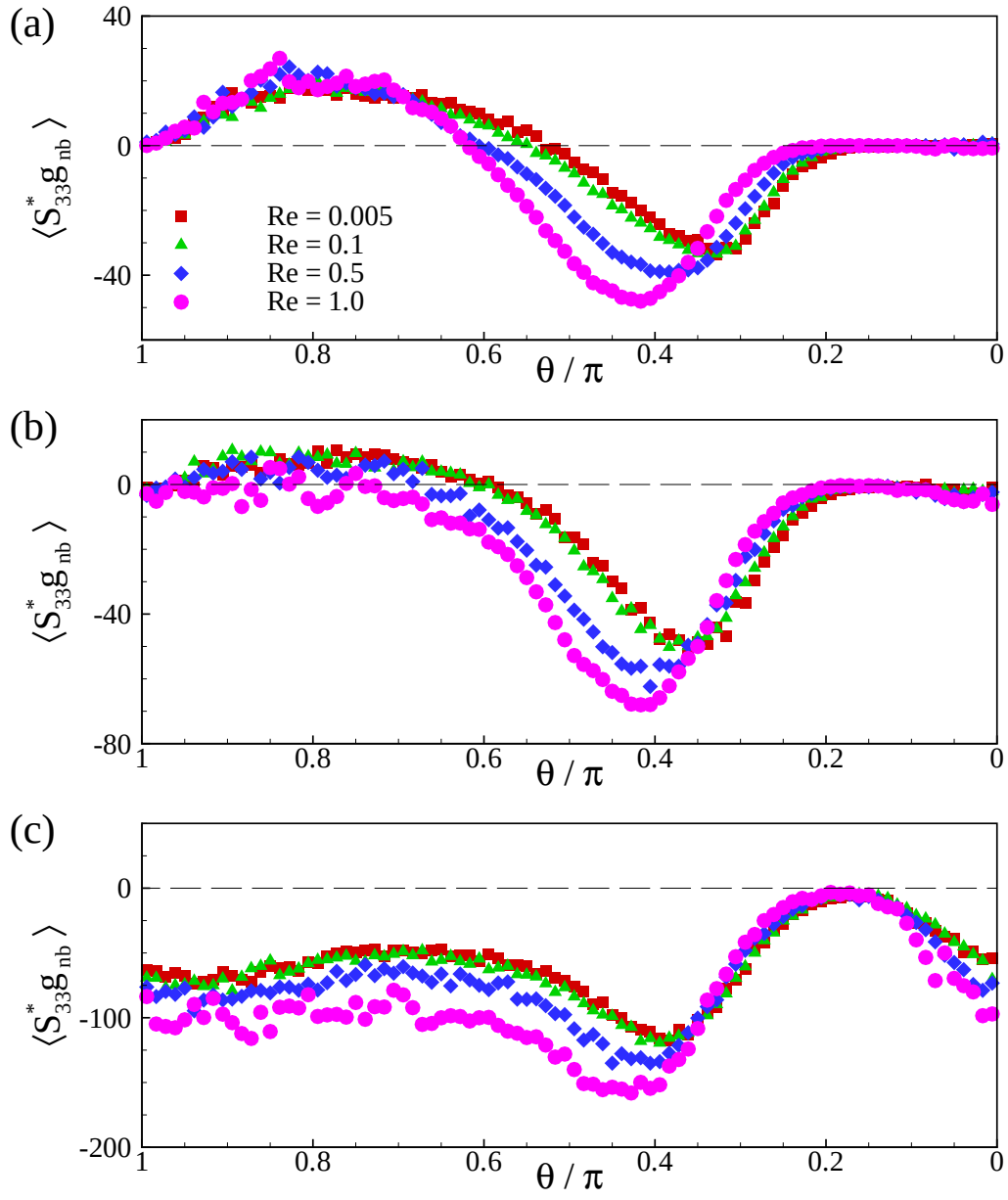

Figure 6.17: The near-contact pair-distribution function weighted by S^*_{33} for (a) $\phi = 0.2$, (b) $\phi = 0.3$, and (c) $\phi = 0.4$. The weighted g_{nb} is normalized by $\mu_0\dot{\gamma}a^3$.

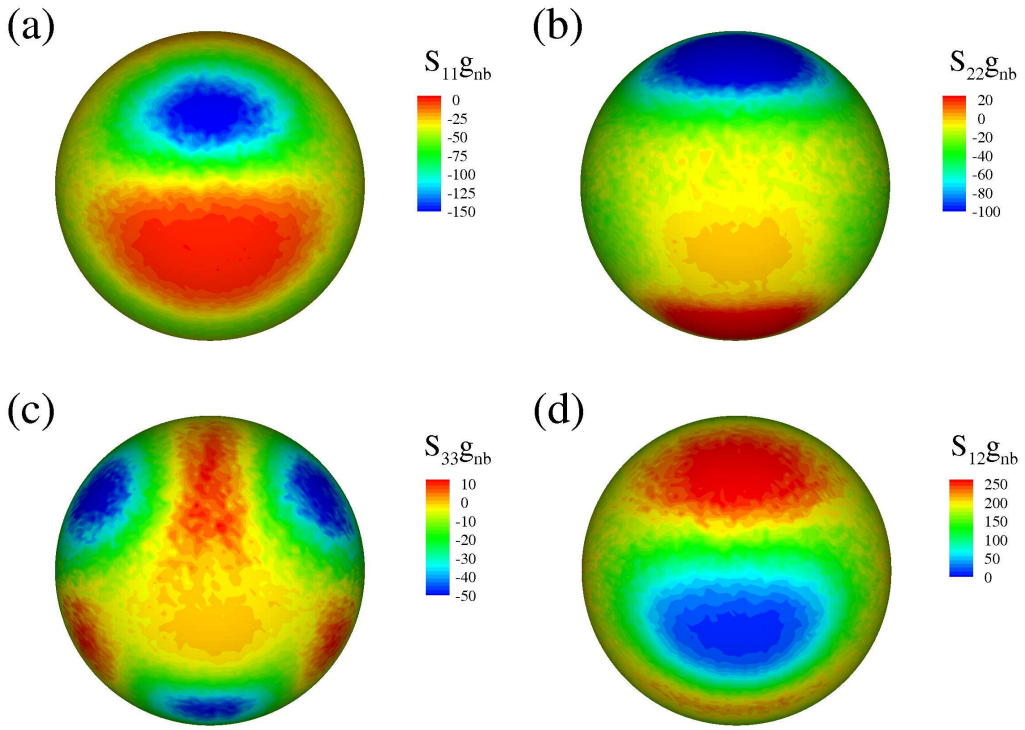

Figure 6.18: The three-dimensional near-contact pair-distribution function $g_nb(\theta, \psi)$ weighted by S^*_{ij} for $\phi = 0.3$; (a) S^*_{11}, (b) S^*_{22}, (c) S^*_{33}, and (d) S^*_{12}. $S^*_{ij} g_{nb}(\theta, \psi)$ is shown in the $y - z$ plane. The flow direction is into the paper; the upper hemisphere represents the compressional axis and the low hemisphere is in the extensional axis.

the volume fraction $0.2 \leq \phi \leq 0.4$. To investigate the effects of finite fluid inertia on suspension dynamics, the Reynolds number $Re_{\dot{\gamma}}$ is changed between 0.005 and 2.

It is shown that the velocity fluctuations normalized by the shear rate and the particle radius $\dot{\gamma}a$ in the velocity-gradient and vorticity directions are decreasing functions of $Re_{\dot{\gamma}}$, while that in the flow direction is augmented at larger $Re_{\dot{\gamma}}$. Under finite inertia, the particle velocity has a longer correlation, which results in the increase in the integral timescale. In the velocity auto-correlation functions, it is found that the effects of the finite inertia are the most pronounced in the intermediate timescale, $0.5 < \dot{\gamma}t < 4$. The tails of the velocity auto-correlation ($\dot{\gamma}t > 4$) for different $Re_{\dot{\gamma}}$ collapse onto one curve, indicating that the memory lost in this later time is closely related to the multiple encounters with the suspended particles. Even though the velocity fluctuation is a decreasing function of $Re_{\dot{\gamma}}$, the diffusivities in the velocity-gradient and vorticity directions increase with the increase in $Re_{\dot{\gamma}}$ due to the changes in the velocity auto-correlation.

Consistent with Kulkarni & Morris [119], the effective viscosity is an increasing function of the Reynolds number. In the range of the simulation parameters ($0.2 \leq \phi \leq 0.4$ and $0.005 \leq Re_{\dot{\gamma}} \leq 2$), the growth of the shear component of the particle stress σ_{12}^{p} exhibits $\sim Re_{\dot{\gamma}}$ behavior. Although the mean shear stress shows a monotonic increase with $Re_{\dot{\gamma}}$, the probability density function indicates that the dynamics is changed significantly with the increase in $Re_{\dot{\gamma}}$. The positive tail of the probability density function for S_{12}^{*} changes from the exponential decay $\sim \exp(-\alpha S_{12}^{*})$ at $Re_{\dot{\gamma}} = 0.005$ to an algebraic decay $\sim {S_{12}^{*}}^{-\beta}$ at $Re_{\dot{\gamma}} = 2$, implying that the intermittency of the particle stresslet grows rapidly with $Re_{\dot{\gamma}}$.

It is shown that the particle pressure grows faster than the effective viscosity as $Re_{\dot{\gamma}}$ increases. However, the changes of the individual normal stress components are not a monotonic function of $Re_{\dot{\gamma}}$. The normal stresses in the flow and vorticity directions (σ_{11}, σ_{33}) are negative and decreasing functions of $Re_{\dot{\gamma}}$. On the other hand, for $\phi = 0.2$, σ_{22} is negative at $Re_{\dot{\gamma}} = 0.005$ and increases with $Re_{\dot{\gamma}}$, which eventually becomes positive for $Re_{\dot{\gamma}} > 0.1$. Similarly, σ_{22} for $\phi = 0.3$ increases at first and then starts decreasing for $Re_{\dot{\gamma}} > 1$. It is shown that the first normal stress difference N_1 is always negative as in Stokes-flow suspensions. N_1 exhibits $\sim Re_{\dot{\gamma}}^{\beta}$ behavior for $Re_{\dot{\gamma}} > 0.1$ and the growth factor β is shown to be a decreasing function of ϕ. Because of the increase of σ_{22}^{p} with $Re_{\dot{\gamma}}$, the second normal stress difference for $\phi \leq 0.3$ becomes positive at larger $Re_{\dot{\gamma}}$.

To investigate the changes in suspension rheology further, a weighted pair-distribution

function is introduced. From the weighted pari-distribution function, it is shown that the increase of the effective viscosity is mainly related to the increase in the frequency and magnitude of the events near the compressive principal axis of shear flow. Even though the probability of the particle encounter near the pole ($\theta = \pi/2$) increases at larger $Re_{\dot{\gamma}}$, the weighted pair-distribution functions for different $Re_{\dot{\gamma}}$ collapse onto one curve, indicating the contributions to the total effective viscosity from the region remains unchanged. The pair-distribution function weighted by S^*_{22} shows that S^*_{22} near the expansive principal axis becomes positive and the region of the positive S^*_{22} grows with $Re_{\dot{\gamma}}$, which explains the increase of σ^P_{22} at larger $Re_{\dot{\gamma}}$. The three-dimensional weighted pair-distribution function shows that S^*_{33} has a complicated structure and the maximum magnitude events are not observed in the plane-of-shear $\psi = \pi/2$. Instead, the maximum magnitude events of negative S^*_{33} are observed around $\psi = \pi/4$ and $3\pi/4$ in the upper hemisphere and those of positive S^*_{33} are around the same ψ in the lower hemisphere.

Chapter 7

Turbulent flow: Modulation of isotropic turbulence seeded with finite size bubbles or particles

7.1 Introduction

In the context of dispersed two-phase flows in liquids, the study of turbulence seeded with bubbles or small particles is a longstanding topic of research. Engineers involved in the chemical industry, oil extraction or materials handling need to predict both aspects of the coupled dynamics. Of the many applications, there have been a number of recent experiments to investigate the dynamics of drag reduction in boundary layer and channel flows through the injection of gas microbubbles [161, 186, 212]. The typical volume fractions encountered in these experiments are in the range of $5 - 30\%$. Microbubble drag reduction has been investigated too using various direct numerical simulations [55, 69, 70, 106, 137, 224]. These illustrate that a range of mechanisms are involved and that the dynamics are a complex interplay of the bubbles with the turbulence and near-wall interactions. Kiger & Pan [109] have made detailed measurements of the turbulence dynamics for solid particles in horizontal channel flow.

Locally homogeneous turbulence is a simpler context in which to investigate the two-phase flow dynamics and is relevant to the small-scale dynamics of more general turbulent flows. The experiments of Lance & Bataille [123] provide measurements of the energy spec-

trum of the turbulent velocity fluctuations with a uniform suspension of bubbles. Changes in the spectrum were noted, as compared to single-phase turbulence, that depended on the bubble size and the bubble concentration. These have been followed by more recent experiments by Rensen *et al.* [181] and Berg *et al.* [213], where a reduction of the spectrum of the energy at large scales and an increase at small scales is observed with a corresponding increase of the dissipation spectrum at the smallest scales. These changes are linked to the bubble size, relative to the Kolmogorov length scale, and the "bubblance" parameter that characterizes the kinetic energy associated with the bubble motion relative to that of the turbulent liquid phase.

Experiments on turbulent two-phase flows are challenging as optical access and phase discrimination are not easy, especially as the volume fraction increases. Computing power has steadily increased over the past two decades making it possible for simulations to approach actual "numerical experiments". Although the direct numerical simulation of homogeneous isotropic turbulence is now well established [237], only a few numerical approaches are able to handle simultaneously all the length scales in a two-phase flow ranging from the surface boundary layers and wakes of individual particles to the largest coherent structures of the flow.

In many two-way coupling simulations, particles have been modeled as point-force source terms in the Navier-Stokes equations, averaged locally over some numerical cell volume of size Δx much larger than a particle. Inherently only a portion of the overall flow is resolved and the disturbance flow generated by individual particles is modeled [21, 93]. The dispersed phase motion is simulated in a Lagrangian framework using a particle tracking, force balance equation to predict each particle trajectory. The fluid forces on a particle are explicitly estimated in terms of a slip velocity between the particle motion and the resolved (larger scale) flow field of the surrounding fluid. The underlying assumption is that the typical size of the particles or bubbles is significantly smaller than all the significant scales of the turbulent fluid flow. This approach is relevant when the turbulent modulation is induced by collective effects and when direct hydrodynamic interactions between particles can be neglected. Such conditions may occur for very low volume fractions of the dispersed phase. Even with these limitations, some basic features have been revealed on modulation of homogeneous turbulence in gas-solid flows [21, 62, 65, 202] and bubble-laden turbulence [148, 149]. The results of the latter simulations are in qualitative agreement with the

experiments [181, 213] as summarized by Berg *et al.* [214]

In many liquid-solid flows, the typical Reynolds number of the carrying flow is often high and the smallest scales of the velocity field are generally smaller than or comparable to the particle (or bubble) diameter. In these contexts, point-force approximations are less applicable because the scale separation is no longer effective. Only a few studies have considered the finite size of the particulate phase in a turbulent flow. Sundaram & Collins [206] among others took this constraint into account by including elastic collisions between particles but the hydrodynamic forcing terms were still assumed to be local point (Dirac delta) functions. More recently, ten Cate *et al.* [208] carried out a fully resolved simulation of a liquid-solid turbulent suspension. By means of the Lattice-Boltzmann method they simulated moderately concentrated two-phase flows, at volume fractions of 2% to 10%, in a sustained homogeneous turbulence. Finite size particles with a solid to fluid density ratio varying from 1.15 to 1.73 generated perturbations in the three-dimensional homogeneous turbulent flow. Fluctuating motions were observed to be enhanced at small scales and the energy spectra showed a weak reduction in the lower wavenumber content. The range of scales involved in the dissipation of fluid kinetic energy are clearly increased when particles are seeded in the flow. Using a new modeling approach, namely PHYSALIS, Zhang & Prosperetti [243] simulated the modulation of decaying homogeneous isotropic turbulence seeded with particles four times larger than the Kolmogorov scale. Neglecting the effect of gravity, they showed in their preliminary study that the presence of particles enhances dissipation whereas the turbulence decay rate of the turbulence is slightly increased.

At low volume fractions a characteristic feature of particle motion in turbulence is for local particle accumulations to develop in response to the local vorticity or rate of strain in the flow. This depends on the inertial response time of the particle and is generally strongest for small particles when the response time matches the Kolmogorov time scale [219, 220]. Particles denser than the surrounding fluid tend to collect in regions of high strain-rate, while particles (or bubbles) less dense tend to collect in regions of high vorticity and lower fluid pressure [145]. Calzavarini *et al.* [30] have shown that the tendency for bubbles to cluster is significantly stronger than for denser particles. For larger particles, where the response time of the particle falls within the inertial sub-range, one may expect particles to exhibit clustering in response to turbulent motions with time scales comparable to those of the particle response time. This has been explored through numerical simulations for gas-solid

turbulent flows by Yoshimoto & Goto [238], where the response time is large compared to Kolmogorov scales but the physical dimensions of the particles remain very small. In general though, there is both an effective *temporal* filtering of the particle response to the turbulence and an effective *spatial* filtering associated with the finite size of the particle in comparison to the spatial scales of the turbulence, as noted for example by Xu & Bodenschatz [223]. These are still open questions.

Recent experiments for isolated particles by Qureshi *et al.* [180], Volk *et al.* [216] and Xu & Bodenschatz [223], based on earlier work by Voth *et al.* [217], have investigated the response of finite size particles to isotropic turbulence. These experiments cover almost neutrally buoyant particles, bubbles and particles with specific density ratios up to 1.4. The experiments are able to achieve a higher Reynolds number, and hence establish more of an inertial sub-range, than is generally possible in numerical simulations. By examining the particle acceleration statistics it is generally observed that for neutrally buoyant particle with diameters five times the Kolmogorov scale or less the response is essentially the same as a Lagrangian fluid element. For larger particles there is a transition in the response as the diameter falls within the inertial sub-range. Qureshi *et al.* [180] observe that for particle diameters larger than fifteen times the Kolmogorov scale, the acceleration variance of neutral particles is consistent with an inertial range scaling.

In this chapter, we investigate the modulation of homogeneous isotropic turbulence induced by spherical bubbles, neutrally buoyant particles and slightly inertial particles at volume fractions of $3 - 6\%$. We exclude the effects of gravitational settling or buoyancy and focus on the effects associated with the finite size (and volume) of the particles, within the range of $6 - 12$ Kolmogorov scales in diameter. The force-coupling method provides a bridge between the point-particle methods used for gas-solid flows and the more detailed resolution of LBM, immersed boundary method or PHYSALIS simulations. FCM is an efficient scheme for simulating large numbers of small particles in dispersed two-phase flow and has been applied previously to simulations of microbubble drag reduction, Xu *et al.* [224] and sedimentation at finite Reynolds numbers, Climent & Maxey [38]. It is worthwhile to note that our goal is not to provide definitive answers to the dynamics of two-phase flow in homogeneous turbulence but to point to the many open issues that still need further investigation.

7.2 Simulation method

7.2.1 Inertial particle simulation

If m_P (m_B for bubbles) and m_F denote the mass of a particle and the mass of displaced fluid, respectively, the force experienced by the fluid due to the presence of the particle is

$$\mathbf{F}^{(n)} = (m_P - m_F)\left(\mathbf{g} - \frac{d\mathbf{V}^{(n)}}{dt}\right) + \mathbf{F}_C^{(n)}. \tag{7.1}$$

This force is the sum of the net external force due to buoyancy of the particles (or bubbles), the inertia excess over the corresponding volume of displaced fluid due to the density difference and a contact force between particles. In the present study we neglect the effect of gravity $\mathbf{g}$ and focus on the inertial interactions between the phases as well as the effects of finite particle size. These conditions may be achieved in experiments under microgravity or where the terminal settling velocity is very small compared to the turbulent velocity scales. For gas bubbles in liquids, the mass is negligible ($m_B \ll m_F$) and the monopole term $m_F d\mathbf{V}/dt$ represents the primary interphase coupling through momentum transfer. Results on bubbly turbulence will be compared to simulations with neutral particles ($m_P = m_F$), where only the force dipole contribution $G_{ij}^{(n)}$ is nonzero, and also with inertial particles ($m_P > m_F$).

The term $\mathbf{F}_C^{(n)}$ represents the effects of short-range hydrodynamic interactions and a rigid-body contact force that prevents bubbles or particles from overlapping. In the present simulations, and as in [224], we assume that bubbles are small enough that they remain spherical and due to surface contamination respond approximately as rigid spheres (no-slip boundary condition). Also, when bubbles come into contact they do not coalesce but eventually separate again. We use an effective repulsion or contact force between bubble or particle surfaces. The contact force for each pair i and j, is a function of the relative position vector $\mathbf{x}_{ij} = \mathbf{Y}^{(i)} - \mathbf{Y}^{(j)}$ and the distance $r_{ij} = \|\mathbf{x}_{ij}\|$. If $r_{ij} < R_{ref}$, the cut-off length scale for the barrier, then the contact force acting on particle i due to particle j is

$$\mathbf{F}_C^{ij} = \frac{F_{ref}}{r_{ij}}\left[\frac{R_{ref}^2 - r_{ij}^2}{R_{ref}^2 - 4a^2}\right]^2 \mathbf{x}_{ij} \tag{7.2}$$

Otherwise the contact force is zero. This force acts along the line of centers of each pair, it

is elastic and conserves momentum.

We fixed the force scale as $F_{ref} = m_F(v_K/\tau_K)$ (see later in the section for definitions and the values in Table7.1) and the cut-off scale as $R_{ref}/2a = 1.2$ in the present simulations. The actual value of the force barrier during a collision is set in response to the proximity of the bubbles (or particles) and the relative turbulent motion leading to the contact. The total force is obtained through a pairwise summation,

$$\mathbf{F}_C^{(i)} = \sum_{i \neq j} \mathbf{F}_C^{ij} \tag{7.3}$$

It is important to include these collisions or contact effects in order to maintain the volume fraction of the dispersed phase. Further details on these short-range interactions are given in Dance *et al.* [49]. At higher volume fractions it is necessary to provide a more detailed representation including viscous lubrication forces and solid-body contact forces. In principle, viscous lubrication forces will prevent contact of perfectly smooth particles but contact occurs in practice through surface roughness and other variations. Tests were made, varying the magnitude of the force F_{ref} and the cut-off distance R_{ref}. The results presented here were found to be insensitive to the specific value of F_{ref} within a broad working range. There was a more obvious effect of varying R_{ref} but for the chosen value this was still not significant, especially at the average concentration levels of 6% or less considered here. Any transient overlap between particles was negligible.

The symmetric part of the force dipole $G_{ij}^{(n)}$, the stresslet term, is set through an iterative procedure to ensure that the strain-rate within the fluid volume occupied by the dispersed phase is zero (when spatially averaged on the appropriate bubble or particle scale σ'). The details of the iterative solver used are given in section 2.4.

For a laminar flow the additional stresslet term leads to an enhanced viscous dissipation. Even for a neutrally buoyant particle moving with the surrounding fluid, any local rate of strain in the flow will be deflected around the particle, see for example Figure 3 of Lomholt & Maxey [135], leading to a locally higher rate of strain and dissipation near the particle. As described in section 4.11 of Batchelor [16], this may be represented by an effective viscosity in a suspension of many particles. Summing the stresslet contributions in a dilute sheared suspension of rigid spheres gives the classical Einstein estimate of the effective viscosity

under conditions of Stokes flow,

$$\mu_{eff} = \mu(1 + 2.5\phi + \alpha\phi^2), \tag{7.4}$$

where ϕ is the volume fraction of the particles. The second-order coefficient α depends on the specific particle configuration [14]. These effects are captured by FCM at low volume fractions, and at larger volume fractions when the appropriate lubrication forces are included [1, 233].

The anti-symmetric part of the dipole corresponds to the sum of an external torque, $\mathbf{T}_{ext}$ and the excess inertia for rotation of the particle (I_P) or bubble (I_B) over the corresponding, appropriately chosen, volume of fluid (I_F) as given by

$$\mathbf{T}^{(n)} = \mathbf{T}^{(n)}_{ext} - (I_P - I_F)\left(\frac{d\mathbf{\Omega}^{(n)}}{dt}\right). \tag{7.5}$$

$d\mathbf{\Omega}/dt$ is the rate of variation of the particle (or bubble) rotation rate. No external torques are applied to the particles in the present simulations, $\mathbf{T}_{ext} = 0$. The rotation rate of a particle changes in response to the viscous stresses exerted by the surrounding fluid, summed over the particle surface, and the moment of inertia of the particles. Neutrally buoyant particles respond quickly and their rotation rate is in equilibrium with the rotation rate of the surrounding fluid at that length scale. The (rigid) bubbles would show the largest discrepancy due to differences in inertia but were found still to come to equilibrium quite quickly. We monitored the amplitude of both symmetric and anti-symmetric parts of the dipole $G^{(n)}_{ij}$ in selected simulations of bubble motion involving both motion in a single vortex and in stationary isotropic turbulence. The antisymmetric contribution is significantly weaker than the stresslet term. It represents less than 8% when averaged over all bubble trajectories. While (7.5) is correct in principle the specification of I_F for FCM is not trivial. We decided to exclude this small effect rather than introduce a possibly inaccurate fluctuating term in the simulations. Hence throughout the simulations $\mathbf{T}^{(n)} = 0$.

Examples of the application of FCM to the motion of particles at low to moderate, finite Reynolds numbers, together with comparisons to fully resolved direct numerical simulations, are given in Liu *et al.* [132] and Maxey *et al.* [147]. A discussion of the response to unsteady flow conditions, including the ability of FCM to capture Basset history forces, is reported

Table 7.1: Simulation parameters of the sustained homogeneous isotropic turbulence (single phase flow). Parameter definitions are given in sections 7.2.2 and 7.2.3. The standard Kolmogorov velocity, length and time scales are v_K, η and τ_K.

Grid	u'	ϵ	ν	Re_λ	λ	T_e	$u'T_e$	η	τ_K	v_K	$k_{max}\eta$
192^3	19.8	5562	0.12	58.7	0.356	0.070	1.39	0.0236	0.0046	5.08	2.1

in Maxey [146]. The formulation of FCM provides a consistent energy budget for both the fluid and particle phases. Viscous dissipation of fluid kinetic energy is evaluated by integration over the whole domain including the volume occupied by the particles. This is required since the representation of the particles involves a spatial smoothing or filtering of the near-surface conditions for each particle and the interior of the particle volume remains an active part of the flow [135, 144].

7.2.2 Turbulent flow simulation

The flow is simulated in a fully periodic domain, of size $2\pi \times 2\pi \times 2\pi$, using a Fourier pseudo-spectral code. The turbulent flow is sustained by a random forcing at low wavenumbers to achieve a statistically stationary state. The simulation procedure is similar to that used by Wang & Maxey [220] with the random forcing term applied over a shell of small wavenumbers [67]. The forcing term is applied to nonzero wavenumbers in the range $0 < k \leq 3$. This unsteady forcing will drive the large length scales of the flow. When a sufficiently large separation between production and dissipation scales occurs the small-scale structures exhibit the universal characteristics of a turbulent flow. Basic data on the single phase turbulence are given in Table 7.1. The simulations are based on a 192^3 grid resolution, for which $k_{max}\eta = 2.1$. Simulations on a 128^3 grid yielded the same results but with a lower resolution, $k_{max}\eta = 1.4$. Both are adequately resolved, with $k_{max}\eta > 1$ [205]. The forcing parameters are the same in all simulations and a balance between the average energy input from the forcing and the viscous dissipation rate ϵ is achieved.

The turbulent kinetic energy K, or turbulence intensity u', is obtained by averaging over space and time after the initial transient (two to three integral time scales) necessary to develop stationary turbulence. This can be also evaluated in the spectral space by

Table 7.2: Parameters of the flow simulations: Bubbles (B, $m_B = 0$), Neutrally-buoyant particles (N, $m_P = m_F$) and Solid particles (S, $m_P = 1.4m_F$). Particle radius $a = 0.1305$ (1) or $a = 0.091$ (2). All simulations include force monopole (M) and dipole terms (D), except S2-M which is based on the monopole only. Parameter definitions are given in sections 7.2.2 and 7.2.3; N_P is the number of particles.

Case	Grid	N_P	Re_λ	u'	ϵ	a/η	a/λ	St	τ_i/τ_K
B1	128^3	1600	59.7	20.18	5827	5.59	0.37	0.23	3.5
B2	192^3	4508	59.2	20.14	5876	3.90	0.26	0.11	1.7
N1	128^3	1600	57.3	19.44	5436	5.50	0.37	0.68	10.1
N2	192^3	4508	58.7	19.77	5574	3.84	0.26	0.33	5.0
S1	128^3	1600	57.0	19.44	5490	5.51	0.37	0.87	12.8
S2	192^3	4508	57.3	19.54	5552	3.84	0.26	0.42	6.3
S2-M	192^3	4508	58.3	19.78	5629	3.86	0.26	0.42	6.3

integrating the energy spectrum function $E(k)$ as

$$K = \frac{3}{2}u'^2 = \frac{1}{2}\left\langle u_i' u_i' \right\rangle = \int_0^{k_{\max}} E(k)dk. \tag{7.6}$$

The rate of kinetic energy dissipation per unit volume, ϵ is balanced by the volumetric power input of the turbulence forcing and it is directly evaluated by integration of the dissipation spectrum $D(k)$ over all the wavenumbers

$$\epsilon = \int_0^{k_{\max}} D(k)dk = 2\nu \int_0^{k_{\max}} k^2 E(k)dk, \tag{7.7}$$

where $\nu = \mu/\rho$ is the kinematic viscosity. Among others, two typical length scales characterize the turbulent fluid motion, namely the Taylor microscale, λ, defined by $\lambda^2 = 15\nu u'^2/\epsilon$, and the Kolmogorov length scale, η, defined by $\eta = (\nu^3/\epsilon)^{1/4}$. The Reynolds number of the single phase flow, based on the Taylor microscale $Re_\lambda = u'\lambda/\nu$ is 59.

7.2.3 Simulation parameters

The primary group of simulations are for bubbles (B), neutrally buoyant particles (N) and inertial solid particles (S) at a volume fraction of approximately 6%. The parameters for these simulations are listed in Table 7.2. Two particle or bubble sizes are considered, with particle radius $a = 0.1305$ or 0.091. For the larger particles, $N = 1600$ and corresponds

to a volume fraction of 6.0% while for the smaller particles, $N = 4508$ and corresponds to a volume fraction of 5.7%. In order to resolve the motion of the particles using FCM, the minimum spatial resolution should be between 5 to 6 grid points to a particle diameter to accurately represent the effect of both the force monopole and dipole terms. The larger particles are simulated adequately with a numerical grid of 128^3 points for which then $a/\Delta x = 2.66$. The smaller particles are simulated on a 192^3 grid for which $a/\Delta x = 2.78$.

Particles or bubbles are initially seeded at random positions in the homogeneous turbulent flow and statistics are computed after a transient period, typically one or two integral time scales. The particle concentrations remain uniform on average but local fluctuations develop in response to the turbulence. These fluctuations depend on the relative inertial response time of the particles (or bubbles) to the turbulence time scales. The bubble response time is defined in terms of the mass of displaced fluid and the added-mass effect. The Stokes drag law provides a convenient reference estimate for defining the response time, so that $\tau_B = a^2/9\nu$. For inertial solid particles, with relative density $\rho^* = \rho_P/\rho$, the particle relaxation time scale is $\tau_P = 2(\rho^* + 1/2)a^2/9\nu$ and $\rho^* = 1$ for neutral particles (index N) while $\rho^* = 1.4$ for the inertial particles (index S). We define the Stokes number St by comparing τ_B (or τ_P) to the turbulence time scale $T_e = u'^2/\epsilon$, for the large eddy turnover time or eddy lifetime. This definition does not account for any specific modification to the drag law based on instantaneous Reynolds number, but it is appropriate as an a priori estimate for the bubble or particle response to the turbulence in the absence of buoyancy effects. The Stokes number (7.8) is also equivalent to comparing the bubble or particle radius a to the Taylor microscale λ, since the rate of viscous dissipation per unit mass ϵ is equal to $15\nu u'^2/\lambda^2$ in homogeneous isotropic turbulence,

$$St = \frac{\tau_i}{T_e} = \frac{5}{3}\alpha_i \frac{a^2}{\lambda^2}. \tag{7.8}$$

In (7.8) the coefficient α_i is equal to 1 for bubbles (B), 3 for neutral particles (N) and 3.8 for inertial particles (S).

The primary data related to the two-phase simulations are summarized in Table 7.2. The case index is a combination of the particle type (B, N or S) and the size of the particle (1 or 2) corresponding respectively to a radius $a = 0.1305$ or $a = 0.091$. The particles or bubbles are larger than the Kolmogorov scale with a length scale ratio a/η varying from

3.8 to 5.6. On the other hand, they are smaller than the Taylor microscale, typically from $\lambda = 2.7a$ to $\lambda = 4a$ meaning that the disperse phase will be interacting with the full range of the most energetic structures of the turbulent flow. For all the simulations, the Stokes number St is low or moderate, based on the estimate (7.8) using the integral time scale. We also provide the values of the particle relaxation time compared to the Kolmogorov time scales.

7.3 Turbulence modulation

In this section we consider the ways in which the Eulerian characteristics of the fluid flow are modified by the presence of the bubbles or particles. As buoyancy forces are excluded, the main issues are the inertial forces associated with a particle (or bubble), which determine the force monopole, and the stresslet component of the force dipole in response to local velocity gradients, specifically the rate of strain. Both the monopole and the stresslet are associated with the finite volume effect of the particles. Generally, a particle moves with the surrounding fluid and motion relative to an otherwise uniform far-field flow arises from inertial forces for a bubble or solid particle. The finite volume effect of a neutrally buoyant particle is associated with the stresslet. The questions we consider are the length scales at which the particle phase and fluid phase interact and how the evolution of the energy spectrum of the fluid phase is modified by the particles. These interactions may be individual or the collective effect of many particles locally.

We compare several different simulations with bubbles, neutrally buoyant particles and solid slightly inertial particles. The important parameters are collected in Table 7.2. The single-phase flow characteristics are identical on the two grids used (128^3, 192^3) and the turbulent Reynolds number Re_λ stays in the range of 57 to 60. This is similar to the conditions for the simulations by [208] of inertial particles in homogeneous turbulence. In order to compare directly with these simulations, we simulate a specific configuration S2 with solid inertial particles of density $\rho_P = 1.4\rho$. All the particles are small compared to the Taylor microscale but larger than the Kolmogorov dissipation length scale η, with particle radius a varying between 3.8 and 5.6η.

Analyzing the results collected in Table 7.2, we see that both the turbulent intensity of the flow and the rate of kinetic energy dissipation by viscosity are essentially constant

with small variations of 4% for u' and 7% for ϵ. A general comment is that the turbulence intensity in all cases is similar because the forcing parameters are kept constant. The total energy input by the forcing is balanced by the turbulent dissipation rate. This is a particular feature of the simulation where all the scales of the flow are resolved. Departures from this may occur due to limited scale separation between the range of forced wavenumbers and those in the dissipation range or where there is a direct interaction of the particle phase and the forcing scales. In two-way coupling simulations using point particles [21, 202], the particles act as a sink of turbulent kinetic energy. Unresolved scales of the order of the particle diameter are modeled by an interphase coupling term. The dissipation by the particles is governed by the slip velocity of the particles relative to the local fluid velocity of the resolved part of the flow. In the fully resolved simulations by [208], they also obtained the result that the rate of energy dissipation is constant over the various two-phase flow conditions studied and that this balances the random forcing power input.

In Figures 7.1 and 7.2, we plot the energy spectra resulting from the simulations with the two different sizes of particles, corresponding to scale ratios $a/\eta = 5.5$ (B1, N1, S1) and $a/\eta = 3.9$ (B2, N2, S3). The wavenumbers are scaled by k_d, based on the particle diameter $d = 2a$ and $k_d d = 2\pi$, following the proposal by [208]. We observe that the large scale kinetic energy content (low wavenumbers) behave similarly because their dynamics are fixed by the forcing scheme and the level of kinetic energy input at low wavenumbers is essentially the same for all the simulations. We expect that the presence of bubbles or particles will lead to interactions with smaller scales. Indeed, a significant increase of kinetic energy at higher wavenumbers is seen for $k/k_d > 0.78$ for the larger particles ($a = 0.37\lambda$) and $k/k_d > 0.65$ for the smaller particles ($a = 0.26\lambda$). Similar features are obtained in the dissipation spectra also shown in Figures 7.1 and 7.2. This enhancement is more closely related to finite size effects than momentum transfer as it is seen equally with bubbles, neutrally buoyant and inertial solid particles. Simulations with only the force monopole term lead to only a weak modification of the energy spectrum, see case S2-M in Figure 7.2. It was unexpected that all three types of particle would induce similar modifications of energy and dissipation spectra regardless of their particular dispersion characteristics and net momentum transfer (monopole). The dynamics instead are more directly controlled by the stresslet contribution. This enforces a zero local rate of strain within the spherical Gaussian envelope so that the flow responds as a solid body within the fluid volume occupied

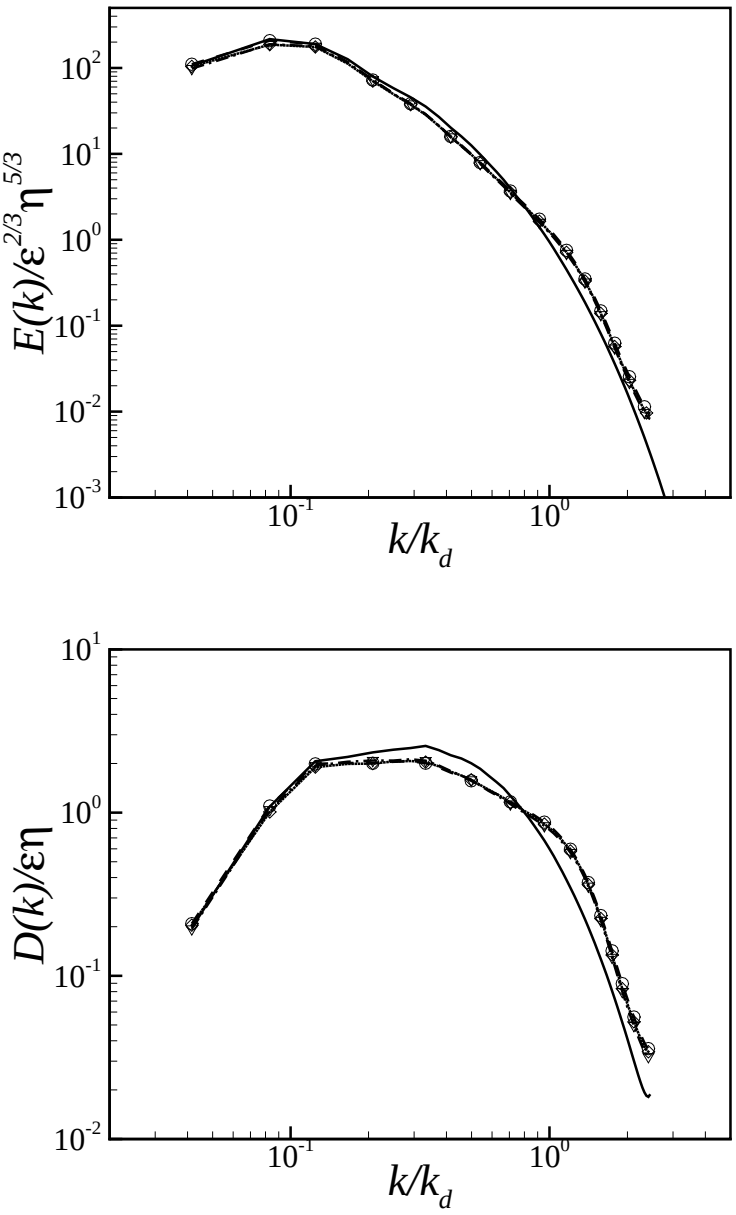

Figure 7.1: Energy (a) and dissipation (b) spectra (grid 128^3). Solid line, single phase flow; dashed line with circles, bubbles B1; dash dot line with triangles, neutral particles N1; dotted line with diamonds, solid particles S1.

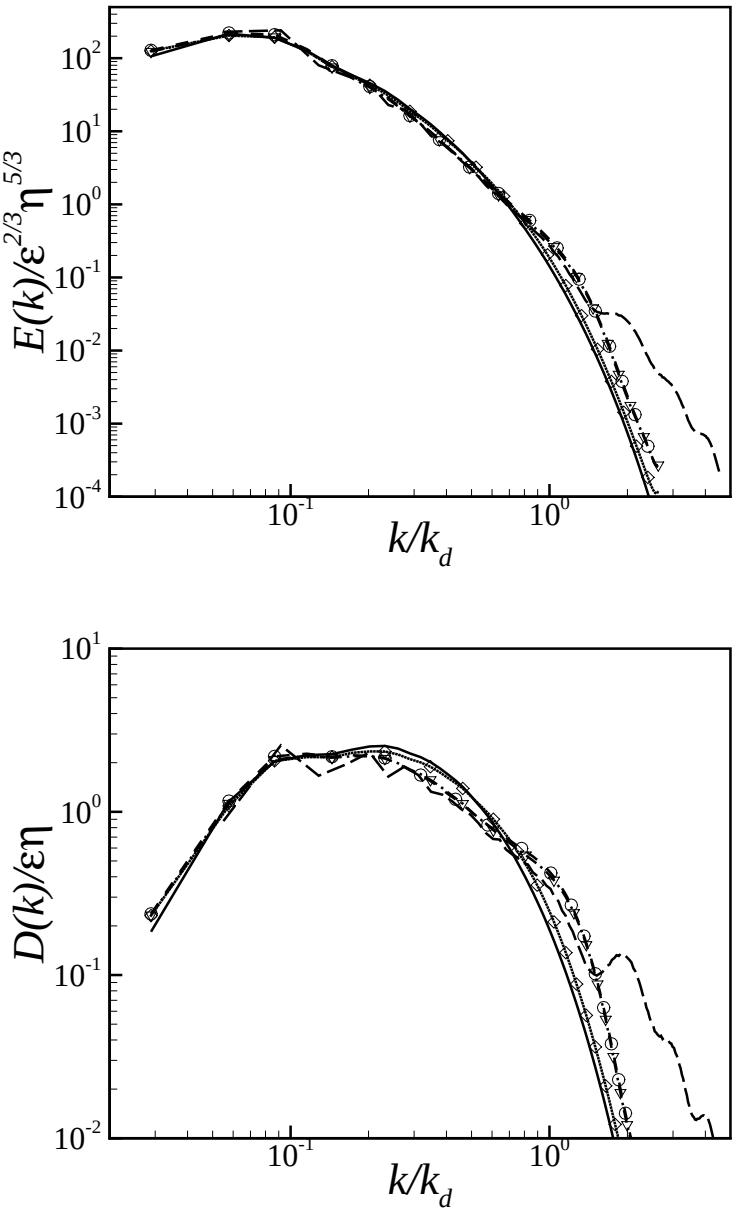

Figure 7.2: Energy (a) and dissipation (b) spectra (grid 192^3). Solid line, single phase flow; dashed line with circles, bubbles B2; dash dot line with triangles, solid particles S2; dotted line with diamonds, solid particles S2-M; Long dash line, data set S2 from [208].

by bubbles or particles. This in turn leads to a significant enhancement of *small scale* kinetic energy and rate of viscous dissipation near each particle surface as local flow variations are deflected around the particle. The local perturbation of the flow by the dispersed phase occurs on the scale of the particle diameter.

At larger scales, $k/k_d < 0.6$, the kinetic energy level is slightly reduced over a range of intermediate wavenumbers. This behavior has already been observed by many authors [21, 148, 208] although the physical origins differ. Buoyancy, for example, plays a major role in the studies of Mazzitelli & Lohse [148]. It is important to note that the pivoting wavenumber k_p, where the transition between enhanced and reduced kinetic energy is different when the size of the bubbles changes. Ten Cate *et al.* [208] investigated distinct configurations varying the volumetric concentration and particle inertia but with constant characteristics of the turbulence ($Re_\lambda = 61$) and a *fixed* particle size $a/\eta = 3.95$. Varying the density ratio and the particle concentration, led to the striking result that the pivoting wavenumber k_p always corresponded to $k_p/k_d = 0.72$. This is very similar to our results, where for case S2: $k_p/k_d = 0.65$ and for this particle size the results for B2, N2 and S2 give k_p/k_d clustered around this value.

The question is whether k_d characterizes the value of k_P as the particle size varies. In Figure 7.3, we show the dissipation spectra for the neutral particles N1 and N2 with the wavenumbers scaled now by the Kolmogorov length scale η. Here the pivoting wavenumber is $k_p\eta = 0.45$ for the larger particles (N1) and $k_p\eta = 0.56$ for the smaller particles (N2). As expected, the value of $k_p\eta$ is larger for the smaller particle, but the increase is only a factor of 1.25 compared to the 1.43 factor for the particle sizes. The observed values of k_p/k_d are 0.78 (N1) and 0.68 (N2) and these differ by a factor of 0.87. The outcome then is that the scaling of k_p by the particle size is a better correlation than a simple scaling with η but the results are not conclusive. Our values for k_p/k_d bracket those of [208] so there may be fluctuation errors. But it is likely that there is a more subtle Reynolds number effect, based on the particle size, which modifies the correlation with particle size.

The simulations of ten Cate *et al.* [208] were performed using a lattice-Boltzmann approach. In analyzing the energy and dissipation spectra, see Figure 7.2, we note that significant oscillations occur in the high wavenumber content that are related to discontinuities in the velocity gradient across particle interfaces. Discontinuities lead to a k^{-4} scaling of the tail of the energy spectrum and k^{-2} for the dissipation spectrum. Although

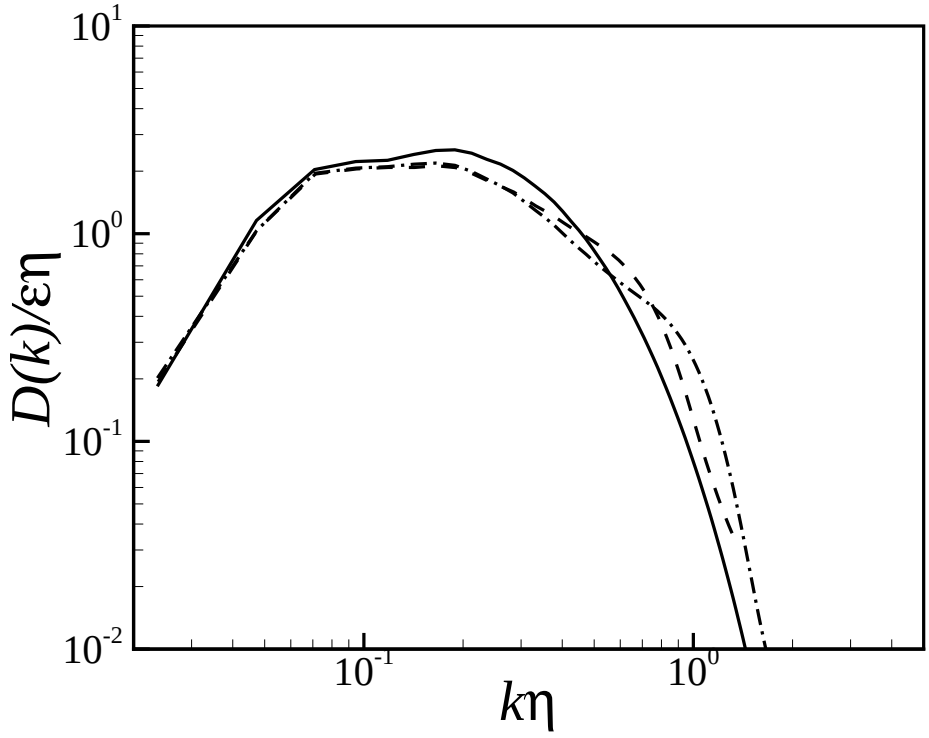

Figure 7.3: Dissipation spectra $D(k)$ plotted against wavenumber scaled as $k\eta$: solid line, single phase flow; dashed line, neutral particles N1; dash dot line, neutral particles N2.

the authors argued that this part of the spectrum contains only 1% of the total energy or dissipation, such oscillations may affect the precise determination of the pivoting wavenumber. There are inherent challenges to measuring and interpreting Fourier spectra in the spatial domain for dispersed two-phase flow. In the present FCM simulations, the spectra remain smooth as the velocity and velocity gradients are continuously defined throughout the whole domain. (Post-processing of the computed volumetric flow field may be used to reconstruct the discontinuous variations.)

As we identify the stresslet as being the main contribution to flow modulation, we consider how this may contribute to the energy transfer between scales. We can use the momentum equation with FCM to derive an evolution equation for the energy spectrum $E(k)$ in wavenumber space. Since the flow is statistically stationary, there is a balance of energy input at large scales by the random forcing $F_R(k)$, direct viscous dissipation $D(k)$, the usual nonlinear energy transfer $T(k)$ and the contributions from the force monopoles $M(k)$ and the force dipoles $H(k)$. The latter two depend on the correlation, in spectral space, of the particle body force $\mathbf{f}(\mathbf{x},t)$ and the fluid velocity $\mathbf{u}(\mathbf{x},t)$. The balance is

$$0 = F_R(k) - D(k) + T(k) + M(k) + H(k) \tag{7.9}$$

where the dissipation spectrum function is $D(k) = 2\nu k^2 E(k)$. The values of $M(k)$ and $H(k)$ can be evaluated directly from the simulation data. First we write

$$f_i^M(\mathbf{x}) = \sum_{n=1}^{N_p} F_i^n \Delta(\mathbf{x} - \mathbf{Y}^n), \tag{7.10}$$

$$f_i^D(\mathbf{x}) = \sum_{n=1}^{N_p} G_{ij}^n \frac{\partial}{\partial x_j} \Delta'(\mathbf{x} - \mathbf{Y}^n). \tag{7.11}$$

Then, the monopole $M(k)$ and the dipole energy transfer functions $H(k)$ are defined as

$$M(k) = \sum_{k-\frac{1}{2} \le |\mathbf{k}| < k+\frac{1}{2}} \hat{f}_i^M(\mathbf{k}) \hat{u}_i(-\mathbf{k}), \tag{7.12}$$

$$H(k) = \sum_{k-\frac{1}{2} \le |\mathbf{k}| < k+\frac{1}{2}} \hat{f}_i^D(\mathbf{k}) \hat{u}_i(-\mathbf{k}), \tag{7.13}$$

in which $\hat{\psi}$ is the Fourier coefficient of a variable ψ.

Figure 7.4 shows the scaled values of the dissipation spectrum $D(k)$ and dipole energy-

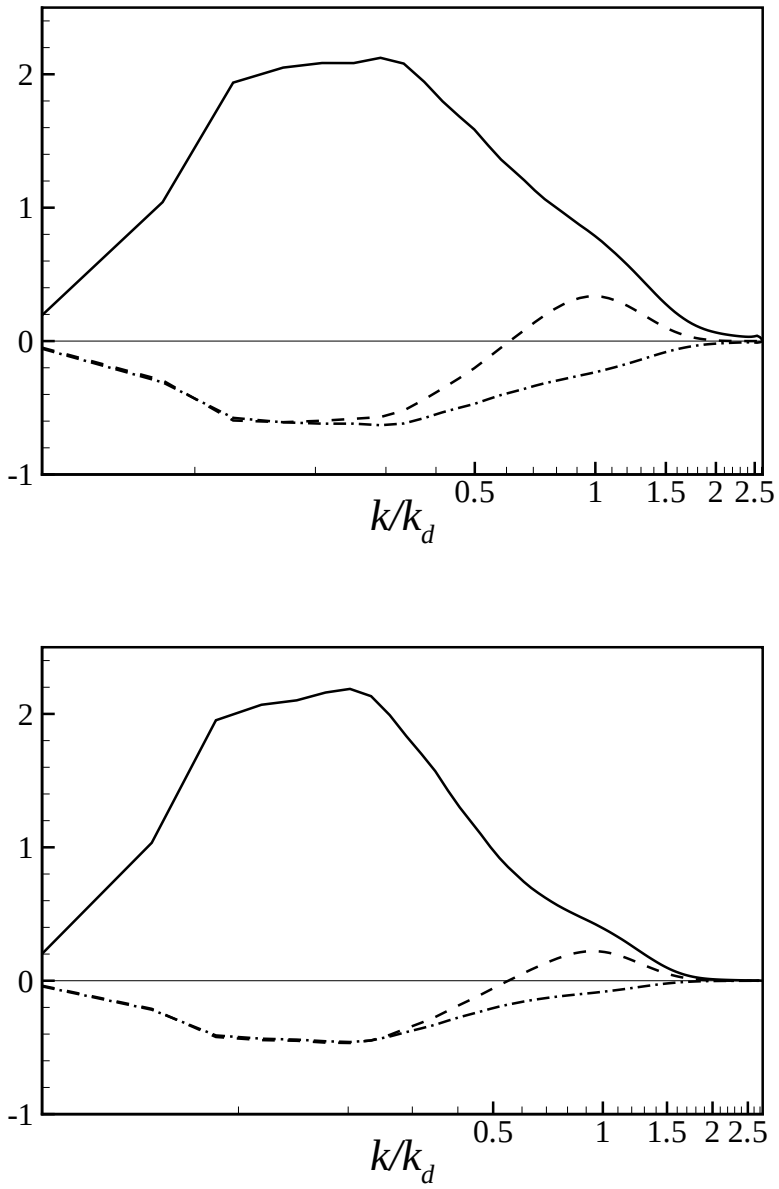

Figure 7.4: Determination of the effective viscosity. (a) Solid line, dissipation rate spectra (N1); dashed line, dipole energy transfer (N1); dash dot line, corresponds to $\nu_{add}/\nu = 0.150$. (b) Solid line, dissipation rate spectra (N2); dashed line, dipole energy transfer (N2); dash dot line corresponds to $\nu_{add}/\nu = 0.105$.

Table 7.3: Additional effective viscosity in turbulent two-phase flow simulations.

Case	B1	N1	S1	B2	N2	S2
ν_{add}/ν	0.142	0.154	0.148	0.101	0.108	0.105

transfer spectrum $H(k)$ for the two cases N1 and N2. The results with bubbles (B) or inertial particles (S) are very similar. The dipole energy-transfer spectrum $H(k)$ shows that the particle stresslets extract energy from large-scale motions and supply it to the small scales.

At low wavenumbers, the dipole contribution acts as an additional dissipation which is consistent with the classical concept of an enhanced effective viscosity in a particulate suspension as noted in section 7.2.1. Analogous to the suspension viscosity effect, we define ν_{add} so as to approximate $H(k)$ by $-2\nu_{add}k^2E(k)$ and then

$$D(k) - H(k) = 2\nu_{eff}k^2E\left(k\right) = 2\left(\nu + \nu_{add}\right)k^2E\left(k\right) \tag{7.14}$$

This approximation is used in the low wavenumber range, $k/k_d < 0.3$, to estimate the additional viscosity ν_{add} by scaling $H(k)$ with the dissipation spectra. Table 7.3 gives ν_{add} for all the simulations. The derived approximations for H(k) are included in Figure 7.4, where we compare results for the neutrally buoyant particles. The values of ν_{add} are consistent for the larger particles with the Stokes-Einstein estimate (7.4) at this volume fraction. However for the smaller particles (N2, S2) and bubbles (B2), the values of ν_{add} are significantly lower. It seems that the additional viscosity is not only dependent on the volumetric concentration but also on the particle or bubble size. We have no explanation for this at present. There is no inherent reason for the Stokes-Einstein estimate to be applicable here in this inherently unsteady, finite Reynolds number context. Additionally, there is no clear separation of scales between the particle size and the scale on which the velocity gradients vary. This is discussed further in Section 7.5.

The inertial forces on solid particles (S1, S2) and the bubbles (B1, B2) contribute to $M(k)$ and this force monopole spectral energy transfer term similarly extracts energy from low wavenumbers and supplies this at high wavenumbers. Even in the absence of inertial forces, short-range collision forces between neutral particles generate a force monopole contribution $M(k)$. Tests were made to evaluate this and the effect of varying the collision force parameters in (7.2). For both cases N1 and N2, there was very little variation in $M(k)$ with the collision parameters and its effect is limited to a narrow range of wavenumbers around $k \sim 0.1k_d$. The values of $M(k)$ are smaller than for $H(k)$. Inertial collisions between particles will contribute to the particle phase stress acting on the flow and will become more

Table 7.4: Lagrangian data following the particles or bubbles for: rms velocity fluctuation, V'; flatness factor for the velocity fluctuations, F_V; rms fluctuation in the acceleration, A'; flatness factor for the acceleration fluctuations, F_A; rms angular velocity, Ω'. The last column gives the value of C_0^*, estimated from the maximum values in Fig. 7.7.

Case	V'	F_V	A'	F_A	Ω'	C_0^*
B1	19.0	2.95	1308.4	6.50	42.7	2.60
N1	18.4	2.83	967.7	5.55	33.4	2.07
S1	18.1	2.79	857.1	5.19	31.1	1.77
B2	19.0	2.95	1400.8	8.07	48.6	2.64
N2	19.1	2.84	1145.0	6.66	38.7	2.43
S2	18.7	2.81	1023.2	6.24	35.6	2.15

significant at higher concentration levels.

A question may be posed as to whether there is a direct effect of the random forcing of the turbulence on the particle–turbulence dynamics. We did turn off the random forcing in some test cases for a short interval after a statistically stationary state was obtained to see if the correlations would change before the turbulence decayed. By and large there was little difference. For example, some spurious artifacts in the monopole contribution $M(k)$ to the energy spectrum transfer at the lowest wave numbers disappeared. The results for H(k) shown in Figure 7.4 did not change.

7.4 Lagrangian statistics

Further details on the Lagrangian statistics of bubbles, neutrally buoyant and solid particles are now presented for the cases B1 to S2. Each of the Lagrangian statistics were obtained from ensemble averages over 10^7 trajectories. Table 7.4 shows the rms fluctuation (in dimensional form) of the particle velocity, V' and the particle acceleration A', together with the corresponding flatness factors, F_V and F_A. The values of V' are only slightly smaller than u' and the flatness factor F_V for all cases is close to 3, indicating that the velocity fluctuations have an essentially Gaussian distribution. The velocity statistics are not sensitive to the type of particle and the values are consistent with the Eulerian statistics.

Unlike the velocity statistics, the acceleration statistics show clear differences. The Lagrangian acceleration is an intermittent quantity and particles may experience large accelerations during the sweeping motion within a vortex [174, 124, 236]. As bubbles tend to

accumulate in the high vorticity regions, the fluctuation levels for the acceleration A' are much larger for the bubbles than the other particles. On the other hand, solid particles tend to accumulate in the low-vorticity (high-strain rate) regions rather than within vortices [30], which results in the lowest value of A'. As the inertia of the solid particle is moderate ($\rho_p/\rho = 1.4$), the difference in the statistics between solid and neutrally-buoyant particles is weaker than it would be for a gas-solid flow.

The rms fluctuations in the particle acceleration A' may be compared to the level of values for a Lagrangian fluid tracer. Yeung & Pope [235] obtained a relation for the acceleration of a tracer particle as $A_T'^2 = 1.92(\epsilon^3/\nu)^{1/2}$ at this Reynolds number. This corresponds to $A_T' = 1508$. The particle accelerations A' for the neutral particles (N1) and (N2) are significantly less, reflecting the finite size of the particles and the limited response to turbulence on scales smaller than the particle.

The rms fluctuations in the particle angular velocity Ω', defined as $\left\langle \Omega_1^2 \right\rangle^{1/2}$ are also consistent with the above description of particles interacting with vortices in the turbulence. The rms data for Ω', in Table 7.4, show similar features for the neutral particles (cases N1 and N2) and the solid inertial particles (cases S1 and S2). The neutral particles showed no tendency to accumulate. There is a 6-8% reduction in the values of Ω' for the solid particles as compared to neutral particles (N1 and N2). The reduction is a weaker effect than the corresponding increase for bubbles. This is in part because the density ratio $\rho_P/\rho = 1.4$ corresponds to slightly inertial particles with $(m_P - m_F)/m_F = 0.4$ while for bubbles this ratio equals -1.

The rms fluctuations in the particle angular velocity Ω' may also be compared with those for a Lagrangian tracer particle, which will rotate with an angular velocity equal to half the local fluid vorticity. On this basis, the rms fluctuating angular velocity of a tracer particle would be $\Omega_T' = 62$. The finite size of a neutrally buoyant particle would reduce this estimate for Ω' to 44.5 for (N1) and to 50 for (N2) using the corresponding dissipation spectra. A further factor is the finite Reynolds number of the particle motion. Poe & Acrivos [173] demonstrated that the angular velocity of a spherical particle freely suspended in a shear flow is reduced at finite Reynolds number relative to the estimate at zero Reynolds number of half the fluid vorticity. This experimental observation is consistent with numerical simulations [11, 218]. In the present conditions, this would lead to a further reduction of $15 - 25\%$ in the angular velocity. FCM captures this effect at low Reynolds

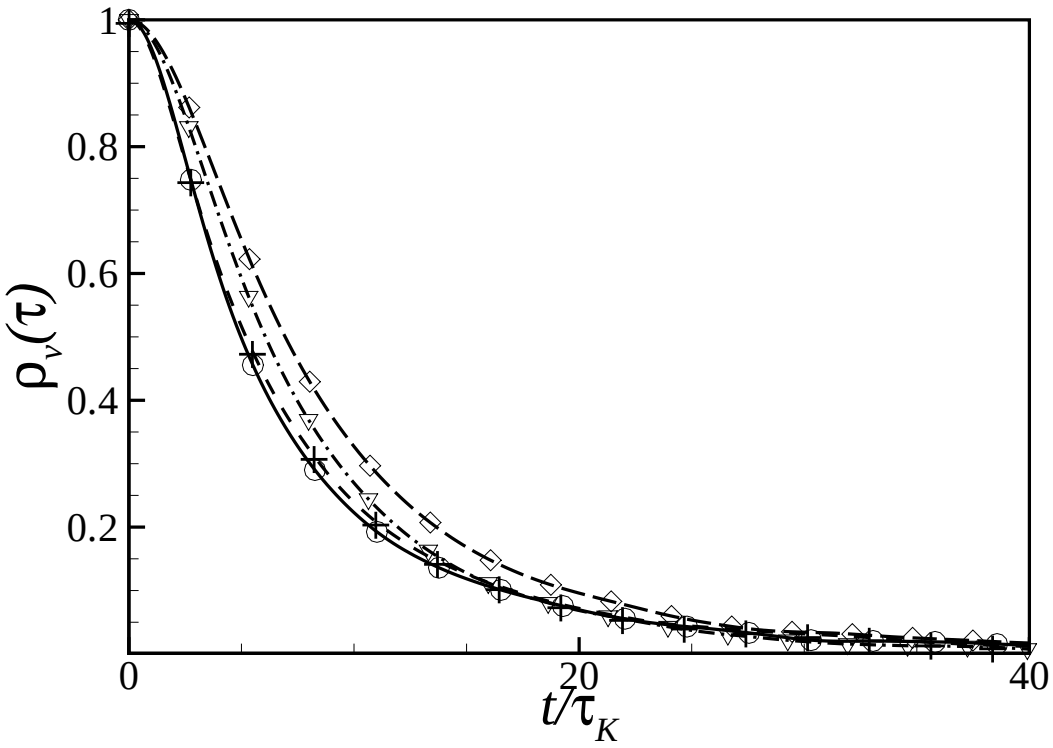

Figure 7.5: Velocity auto-correlation function. Solid line with circles, B1; dashed line with crosses, B2; dash dot line with triangles, N1; long dash line with diamonds, S1.

numbers [218] and the results for Ω' for the neutral particles in table 7.4 fit this general picture.

The Lagrangian velocity auto-correlation function $\rho_v(t)$ is shown in Figure 7.5. The auto-correlations $\rho_v(t)$ for the two different sizes of bubbles are almost identical and decay faster when compared to neutrally-buoyant and solids particles at early time ($t/\tau_K < 15$). However, later $t/\tau_K > 15$, the rate of decay for neutrally-buoyant particles becomes similar to bubbles, while $\rho_v(t)$ of solid particles is always larger than the two others. Once trapped in a vortex, bubbles move toward the vortex core exhibiting rotational motion that results in the faster decay of $\rho_v(t)$ at early time. The inertial solid particles are swept outside these small-scale structures of the turbulence. As a result, ρ_v decays more slowly as compared to bubbles and neutrally-buoyant particles. Collision contacts between bubbles are more likely than between the other particles due to the effects of local accumulations and this would further influence the relative correlation time scales.

Figure 7.6 shows the probability density function (pdf) of the acceleration. The pdf has

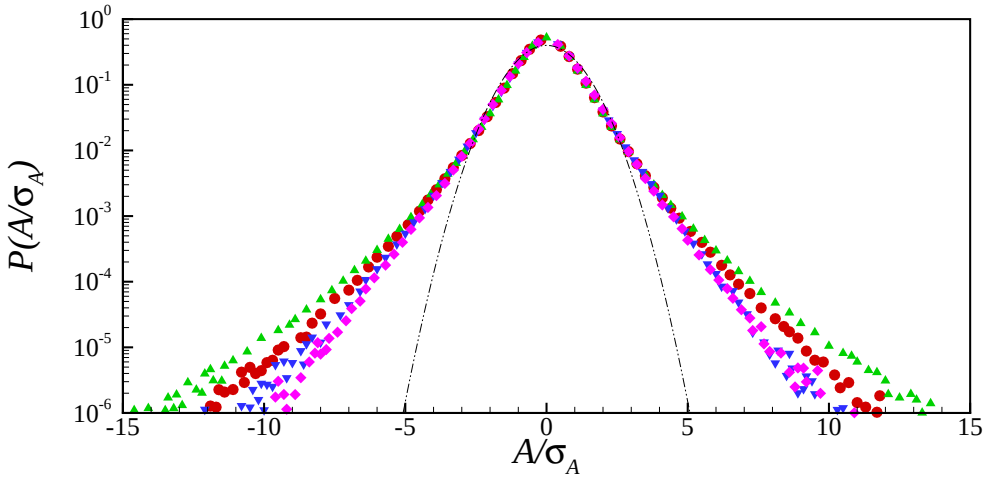

Figure 7.6: Probability density function of particle acceleration. Legend for symbols: circle, B1; triangle, B2; nabla, N1; diamond, S1.

very long tails compared to a Gaussian distribution indicating a high level of intermittency of the acceleration [174]. When scaled by corresponding rms accelerations σ_a the pdf's are very similar in the central region, $|a|/\sigma_a < 3$. This indicates that the differences in the acceleration statistics between the different particles or bubbles, and different sizes, come from the intermittent events, which are closely related to the coherent vortical structures [124]. These features of the pdf's are consistent with the experimental observations, obtained at higher Reynolds numbers [180, 216, 223].

The Lagrangian acceleration correlation function for fluid tracers is known to decay much faster than the velocity correlation [235] and has zero integral time scale. Yeung & Pope [235] found that the acceleration auto-correlation crosses zero at about $2\tau_K$ and this varies only slightly with the turbulent Reynolds number. Mordanta *et al.* [157] showed that the auto-correlation of the acceleration magnitude decays slowly and argued that this long-time correlation is a key feature of intermittency in turbulence. Lee *et al.* [124] suggested that this different behavior of acceleration and acceleration magnitude comes from the rotational motion of particles in a vortex in that the zero-crossing time of the acceleration auto-correlation is related to the rotational time-scale of a particle as it is swept around in a vortex.

The acceleration auto-correlation function $\rho_A(t)$ is presented in Figure 7.7. The zero-crossing time of the auto-correlation function for smaller bubbles (B1) and larger bubbles

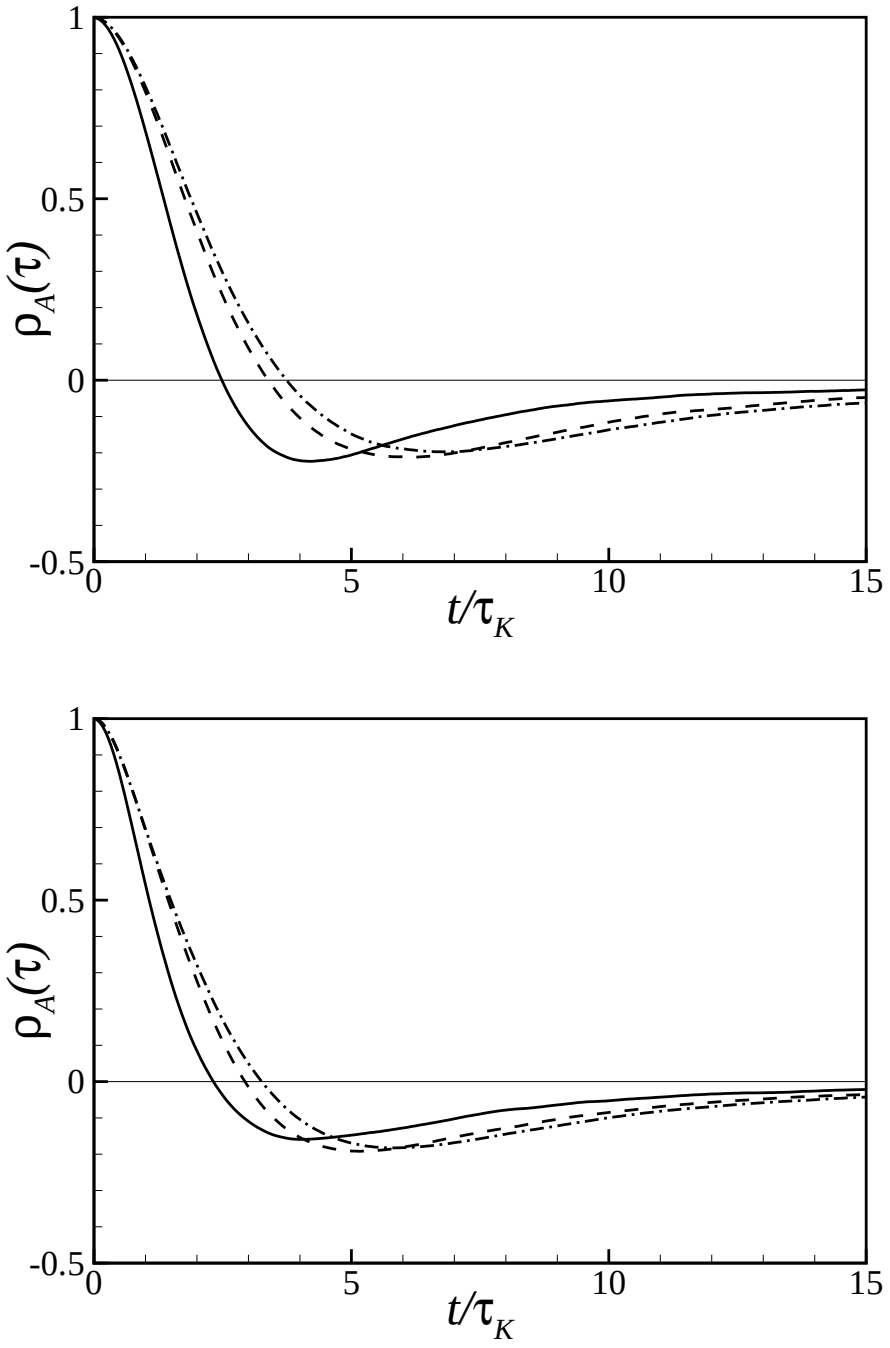

Figure 7.7: Acceleration auto-correlation function. (a) Solid line, B1; dashed line, N1; dash dot line, S1. (b) Solid line, B2; dashed line, N2; dash dot line, S2.

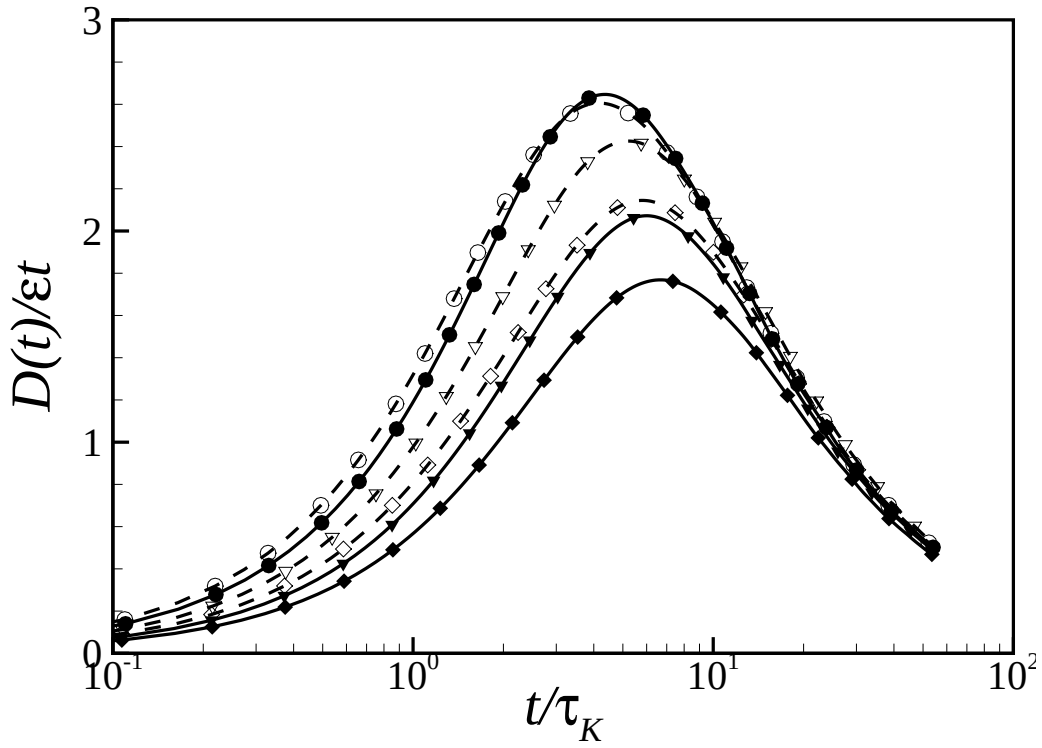

Figure 7.8: Normalized velocity structure function. Solid line with solid circles, B1; solid line with solid triangles, N1; solid line with solid diamonds, S1; dashed line with open circles, B2; dashed line with open triangles, N2; dashed line with open diamonds, S2.

(B2) are, respectively, 2.33 and $2.50\tau_K$. These values are smaller than for neutrally-buoyant and solid particles. At early times ($t < 2\tau_K$), $\rho_A(t)$ for the neutrally-buoyant and the solid particles are only slightly different. Due to the effects of inertia, $\rho_A(t)$ for the solid particles decays more slowly than for the neutrally-buoyant particles. Both Volk *et al.* [216] and Xu & Bodenschatz [223] have measured the acceleration autocorrelations for a range of isolated particles and particle sizes at high Reynolds numbers. The first zero-crossing for bubbles, $a/\eta = 4.4$, is earlier than for neutral or denser particles and for larger neutrally buoyant particles, $a/\eta = 7.4$ the autocorrelation extends further [216]. Both observations are consistent with the present simulations but it is not possible to make a quantitative comparison.

Finally we examine the Lagrangian velocity structure function. Figure 7.8 shows the

velocity structure function $D_L(t)$,

$$D_L(t) = \left\langle (V(s+t) - V(s))^2 \right\rangle, \tag{7.15}$$

where $D_L(t)$ is normalized by ϵt. In a high Reynolds number inertial sub-range $D_L(t)/\epsilon t$ would be a constant C_0. The results shown for the two different sizes of bubbles are similar. For both neutrally buoyant and solid particles, the maximum value of $D_L(t)$ is greater for the smaller particle size while the time at which the maximum is attained is shorter. For the present simulations there is no inertial sub-range as the Reynolds number is too low. From the normalized velocity structure function, we can provisionally evaluate C_0^* as a low Reynolds number analog to the Kolmogorov constant C_0 [235, 190] for comparison purposes. Estimates of C_0^* are given in Table 5, based on the maximum values shown in Figure 7.8. The estimates of C_0^* for the bubbles (cases B1 and B2) are about 2.6, which is similar to that of a fluid particle [235]. The peak value for the bubbles is observed at approximately $4.3\tau_K$.

7.5 Conclusions

In this chapter, we have examined a number of issues relating to the dynamics of finite-size particles at low to moderate volume fractions in liquid-solid or liquid-bubble turbulence. The results for the dissipation spectra in Section 7.3 show that the particles enhance the small scale turbulence at length scales below the particle size. This is determined primarily by the finite size of the particle and not by the specific density of the particle. The scaling of the pivoting wavenumber k_P by the particle diameter, through k_d, as proposed by ten Cate *et al.* [208], is consistent with the present results but does not fully match them. There may be an additional dependence for example on d/η.

In describing the dynamics of the energy spectra, it would appear possible to represent the transfer of energy from large scales to small scales by the particle phase through the use of an effective suspension viscosity, at least for scales substantially larger than the particle. The characteristics of this viscosity are more complex than a simple application of the Stokes-Einstein result for dilute suspensions. There is limited fundamental information at present on the rheology of particle suspensions at finite Reynolds numbers. Recent numerical simulations by Kulkarni & Morris [119] for neutrally buoyant particles in a steady Couette

flow indicate that the Stokes-Einstein estimate should still apply at volume fractions of 5%.

The contribution $H(k)$ from the force dipoles to the spectral energy transfer in (7.9) represents a sum over the stresslet components of all the particles. The particle contribution to the bulk stress in a finite Reynolds number flow depends not only on this but also a local volume average of the symmetric moments of the particle accelerations and a Reynolds stress term [13, 119]. The latter is for the smaller-scale disturbance flow around each particle relative to the local volume averaged flow velocity. In the present formulation these other terms are included in the nonlinear inertial transfer term $T(k)$.

The effective viscosity of viscous suspension flows depends too on the relative positions of particles and localized concentrations of particles should have an observable effect [89]. In the present context, the bulk concentration of 6%, or less, is still relatively low and such effects may be limited as seen in the small variation of ν_{eff} in Table 7.3, even though the bubbles and solid particles have some tendency to cluster. The dynamics of viscous suspensions are governed by the velocity fluctuations created by the disturbance flows of the individual particles randomly dispersed in the flow and the correlations between these flows is important. Particle suspensions in turbulent flow are subject to the underlying turbulence and the correlations of the disturbance flows with the turbulence are more significant.

There is evidence too for the spatial filtering effect from the finite particle size on the response to the turbulent motion. For example, for a neutrally buoyant particle, this is a function of the particle size relative to the Kolmogorov scale, or to the Taylor microscale. As indicated in (7.8), the Stokes number St is closely related to the ratio of the particle size to the Taylor microscale. Similarly the ratio τ_P/τ_K is closely related to the ratio of the particle size to the Kolmogorov length scale. The present simulations are at too low a Reynolds number to establish an inertial subrange but the particle diameters are 7 to 11 times larger than the Kolmogorov scales and so fall within the transition range described by Qureshi *et al.* [180]. This is in addition to any inertial response linked to the specific density of the particle.

Chapter 8

Concluding Remarks

8.1 Summary and discussions

The main objective of this thesis was to enhance our understanding on fundamental physics of solid-liquid multiphase flows under a wide range of flow conditions. The study of bulk rheology and dynamics of suspensions of solid particles in Stokes flows, *i.e.* at zero Reynolds number, dates back to 1950s. However, most studies have been focused on homogeneous system without any solid boundaries. In this research, we introduced one of the most fundamental inhomogeneities, namely suspensions bounded by two parallel walls, and thoroughly studied the effects of the basic inhomogeneity on the mechanical property and dynamics of suspension flows. In high-Reynolds-number turbulent-flow suspensions, we demonstrated the turbulence modulation by the suspensions of heavy, neutrally-buoyant, or negatively buoyant particles of finite size, larger than the Kolmogorov scale, which is an extension of the conventional approaches of assuming suspensions of point particles. As a first step to fill the gap in the previous studies of the suspension flows in zero-Reynolds-number Stokes and high-Reynolds-number turbulent flows, we studied the effects of fluid inertia on rheology and suspension dynamics for the particle-scale Reynolds number of $O(10^{-3}) \sim O(1)$. One of the most important contribution of this study is that we established a robust and general simulation technique to study suspensions of solid spherical particles of any volume fractions under a geometrical confinement for a wide range of Reynolds numbers. In this chapter, the major results of each chapters are briefly discussed.

In this study, the force-coupling method (FCM) was used for the numerical simulations of suspensions of rigid spherical particles. In Chapter 2, we showed that the force-coupling

method for Stokes flow is a matrix free method to solve the grand mobility matrix. From the positive semi-definiteness of some Galerkin-type discretizations, such as spectral or spectral-element method, it is shown that, even with solid boundaries, the FCM grand mobility matrix is symmetric positive semi-definite. Based on the symmetric positive semi-definiteness, a conjugate gradient procedure for FCM is proposed. As a particle is represented by regularized multipoles, instead of dirac delta functions, the force-coupling method underestimates the near-field viscous lubrication interactions between particles, while the far-field solution matches the analytical solution exactly. We developed a robust and efficient method, lubrication-corrected FCM (LC-FCM), to solve the far-field multibody and near-field lubrication interactions simultaneously. Using a preconditioned conjugated gradient method, we showed that the near-field calculation can be replaced by a few vector summations and the overall computational cost is almost the same with the standard FCM. LC-FCM has been tested thoroughly and shown to be able to simulate suspensions of rigid spheres for a wide range of volume fractions with a very good accuracy. We extended the numerical method for the simulations of suspension flows of non-zero Reynolds number, *i.e.* Navier-Stokes flows.

First, we studied the effects of a geometric confinement on rheology and particle dynamics of concentrated suspensions of hard spheres through the FCM simulations of wall-bounded Couette-flow suspensions at zero Reynolds number in Chapter 3. We found that coherent structures develop near the solid boundary, namely near-wall particle layers. The correlations of the wall layer extend 6-7 particle radii into the flow for $\phi \geq 0.3$ and this near-wall density fluctuation is independent of the channel height H_y. Due to the changes in the suspension microstructure near the wall, rheology of the bulk fluid becomes a function of both the volume fraction and the channel height. Once a particle moves into one of these near-wall particle layers, the particle resides around an equilibrium position of the particle layer for a long time compared to the diffusive timescale, which results in an anomalous diffusion. By investigating the mean-square displacement of the suspended particles near the core of a channel for a range of volume fraction and channel height, we suggest that the subdiffusivity observed for the particles in the quasi-homogeneous core region is a consequence of the restriction on the largest dynamic lengthscale of suspension flows by the available lengthscale set by the channel height. To support the argument, we estimate the particle shear stress from the momentum conservation equations shown in Chapter 4,

Table 8.1: Changes in the particle shear stress with the channel height.

H_y/a	20	30	40	Sierou & Brady[197]
σ_{12}^p	4.18	4.45	4.50	4.49 ± 0.037

(4.14). In 3.2, we computed the particle shear stress from a volume average. However, in an inhomogeneous system, the volume-averaged shear stress is not the shear stress measured on the wall. Integrating the momentum conservation equations over a control volume, of which upper boundary is located on the center of the channel and lower boundary is on the liquid-wall interface, and summing the particle- and fluid-phase shear stress, the wall shear stress τ^w observable in the experiments is given by

$$\tau^w = \langle \chi_p \sigma_{12} \rangle|_{y=H_y/2} + \mu\dot{\gamma}. \tag{8.1}$$

This relation indicates that the measured shear stress depends on the particle shear stress in the quasi-homogeneous region near the core of the channel, which explains the discrepancy in the wall shear stress and the volume-averaged stress shown in Kulkarni & Morris [119]. Table 8.1 shows the particle-phase shear stress for the volume fraction $\phi = 0.40$ at various channel heights. It is shown that the particle shear stress is an increasing function of the channel height and it approaches the value computed in the homogeneous linear shear flow by Sierou & Brady [197]. The particle shear stress for the channel height of $H_y/a = 40$ is almost the same as that in [197], at which channel height the particles in the core of the channel exhibit a normal diffusive behavior.

In the second half of Chapter 3, we investigated a non-equilibrium phase transition observed in the non-Brownian suspensions at high volume fractions. At high volume fractions, the suspended particles are self-assembled into linear strings which are organized as a hexagonal array in the plane perpendicular to the flow direction. The hexagonal structure starts to form near the wall first and extends to the core of the channel as the volume fraction increases. It is shown that the ordering transition and crystal structures are dependent on both the volume fraction and the channel height. We showed that, by introducing a disturbance in the crystal structure, the mechanical property of the suspension flows can be altered. Here, we investigated the effects of an external torque on the suspended particle as a model for a DC electro-rotation of suspended particles (Quincke rotation). It is found

that the response of the order structure to the external torque is asymmetric to the sign of the torque and also nonlinear to the magnitude of the torque.

In Poiseuille flows, the stress is a function of the distance from the wall. As a consequence of this inhomogeneous stress field, the suspended particles migrate to the core of the channel. To investigate the stress system of Poiseuille-flow suspensions, we performed FCM simulations for the volume fractions $0.2 \leq \phi \leq 0.4$ and the simulation results are shown in Chapter 4. It is shown that the velocity and local volume fraction profiles computed from FCM agree very well with previous experiments. Consistent with the previous stress induced migration hypothesis, the particle normal stresses are almost uniform except very near the wall and core of the channel. We estimated the local particle pressure and shear stress from the simulation data and showed that the local rheology assumption in the suspension balance model is valid, again, except in the wall and core regions. The particle layering and the following changes in the dynamics and rheology in the near wall region are expected from the results in Chapter 3. On the other hand, the suspensions near the core of the channel exhibit very interesting anomalous behavior. We found that the particle shear stress becomes negative near the channel core, even though the local shear rate remains positive. Around the core of the channel, the local volume fraction is close to the maximum random packing and the local strain rate becomes very small, which violate the local rheology and local homogeneity assumptions in continuum theories. The anomalous behavior around the core of the channel is a subject of further investigation.

We studied the hydrodynamic interaction between spinning particles at finite Reynolds number in Chapter 5. It is shown that a secondary meridional circulation develops around a spinning particle at finite Reynolds numbers and, due to this secondary flow, there is a net repulsive hydrodynamic force between a pair of rotating coplanar spheres. Although qualitatively correct, we found that FCM underestimates the magnitude of the secondary flow. It is shown that adding a correction force based on the perturbation analysis can improve the result. However, development of a general and robust correction scheme needs further studies.

In Chapter 6, the effects of fluid inertia on rheology and particle dynamics are studied for the volume fractions $0.2 \leq \phi \leq 0.4$ for the range of the particle Reynolds numbers $0.005 \leq Re_{\dot{\gamma}} \leq 2$. Unexpectedly, the velocity fluctuation is found to be a decreasing function of $Re_{\dot{\gamma}}$. However, as the motion of the particles has a longer correlation at finite $Re_{\dot{\gamma}}$, the

diffusivity increases at larger $Re_{\dot{\gamma}}$. It is shown that the particle shear stress increases with the increase in $Re_{\dot{\gamma}}$. On the other hand, the particle normal stresses exhibit non-monotonic behaviors. The normal stresses in the flow and vorticity directions decrease as $Re_{\dot{\gamma}}$ increases. The normal stress in the velocity-gradient direction is shown to be an increasing function of $Re_{\dot{\gamma}}$ at $\phi = 0.2$, while that for $\phi = 0.3$ increases at first and starts to decrease when $Re_{\dot{\gamma}} \geq 0.1$, which changes to a monotonically decreasing function of $Re_{\dot{\gamma}}$ at $\phi = 0.4$. We introduced a weighted pair-distribution function in the plane of shear to investigated the microstructural changes at finite Reynolds number in more details. The normal stress in the flow direction shows a monotonic decrease at the increase in $Re_{\dot{\gamma}}$ over all azimuthal angles θ. The normal stress in the velocity-gradient direction has positive and negative peaks around the compressive and expansive principal axes, respectively, at $Re_{\dot{\gamma}} = 0.005$. For $\phi = 0.2$, the positive peak grows rapidly with the increase in $Re_{\dot{\gamma}}$, while the growth of positive peak is significantly attenuated at larger ϕ, which explains the non-monotonic behavior of the normal stress in the velocity-gradient direction. It is important to note that all the variables in this study is normalized by the shear rate $\dot{\gamma}$. At zero Reynolds number, the only timescale is the shear rate $\dot{\gamma}$. In other words, a suspension quantity obtained in a Couette device with a shear rate $\dot{\gamma}_1$ should be identical to the same quantity obtained in a same Couette device with a different shear rate $\dot{\gamma}_2$, once normalized by the corresponding shear rates. However, this is no longer true at finite Reynolds numbers. There may exist multiple timescales. For example, it is shown that, at short time, the decaying rate of the velocity auto-correlation is an increasing function of $Re_{\dot{\gamma}}$, which changes to a decreasing function of $Re_{\dot{\gamma}}$ at the intermediate timescale. Determining the characteristic timescale of suspensions under finite fluid inertia is a subject of further investigation.

In Chapter 7, we considered the modulation of turbulence by suspensions of finite-sized heavy particles, neutrally-buoyant particles, or bubbles in isotropic turbulence. The particle size is chosen to be in between the Kolmogorov scale and the Taylor microscale. To maintain turbulence, a stochastic forcing is applied at small wave numbers. It is shown that the major effect of the finite-size particles is to redistribute the turbulent kinetic energy and dissipation rate, instead of simply increasing or decreasing a certain wave number mode. The turbulent kinetic energy at the lengthscales smaller than the particle diameter is noticeably augmented, the turbulent energy is attenuated over a range of intermediate wavenumbers, lengthscales larger than the particle size. It is shown that the Eulerian statistics, such as

the turbulent kinetic energy and dissipation rate spectra, are not altered noticeably by the types of the suspended particles, positively, neutrally, or negatively buoyant particles, while the effects of the particle inertia are pronounced in the Lagrangian statistics. It is shown that both the velocity and acceleration auto-correlations of the bubbles decay faster than those of the neutrally buoyant particles. The heavy particles have the longest correlation time among the types of the particles considered. Near a vortex tube, bubbles tend to spiral inward to the core of a vortex core, while neutrally-buoyant particles rotate around the vortex following the streamline. On the other hand, heavy particles, which has a long relaxation time, tend to penetrate the vortex. These different responses near a vortex explain the differences observed in the Lagrangian statistics.

8.2 Future directions

In this thesis, we developed LC-FCM to simulate wall-bounded suspension flows. As a first step to understand fundamental physics of wall-bounded suspensions, we focused on an idealized system, suspensions of monodisperse hard spheres with a short-ranged repulsive potential force. However, it should be noted that still there is a gap between the idealized numerical and laboratory experimental systems. One of the open questions in the numerical simulation of suspension flows is the effects of the interparticle potential force. Mathematically, spheres immersed in liquid can never contact because the lubrication force becomes singular as the gap between two spheres goes to zero. In experiments, the suspended particles are not perfect spheres and small asperities on the particle surface result in an actual contact between the suspended particles. Most, if not all, of the numerical techniques use a short-ranged repulsive potential force to model such a non-hydrodynamic effect. Even though it is now well known that the computed rheology depends on the form of this short-ranged force, there has been no systematic study to find a physically sound model of non-hydrodynamic forces. For a more realistic computer simulation, one needs to construct a more robust contact force model.

Another important issue in the computer simulations of suspension flows is that the suspended particles in physical systems are polydispersed, while most simulations have been working on monodisperse systems. Even for the bi-disperse suspensions, there are only very limited number of numerical studies and most of them are either in two-dimensional simu-

lations [31, 32] or in semi-dilute limit [2]. In LC-FCM, provided that the analytical solution is given in literature, it is very straightforward to extend to polydisperse suspensions. In the standard FCM, the polydisperse simulation can be done simply by changing the length-scales (σ_M and σ_D) of the regularized multipoles according to the particle radius. The only additional effort to use LC-FCM for polydisperse suspensions is computing two-body FCM resistance matrices for each particle size ratio numerically. Including the new two-body lubrication matrix into the LC-FCM formulation given in 2.3.1 is trivial.

In this thesis, we considered only one of the most fundamental confinements, suspension flows bounded by two parallel walls. However, in most engineering flows, the flow geometry is much more complicated. For example, many microfluidic mixing devices use chaotic mixing strategies, in which three-dimensional flow structure is important. In LC-FCM, one can simulate these three-dimensional suspension flows without any additional complications.

In 2.4, LC-FCM for finite inertia suspensions was developed and we studied the effects of finite fluid inertia on suspension dynamics in Chapter 6. The suspension dynamics at finite Reynolds number is a virtually unexplored field. Here, we investigated the dynamics in a homogeneous linear shear flow, in which the bulk lengthscale is indefinite. In a wall-bounded system, there is a clear separation of the scales. The bulk dynamics is related to the Reynolds number based on the characteristic length of the confinement and the bulk flow rate, while the particle-scale local dynamics is determined by the particle-scale Reynolds number. However, there is no study about the interplay between the bulk dynamics and the particle-scale dynamics. LC-FCM simulations for the finite-inertia wall-bounded suspensions can be conducted easily by modifying the current LC-FCM code for the wall-bounded Stokes flows.

In Chapter 7, we showed that the Eulerian statistics are not sensitive to the types of the suspended particles, whether they are heavy, neutrally-buoyant, or light particles, while the effects of the particle inertia are reflected in the Lagrangian statistics. In the same context, it would be instructive to investigate the modulation of turbulence by particle suspensions from the Lagrangian statistics of fluid element (massless and volumeless tracer particle). Study of the Lagrangian dynamics of tracer particles is important in understanding the turbulent mixing and heat transfer. This study can be readily conducted by using the standard FCM technique with some additional functions to compute the fluid velocity at the location of a tracer particle from an interpolation from the neighboring grid points.

When we performed the simulations, the particle acceleration term was treated explicitly. Due to the severe CFL condition, the simulations were limited only to the low Stokes-number particles, of which density ρ_p is close to that of the fluid density ρ_f, $\rho_p/\rho_f < 2$. In 2.4, we presented an implicit discretization of the particle acceleration term, which can be used for any density ratio. It will be interesting to investigate the turbulence-particle interaction for suspensions of large Stokes-number particles, *i.e.* gas-solid multiphase turbulent flows.

Appendix A

Analytical resistance functions

The theoretical, asymptotic expressions for the particle-wall resistance functions can be found in the literature [42, 22, 50]. Due to the typographical errors in some sources, we list the near-field forms of the resistance functions used in the simulation.

For the particle-wall interactions, as the gap $\epsilon \to 0$,

$$\begin{aligned}
X^A &= \frac{1}{\epsilon} - \frac{1}{5}\log\epsilon + 0.8193 - \frac{1}{21}\epsilon\log\epsilon, \\
Y^A &= -\frac{8}{15}\log\epsilon + 0.9557 - \frac{64}{375}\epsilon\log\epsilon, \\
Y^B &= \frac{2}{15}\log\epsilon + 0.2568 + \frac{86}{375}\epsilon\log\epsilon, \\
X^C &= 1.2021 + \frac{1}{2}\epsilon\log\epsilon, \\
Y^C &= -\frac{2}{5}\log\epsilon + 0.3720 - \frac{66}{125}\epsilon\log\epsilon, \\
Y^G &= -\frac{2}{3}\left(\frac{7}{10}\log\epsilon + 0.923 + \frac{221}{250}\epsilon\log\epsilon\right), \\
Y^H &= \frac{1}{10}\log\epsilon + 0.0916 - \frac{2}{250}\epsilon\log\epsilon.
\end{aligned}$$

The near-field form of the particle-particle resistance functions is given in Table A.1.

Table A.1: Near field forms of scalar resistance functions

X_{11}^A	=	$\frac{1}{4}\epsilon^{-1} - \frac{9}{40}\log\epsilon - \frac{3}{112}\epsilon\log\epsilon + 0.9946 + O(\epsilon)$
X_{12}^A	=	$-\frac{1}{4}\epsilon^{-1} + \frac{9}{40}\log\epsilon + \frac{3}{112}\epsilon\log\epsilon - 0.3510 + O(\epsilon)$
X_{11}^C	=	$\frac{1}{8}\epsilon\log\epsilon + 1.0518 + O(\epsilon)$
X_{12}^C	=	$-\frac{1}{8}\epsilon\log\epsilon - 0.1503 + O(\epsilon)$
X_{11}^G	=	$\frac{1}{4}\epsilon^{-1} - \frac{9}{40}\log\epsilon - \frac{39}{280}\epsilon\log\epsilon - 0.3127 + O(\epsilon)$
X_{12}^G	=	$-\frac{1}{4}\epsilon^{-1} + \frac{9}{40}\log\epsilon + \frac{39}{280}\epsilon\log\epsilon + 0.1300 + O(\epsilon)$
Y_{11}^A	=	$-\frac{1}{6}\log\epsilon + 0.9983 + O(\epsilon)$
Y_{12}^A	=	$\frac{1}{6}\log\epsilon - 0.2737 + O(\epsilon)$
Y_{11}^B	=	$\frac{1}{6}\log\epsilon + \frac{1}{12}\epsilon\log\epsilon + 0.1594 + O(\epsilon)$
Y_{12}^B	=	$-\frac{1}{6}\log\epsilon - \frac{1}{12}\epsilon\log\epsilon - 0.0011 + O(\epsilon)$
Y_{11}^C	=	$-\frac{1}{5}\log\epsilon - \frac{47}{200}\epsilon\log\epsilon + 0.7029 + O(\epsilon)$
Y_{12}^C	=	$-\frac{1}{20}\log\epsilon - \frac{31}{500}\epsilon\log\epsilon + 0.0274 + O(\epsilon)$
Y_{11}^G	=	$-\frac{1}{12}\log\epsilon - \frac{1}{24}\epsilon\log\epsilon - 0.0947 + O(\epsilon)$
Y_{12}^G	=	$\frac{1}{12}\log\epsilon + \frac{1}{24}\epsilon\log\epsilon + 0.0687 + O(\epsilon)$
Y_{11}^H	=	$-\frac{1}{40}\log\epsilon - \frac{137}{2000}\epsilon\log\epsilon - 0.0741 + O(\epsilon)$
Y_{12}^H	=	$-\frac{1}{10}\log\epsilon - \frac{113}{2000}\epsilon\log\epsilon - 0.0294 + O(\epsilon)$

Bibliography

[1] M. Abbas. *Auto-diffusion de particules dans un ecoulement cisaille: Des interactions hydrodynamiques aux effets collisionnels*. PhD thesis, Institut National Polytechnique de Toulouse, 2008.

[2] M. Abbas, E. Climent, O. Simonin, and M. R. Maxey. Dynamics of bidisperse suspensions under Stokes flows: Linear shear flow and sedimentation. *Phys. Fluids*, 18:121504, 2006.

[3] J.R. Abbott, N. Tetlow, A.L. Graham, S.A. Altobelli, E. Fukushima, L.A. Mondy, and T.S. Stephens. Experimental observation of particle migration in concentrated suspensions: Couette flow. *J. Rheol.*, 35:773, 1991.

[4] B. J. Ackerson. Shear induced order and shear processing of model hard-sphere suspensions. *J. Rheol.*, 34:553, 1990.

[5] A. Acrivos. The rheology of concentrated suspensions of non-colloidal particles. In M. C. Roco, editor, *Particulate two-phase flow*, page 169. Butterworth-Heinemann, 1993.

[6] A. Acrivos. Shear-induced particle diffusion in concentrated suspensions of noncolloidal particles. *J. Rheol.*, 39:813, 1995.

[7] E. S. Asmolov. Shear-induced self-diffusion in a wall-bounded dilute suspension. *Phys. Rev. E*, 77:066312, 2008.

[8] I. Babuška. Error bounds for the finite element method. *Numer. Math.*, 16:322, 1971.

[9] J. A. Backer, C. P. Lowe, H. C. J. Hoefsloot, and P. D. Iedema. Poiseuille flow to measure the viscosity of particle model fluids. *J. Chem. Phys.*, 122:154503, 2005.

[10] J. C. Bacri, R. Perzynski, M. I. Shliomis, and G. Burde. Negative-viscosity effect in a magnetic fluid. *Phys. Rev. Lett.*, 75:2128, 1995.

[11] P. Bagchi and S. Balachandar. Effect of free rotation on the motion of a solid sphere in linear shear flow at moderate Re. *Phys. Fluids*, 14:2719, 2002.

[12] S. Balachandar and J. K. Eaton. Turbulent dispersed multiphase flow. *Ann. Rev. Fluid Mech.*, 42:111, 2010.

[13] G. K. Batchelor. The stress system in a suspension of force-free particles. *J. Fluid Mech.*, 41:545, 1970.

[14] G. K. Batchelor and J. T. Green. The determination of the bulk stress in a suspension of spherical particles to order c^2. *J. Fluid Mech.*, 56:401, 1972.

[15] G. K. Batchelor and J. T. Green. The hydrodynamic interaction of two small freely-moving spheres in a linear flow field. *J. Fluid Mech.*, 56:375, 1972.

[16] G.K. Batchelor. *An Introduction to Fluid Dynamics*. Cambridge University Press, 1967.

[17] W. G. Bickley. The secondary flow due to a sphere rotating in a viscous liquid. *Philos. Mag.*, 25:746, 1938.

[18] J. R. Blake and A. T. Chwang. Fundamental singularities of viscous flow. *J. Engng. Math.*, 8:23, 1974.

[19] J. J. Bluemink, D. Lohse, A. Prosperetti, and L. van Wijngaarden. A sphere in a uniformly rotating or shearing flow. *J. Fluid Mech.*, 600:201, 2008.

[20] E. Bodenschatz, S. P. Malinowski, R. A. Shaw, and F. Stratmann. Can we understand clouds without turbulence? *Science*, 327:970, 2010.

[21] M. Boivin, O. Simonin, and K. Squires. Direct numerical simulation of turbulence modulation by particles in isotropic turbulence. *J. Fluid Mech.*, 375:235, 1998.

[22] G. Bossis, A. Meunier, and J. D. Sherwood. Stokesian dynamics simulations of particle trajectories near a plane. *Phys. Fluids A*, 3:1853, 1991.

[23] J. F. Brady. Computer simulation of viscous suspensions. *Chem. Engng. Science*, 56:2921, 2001.

[24] J. F. Brady and G. Bossis. Stokesian Dynamics. *Annu. Rev. Fluids*, 20:111, 1988.

[25] J. F. Brady and J. F. Morris. Microstructure of strongly sheared suspensions and its impact on rheology and diffusion. *J. Fluid Mech.*, 348:103, 1997.

[26] V. Breedveld, D. van den Ende, D. Jomgschaap, and R. Mellema. Shear-induced diffusion and rheology of noncolloidal suspensions: Timescales and particle displacements. *J. Chem. Phys.*, 114:5923, 2001.

[27] H. Brenner. Rheology of two-phase systems. *Annu. Rev. Fluid Mech.*, 2:137, 1970.

[28] H. Brenner and M. E. O'Neill. On the Stokes resistance of multiparticle systems in a linear shear field. *Chem. Engng. Sci.*, 27:1421, 1972.

[29] F. Brezzi. On the existence, uniqueness and approixmation of saddle-point problems arising from Lagrangian multipliers. *RAIRO Anal. Numer.*, 8 R2:129, 1974.

[30] E. Calzavarini, M. Kerscher, D. Lohse, and F. Toschi. Dimensionality and morphology of particle and bubble clusters in turbulent flow. *J. Fluid Mech.*, 607:13, 2008.

[31] C. Y. Chang and R. L. Powell. Dynamic simulation of bimodal suspensions of hydrodynamically interacting spherical particles. *J. Fluid Mech.*, 253:1, 1994.

[32] C. Y. Chang and R. L. Powell. Self-diffusion of bimodal suspensions of hydrodynamically interacting spherical particles in shearing flow. *J. Fluid Mech.*, 281:51, 1994.

[33] B. Chun and A. J. C. Ladd. Inertial migration of neutrally buoyant particles in a square duct: An investigation of multiple equilibrium positions. *Phys. Fluids*, 18:031704, 2006.

[34] B. Cichocki, M. L. Ekiel-Jezewska, and E. Wajnryb. Lubrication corrections for three-particle contribution to short-time self-diffusion coefficients in colloidal dispersions. *J. Chem. Phys.*, 111:3265, 1999.

[35] B. Cichocki and B. U. Felderhof. Short-time diffusion coefficients and high frequency viscosity of dilute suspensions of spherical Brownian particles. *J. Chem. Phys.*, 89:1049, 1988.

[36] B. Cichocki, R. B. Jones, R. Kutteh, and E. Wajnryb. Friction and mobility for colloidal spheres in Stokes flow near a boundary: The multipole method and applications. *J. Chem. Phys.*, 112:2548, 2000.

[37] E. Climent. Personal communacation. 2007.

[38] E. Climent and M.R. Maxey. Numerical simulations of random suspensions at finite reynolds numbers. *Int. J. Multiphase Flow*, 29:579, 2003.

[39] E. Climent, K. Yeo, M. R. Maxey, and G. E. Karniadakis. Dynamic self-assembly of spinning particles. *J. Fluid Eng.*, 129:379, 2007.

[40] I. Cohen, T. G. Mason, and D. A. Weitz. Shear-induced configurations of confined colloidal suspensions. *Phys. Rev. Lett.*, 93:046001, 2004.

[41] G. R. Cokelet. Viscometric, *in vitro* and *in vivo* blood viscosity relationships: how are they related? *Biorheol.*, 36:343, 1999.

[42] R. M. Corless and D. J. Jeffrey. Stress moments of nearly touching spheres in low Reynolds number flows. *J. Appl. Math. Phys. (ZAMP)*, 39:874, 1988.

[43] L. Corté, P. M. Chaikin, J. P. Gollub, and D. J. Pine. Random organization in periodically driven systems. *Nature Phys.*, 4:420, 2008.

[44] L. Corté, S. J Gerbode, W. Man, and D. J. Pine. Self-organized criticality in sheared suspensions. *Phys. Rev. Lett.*, 103:248301, 2009.

[45] D. J. Courtemanche and F. van Swol. Wetting state of a crystal-fluid system of hard spheres. *Phys. Rev. Lett.*, 69:2078, 1992.

[46] S. Cutillas, G. Bossis, and A. Cebers. Flow-induced transition from cylindrical to layered patterns in magnetorheological suspensions. *Phys. Rev. E*, 57:804, 1998.

[47] F. R. Da Cunha and E. J. Hinch. Shear-induced dispersion in a dilute suspension of rough spheres. *J. Fluid Mech.*, 309:211, 1996.

[48] G. G. Dahlquist. A special stability problem for linear multistep methods. *BIT*, 3:27, 1963.

[49] S. L. Dance, E. Climent, and M. R. Maxey. Collision barrier effects on the bulk flow in a random suspension. *Phys. Fluids*, 16:828, 2004.

[50] S. L. Dance and M. R. Maxey. Incorporation of lubrication effects into force-coupling method for particulate two-phase flow. *J. Comput. Phys.*, 189:212, 2003.

[51] S. L. Dance and M. R. Maxey. Particle density stratification in transient sedimentation. *Phys. Rev. E*, 68:031403, 2003.

[52] A. Deboeuf, G. Gauthier, J. Martin, Y. Yurkovetsky, and J. F. Morris. Particle pressure in a sheared suspension: A bridge from osmosis to granular dilatancy. *Phys. Rev. Lett.*, 102:108301, 2009.

[53] S. C. R. Dennis, S. N. Singh, and D. B. Ingham. The steady flow due to a rotating sphere at low and moderate Reynolds number. *J. Fluid Mech.*, 101:257, 1980.

[54] D. Derks, Y.L. Wu, A. van Blaaderen, and A. Imhof. Dynamics of colloidal crystals in shear flow. *Soft Matter*, 5:1060, 2009.

[55] Suchuan Dong, Jin Xu, Martin Maxey, and George Karniadakis. Microbubble dynamics in turbulent channel flow. In *2nd International Symposium on Seawater Drag Reduction, Busan, Korea*, 2005.

[56] J. J. Dongarra, I. S. Duff, D. C. Sorensen, and H. A. van der Vorst. *Numerical Linear Algebra on High-Performance Computers*. SIAM, 1998.

[57] D. I. Dratler and W. R. Schowalter. Dynamic simulation of suspensions of non-Brownian hard spheres. *J. Fluid Mech.*, 325:53, 1996.

[58] G. Drazer, J. Koplik, B. Khusid, and A. Acrivos. Deterministic and stochastic behavior of non-Brownian spheres in sheared suspensions. *J. Fluid Mech.*, 460:307, 2002.

[59] G. Drazer, J. Koplik, B. Khusid, and A. Acrivos. Microsturucture and velocity fluctuations in sheared suspensions. *J. Fluid Mech.*, 511:237, 2004.

[60] G. Drazer and D. H. Zanette. Experimental evidence of power-law trapping-time disributions in porous media. *Phys. Rev. E*, 60:5858, 1999.

[61] D. A. Drew. Mathematical modeling of two-phase flow. *Ann. Rev. Fluid Mech.*, 15:261, 1983.

[62] O.A. Druzhinin and S. Elghobashi. On the decay rate of isotropic turbulence laden with microparticles. *Phys. Fluids*, 11:602, 1999.

[63] L. Durlofsky, J. F. Brady, and G. Bossis. Dynamic simulation of hydrodynamically interacting particles. *J. Fluid Mech.*, 180:21, 1987.

[64] E. C. Eckstein, D. G. Bailey, and A. H. Shapiro. Self-diffusion of particles in shear flow of a suspension. *J. Fluid Mech.*, 79:191, 1977.

[65] S. Elghobashi and G.C. Truesdell. On the two-way interaction between homogeneous turbulence and dispersed solid particles. Part I: Turbulence modification. *Phys. Fluids*, 5:1790, 1993.

[66] H. B. Eral, D. van den Ende, F. Mugele, and M. H. G. Duits. Influence of confinement by smooth and rough walls on particle dynamics in dense hard-sphere suspensions. *Phys. Rev. E*, 80:061403, 2009.

[67] V. Eswaran and S. Pope. An examination of forcing in direct numerical simulations of turbulence. *Comput. Fluids*, 16:257, 1988.

[68] S. Feng, A. L. Graham, R. Abbott, and H. Brenner. Antisymmetric stresses in suspensions: vortex viscosity and energy dissipation. *J. Fluid Mech.*, 563:97, 2006.

[69] A. Ferrante and S. Elghobashi. On the physical mechanisms of drag reduction in a spatially-developing turbulent boundary layer laden with bubbles. *J. Fluid Mech.*, 503:345, 2004.

[70] A. Ferrante and S. Elghobashi. Reynolds number effect on drag reduction in a microbubble-laden spatially developing turbulent boundary layer. *J. Fluid Mech.*, 543:93, 2005.

[71] M. Fialkowski, K. J. M. Bishop, R. Klajn, S. K. Smoukov, C. J. Campbell, and B. A. Grzybowski. Principles and implementations of dissipative (dynamic) self-assembly. *J. Phys. Chem. B*, 110:2482, 2006.

[72] A. Fortini and M. Dijkstra. Phase behaviour of hard spheres confined between parallel hard plates: manipulation of colloidal crystal structures by confinement. *J. Phys.: Condenses. Matter*, 18:L371, 2006.

[73] N. A. Frankel and A. Acrivos. On the viscosity of a concentrated suspension of solid spheres. *Chem. Engng. Sci.*, 22:847, 1967.

[74] P. Ganatos, R. Pfeffer, and S. Weinbaum. A numerical-solution technique for three-dimensional Stokes flows, with application to the motion of strongly interacting spheres in a plane. *J. Fluid Mech.*, 84:79, 1978.

[75] P. Ganatos, S. Weinbaum, and R. Preffer. A strong interaction theory for the creeping motion of a sphere between plane parallel boundaries. Part 1. Perpendicular motion. *J. Fluid Mech.*, 99:739, 1980.

[76] P. Ganatos, S. Weinbaum, and R. Preffer. Gravitational and zero-drag motion of a sphere of arbitrary size in an inclined channel at low Reynolds number. *J. Fluid Mech.*, 124:27, 1982.

[77] C. Gao, S. D. Kulkarni, J. F. Morris, and J. F. Gilchrist. Direct investigation of anisotropic suspension structure in pressure-driven flow. *Phys. Rev. E*, 81:041403, 2010.

[78] C. Gao, B. Xu, and J. F. Gilchrist. Mixing and sgregation of microspheres in microchannel flows of mono- and bidisperse suspensions. *Phys. Rev. E*, 79:036311, 2009.

[79] J. F. Gilchrist. Private communication. 2010.

[80] S. Granick. Soft matter in a tight spot. *Phys.Today*, 52:26, 1999.

[81] B. A. Grzybowski, H. A. Stone, and G. M. Whitesides. Dynamic self-assembly of magnetized, millimeter-sized objects rotating at a liquid-air interface. *Nature*, 405:1033, 2000.

[82] B. A. Grzybowski, H. A. Stone, and G. M. Whitesides. Dynamic self-assembly of magnetized disks rotating at the liquid-air interface. *PNAS*, 99:4147, 2002.

[83] J. S. Guasto, A. S. Ross, and J. P. Gollub. Hydrodynamic irreversibility in particle suspensions with nonuniform strain. *Phys. Rev. E*, 81:061401, 2010.

[84] R. E. Hampton, A. A. Mammoli, A. L. Graham, N. Tetlow, and S. A. Altobelli. Migration of particles undergoing pressure-driven flow in a circular conduit. *J. Rheol.*, 41:621, 1997.

[85] M. Han, C. Kim, M. Kim, and S. Lim. Particle migration in tube flow of suspensions. *J. Rheol.*, 43:1157, 1999.

[86] T. Hao. Electrorheological fluids. *Adv. Mater.*, 13:1847, 2001.

[87] J. Happel and H. Brenner. *Low Reynolds Number Hydrodynamics*. Prentice-Hall, 1965.

[88] M. D. Haw, W. C. K. Poon, and P. N. Pusey. Direct observation of oscillatory-shear-induced order in colloidal suspensions. *Phy. Rev. E*, 57:6859, 1998.

[89] E.J. Hinch. An averaged-equation approach to particle interactions in a fluid suspension. *J. Fluid Mech.*, 83:695, 1977.

[90] J. M. A. Hoffman. *Ph.D Thesis*. Technische University Eindhoven, 1999.

[91] H. H. Hu. Direct simulations of flows of solid-liquid mixtures. *Int. J. Multiphase flows*, 22:335, 1996.

[92] H. H. Hu, D. D. Joseph, and M. J. Crochet. Direct simulation of fluid-particle motions. *Thoer. Comput. Fluid Dyn.*, 3:285, 1992.

[93] W. Hwang and J.K. Eaton. Homogeneous and isotropic turbulence modulation by small heavy ($St \sim 50$) particles. *J. Fluid Mech.*, 564:361, 2006.

[94] W. T. Hwang and J. K. Eaton. Homogeneous and isotropic turbulence modulation by small heavy ($St \sim 50$) particles. *J. Fluid Mech.*, 564:361, 2006.

[95] W. T. Hwang and J. K. Eaton. Turbulence attenumation by small particles in the absence of gravity. *Int. J. Multiphase Flow*, 32:1386, 2006.

[96] K. Ichiki. Improvement of the Stokesian Dynamics method for systems with a finite number of particles. *J. Fluid Mech.*, 452:231, 2002.

[97] M. S. Ingber, S. Feng, A. L. Graham, and H. Brenner. The analysis of self-diffusion and migration of rough spheres in nonlinear shear flow using a traction-corrected boundary element method. *J. Fluid Mech.*, 598:267, 2008.

[98] L. Isa, R. Besseling, and W. C. K. Poon. Shear zones and wall slip in the capillary flow of concentrated colloidal suspensions. *Phys. Rev. Lett.*, 98:198305, 2008.

[99] S. C. Jana, B. Kapoor, and A. Acrivos. Apparent wall slip velocity coefficients in concentrated suspensions of noncolloidal particles. *J. Rheol.*, 39:1123, 1995.

[100] I. M. Jánosi, T. Tél, D. E. Wolf, and J. A. C. Gallas. Chaotic particle dynamics in viscous flows: The three-particle stokeslet problem. *Phys. Rev. E*, 56:2858, 1997.

[101] D. J. Jeffrey and Y. Onishi. Calculation of the resistance and mobility functions for two unequal rigid spheres in low-Reynolds-number flow. *J. Fluid Mech.*, 139:261, 1984.

[102] T. B. Jones. Quincke rotation of spheres. *IEEE Trans. IAS*, IA-20:845, 1984.

[103] G. E. Karniadakis, M. Israeli, and S. A. Orszag. High-order splitting methods for incompressible Navier-Stokes equations. *J. Comput. Phys.*, 97:414, 1991.

[104] G. E. Karniadakis and S. J. Sherwin. *Spectral/hp Element Methods for Computational Fluid Dynamics*. Oxford University Press, New York, 2005.

[105] A. Karnis, H. L. Goldsmith, and S. G. Mason. The kinetics of flowing dispersions: Concentrated suspensions of rigid particles. *J. Colloid Interface Sci.*, 22:531, 1966.

[106] T. Kawamura and Y. Kodama. Numerical simulation method to resolve interactions between bubbles and turbulence. *Int. J. Heat and Fluid Flow*, 23:627, 2002.

[107] E. E. Keaveny. *Ph.D Thesis*. Brown University, 2008.

[108] E. E. Keaveny and M. R. Maxey. Interaction between comoving magnetic microswimmers. *Phys. Rev. E*, 77:041910, 2008.

[109] K.T. Kiger and C. Pan. Suspension and turbulence modification effects of solid particulates on a horizontal turbulent channel flow. *J. Turbulence*, 3:N19, 2002.

[110] S. Kim and S. J. Karrila. *Microhydrodynamics: Principles and Selected Applications*. Butterworth-Heinemann, 1991.

[111] D. J. Klingenberg. Magnetorheology: Application and Challenges. *AIChE J.*, 47:246, 2001.

[112] C. J. Koh, L. G. Leal, and P. A. Hookham. An experimental investigation of concentrated suspension flow in a rectangular channel. *J. Fluid Mech.*, 256:1, 1994.

[113] A. Komnik, J. Harting, and H. J. Herrmann. Transport phenomena and structuring in shear flow of suspensions near solid walls. *J. Stat. Mech.: Theor. Exp.*, page P12003, 2004.

[114] C. A. Kossack and A. Acrivos. Steady simple shear flow past a circular cylinder at moderate Reynolds number: a numerical solution. *J. Fluid Mech.*, 66:353, 1974.

[115] I. M. Krieger and T. J. Dogherty. A mechanism for non-newtonian flow in suspensions of rigid spheres. *Trans. Soc. Rheol.*, 3:137, 1959.

[116] J. Kromkamp, D. van den Ende, D. Kandhai, R. van der Sman, and R. Boom. Lattice Boltzmann simulation of 2d and 3d non-Brownian suspensions in Couette flow. *Chem. Engng. Sci.*, 61:858, 2006.

[117] J. Kromkamp, D. van den Ende, D. Kandhai, R. van der Sman, and R. M. Boom. Shear-induced self-diffusion and microstructure in non-Brownian suspensions at non-zero Reynolds numbers. *J. Fluid Mech.*, 529:253, 2005.

[118] P. M. Kulkarni and J. F. Morris. Pair-sphere trajectories in finite-Reynolds-number shear flow. *J. Fluid Mech.*, 596:413, 2008.

[119] P. M. Kulkarni and J. F. Morris. Suspension properties at finite Reynolds number from simulated shear flow. *Phys. Fluids*, 20:040602, 2008.

[120] S. D. Kulkarni and J. F. Morris. Ordering transition and structural evolution under shear in Brownian suspensions. *J. Rheol.*, 53:417, 2009.

[121] A. J. C. Ladd. Hydrodynamic transport coefficients of random dispersions of hard spheres. *J. Chem. Phys.*, 93:3484, 1990.

[122] H. Lamb. *Hydrodynamics*. Cambridge University Press, Cambridge, UK, 1932.

[123] M. Lance and J. Bataille. Turbulence in the liquid phase of a uniform bubbly air-water flow. *J. Fluid Mech.*, 222:95, 1991.

[124] C. Lee, K. Yeo, and J.-I. Choi. Intermittent nature of acceleration in turbulence. *Phys. Rev. Lett.*, 92:144502, 2004.

[125] A.W. Lees and S.F. Edwards. The computer study of transport processes under extreme conditions. *J. Phys. C*, 5:1921, 1972.

[126] D. Leighton and A. Acrivos. The shear-induced migration of particles in concentrated suspensions. *J. Fluid Mech.*, 181:415, 1987.

[127] E. Lemaire, L. Lobry, N. Pannacci, and F. Peters. Viscosity of an electro-rheological suspension with internal rotations. *J. Rheol.*, 52:769, 2008.

[128] D. Lhuillier. Migration of rigid particles in non-Brownian viscous suspensions. *Phys. Fluids*, 21:023302, 2009.

[129] C. N. Likos. Effective interations in soft condensed matter physics. *Phys. Rep.*, 348:267, 2001.

[130] C.-J. Lin, J. H. Peery, and W. R. Schowalter. Simple shear flow round a rigid sphere: inertial effects and suspension rheology. *J. Fluid Mech.*, 44:1, 1970.

[131] D. Liu, E. E. Keaveny, M. R. Maxey, and G. E. Karniadakis. Force coupling method for flows with ellipsoidal particles. *J. Comput. Phys.*, 228:3559, 2009.

[132] D. Liu, M.R. Maxey, and G.E. Karniadakis. A fast method for particulate microflows. *J. Microelectromech. Sys.*, 11:691–702, 2002.

[133] D. Liu, M.R. Maxey, and G.E. Karniadakis. Modeling and optimization of colloidal micro-pumps. *J. Micromech. Microeng.*, 14:567–575, 2004.

[134] L. Lobry and E. Lemaire. Viscosity decrease induced by a DC electric field in a suspension. *J. Electrost.*, 47:61, 1999.

[135] S. Lomholt and M. R. Maxey. Force-coupling method for particulate two-phase flow: Stokes flow. *J. Comput. Phys.*, 184:381, 2003.

[136] S. Lomholt, B. Stenum, and M. R. Maxey. Experimental verification of the force coupling method for particulate flows. *Int. J. Multiphase flow*, 28:225, 2002.

[137] J. Lu, A. Fernandez, and G. Tryggvason. The effect of bubbles on the wall shear in a turbulent channel flow. *Phys. Fluids*, 17:095102, 2005.

[138] F. Lucci, A. Ferrante, and S. E. Elghobashi. Modulation of isotropic turbulence by particles of Taylor-lengthscale size. *J. Fluid Mech.*, 650:5, 2010.

[139] M. K. Lyon and L. G. Leal. An experimental study of the motion of concentrated suspensions in two-dimensional channel flow. Part 1. Monodisperse systems. *J. Fluid Mech.*, 363:25, 1998.

[140] Y. Maday, D. Meiron, A. T. Patera, and E. M. Rønquist. Analysis of iterative methods for the steady and unsteady stokes problem: application to spectral element discretizations. *SIAM J. Sci. Comput.*, 14:310, 1993.

[141] M. Marchioro and A. Acrivos. Shear-induced particle diffusivities from numerical simulations. *J. Fluid Mech.*, 443:101, 2001.

[142] M. Marchioro, M. Tanksley, and A. Prosperetti. Mixture pressure and stress in disperse two-phase flow. *Int. J. Multiphase flow*, 25:1395, 1999.

[143] M. Marchioro, M. Tanksley, and A. Prosperetti. Flow of spatially non-uniform suspensions. Part I: Phenomenology. *Int. J. Multiphase flow*, 26:783, 2000.

[144] M. R. Maxey and B. K. Patel. Localized force representations for particles sedimenting in Stokes flow. *Int. J. Multiphase Flow*, 27:1603 – 1626, 2001.

[145] M.R. Maxey. The motion of small spherical particles in a cellular flow field. *Phys. Fluids*, 30:1915, 1987.

[146] M.R. Maxey. Examples of fluid-particle interactions in dispersed two-phase flows. In *Paper AIAA 99-3691, 30th AIAA Fluid Dynamics Conference, Norfolk, VA.*, 1999.

[147] M.R. Maxey, D. Liu, S. Dong, and G.E. Karniadakis. New advances in force-coupling method: from micro to macro. In S. Balachandar and A. Prosperetti, editors, *Proceedings of IUTAM Symposium on Computational Approaches to Disperse Multiphase Flow*, page 237. Springer, 2006.

[148] I.M. Mazzitelli and D. Lohse. The effect of microbubbles on developed turbulence. *Phys. Fluids*, 15:L5, 2003.

[149] I.M. Mazzitelli, D. Lohse, and F. Toschi. On the relevance of the lift force in bubbly turbulence. *J. Fluid Mech.*, 488:283, 2003.

[150] J. M. McMullan and N. J. Wagner. Directed self-assembly of suspensions by large amplitude oscillatory shear flow. *J. Rheol.*, 53:575, 2009.

[151] J. R. Melrose and R. C. Ball. "Contact networks" in continuously shear thickening colloids. *J. Rheol.*, 48:961, 2004.

[152] A. Meunier and G. Bossis. The influence of surface forces on shear-induced tracer diffusion in mono and bidisperse suspensions. *Eur. Phys. J. E*, 506:285, 2004.

[153] V. N. Michailidou, G. Petekidis, J. W. Swan, and J. F. Brady. Dynamics of concentrated hard-sphere colloids near a wall. *Phys. Rev. Lett.*, 102:068302, 2009.

[154] D. R. Mikulencak and J. F. Morris. Stationary shear flow around fixed and free bodies at finite Reynolds number. *J. Fluid Mech.*, 520:215, 2004.

[155] R. M. Miller and J. F. Morris. Normal stress-driven migration and axial development in pressure-driven flow of concentrated suspensions. *J. Non-Newtonian Fluid Mech.*, 135:149, 2006.

[156] J. Mittal, T. M. Truskett, J. R. Errington, and G. Hummer. Layering and position-dependent diffusive dynamics of confined fluids. *Phys. Rev. Lett.*, 100:145901, 2008.

[157] N. Mordant, J. Delour, E. Levque, A. Arneodo, and J-F. Pinton. Long time correlations in lagrangian dynamics : a key to intermittency in turbulence. *Phys. Rev. Lett.*, 89:254502, 2002.

[158] J. F. Morris. Anomalous migration in simulated oscillatory pressure-driven flow of a concentrated suspension. *Phys. Fluids*, 13:2457, 2001.

[159] J. F. Morris. A review of microstructure in concentrated suspensions and its implications for rheology and bulk flow. *Rheol. Acta*, 48:909, 2009.

[160] J. F. Morris and F. Boulay. Curvilinear flows of noncolloidal suspensions: The role of normal stresses. *J. Rheol.*, 43:1213, 1999.

[161] Y. Murai, H. Fukuda, Y. Oishi, Y. Kodama, and F. Yamamoto. Skin friction reduction by large air bubbles in a horizontal channel flow. *Int. J. Multiphase Flow*, 33:147, 2007.

[162] N.-Q. Nguyen and A. J. C. Ladd. Lubrication corrections for lattice-Boltzmann simulations of particle suspensions. *Phys. Rev. E*, 66:046708, 2002.

[163] N.-Q. Nguyen and A. J. C. Ladd. Sedimentation of hard-sphere suspensions at low Reynolds number. *J. Fluid Mech.*, 525:73, 2005.

[164] P. R. Nott and J. F. Brady. Pressure-driven flow of suspensions: simulation and theory. *J. Fluid Mech.*, 275:157, 1994.

[165] C. R. Nugent, K. V. Edmond, H. N. Patel, and E. R. Weeks. Colloidal glass transition observed in confinement. *Phys. Rev. Lett.*, 99:025702, 2007.

[166] K. C. Nunan and J. B. Keller. Effective viscosity of a periodic suspension. *J. Fluid Mech.*, 142:269, 1984.

[167] J. M. Ottino. Mixing, chaotic advection, and turbulence. *Ann. Rev. Fluid Mech.*, 22:207, 1990.

[168] W. Pan, B. Caswell, and G. E. Karniadakis. Rheology, microstructure and migration in Brownian colloidal suspensions. *Langmuir*, 26:133, 2010.

[169] F. Parsi and F. Gadala-Maria. Fore-and-aft asymmetry in a concentrated suspension of solid spheres. *J. Rheol.*, 31:725, 1987.

[170] M. Parthasarathy and D. J. Klingenberg. Electrorheology: Mechanisms and models. *Mat. Sci. Engng. Rep.*, R17:57, 1996.

[171] N. A. Patankar and H. Hu. Finite Reynolds number effect on the rheology of a dilute suspension of neutrally buoyant circular particles in a newtonian fluid. *Int. J. Multiphase Flow*, 28:409, 2002.

[172] D. J. Pine, J. P. Gollub, J. F. Brady, and A. M. Leshansky. Chaos and threshold for irreversibility in sheared suspensions. *Nature*, 438:997, 2005.

[173] G.G. Poe and A. Acrivos. Closed-streamline flows past rotating single cylinders and spheres: inertia effects. *J. Fluid Mech.*, 72:605, 1975.

[174] A. La Porta, G.A. Voth, A.M. Crawford, J. Alexander, and E. Bodenschatz. Fluid particle accelerations in fully developed turbulence. *Nature*, 409:1017, 2001.

[175] C. Pozrikidis. A spectral element method for particulate Stokes flow. *J. Comput. Phys.*, 156:360, 1999.

[176] C. Pozrikidis. Dynamical simulation of the flow of suspensions: wall-bounded and pressure-driven channel flow. *Ind. Engng. Chem. Res.*, 41:6312, 2002.

[177] C. Pozrikidis. Flipping of an adherent blood platelet over a substrate. *J. Fluid Mech.*, 568:161, 2006.

[178] D. Psaltis, S. R. Quake, and C. Yang. Developing optofluidic technology through the fusion of microfluidics and optics. *Nature*, 442:381, 2006.

[179] P. N. Pusey and W. van Megen. Phase behaviour of concentrated suspensions of nearly hard colloidal spheres. *Nature*, 320:340, 1986.

[180] N.M. Qureshi, M. Bourgoin, C. Baudet, A. Cartellier, and Y. Gagne. Turbulent transport of material particles: An experimental study of finite size effects. *Phys. Rev. Lett.*, 99:184502, 2007.

[181] J. Rensen, S. Luther, and D. Lohse. The effects of bubbles on developed turbulence. *J. Fluid Mech.*, 538:153, 2005.

[182] S. A. Rice. Structure in confined colloid suspensions. *Chem. Phys. Lett.*, 479:1, 2009.

[183] R. S. Rogallo. *Technical Report 81315*. NASA, 1981.

[184] W. B. Russel, D. A. Saville, and W. R. Schowalter. *Colloidal Dispersions*. Cambridge University Press, 1989.

[185] P. G. Saffman. On the settling speed of free and fixed suspensions. *Stud. Appl. Math. LII*, page 115, 1973.

[186] W.C. Sanders, E.S. Winkel, D.R. Dowling, M. Perlin, and S.L. Ceccio. Bubble friction drag reduction in a high-Reynolds-number flat-plate turbulent boundary layer. *J. Fluid Mech.*, 552:353, 2006.

[187] A. S. Sangani and G. Mo. An o(n) algorithm for Stokes and Laplace interactions of particles. *Phys. Fluids*, 8:1990, 1996.

[188] P. S. Sarangapani and Y. Zhu. Impeded structural relaxation of a hard-sphere colloidal suspension under confinement. *Phy. Rev. E*, 77:010501(R), 2008.

[189] O. Sawatzki. Flow field around a rotating sphere. *Acta Mech.*, 9:159, 1970.

[190] B.L. Sawford. Reynolds number effects in Lagrangian stochastic models of dispersion. *Phys. Fluids A*, 3:1577, 1991.

[191] M. Schmidt and H. Löwen. Freezing between two and three dimensions. *Phys. Rev. Lett.*, 76:4552, 1996.

[192] M. Schmidt and H. Löwen. Phase diagram of hard spheres confined between two parallel plates. *Phys. Rev. E*, 55:7228, 1997.

[193] G. Segrè and A. Silberberg. Behaviour of macroscopic rigid spheres in Poiseuille flow Part 2. Experimental results and interpretation. *J. Fluid Mech.*, 14:136, 1962.

[194] D. Semwogerere, J. F. Morris, and E. R. Weeks. Development of particle migration in pressure-driven flow of a brownian suspension. *J. Fluid Mech.*, 581:437, 2007.

[195] D. J. Shaw. *Introduction to Colloid and Surface Chemistry.* Butterworths, Boston, London, 1980.

[196] A. Sierou and J. F. Brady. Accelerated Stokesian Dynamics simulations. *J. Fluid Mech.*, 448:115, 2001.

[197] A. Sierou and J. F. Brady. Rheology and microstructure in concentrated noncolloidal suspensions. *J. Rheol.*, 46:1031, 2002.

[198] A. Sierou and J. F. Brady. Shear-induced self-diffusion in non-colloidal suspensions. *J. Fluid Mech.*, 506:285, 2004.

[199] A. Singh and P. R. Nott. Normal stresses and microstructure in bounded sheared suspensions via Stokesian Dynamics simulations. *J. Fluid Mech.*, 412:279, 2000.

[200] J. R. Smart and D. T. Leighton. Measurement of the hydrodynamic surface roughness of noncolloidal spheres. *Phys. Fluids A*, 1:52, 1989.

[201] T. H. Solomon, E. R. Weeks, and H. L. Swinney. Observation of anomalous diffusion and lévy flights in a two-dimensional rotating flow. *Phys. Rev. Lett.*, 71:3975, 1993.

[202] K.D. Squires and J.K. Eaton. Particle response and turbulence modification in isotropic turbulence. *Phys. Fluids A*, 2:1191, 1990.

[203] J. J. Stickel and R. L. Powell. Fluid mechanics and rheology of dense suspensions. *Ann. Rev. Fluid Mech.*, 37:129, 2005.

[204] G. Subramanian and D. L. Koch. Inertial effects on the transfer of heat or mass from neutrally buoyant spheres in a steady linear velocity field. *Phys. Fluids*, 18:073302, 2006.

[205] S. Sundaram and L.R. Collins. Collision statistics in an isotropic particle-laden turbulent suspension. Part 1. Direct numerical simulation. *J. Fluid Mech.*, 335:75, 1997.

[206] S. Sundaram and L.R. Collins. A numerical study of the modulation of isotropic turbulence by suspended particles. *J. Fluid Mech.*, 379:105, 1999.

[207] J. W. Swan and J. F. Brady. Simulation of hydrodynamically interacting particles near a no-slip boundary. *Phys. Fluids*, 19:113306, 2007.

[208] A. ten Cate, J.J. Derksen, L.M. Portela, and H.E.A. van den Akker. Fully resolved simulations of colliding monodisperse spheres in forced isotropic turbulence. *J. Fluid Mech.*, 519:233, 2004.

[209] F. Toschi and E. Bodenschatz. Lagrangian properties of partices in turbulence. *Ann. Rev. Fluid Mech.*, 41:375, 2009.

[210] A. Tözeren and R. Skalak. Stress in a suspension near rigid boundaries. *J. Fluid Mech.*, 82:289, 1977.

[211] K. V. Tretiakov, K. J. M. Bishop, and B. A. Grzybowski. The dependence between forces and dissipation rates mediating dynamic self-assembly. *Soft Matter*, 5:1279, 2009.

[212] T.H. van den Berg, S. Luther, D.P. Lathrop, and D. Lohse. Drag reduction in bubbly Taylor-Couette turbulence. *Phys. Rev. Lett.*, 94:044501, 2005.

[213] T.H. van den Berg, S. Luther, and D. Lohse. Energy spectra in microbubbly turbulence. *Phys. Fluids*, 18:038103, 2005.

[214] T.H. van den Berg, S. Luther, I.M. Mazzitelli, J.M. Rensen, F. Toschi, and D. Lohse. Turbulent bubbly flow. *J. Turbulence*, 7:N14, 2006.

[215] R. Verberg and D. L. Koch. Rheology of particle suspensions with low to moderate fluid inertia at finite particle inertia. *Phys. Fluids*, 18:083303, 2006.

[216] R. Volk, E. Calzavarini, G. Verhille, D. Lohse, N. Mordant, J.-F. Pinton, and F. Toschi. Acceleration of heavy and light particles in turbulence: Comparison between experiments and direct numerical simulations. *Physica D*, 237:2084, 2008.

[217] G.A. Voth, A. La Porta, A.M. Crawford, J. Alexander, and E. Bodenschatz. Measurement of particle accelerations in fully developed turbulence. *J. Fluid Mech.*, 469:121, 2002.

[218] L.-P. Wang. Private communication. 2009.

[219] L.-P. Wang and M.R. Maxey. The motion of microbubbles in a forced isotropic and homogeneous turbulence. *Applied Scientific Res.*, 51:291, 1993.

[220] L.-P. Wang and M.R. Maxey. Settling velocity and concentration distribution of heavy particles in homogeneous isotropic turbulence. *J. Fluid Mech.*, 256:27, 1993.

[221] H. J. Wilson. An analytic form for the pair distribution function and rheology of a dilute suspension of rough spheres in plane strain flow. *J. Fluid Mech.*, 534:97, 2005.

[222] Y.L. Wu, D. Derks, A. van Blaaderen, and A. Imhof. Melting and crystallization of colloidal hard-sphere suspensions under shear. *PNAS*, 106:10564, 2009.

[223] H. Xu and E. Bodenschatz. Motion of inertial particles with size larger than Kolmogorov scale in turbulent flows. *Physica D*, 237:2095, 2008.

[224] J. Xu, M. R. Maxey, and G. E. Karniadakis. Numerical simulation of turbulent drag reduction using micro-bubbles. *J. Fluid Mech.*, 468:271, 2002.

[225] J. Xu, M.R. Maxey, and G.E. Karniadakis. DNS of turbulent drag reduction using micro-bubbles. In *AIAA 2003-1280, 41st Aerospace Sciences Meeting, Reno*, 2003.

[226] Y. G. Yan, J. F. Morris, and J. Koplik. Hydrodynamic interaction of two particles in confined linear shear flow at finite Reynolds number. *Phys. Fluids*, 19:113305, 2007.

[227] K. Yapici, R. L. Powell, and R. J. Philips. Particle migration and suspension structure in steady and oscillatory plane Poiseuille flow. *Phys. Fluids*, 21:053302, 2009.

[228] K. Yeo, S. Dong, E. Climent, and M. R. Maxey. Modulation of homogeneous turbulence seeded with finite size bubbles or particles. *Int. J. Multiphase Flow*, 36:221, 2010.

[229] K. Yeo and M. R. Maxey. Anomalous diffusion in wall-bounded non-Brownian suspensions under steady shear. *Europhys. Lett.*, 92:24008, 2010.

[230] K. Yeo and M. R. Maxey. Dynamics of concentrated suspensions of non-colloidal particles in Couette flow. *J. Fluid Mech.*, 649:205, 2010.

[231] K. Yeo and M. R. Maxey. Ordering transitions of non-Brownian suspensions in confined steady shear flow. *Phys. Rev. E*, 81:051502, 2010.

[232] K. Yeo and M. R. Maxey. Rheology and ordering transitions of non-Brownian suspensions in a confined shear flow: Effects of external torques. *Phys. Rev. E*, 81:062501, 2010.

[233] K. Yeo and M. R. Maxey. Simulation of concentrated suspensions using the force-coupling method. *J. Comput. Phys.*, 229:2401, 2010.

[234] K. Yeo and M. R. Maxey. Numerical simulations of concentrated suspensions of monodisperse particles in a Poiseuille flow. *J. Fluid Mech.*, in revision, 2011.

[235] P.K. Yeung and S.B. Pope. Lagrangian statistics from direct numerical simulations of isotropic turbulence. *J. Fluid Mech.*, 207:531, 1989.

[236] P.K. Yeung, S.B. Pope, A.G. Lamorgese, and D.A. Donzis. Acceleration and dissipation statistics of numerically simulated isotropic turbulence. *Phys. Fluids*, 18:065103, 2006.

[237] P.K. Yeung, S.B. Pope, and B.L. Sawford. Reynolds number dependence of Lagrangian statistics in large numerical simulations of turbulence. *J. Turbulence*, 7:N58, 2006.

[238] H. Yoshimoto and S. Goto. Self-similar clustering of inertial particles in homogeneous turbulence. *J. Fluid Mech.*, 577:275, 2007.

[239] W. R. Young. Arrested shear dispersion and other models of anomalous diffusion. *J. Fluid Mech.*, 193:129, 1988.

[240] Y. Yurkovetsky. *Ph.D Thesis*. California Institute of Technology, 1997.

[241] I. E. Zarraga, D. A. Hill, and D. T. Leighton. The characterization of the total stress of concentrated suspensions of noncolloidal spheres in Newtonian fluids. *J. Rheol.*, 44:185, 2000.

[242] Q. Zhang and A. Prosperetti. Physics-based analysis of the hydrodynamic stress in a fluid-particle system. *Phys. Fluids*, 22:033306, 2010.

[243] Z. Zhang and A. Prosperetti. A second-order method for three-dimensional particle simulation. *J. Comp. Phys.*, 210:292, 2005.

[244] M. Zurita-Gotor, J. Blawzdziewicz, and E. Wajnryb. Swapping trajectories: a new wall-induced cross-streamline particle migration mechanism in a dilute suspension of spheres. *J. Fluid Mech.*, 592:447, 2007.